Institute of Experimental Pharmacology and Toxicology
(Director: Prof. Dr. Thomas Eschenhagen)
Center for Experimental Medicine
University Medical Center Hamburg-Eppendorf

Murine engineered heart tissue (EHT) as a tool for modeling cardiac diseases and angiogenesis screening

Dissertation

In fulfillment of the requirements for the degree
Doctor of Natural Sciences

Submitted to the Department of Chemistry
Faculty of Mathematics, Informatics and Natural Sciences
University of Hamburg

by
Andrea Stöhr

Hamburg, 2012

“He looked tenderly into the rushing water, the transparent green, the crystal lines of this secret-filled sketch... The river looked at him with a thousand eyes: green ones, white ones, crystal ones, sky-blue ones… It seemed to him that he would understand this water and its secrets, and would also understand many other things, many secrets and all secrets… He saw that this water ran and ran incessantly, and nevertheless was always there at all times, the same and yet new every moment!”

Hermann Hesse, Siddhartha

.

1. Referee: Prof. Dr. Hans-Jürgen Duchstein
2. Referee: Prof. Dr. Thomas Eschenhagen

Date of the disputation: 09.11.2012

Declaration

I declare that the work reported in the dissertation submitted to the University of Hamburg and entitled

"Murine engineered heart tissue (EHT) as a tool for modeling cardiac diseases and angiogenesis screening"

was realized in person in the Institute of Experimental Pharmacology and Toxicology under the supervision of Prof. Dr. Thomas Eschenhagen. All sources of information as well as the results obtained in collaboration with other people are pointed out.

The dissertation has not been submitted in whole or in part for a degree at any other University.

Hamburg, August 2012

_____

Andrea Stöhr

Table of Contents

1 Introduction 1

1.1 Cardiovascular diseases 1

1.1.1 Heart failure 2
1.1.2 Hypertrophic cardiomyopathy 4

1.2 Mechanisms of cardiac contraction and relaxation 6

1.3 Cardiac myosin-binding protein C (cMyBP-C) 9

1.4 Animal models in biomedical research 11

1.4.1 Genetically modified mice to study human diseases 11

1.5 Tissue engineering 14

1.5.1 Engineered heart tissue (EHT) 14
1.5.2 Engineered heart tissue as a patch for the heart 17

1.6 Angiogenesis 20

1.7 Objectives 23

1.8 Concept 24

2 Material and Methods 25

2.1 Animal models 25

2.1.1 Animal models used for disease modeling 25
2.1.1.1 The homozygous *Mybpc3*-targeted knock-out mouse model 25
2.1.1.2 The homozygous *Mybpc3*-targeted knock-in mouse model 26
2.1.2 Animal models used for angiogenesis screening 27
2.1.2.1 The BMX-Cre-ER^{T2}-Rosa26-LacZ and the VE-Cadherin-Cre-ER^{T2}-Rosa26-LacZ mouse model 27

2.2 Genotyping 29

2.3 Induction of Cre expression in adult mice *in vivo* 30

2.4 Methods of cell culture 30

2.4.1 Organ extraction 30
2.4.2 Isolation of neonatal mouse heart cells with a trypsin-based digestion 30
2.4.3 Isolation of neonatal mouse heart cells with a collagenase-based digestion 32
2.4.4 Preparation of chick embryo extract (CEE) 32
2.4.5 Generation of fibrin-based mini EHTs in a 24-well format 33
2.4.6 EHT culture 35
2.4.6.1 Application of growth factors during EHT culture 35
2.4.7 Transduction of murine EHT with an adenovirus 36
2.4.8 Transfection of murine EHT 36

2.5 EHT contraction analysis 37

2.5.1 Video-optical recording 37
2.5.2 Measurement in electrically stimulated and perfused EHT 39
2.5.2.1 Experimental set-up and procedure 39
2.5.2.2 Measurement of contractile parameters with the IonOptix software 40

2.5.2.3 Fura-2 staining of EHT ... 41
2.5.2.4 Simultaneous measurements of force and intracellular Ca^{2+} transient with the CTMV software ... 43

2.6 EHT as a graft for transplantation studies ... 45

2.6.1 Immunodeficient mouse models ... 45
2.6.2 Implantation of EHT onto murine hearts ... 46
2.6.3 Mouse heart extraction ... 48
2.6.4 Perfusion fixation through the heart according to Langendorff ... 48
2.6.5 Implantation of EHT into the dorsal mouse skin ... 49

2.7 Histological analysis ... 50

2.7.1 X-gal staining ... 50
2.7.2 Paraffin embedding ... 51
2.7.3 Hematoxylin and Eosin staining ... 52
2.7.4 Eosin staining of X-gal-stained EHT cross sections ... 53
2.7.5 Immunohistochemistry ... 53
2.7.6 Immunofluorescence staining ... 53

2.8 Molecular analysis ... 54

2.8.1 RNA analysis ... 54
2.8.1.1 RNA isolation ... 54
2.8.1.2 Reverse transcription (RT) ... 54
2.8.1.3 Quantitative RT-PCR ... 55
2.8.2 DNA analysis ... 56
2.8.2.1 Isolation of DNA ... 56
2.8.3 Protein analysis ... 56
2.8.3.1 Protein extraction ... 56
2.8.3.2 Trizol based isolation of proteins ... 57
2.8.3.3 Determination of the protein concentration ... 57
2.8.3.4 SDS-PAGE ... 58
2.8.3.5 Western blot analysis ... 59

2.9 Statistical analysis ... 60

3 Results ... 61

3.1 Basic observations ... 61

3.1.1 Cell concentration in mouse EHT ... 62
3.1.2 EHT volume ... 65
3.1.3 Medium supplements ... 65

3.2 Modeling HCM: Results of *Mybpc3*-targeted KO and KI mouse EHTs ... 67

3.2.1 Histological analysis ... 68
3.2.1.1 Hematoxylin/eosin staining ... 68
3.2.1.2 Immunofluorescence staining ... 69
3.2.2 Video-optical recording ... 70
3.2.2.1 Contractile analysis under standard culture conditions ... 70
3.2.2.2 The Ca^{2+}-sensitizing drug EMD 57033 ... 73
3.2.3 Measurements of electrically stimulated EHTs ... 76
3.2.3.1 Effect of stimulation frequency ... 76
3.2.3.2 Response to external Ca^{2+} ... 81
3.2.3.3 Pharmacological provocation test ... 83
3.2.3.3.1 Verapamil ... 83
3.2.3.3.2 EMD 57033 in WT EHT ... 85
3.2.3.3.3 Effect of Ca^{2+} sensitization versus β-adrenergic stimulation ... 86
3.2.3.3.4 Ca^{2+} desensitization to rescue KO's phenotype ... 88
3.2.3.4 Simultaneous force and Ca^{2+} transient measurements in EHT ... 89

3.2.3.4.1 Ca^{2+} transient and force measurements in WT, KO and KI ... 91
3.2.3.4.2 Effect of EMD 57033 on Ca^{2+} transient and force in Fura-2-stained KO EHT ... 92
3.2.4 Molecular analysis of WT, KO and KI EHT ... 94
3.2.4.1 Determination of cMyBP-C and hypertrophic gene markers ... 94
3.2.4.2 DNA and RNA content ... 98
3.2.5 First attempts for gene therapy in KO EHT ... 99
3.2.5.1 Wild-type cMyBP-C adenovirus transduction ... 99
3.2.5.1.1 UV-light images ... 99
3.2.5.1.2 Video-optical recording ... 99
3.2.5.1.3 Measurements under electrical stimulation and perfusion ... 100
3.2.5.1.4 Immunofluorescence analysis ... 101
3.2.5.1.5 Molecular analysis ... 102
3.3 Visualization of endothelial cells in EHT ... 104
3.3.1 Establishment of BMX- and VE-Cadherin-Cre-ER^{T2}-Rosa26-LacZ mouse matings ... 104
3.3.2 Visualizing endothelial cells in EHT: VE-Cadherin versus BMX EHT ... 105
3.3.2.1 Characterization of BMX EHT ... 105
3.3.2.2 Characterization of VE-Cadherin EHT ... 107
3.3.2.3 Effect of different oxygen concentrations on endothelial cell density ... 109
3.3.3 Quantification of endothelial cells in EHT ... 110
3.3.3.1 Effect of growth factors on endothelial cell proliferation or migration ... 110
3.3.3.2 Effect of serum on vessel-like structure in VE-Cadherin EHT ... 111
3.3.3.3 Effect of microRNA-24 on endothelial cell density ... 113
3.4 EHT as a graft ... 115
3.4.1 Implantation of VE-Cadherin EHT into the dorsal skin ... 115
3.4.2 Implantation of mouse EHT onto the heart ... 116
4 Discussion ... 119
4.1 Establishment of murine fibrin-based mini EHT ... 120
4.1.1 Mouse matings and neonatal pups ... 121
4.1.2 Cell population and concentration ... 121
4.1.3 Murine EHT culture ... 122
4.2 Histological and physiological characterization of murine EHT ... 124
4.3 Murine EHT for modeling HCM ... 125
4.3.1 Contractile analysis under standard culture conditions ... 126
4.3.2 Measurements under electrical stimulation and perfusion ... 127
4.3.2.1 The effect of Ca^{2+} and pharmacological provocation tests ... 129
4.3.2.2 Effects of β-adrenergic stimulation ... 132
4.3.2.3 Evaluation of Ca^{2+} transient measurements in EHTs and the effect of Fura-2 ... 133
4.3.3 Molecular characterization of disease-specific EHT ... 134
4.3.4 Gene therapeutic approach ... 136
4.4 Endothelial cell labeling in mouse EHT ... 137
4.5 EHT as graft for implantation studies ... 140
4.6 Outlook ... 141
4.6.1 EHT for cardiac disease modeling ... 141
4.6.2 EHT for angiogenesis studies ... 142
5 Summary ... 143
5 Zusammenfassung ... 145

6 Literature 147

7 Appendix 160

7.1 List of abbreviations 160

7.2 List of chemicals 166

7.3 H- & P-Phrases 171

7.4 Consumable material 176

7.5 Laboratory equipment 177

7.6 Antibody list 178

7.7 Primer list and other tables 179

7.8 Supplemental figures 181

7.8.1 Effect of soluble growth factors on endothelial cell density in BMX EHTs in the presence of AraC 181

7.9 Structural formula 182

7.10 Curriculum vitae 183

7.11 Publications and congress participations 184

8 Acknowledgement 186

1 Introduction

The human heart is one of the most fascinating and important organs in living beings with a circulatory system. It works tirelessly from the moment it begins beating until it stops at the end of the lifetime. In an average life, the heart beats more than 2.5 billion times, without ever pausing to rest. The task of this muscular organ is to maintain the circulation of blood over a life time period by pumping the blood to the organs, tissues and cells of the body. A continuous blood flow throughout the vessels is achieved by repeated, rhythmic contractions. The sinoatrial node (SA) region in the human heart functions as a pacemaker, setting the rate and timing at which all cardiomyocytes contract. Few cells in the SA are able to generate electrical impulses, and since cardiomyocytes are electrically coupled by inter-calated disks between adjacent cells, this action potential can spread through the walls of the atria and subsequently to the walls of the ventricle. This entire cycle, a single heart beat, lasts about 0.8 seconds in humans and approximately 0.1–0.2 seconds in mice. It ensures a basic rhythm of about 70 heart beats per minute in humans. During the heart cycle electrical currents are produced, which spread throughout the body and can be recorded as electrocardiogram (ECG). Heart rate and force of contraction can be regulated by various mechanisms, which include the Frank-Starling mechanism, the positive force-frequency relationship and the regulation by the autonomous nervous system.

1.1 Cardiovascular diseases

Cardiovascular disease is the most common reason for morbidity and mortality worldwide, associated with enormous health care costs. In 2008, the leading cause of death worldwide was ischaemic heart disease (12.8%; 7.25 million people), followed by stroke and other cerebrovascular disease (10.8%; 6.15 million people). In high-income countries of our western world more than two thirds of all people live beyond the age of 70 and predominantly die of chronic diseases as cardiovascular disease, chronic obstructive lung disease, cancers, diabetes or dementia (WHO 2008). The prolonged life expectancy in rich countries is due to improved supply of nutrition and health care systems. Malnutrition in low- or middle-income countries remains the leading risk factor for health loss (Lopez et al. 2006).

1.1.1 Heart failure

Congestive heart failure (HF) has become an increasingly frequent reason for hospitalization. The Framingham Heart Study indicated that the incidence of HF increases with age and is higher in men than in women (Ho et al. 1993). HF is a clinical syndrome associated with high morbidity, mortality, quality of life impairment and characterized by impaired cardiac output that cannot meet the body's metabolic needs (Chiariello & Perrone-Filardi 1999; Jackson et al. 2000). It develops as a consequence of cardiac diseases like coronary artery disease, hypertension, valvular defects, alcohol misuse or viral infection (Cowie et al. 1997). In the general population, the prevalence of coronary artery disease and hypertension are found to be the main factors that predispose to the disease. Damage of myocardial tissue initially results in impaired pump function of the heart. Besides the resulting impaired ejection fraction (systolic heart failure), other forms are primarily characterized by an insufficient ventricular filling (diastolic heart failure) and can also lead to low cardiac output (Desai & Fang 2008). Clinically, symptoms and signs produced by complex circulatory and neurohumoral responses to cardiac dysfunction can be recognized. In general, predictive values for HF can be the shortness of breath, exercise intolerance and edema.

Numerous clinical studies could show that positive inotropic drugs increase the mortality when administered chronically in HF patients (for review see Stevenson 2003). In contrast, β-blockers, despite their acute force-reducing effects, decreased mortality when given at slowly increasing doses (Waagstein et al. 1975; Packer 1996). In fact, even an increase in the pumping force of the heart after several months of treatment was observed. These results can be explained by the following underlying mechanisms: After myocardial infarction reductions in pumping capacity initiate the activation of the sympathetic nervous system, resulting in a higher plasma concentration of norepinephrine. Via activation of cardiac β-adrenergic receptors, stimulatory G (Gs) proteins lead to the production of cAMP, which increases the heart rate and activates protein kinases inducing phosphorylation of proteins that determine force (for review see Feldman et al. 2005). Therefore the heart function is powerfully stimulated, accompanied by overproportional increases in energy consumption. These changes can induce a vicious cycle, accelerating the decline of pump function or cause sudden death (Figure 1.1; Eschenhagen 2008). However, a desensitization process is initiated within minutes and cardiomyocytes in failing hearts lose their responsiveness to norepinephrine over time. This can exaggerate exercise intolerance in heart failure, but it is also protective for cardiomyocytes regarding the consequences of β-adrenergic overstimulation, namely arrhythmias, energy depletion, hypertrophy and apoptosis. For this reason drugs that further stimulate the heart by overcoming desensitization cause mortality.

In contrast, β-blockers protect the heart from chronic sympathetic stimulation.

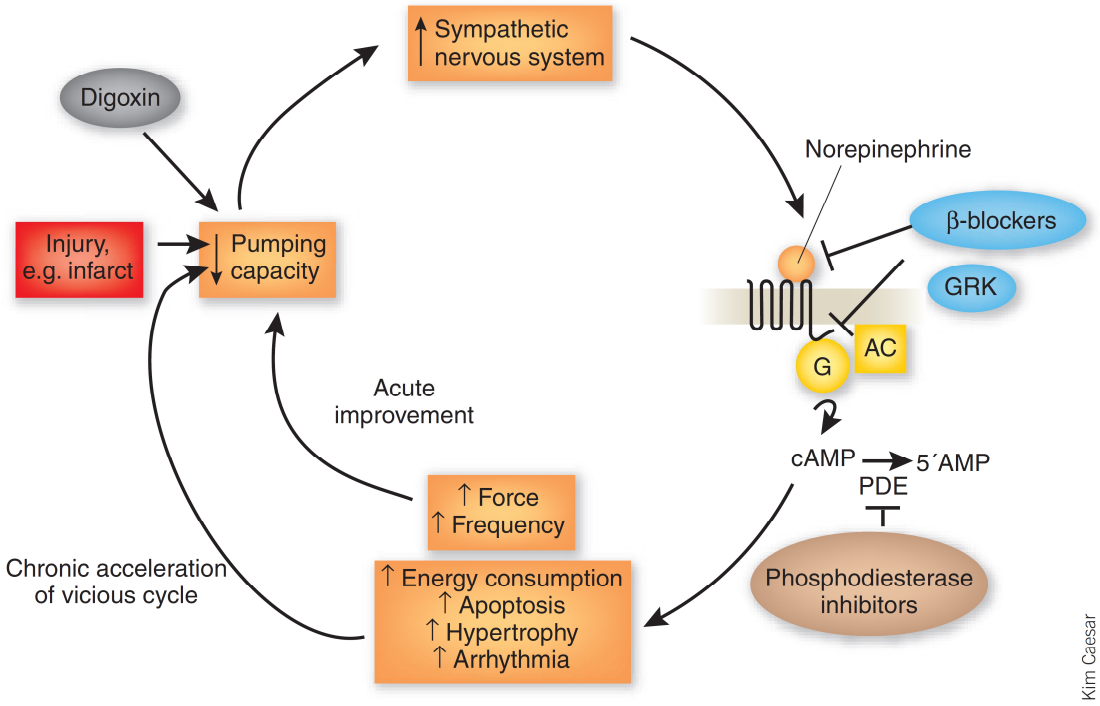

Figure 1.1: Vicious cycle in heart failure. An injury which reduces cardiac pumping capacity activates neurohumoral mechanisms, including the sympathetic nervous system. An acute increase in norepinephrine induces stabilized perfusion of crucial organs by redirecting blood flow away from skin, muscels, kidney and gut and stimulating heart rate and force. If the primary pumping defect of the heart continues, the increased sympathetic tone turns peripheral vasoconstriction, which imposes increased load on the failing heart. This further reduces cardiac output. Additionally, cardiomyocyte stimulation leads to adverse effects including overproportional increase in energy consumption, cell death, fibrosis, hypertrophy and arrhythmia. Via binding to β-adrenergic receptors norepinephrine stimulates G proteins (Gs), adenylyl cyclases (AC) and the second messenger cAMP, thereby G protein-coupled receptor kinase (GRK) phosphorylates β-adrenergic receptors. Collectively, these changes accelerate the decline of the heart function and constitute a vicious cycle. In heart failure, the signaling cascade is normally desensitized in response to chronic norepinephrine stimulation, an adaptation that can be viewed as mainly beneficial (from Eschenhagen 2008).

The purpose of treating HF is to reduce mortality and morbidity and increase quality of life. Angiotensin-converting enzyme inhibitors (ACEIs) should be used in all patients with symptomatic HF and a left ventricular ejection fraction <40%, since they inhibit the activated sympathic renin-angiotensin-aldosterone system (RAAS). RAAS plays an important role in regulating blood volume and systemic vascular resistance, which together influence cardiac output and arterial pressure. The SOLVD study (1991) showed that ACEI treatment improves ventricular function and patient well-being. Other studies showed that β-blockers are beneficial (CIBIS, 1999 and MERIT, 1999), which are recommended in all patients with symptomatic HF and a left ventricular ejection fraction <40%. In patients with moderate to severe HF aldosterone antagonists (MRAs) could be given at a low dose. The EMPHASIS

trial showed that the MRA eplerenone reduced the risk of the primary endpoint of cardiovascular death or HF hospitalization (Butler et al. 2012). Angiotensin receptor blockers (ARB) are recommended when patients stay symptomatic under the normal treatment. However, the combination of ACEIs and ARB should be avoided (Ma et al. 2010). Digoxin may be used to slow rapid ventricular rate in the case of atrial fibrillation (AF). Diuretics are recommended in patients with HF and clinical signs or symptoms of congestion (Dickstein et al. 2008). Newer therapeutic approaches with Ca^{2+} sensitizers like levosimendan, the late sodium current inhibiting drug ranolazine or drugs which affect the intracellular Ca^{2+} storage or release have not yet shown clear therapeutic benefit. The life expectancy of patients with chronic HF is only 50% in 5 years.

1.1.2 Hypertrophic cardiomyopathy

Hypertrophic cardiomyopathy (HCM) is one of the most common inherited cardiac diseases with an estimated prevalence of 1:500 (Maron et al. 1995; Taylor et al. 2004). This autosomal dominant disease is caused by mutations in genes encoding proteins of the myofilament apparatus. Multiple causative mutations in at least 10 different genes encoding sarcomeric proteins have been identified including *MYH7* (β-myosin heavy chain)*, MYBPC3* (cardiac myosin-binding protein C), *TNNT2* (cardiac troponin T), *TNNI3* (cardiac troponin I), *TPM1* (alpha-tropomyosin), *MYL3* (myosin light chain) and *ACTC1* (cardiac actin; Konno et al. 2010; Marian 2010; Schlossarek et al. 2011; Watkins et al. 2011). The phenotype of HCM patients is typically very heterogenous with some patients developing dyspnoe, chest pain, heart failure, arrhythmias and sudden cardiac death, and others remaining asymptomatic until late in life (Elliott et al. 2008; Gersh et al. 2011). HCM is characterized by a thickened but nondilated left ventricle in the absence of other cardiac or systemic condition capable of producing the magnitude of hypertrophy event (Maron 2008). Some patients develop left ventricular (LV) outflow obstruction, a highly visible feature of the disease. However, obstruction to LV outflow is variable and many patients have the nonobstructive form. Hearts of HCM-patients are usually increased in weight, often more than 500 g. The LV cavity is characteristically small or normal in size and the greater LV mass is almost entirely the result of increased, asymmetrical wall thickness (Figure 1.2). Clinical diagnosis of HCM can be made with two-dimensional echocardiographic imaging or cardiac magnetic resonance imaging (CMR) by virtue of its high-resolution tomographic imaging capability.

Hypertrophy may be diffuse and can involve portions of both the ventricular septum and LV free wall. Currently, there is no evidence that the right ventricle is often substantially involved in the cardiomyopathic process. Cardiomyocytes in the ventricular septum and LV free wall show increased diameter and altered morphology. Many myocytes and myofibrils are arranged in chaotic disorganized patterns (Figure 1.2; Geisterfer-Lowrance et al. 1990), which can be observed in nearly all HCM patients. It is likely that a disorganized architectural pattern could impair transmission of electrophysiological impulses and predispose to disordered patterns and increased dispersion of electrical depolarization and repolarization. This could be responsible for reentry ventricular tachyarrhythmias and sudden death (Kelly & Strauss 1994). Abnormalities in LV relaxation and filling can be identified in about 80% of HCM patients which are responsible for heart failure symptoms of exertional dyspnea (Mann 2007).

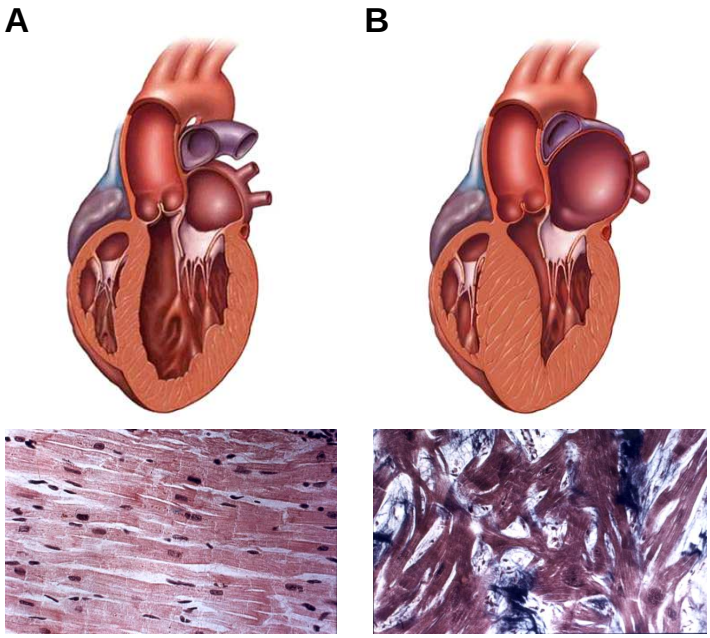

Figure 1.2: Characteristics of hypertrophic cardiomyopathy (HCM). The upper panels show a schematic longitudinal cardiac section of a healthy [**A**] and a HCM [**B**] heart. The interstitial wall thickness of the left ventricle is increased. The bottom panels show transversal Sirius Red-stained sections of a healthy [**A**] and a HCM [**B**] heart. **B:** The cardiomyocytes lost their parallel arrangement and interstitial fibrosis (blue) was found (from the Mayo clinic website (upper part) and from Geisterfer-Lowrance et al. 1990 (lower part)).

Characteristic diversity of the HCM phenotype is likely attributable to the disease-causing mutations, as well as to the influence of modifier genes and other factors (Friedrich & Carrier 2012). Evidence suggests mutations in *MYBPC3* to be associated with a milder disease than mutations in *MYH7* and other genes (Schlossarek et al. 2011). The overall genotype-phenotype correlation is poor (Santos et al. 2011), suggesting that unknown other factors

such as modifier gene variants, epigenetic mechanisms or environmental factors affect onset and course of the disease (Friedrich et al. 2009; Coto et al. 2010). In addition, also nonsarcomeric protein mutations in two genes involved in cardiac metabolism (PRKAG2 and LAMP-2) are responsible for primary cardiac glycogen storage cardiomyopathies with a clinical presentation mimicking or indistinguishable from sarcomeric HCM and often associated with ventricular pre-excitation (Maron 2008). There are also many other diseases associated with prominent thickening of the LV wall, which may mimic typical HCM caused by sarcomeric protein mutations. In consequence, the identification of a (likely) disease-causing mutation does not allow prediction of the course of HCM and therapy stratification, for example the early implantation of implantable cardioverter/defibrillators (ICD). Risk prediction may be improved by the identification of early clinical signs, e.g. diastolic dysfunction (Schlossarek et al. 2011), biomarkers (Cambronero et al. 2009) or the development of new *in vitro* approaches.

1.2 Mechanisms of cardiac contraction and relaxation

75% of the myocardial mass consists of cardiomyocytes held together by surrounding collagen I connective tissue, which is the main component of the cardiac extracellular matrix (Opie 2008). Myofilaments in the cardiomyocytes own contractile proteins, are connected to each other and fill as rod-like bundles the myocyte. A process called excitation-contraction coupling enables the chambers of the heart to contract and relax (for review see Bers 2002; Eschenhagen 2010). Intracellular Ca^{2+} is considered as the central regulator of cardiac contractiltiy. A cardiac action potential induces membrane depolarization, thereby activating L-type Ca^{2+}-channels (LTCCs) and Ca^{2+} enters the cell. This small influx of Ca^{2+} triggers the release of more Ca^{2+} from the sarcoplasmatic reticulum (SR) via binding to large tetrameric ryanodine-sensitive channels (RyR2; Figure 1.3). The SR is the Ca^{2+}-store of the myocytes and contains Ca^{2+} bound to the protein calsequestrin. Within a mammalian myocyte the free Ca^{2+}-ion concentration in the loaded SR is probably 0.5-1.0 mM, which is 5,000-10,000-fold higher than diastolic Ca^{2+}-ion concentration in the cytosplasm (Shannon et al. 2000). The mechanism of triggered Ca^{2+}-release is called Ca^{2+}-induced Ca^{2+}-release (CICR). The increase in intracellular Ca^{2+}-ions is necessary to induce the cardiac contraction by initiating conformation changes in the myofilaments. Half-maximal activation of contraction requires about 70 µM of Ca^{2+} in the cytosol. Interestingly, the concentration of free intracellular Ca^{2+} to half-activate the myofilament response is only ~600 nM. This argues for the fact that intracellular Ca^{2+} is heavily buffered such that it takes more than 100 µM Ca^{2+} in the cytosol

to raise intracellular, free Ca^{2+}. Therefore the amount of total Ca^{2+}-influx plus release that is required for a given level of contractile force is starting from diastolic Ca^{2+} ~150 µM (Bers 2000).

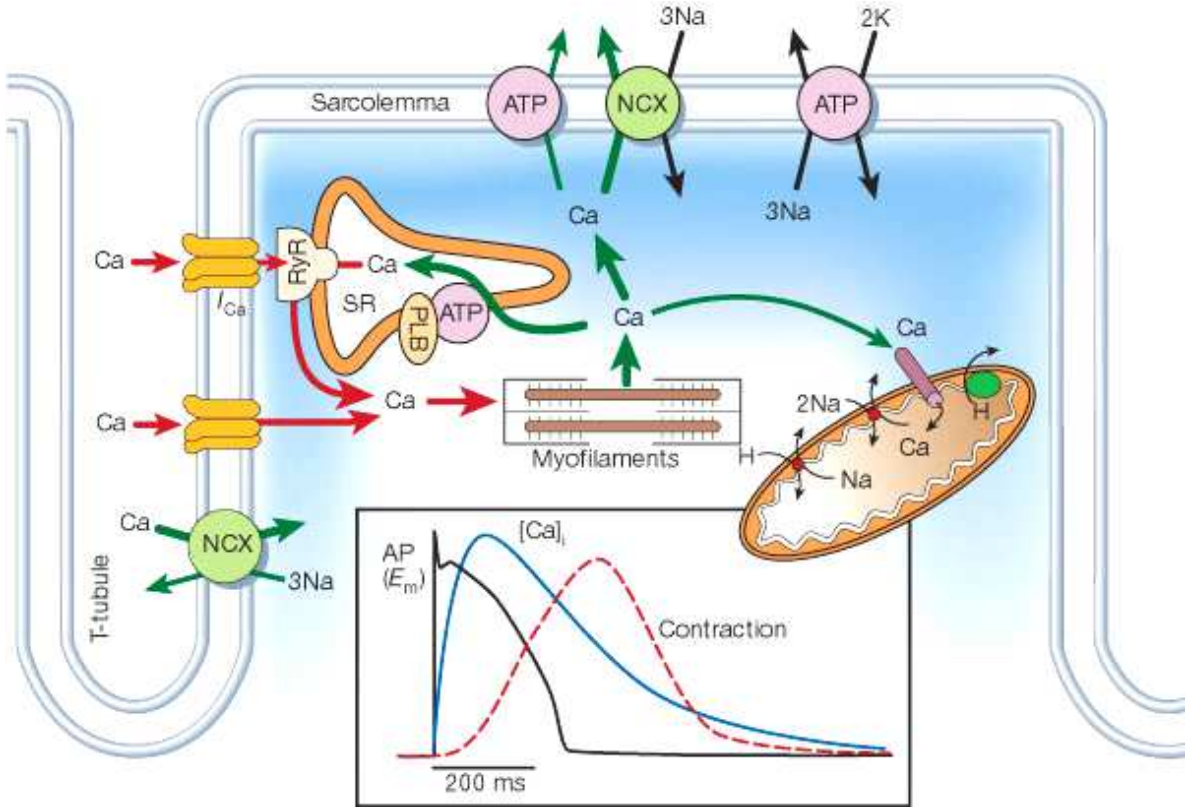

Figure 1.3: Ca^{2+}-transport in ventricular myocytes during excitation-contraction coupling. Red arrows point the increase of intracellular Ca^{2+} concentrations (L-type Ca^{2+}-channels); green arrows point the remove of Ca^{2+} from the cytosol (sarcoplasmatic reticulum Ca^{2+}-ATPase (SERCA) and Na^+/Ca^{2+} exchanger (NCX)). The inset shows the time course of an action potential, intracellular Ca^{2+} transient ($[Ca]_i$) and contraction (measured in a rabbit ventricular myocyte). AP, action potential; I_{Ca}, inward Ca^{2+} current; PLB, phospholamban; ATP, ATPase; RyR, ryanodine receptor; SR, sarcoplasmatic reticulum (from Bers 2002).

The thin actin filament and the thick myosin filament are the major molecules involved in the contraction-relaxation cycle. As Ca^{2+} increasingly arrives at the start of the contractile cycle and interacts with troponin C, the activated troponin C binds tightly to the inhibitory molecule, troponin I (de Tombe 2003). The latter is moving to a new position on the thin filament, thereby weakening the interaction between troponin T and tropomyosin. Tropomyosin subsequently is repositioned on the thin filament and the actin-myosin interaction can take place. During the phase of contraction the filaments slide over each other and pull together the two ends of the fundamental contractile unit, the sarcomere (Figure 1.4). The sarcomere is limited on each side by the Z-line to which the actin filaments are attached. The interaction of the myosin head domain (S1) with actin filaments is called cross-bridge cycling. The

sarcomere shortens when actin filaments move towards the center of the sarcomere, so the Z-lines come closer together. To achieve this ATP is needed. The elasticity of the sarcomere is provided by a giant protein named titin, which acts as a third filament. Titin also tethers the myosin molecule to the Z-line and thereby stabilizes the contractile proteins. It is able to stretch and relax and thereby explains the stress-strain relation of cardiac and skeletal muscle and has also plenty other functions (Opie 2008; de Tombe 2003).

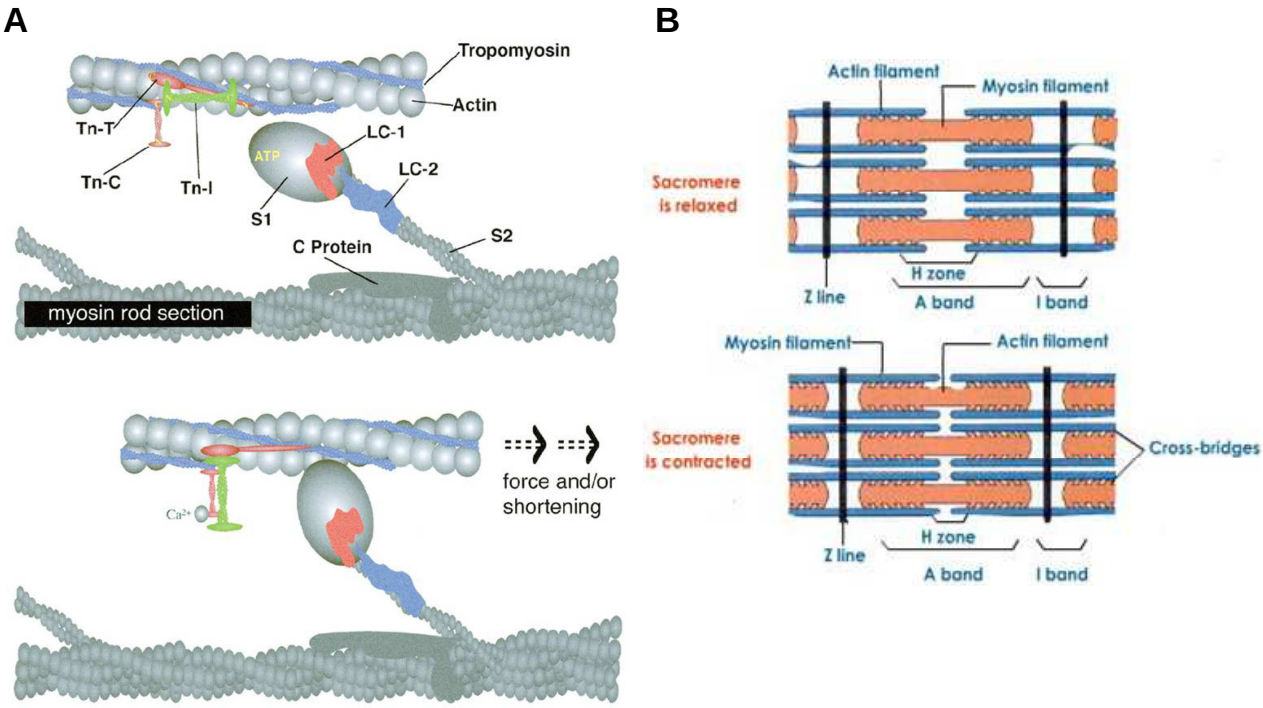

Figure 1.4: Sarcomere structure showing major proteins involved in contractile activation and regulation. Top panel shows the relaxed state of the sarcomere in diastole and the bottom panel systolic conditions during cross-bridge formation [**A**]. The thin filament is composed of actin, tropomyosin, and the hetero-trimer troponin (composed of the troponins Tn-T, Tn-C and Tn-I). The thick filament is composed of myosin, a globular head portion (S1), a hinged stalk region (S2) and a rod section. The S1 is associated with light-chain 1 and 2 (LC-1 and LC-2), containing both the ATP hydrolysis domain and the actin binding domain. The cardiac myosin-binding protein C (cMyBP-C) is associated with the myosin rod section (from de Tombe 2003). Sarcomere shown in a relaxed and in a contracted state (**B**; from the TutorVista homepage).

During the phase of relaxation Ca^{2+} is removed from the cytosol via either the reuptake into the SR, which is achieved by the sarcoplasmatic reticulum Ca^{2+}-ATPase (SERCA) or extrusion via the Na^{+}/Ca^{2+} exchanger (NCX). Under regular conditions the amount of Ca^{2+} entering the cell is exactly matched by the amount of Ca^{2+} leaving via the NCX (Ca^{2+} homoestasis). The Ca^{2+} in the SR is kept until the next wave of depolarisation.

Additionally, several mechanisms exist to modulate force development and relaxation. E.g. regulation by the positive force-frequency relationship or the Frank-Starling mechanism, which is defined by the increase in force in response to stretch (Endoh 2006). Both mechanisms increase the contractile force in response to stretch and stimulation frequency, respectively. The most important mechanism in regulation is the already mentioned activation of β-adrenergic receptors, which stimulate the system at numerous levels via protein kinase A (PKA). The phosphorylation of LTCCs increases their open probability, allowing more Ca^{2+} to enter the cell. Phosphorylated phospholamban activates SERCA, resulting in an increased reuptake of Ca^{2+}. PKA also phosphorylates troponin I and cMyBP-C, which desensitizes the myofilaments to Ca^{2+} and facilitates relaxation (for review see Bers 2002; Eschenhagen 2010).

1.3 Cardiac myosin-binding protein C (cMyBP-C)

The cardiac myosin-binding protein C (cMyBP-C) is a large modular protein (~140-150 kD) and is located in doublets in the C-zone of the A-band of the sarcomere. It consists of immunoglobulin (IgC2-like) and fibronectin (FN3) domains. From the N- to the C-terminus 11 modules are labelled as C0-C10 and four phosphorylation sites are localized in the cMyBP-C motif (Figure 1.5). In general, MyBP-C exists in three isoforms: the slow-skeletal, the fast skeletal and the cardiac isoform. The cardiac isoform includes a series of residues containing phosphorylation sites and an additional immunoglobulin module at the N terminus that are not present in skeletal isoforms. cMyBP-C is expressed in human and murine heart during development and adult life and is thought to play an important structural and functional role during cardiac contraction in health and disease. In detail, cMyBP-C interacts with several sarcomeric components like the S2 fragment of myosin, the light meromyosin and titin (Schlossarek et al. 2011). In addition, a potential actin-binding sequence exists. However, the precise organization of cMyBP-C within the sarcomere is still not completely understood. cMyBP-C may stabilize the thick filaments but is not essential for sarcomere function, as seen in cMyBP-C knock-out (KO) mouse models (Carrier et al. 2004). However, it is thought to play a role in the formation of the sarcomeric myofibers as a result of binding to myosin and titin. Interestingly, the absence of cMyBP-C brings myosin heads closer to the thin filament and therefore increases the probability of myosin being weakly bound to actin. As a result, the likelihood of cross-bridge binding is increased. This results in a pronounced increase in sensitivity to external Ca^{2+} of isometrically contracting KO left atria, which were

able to beat even in the nominal absence of external Ca^{2+} (Pohlmann et al. 2007). Therefore cMyBP-C acts as a physical restraint on the myosin heads, keeping them near to the thick filament and thus reducing the probability of their interaction with actin during diastole.

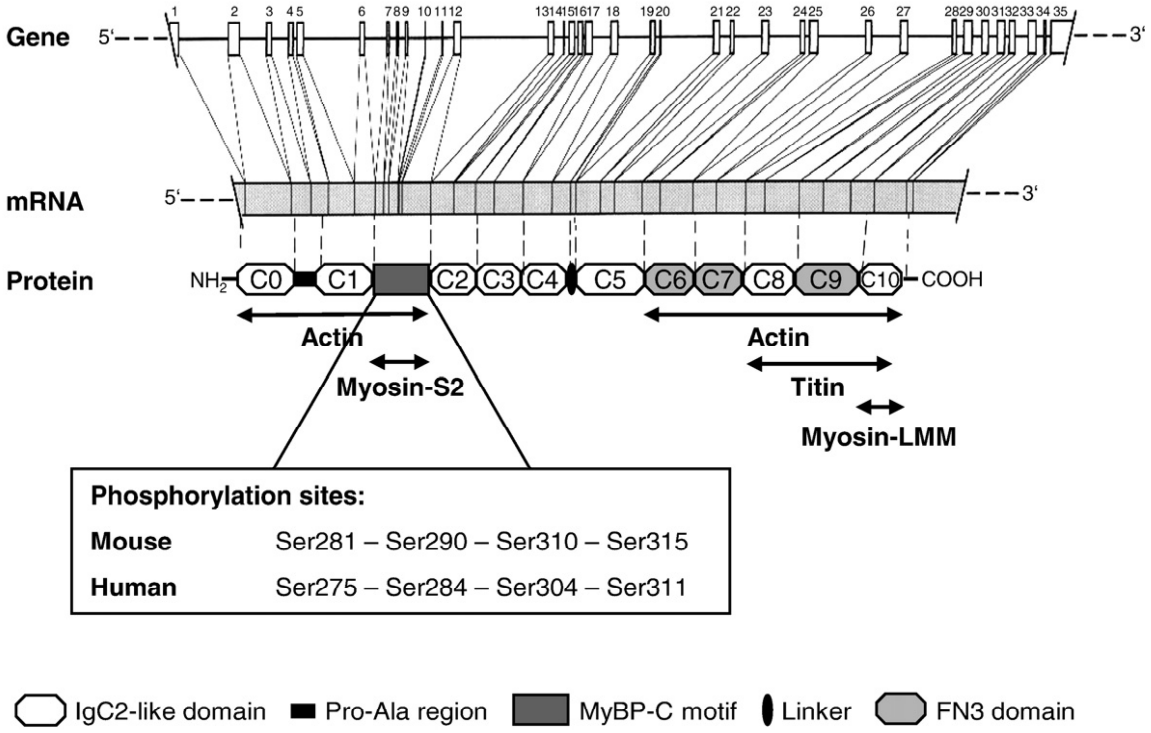

Figure 1.5: Schematic organization of the human *MYBPC3* gene and alignment of exons with structural domains of the protein. Top panel, the schematic organization of the *MYBPC3* gene with locations of exons, coding for structural domains, shown by boxes and introns by horizontal lines is illustrated. In the middle, the resulting mRNA is depicted. On the bottom, the structural domains of the cMyBP-C protein are shown. The localization of the domains involved in binding to other sarcomeric proteins is indicated as well as the phosphorylation sites in mouse or human (from Schlossarek et al. 2011).

The absence of cMyBP-C results in eccentric left ventricular hypertrophy, myocardial disarray, interstitial fibrosis and diastolic dysfunction in homozygous KO mice (Harris 2002; Carrier et al. 2004).

Phosphorylation of cMyBP-C is essential in the regulation of thick and thin filament interaction during contraction (Winegrad 1999; Carrier 2007) and has been shown to be regulated upon β-adrenergic stimulation by PKA, Ca^{2+}/calmodulin kinase II (CaMKII), by PKCε and PKD. PKA-induced Ca^{2+} desensitization of the myofilaments results from phosphorylation of both cardiac Tn-I and cMyBP-C (Schlossarek et al. 2011). cMyBP-C phosphorylation reduces its binding affinity to actin and abolishes binding to myosin, resulting in stronger actin-myosin interaction, which is thought to be cardioprotective (Sadayappan et

al. 2005). Reduced cMyBP-C phosphorylation levels have been shown in human and experimental heart failure (El-Armouche et al. 2007; Decker et al. 2005; El-Armouche et al. 2006).

At least 185 HCM-associated mutations were identified in the *MYBPC3* gene (Schlossarek et al. 2011). Several missense mutations have been described that may result in stable mutant proteins incorporated into the sarcomere, 61% of the known mutations are frameshift or nonsense. Frameshift mutations result in a premature termination codon in the mRNA and are expected to produce C-terminal truncated cMyBP-Cs lacking myosin- and/or titin-binding sites. However, studies in mice and humans were unable to detect such proteins in affected hearts, suggesting that they are highly unstable. Three quality control systems have been implicated in their removal from the heart: the nonsense-mediated mRNA decay (NMDA), the ubiquitin-proteasome system (UPS) and autophagy (Carrier et al. 2010). The molecular mechanisms by which *MYBPC3* mutations lead to HCM remain elusive and are currently studied in our institute with different mouse models (Carrier et al. 2004; Vignier et al. 2009).

1.4 Animal models in biomedical research

The use of animal models in biomedicine has become fundamental to all aspects of research from studying basic biological mechanisms to the understanding of disease pathology and the development of new medicines. Since a huge number of human characteristics are shared with many species, these models can help understanding human biology at the cellular and molecular level in health and disease.

1.4.1 Genetically modified mice to study human diseases

Currently over 95% of transgenic animals used in biomedical research are mice. Especially for the field of cardiovascular research the development of genetically modified mice was very important. Mice offer many advantages: a short reproduction cycle (21 days), small body, simplicity of genetic manipulation and, with the completion of the sequencing of the mouse and human genome, the possibility to do comparative genetics. It has been observed that similar genes (over 80%) and signalling pathways regulate the development of the heart and vasculature in both species, so comparisons can be performed easily (Nabel 2008).

Transgenesis in mice either means transferring DNA into an animal or altering DNA already in the animal. The gene of interest has to be cloned and fused to a transcriptional regulatory sequence that programs its expression in specific tissues. Further steps have to be done as shown in Figure 1.6.

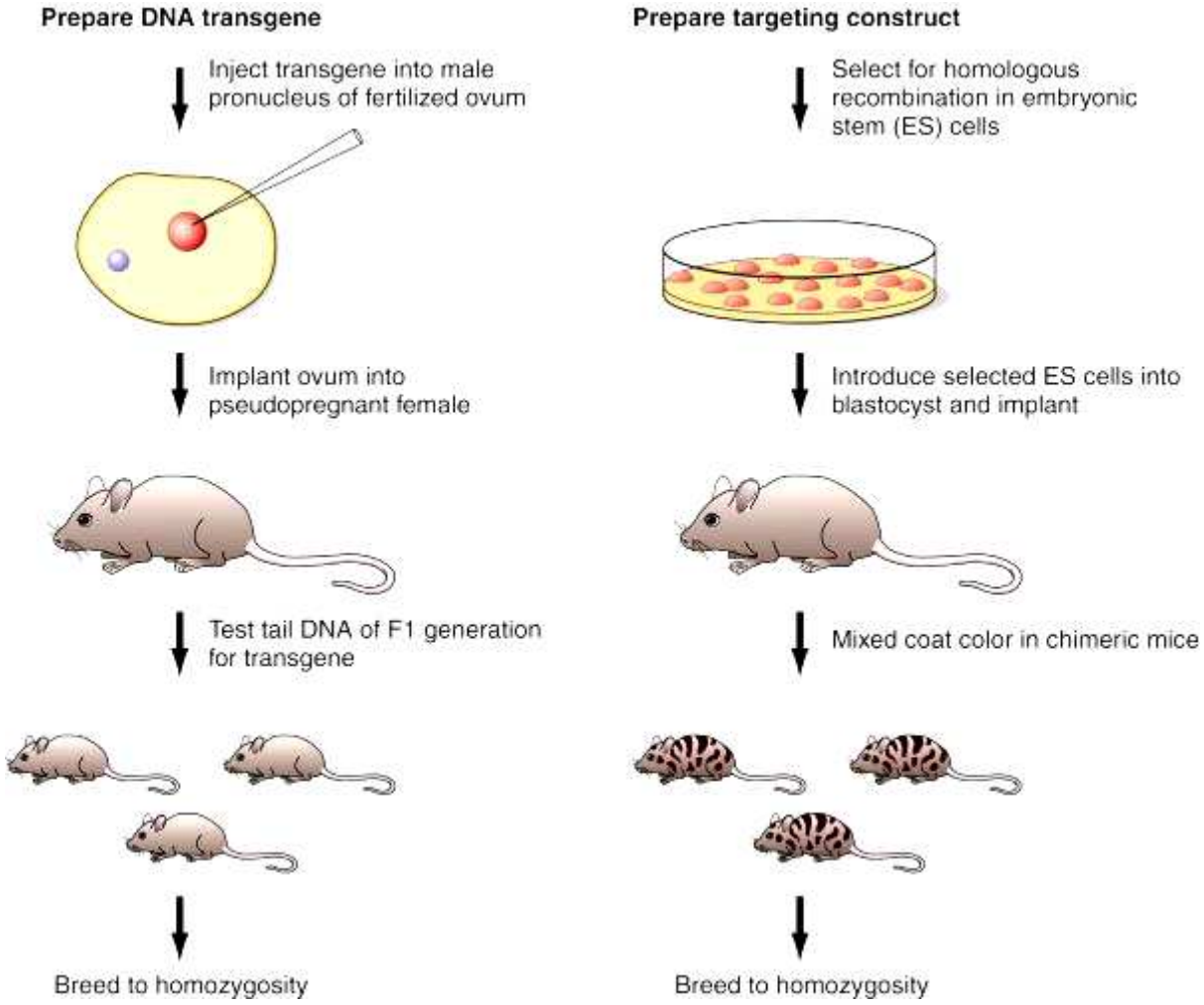

Figure 1.6: Transgenic mouse models. The left scheme shows transgenic mice which are generated by pronuclear injection of foreign DNA into fertilized mouse oocytes and subsequent transfer into the oviduct of pseudopregnant foster mothers, which lasts about 1 month, leading to random integration of the transgene. The right scheme shows the procedure for targeted mutagenesis (gene knock-out/knock-in): Embryonic stem cells (ESCs) are transfected with the targeted transgene. This transgene undergoes a homologous recombination with the wild-type gene. After selection, positive ESCs are introduced into blastocysts and implanted into foster mothers. Chimeric mice can be identified based on the mixed coat colour of the offspring. Heterozygous mice, carrying one copy of the gene of interest are bred to obtain mice homozygous for the mutant allele. This process lasts about 9-12 months (from the McGraw Hill homepage).

Regarding HCM, much knowledge about the molecular pathogenesis and signaling mechanisms has been derived from mouse models since human studies are limited because of small numbers of individuals carrying the same mutation and the difficulty to get

myocardial tissue from patients. Until now, several models have been generated which carry mutations in genes encoding sarcomeric proteins such as α-myosin heavy chain (α-MHC), cardiac troponin T, α-tropomyosin or cMyBP-C (Marian & Roberts 2001). cMyBP-C knock-out mouse models served for studies to understand the role of cMyBP-C in the cardiac contraction-relaxation cycle (Carrier et al. 2004). The first mouse models expressing a mutant cMyBP-C lacking myosin and titin binding domains or PKA-dependent phosphorylation sites were generated in the late 90s (Yang et al. 1998; Yang et al. 1999; Yang et al. 2001). In the last year a model was developed, which carries a point mutation in exon 6 of the *Mybpc3* gene encoding cMyBP-C, associated with a severe phenotype in humans for mimicking the disease (Vignier et al. 2009). The phenotype of HCM mouse models are to some extent similar to those observed in human HCM. Myocyte disarray, interstitial fibrosis and diastolic dysfunction are common; however, unlike human HCM, significant cardiac hypertrophy is often absent in transgenic mouse models (Marian & Roberts 2001; Houser et al. 2012).

The phenotype of mutant mice can be studied either *in vivo* or *in vitro*. *In vivo* experiments cannot distinguish precisely between the effect of a mutation in a gene and the effect of neurohumoral activation or potential compensatory mechanisms that may take place in the animal. For this reason single cardiomyocytes are frequently analyzed from genetically modified mice. Single cells can be easily isolated from adult or neonatal animals and have been shown to be useful to address questions like basic contractility, sensitivity to external Ca^{2+} concentrations and others (Pohlmann et al. 2007). Yet, adult murine cardiomyocytes have to be analyzed immediately after isolation, are difficult to culture and often die during experimental procedure. Neonatal murine cardiomyocytes can be cultured for few days only and are overgrown rapidly with fibroblasts. They show poor alignment and cellular orientation and do not form large units of electrically coupled cells, thereby exacerbating the measurement of force. These disadvantages limit the use of 2-D cultures in general. Prolongation of cell life duration is longing for an environmental condition that represents the *in vivo* situation more closely. The technique of tissue engineering offers a three dimensional form of cell culture (1.5), which improves survival and the process of cell maturation. Taken together, the combination of cell culture in a defined environment like an artificial tissue *in vitro* by the use of genetically modified mice provides an accurate and convenient way to evaluate the function of specific genes in cardiovascular diseases.

1.5 Tissue engineering

The term tissue engineering can be defined as the application of principles and methods of engineering and life sciences toward fundamental understanding of structure-function relationship in normal and pathological mammalian tissues and the development of biological substitutes to restore, maintain, or improve functions (US National Science Foundation, 1987). Tissue engineering aims at generating functional 3-D tissues outside of the body that can be tailored in size, shape, and function according to the respective needs before implanting them into the body (for review see Eschenhagen & Zimmermann 2005). Improved tissue engineered *in vitro* models can be used for preclinical drug development (*in vitro* disease modeling or toxicology).

It all started with the idea to restore damaged parts of the body to preserve and to prolong a healthy life. And indeed, end-stage organ failure is still a key challenge for the medical community because of aging population and the limited number of suitable donor organs available (Badylak et al. 2012). How comfortable would it be to just generate whole organs in the dish as living graft, e.g. for people suffering from chronic kidney (Caldas et al. 2011) or heart diseases (Eschenhagen & Zimmermann 2005)? Current approaches in the field of regenerative medicine are aiming to generate bone constructs (Marolt et al. 2012), cartilages (Kock et al. 2012), vascular grafts (Shinoka et al. 2003) or hair follicles (Lindner et al. 2011). The present studies are still preliminary but indicate that the dream of generating artificial organs could become true one day.

1.5.1 Engineered heart tissue (EHT)

Cardiovascular disease comprises malfunction of heart valves, blood vessels and myocardium, all of which are subject to tissue-engineering approaches (Eschenhagen et al. 2007). Tissue-engineered heart valves could help children with congenital cardiac malformation and offer the possibility to obtain totally autologous biological valves for adults with acquired valve defects. Cardiac tissue engineering has several roots: developmental biology, cardiac muscle cell biology, and material science. The first 3-D heart tissues were generated already in the late 1950s from embryonic chick heart cells (for review see Eschenhagen & Zimmermann 2005). At this time it has been shown that cell aggregates were functionally more similar to intact heart tissue than 2-D cultures. Hydrogel-based cardiac tissue engineering was introduced in the 1990s and is describing techniques to constitute engineered tissues from matrix (collagen I, fibrinogen) and cardiomyocytes *in vitro*,

resembling adult cardiac tissue in morphology and function (Eschenhagen et al. 1997; Hansen et al. 2010). This enterprise started with experiments where cardiomyocytes from embryonic chick heart cells were cultured in a collagen-based extracellular matrix to produce spontaneously beating 3-D heart-like tissue (Eschenhagen et al. 1997). Cardiomyocytes formed contractile 3-D tissues, allowing direct measurement of isometric contractile force. In immunohistochemistry and electron microscopy highly organized tissue-like structures of α-actin positive cardiomyocytes could be observed, exhibiting typical cross-striation, sarcomeric myofilament organization, intercalated discs, desmosomes, and tight junctions. This early approach opened the way to develop engineered heart tissue from neonatal rat heart cells (EHT; Zimmermann et al. 2000) which is used worldwide by several groups now. EHTs were generated either in a plane system with Velcro strips for fixation to silicone tubes or in a ring system. Those EHTs showed typical features of neonatal rat heart, including a positive force-length and a negative force-frequency relation, high sensitivity to external Ca^{2+}, modest positive inotropic and pronounced positive lusitropic effects of isoprenaline. Later, it was demonstrated that ring-shaped EHTs subjected to phasic mechanical stretch display important hallmarks of differentiated myocardium (Fink et al. 2000; Zimmermann et al. 2002). Cardiomyocytes in stretched EHTs formed interconnected, longitudinally orientated cardiac muscle bundles, resembling adult rather than immature native tissue. At this time, EHTs consisted of a reconstitution mix containing freshly isolated cardiomyocytes from neonatal rats with collagen type I, a basement membrane protein mixture (Matrigel) and serum-containing culture medium. This mix was pipetted into circular casting molds, incubated for 45 min at 37 °C and 5% CO_2 and culture medium was added to the dish. EHTs were cultured for 7 days until they were transferred into a stretch device (Figure 1.7).

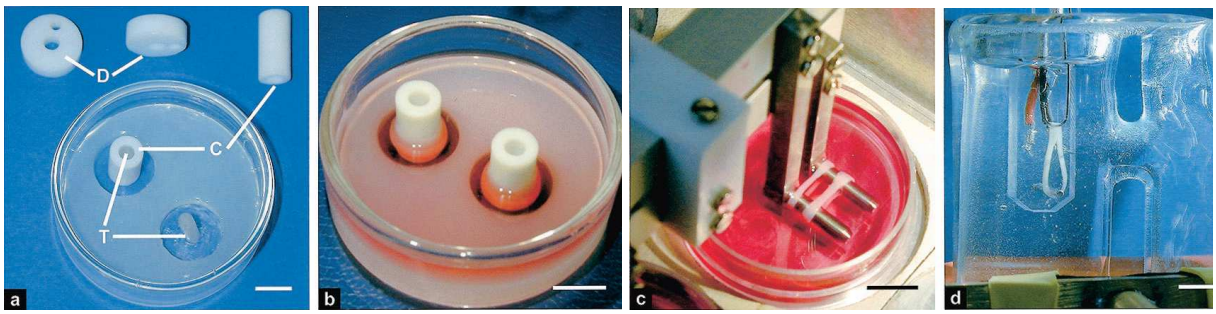

Figure 1.7: Experimental set-up for EHT preparation, culture, and analysis of contractile function. Casting mold assembly with silicone tubing (T) which was glued on glass dish and Teflon disks (D) or cylinders (C) were placed over silicone tubings and functioned as removable spacers, respectively [**a**]. EHT condensation around the Teflon cylinder during the first days of culture [**b**]. EHTs after transfer in a stretch device to continue culture under unidirectional and cyclic stretch (**c**; 10%, 2 Hz). EHT in a thermostated organ bath (**d**; from Zimmermann 2002).

Just around that time another technique to generate artificial cardiac tissue was described (Shimizu 2002). Here, neonatal rat cardiomyocytes were cultured on cell surfaces coated with a temperature-responsive polymer, from which confluent cells detached as a cell sheet simply by reducing the temperature. These cell sheets could be layered 3-dimensionally. When 4 sheets were layered, they began to pulse simultaneously and showed connexin-43 expression between the sheets, indicating morphological and electrical communication. Matrix-free layered cell sheets were further taken for implantation studies successfully.

Most other groups made attempts to generate 3-D cardiac tissues in the dish by the use of prefabricated solid extracellular matrices. E.g. polyglycolic acid was used as a scaffold in combination with bioreactor cultures (Carrier et al. 1999). Alternatively, fetal rat ventricular cells were seeded on gelatin scaffolds, cultured for 7 days *in vitro* and were implanted onto cryo-infarcted hearts (Li et al. 1999). Spontaneous contractile activity could be reported, but the histological microphotographs showed poor sarcomere development. Furthermore, alginate scaffolds were seeded with fetal cardiac cells (Leor et al. 2000). However, the high stiffness of these nonelastic biomaterials resulted in poor tissue-like formation in terms of cell alignment, cell-cell contact development or integration into the host myocardium after implantation.

For this reason the use of liquid hydrogel-based matrix cell entrapment approaches seemed to be the promising technique for the future (Eschenhagen & Zimmermann 2005). However, collagen I had the disadvantages of slow polymerization which led to an inhomogenous cell distribution in the matrix and required high cell numbers in circular EHTs. The extensive handling necessary to transfer EHTs to the stretch-device gave rise to experimental variability. For this reason a miniaturized EHT format was established in our group, offering the possibility for multiwell-testing and automated evaluation of contractile parameters (Figure 1.8; Hansen et al. 2010). Collagen I was exchanged with fibrinogen, a 340-kDa glycoprotein, which is present in blood plasma and can be purified from different species (bovine or human). After adding of thrombin fibrinogen quickly polymerizes to a fibrin polymer, which is biodegradable by the enzyme plasmin. Advantages of fibrin polymer are its nonlinear elasticity resulting in a higher elastic modulus under shear stress and its softness in comparison to other filamentous biopolymers (Janmey et al. 2009).

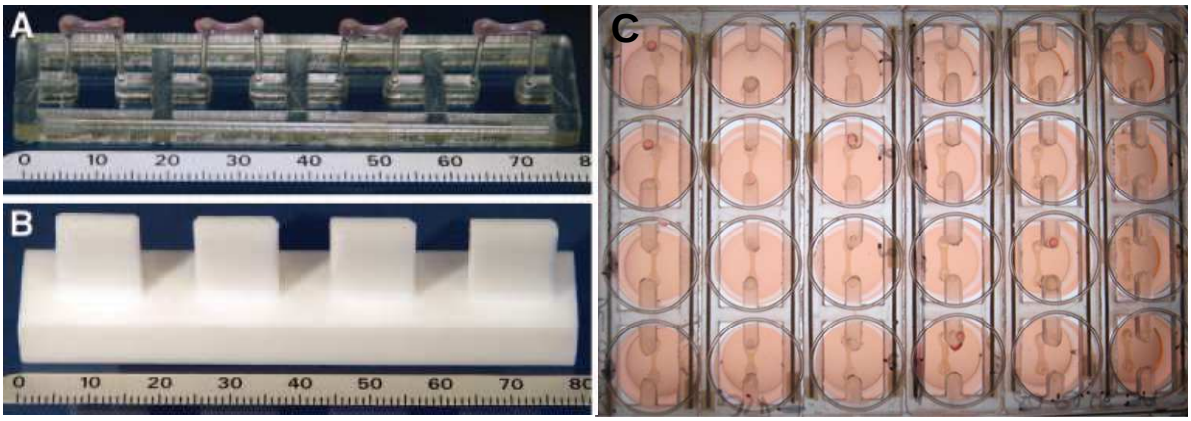

Figure 1.8: Equipment for casting and cultivation of fibrin-based mini EHTs. Silicone post rack with four EHTs [**A**] and Teflon spacer to generate casting molds [dimensions: length x width x height: 21 mm x 3 mm x 13.5 mm; **B**] turned upside down, scale in millimeter, respectively. View from above [**C**]: 6 Silicone racks with 4 EHTs each were cultured in a 24-well plate in parallel (adapted from Hansen et al. 2010).

Up to now, fibrin-based miniaturized EHTs have successfully been generated with neonatal rat and human embryonic stem cell (hESC)-derived cardiomyocytes (Hansen et al. 2010; Eschenhagen 2011; Schaaf et al. 2011). EHTs were used as a screening platform to study effects of medium supplements or to detect potential cardiotoxic drug effects *in vitro*.

1.5.2 Engineered heart tissue as a patch for the heart

In the last decade progress in tissue engineering and stem cell technologies have encouraged attempts to bioengineer 3-D heart muscle equivalents for cardiac regeneration. Since cardiomyocytes are terminally differentiated and do not proliferate like endothelial cells or fibroblasts in the heart, the loss of cardiomyocytes after myocardial infarction cannot be compensated by endogenous mechanisms. Cell-based therapies are generally performed using two different approaches: Either injection of isolated cells directly into the myocardium (Qian et al. 2012) or construction of cardiomyocyte-patches *in vitro*, which are surgically attached to the myocardium for the replacement of impaired tissue. First studies were done a couple of years ago, were rat EHTs were implanted on uninjured rat hearts (Zimmermann et al. 2002; Zimmermann et al. 2004). Already 12 days after implantation EHTs seemed likely vascularized and the muscle-like structure was preserved. Transmission electron microscopy showed implanted cardiomyocytes around newly founded blood vessels (Figure 1.9). Furthermore, ultrastructural analysis demonstrated that implanted EHTs surpassed their preimplantation degree of differentiation.

In another approach 3-D cell sheet grafts were implanted into dorsal subcutaneous tissue of nude rats (Shimizu 2002). Functionality of grafts preserved *in vivo* as detected by the spontaneous beating. Histological analyses after 3 weeks showed characteristic structures of heart tissue and multiple neovascularization within contractile tissues and vessels growing into cardiac grafts. These studies indicated that engineered cardiac tissue survived *in vivo* and could serve for regeneration of diseased heart. And indeed, some years later it was shown that EHT grafts could improve systolic and diastolic function in infarct-induced rat hearts (Zimmermann et al. 2006). Here, EHTs were implanted on myocardial infarct areas, forming a thick muscle layer which was electrically coupled to native myocardium without inducing arrhythmias. Fractional area shortening (FAS) of sham-operated myocardial infarcted rat hearts further worsened, whereas FAS remained unchanged in the EHT-grafted group. Cardiomyocytes from the EHT remained in the graft and no additional, potentially stem cell-derived host-cardiomyocytes invaded the graft, as detected by DAPI staining of cells from EHT. Interestingly, DAPI-positive blood vessels were detected in the region between EHT and host myocardium, implicating that endothelial cells from EHT led to the formation of new blood vessels connecting host myocardium and transplant (Figure 1.9).

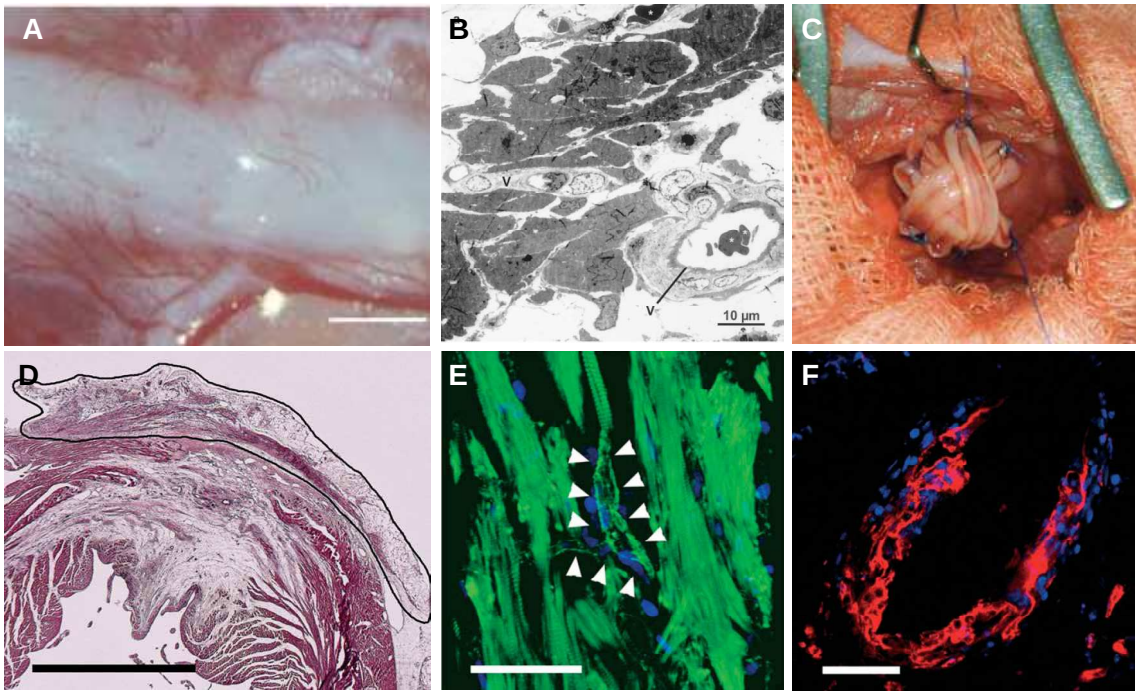

Figure 1.9: EHT graft and morphology 2 and 4 weeks after engraftment. Explanted heart with EHT 14 days after implantation [**A**]. Transmission electron microscopy of grafted EHTs 14 days after implantation [**B**]. V means vessel. Multiloop-EHTs (consisting of 5 single EHT stack) on rat hearts [**C**]. H&E staining of paraffin sections through the infracted left ventricular free wall showed a thick cardiac muscle formation on the top of the infarct scar [**D**]. Immunofluorescence staining showed vascularized EHT grafts *in vivo* (**E:** actin, green; nuclei, blue; arrows indicate a putative vessel) and newly formed vessels containing DAPI positive endothelial cells coming from EHT graft (**F:** lectin, red; nuclei, blue), from Zimmermann et al. 2002 [A and B] and Zimmermann et al. 2006 [C, D, E and F].

Neovascularization of engineered myocardial tissue based on the cell sheet-tissue engineering approach could be promoted by adding endothelial cells (ECs) to the construct (Sekine et al. 2008). GFP-labeled ECs were detected to form a cell network within the cardiomyocyte sheets. 3-D patch-like tissue grafts were implanted onto infarcted rat hearts. 4 weeks after transplantation, recovery of cardiac function improved using grafts with high EC densities. Finally, blood vessels originating from the EC-positive graft seemed to bridge into the myocardium to connect with capillaries of the host myocardium (Figure 1.10).

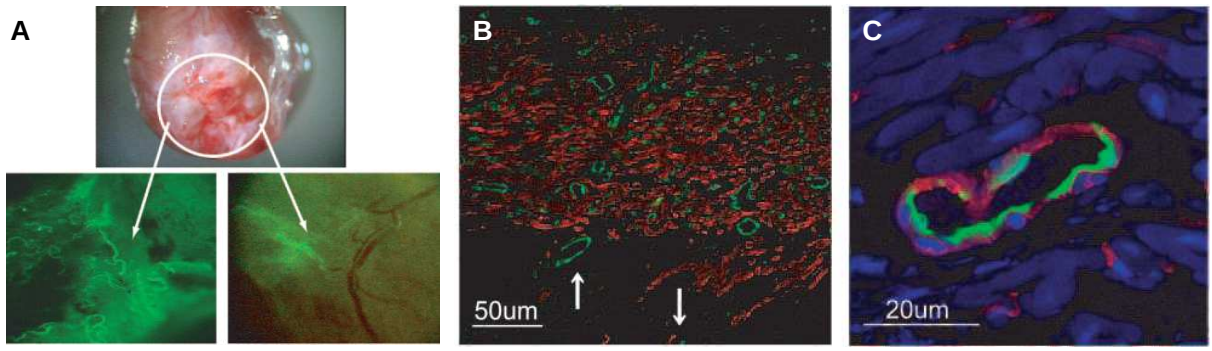

Figure 1.10: Contribution of endothelial cell (EC) networks to the neovascularization of ischemic hearts. Macroscopic view demonstrating capillary formation in EC-positive myocardial tissues [**A**]. GFP-expressing blood vessels originated from the transplanted cardiac grafts [**B**]. Immunostaining for troponin T and GFP. Arrows in B indicate vessels originating from the transplanted tissue grafts. Staining with isolectin B4 and anti-GFP antibodies demonstrated that fused blood vessels containing both host and graft-derived ECs were present in the engineered myocardial tissues (**C**; from Sekine et al. 2008).

In most studies ECs were detected by immunohistochemistry or immunofluorescence staining which have limited specificity and sensitivity. Labeled ECs in engineered tissue grafts can help to distinguish between ECs originating from the graft and the host myocardium. Distinct analysis of labeled vessels will help to investigate pro-angiogenic growth factors, which could improve vessel connection between the graft and the host myocardium. In general, this connection is very important, since nutrition provided by vessels is crucial for survival of the cells in the patch. One import goal in the field of tissue-engineered graft studies is to enlarge the size of the tissue-engineered cardiac patch. The EHT patch should have a size offering contractile features that can support human failing hearts one day. However, there is still a limitation regarding the metabolic supply of the cells in the inner part of the EHT, since diffusion is the main route of supply to nutrition and oxygen, which is limited to a distance of ~100 µm (Frerich et al. 2001). Therefore a sufficient vascular network within the construct is a very important parameter for the survival of enlarged cardiac tissue patches.

Another limitation is the use of collagen-based EHT patches. The lack of collagen I degradation *in vivo* may result in enhanced stiffening of the graft region, thereby potentially triggering arrhythmias. We hypothesized that fibrin-based EHTs may serve as more physiologic grafts given that matrix fibrin is biodegraded *in vivo.* A previous study showed that fibrin-implants in mice were almost completely biodegraded after 6 weeks *in vivo* (Ehrbar et al. 2008).

1.6 Angiogenesis

The development of blood vessels from *in situ* differentiating endothelial cells (EC) is called vasculogenesis, whereas sprouting of new blood vessels from the pre-existing ones is termed angiogenesis or neovascularization (Pandya et al. 2006). Angiogenesis is essential during tissue repair, fetal development and the female reproduction cycle. Inadequate angiogenesis can lead to coronary artery disease, therefore therapeutic approaches aim for stimulating angiogenesis to cure coronary artery disease, cardiac failure or tissue injury. A complex interplay between cells and their environment regulates physiological angiogenesis. The balance between pro-angiogenic and anti-angiogenic growth factors and cytokines tightly controls angiogenesis. In the past several pro-angiogenic molecules like vascular endothelial growth factor (VEGF), platelet-derived growth factor (PDGF), fibroblast growth factors (FGF) and insulin-like growth factor (IGF) have been identified (Griffioen & Molema 2000). VEGF as the most important growth factor regulates EC proliferation, permeability and survival (Figure 1.11). It stimulates capillary formation *in vivo* and has direct mitogenic actions that are restricted to ECs. In animal models of chronic myocardial ischemia, perivascular or intracoronary administration of VEGF improved the collateral flow (Banai et al. 1994). Interestingly, interleukin 1-β, PDGF and transforming growth factor β (TGF-β) stimulate VEGF production by smooth muscle cells, synergistically increasing the effect of VEGF (Pandya et al. 2006).

Another important stimulus for angiogenesis is the local oxygen concentration (Carroll & Ashcroft 2005). Low oxygen concentrations are known to induce the expression of hypoxia-inducible factors (HIF; Pugh and Ratcliffe 2003). HIF-1α, which is expressed under hypoxia, can react with HIF-response elements (HRE) to induce transcriptional activity and thereby regulating genes involved in angiogenesis, apoptosis or glucose metabolism.

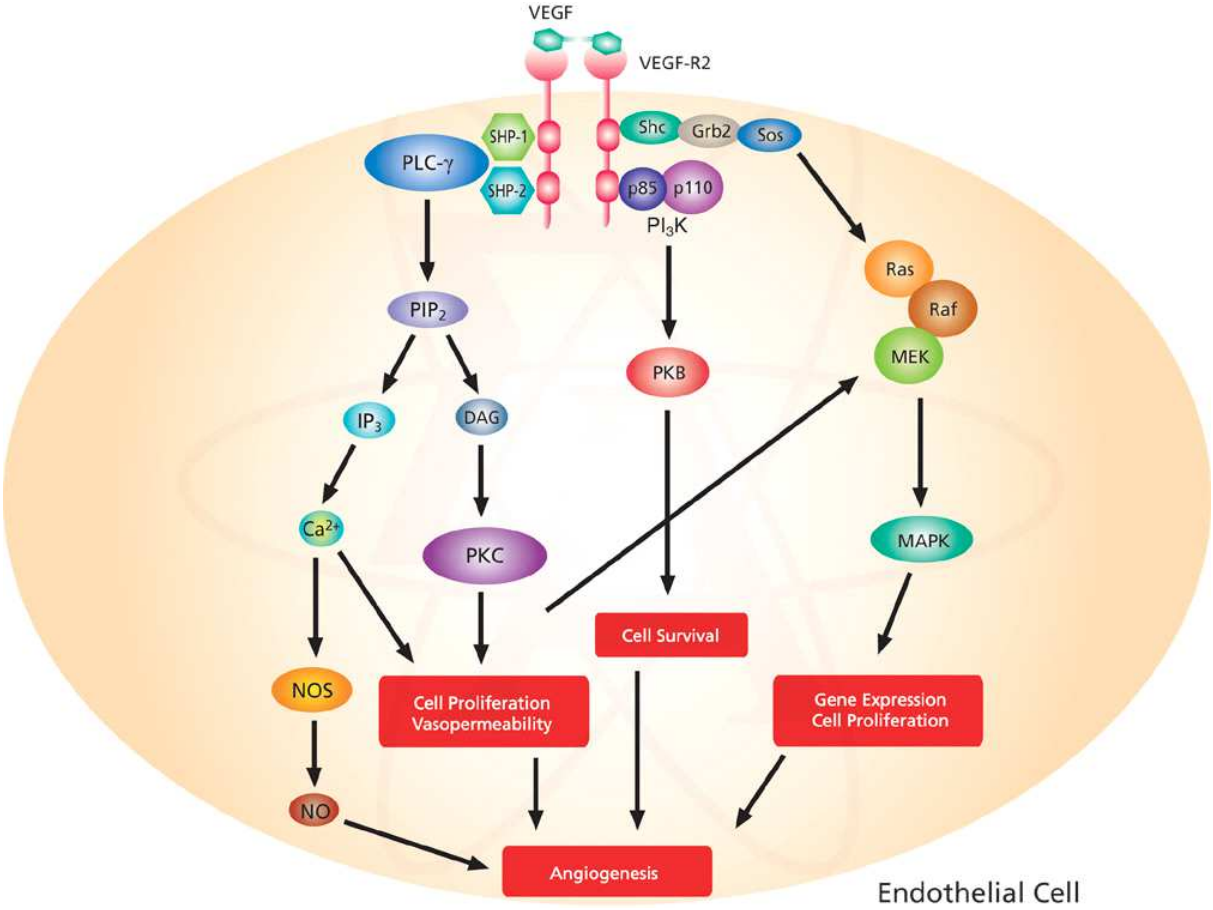

Figure 1.11: Signaling pathway activated by VEGF. VEGF regulates several endothelial cell functions, including proliferation, differentiation, permeability, vascular tone, and the production of vasoactive molecules. Upon ligand binding, the receptor tyrosines are phosphorylated, allowing the receptor to associate with and activate a range of signaling molecules, including phosphatidylinositol 3-kinase (PI3K), Shc, Grb2, and the phosphatases SHP-1 and SHP-2. VEGF receptor activation can induce activation of the MAPK cascade via Raf stimulation leading to gene expression and cell proliferation, activation of PI3K leading to PKB activation and cell survival, activation of PLC-g leading to cell proliferation, vasopermeability, and angiogenesis (from the Sigma-Aldrich homepage).

Besides this, angiogenesis can be modified via small noncoding RNAs (microRNAs, miRNAs). microRNAs are 18 to 24 nucleotides in length that serve the pivotal function of regulating gene expression (Sun et al. 2010). Single-stranded miRNA bind to messenger RNAs (mRNAs) to interfere with the translational process (Figure 1.12). Interestingly, only 1% of the genomic transcripts in mammalian cells encode for miRNA, but nearly one-third of the encoded genes are regulated by miRNAs.

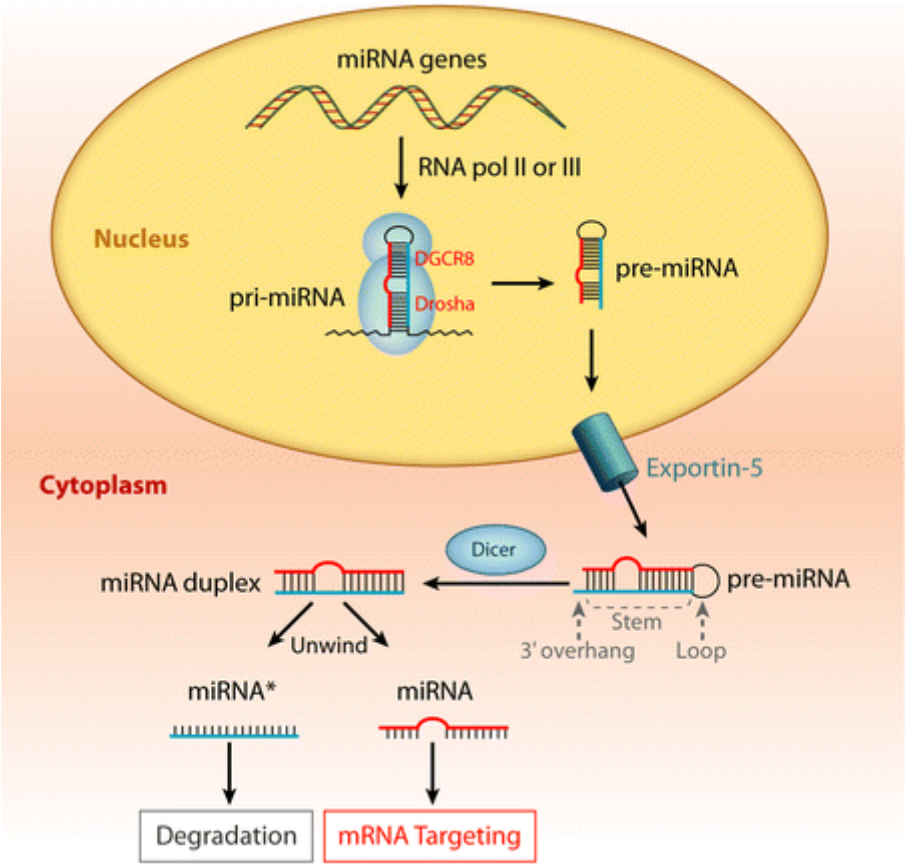

Figure 1.12: Biogenesis and functional targeting of miRNA. pri-miRNA (a 60–80-nucleotide hairpin stem-loop) is transcribed from the miRNA gene by RNA pol II or III and then cleaved by the Drosha/DGCR8 complex to result in the pre-miRNA (with a 22-bp stem and a 2-nucleotide 3' overhang) into the nucleus. After being exported from the nucleus to the cytoplasm by Exportin-5, pre-miRNA is further cleaved by Dicer to remove the terminal loop. After unwinding, one strand of miRNA acts as the functional guide strand and binds to the target mRNA. The complementary strand is rapidly degraded (from Sun et al. 2010).

1.7 Objectives

The initial goal of this study was to establish coherent contracting mouse engineered heart tissue (EHT) to address the following questions:

(1) Is the established EHT format suitable to detect a phenotype of genetically determined cardiac diseases and can pharmacological or molecular therapies rescue a disease phenotype?

(2) Do EHTs exhibit endothelial cell (EC) networks and which interventions can improve vascularization *in vitro*? Can fibrin-based EHTs serve for transplantation studies and do they develop vessel connection to the host myocardium *in vivo*?

(1) Here we studied two questions which we feel are important on the way to human disease modeling of cardiomyopathies: Is it possible to detect a specific phenotype in EHT derived from genetically defined mouse models of HCM? Does this technology provide any additional information which exceeds what was already known from the mouse model? We directly isolated cardiomyocytes from mice to generate EHTs. We chose two well-characterized mouse models of HCM that are similar, but also exhibit subtle differences in their phenotypes. Homozygous *Mybpc3*-targeted knock-out (KO) mice and *Mybpc3*-targeted knock-in (KI) mice exhibit a complete lack and 80% reduction in cMyBP-C protein levels, respectively, and develop marked eccentric left ventricular hypertrophy and reduced fractional shortening over time (Vignier et al. 2009). Previous studies suggest that increased Ca^{2+} sensitivity is the primary consequence of a defect in cMyBP-C (Pohlmann et al. 2007) and directly responsible for diastolic dysfunction (Fraysse et al. 2012). This could be the key pathomechanism of HCM (Huke and Knollmann 2010). Thus, we focused our analyses on contractile function, responses to different Ca^{2+} concentrations, the Ca^{2+} sensitizer EMD 57033 (Tsutsui et al. 2001), and Ca^{2+} transient. First approaches for molecular gene therapy were done by the use of an adenovirus encoding the human *MYBPC3* gene.

(2) To detect potential vessel-like structures in EHT two transgenic mouse lines (BMX-/VE-Cadherin-Cre-ER^{T2}-Rosa26-LacZ) with labeled ECs were established for studying vessel formation a) in the EHT construct *in vitro* or b) after cardiac surgery in the EHT graft on the host myocardium. Neonatal mice of those lines served as a source for EHT generation. During culture we studied angiogenesis-modifying compounds such as serum itself and growth factors (VEGF, PDGF and IGF) in EHT (1.8). EC-labeled EHTs served for investigating the effect of the antiangiogenic microRNA-24 (miR-24) in cooperation with the laboratory of Thomas Thum, Hannover. miR-24 has been shown to be enriched in cardiac

ECs and upregulated after cardiac ischemia. Therefore miR-24 overexpression might result in an impaired angiogenesis, silencing might prevent EC apoptosis (Fiedler et al. 2011). For *in vivo* studies EC-labeled EHTs were implanted in immunodeficient mice. Here cell survival, graft vascularization and connection to the host myocardium were studied.

1.8 Concept

To optimize angiogenesis in tissue-engineered scaffolds the European project *Angioscaff* was founded. 29 collaboration partners work together to develop scaffolds that are injectable or implantable into the human body and serve as a support for either infiltrating endogenous cells or transplanted exogenous cells. These scaffolds should be bioactive, i.e. they should bind biomolecules to induce physiological angiogenesis. The extracellular matrix (ECM) could provide signaling via adhesion molecules and growth factors bound to ECM polysaccharide components. Cells can locally degrade and remodel the matrix to create pores into which ECs can migrate during sprouting. The observation that physiological angiogenesis proceeds in response to ECM-bound factors leads to the wish to produce responsive and active ECMs which are consistent with surgical practice in humans. In this context, the initiator Jeffrey Hubbell chose fibrinogen as a suitable scaffold, since during wound healing fibrin clots naturally provide a three-dimensional scaffold that induces cell infiltration and regeneration. Synthetic peptides or recombinant protein morphogens were formed with a domain that binds to fibrin during coagulation under the enzymatic influence of the coagulation transglutaminase factor XIIIa (Hubbell 2003; Urech et al. 2005). With this technique proangiogenic factors such as VEGF, PDGF or IGF can be bound into the EHT matrix to generate angiogenesis-inducing scaffolds (Martino et al. 2011). Growth factor morphogens with engineered fibrin-binding activity were generated by introducing a special TG-binding domain (TG-VEGF165, TG-PDGF, TG-IGF).

The overall goal of our group was to study the influence of different matrix materials and growth factors on spontaneously occurring angiogenesis in EHT *in vitro* and *in vivo*. For this purpose endothelial cell reporter mouse lines (2.1.2) served as a central experimental tool.

2 Material and Methods

2.1 Animal models

The investigations conform to the guide for the care and use of laboratory animals published by the NIH (Publication No. 85-23, revised 1985).

2.1.1 Animal models used for disease modeling

2.1.1.1 The homozygous *Mybpc3*-targeted knock-out mouse model

The *Mybpc3*-targeted knock-out (KO) mouse model is a transcriptional knock-out and was generated as previously described (Carrier et al. 2004) and mice were kindly provided by Lucie Carrier. Briefly, the gene was inactivated by targeted deletion of exons 1 and 2 of the *Mypbc3* gene, which included the transcription initiation site (Figure 2.1). As a result, no cardiac myosin-binding protein C (cMyBP-C) mRNA and protein in these mice could be detected. The homozygous KO mice developed eccentric left ventricular (LV) hypertrophy with a decreased fractional shortening (measured by echocardiography) and a significant increase in LV mass to body weight (BW) ratio at the age of 3-4 months. At the age of 9 months these mice show an impaired relaxation (Pohlmann et al. 2007). Adult ventricular cardiomyocytes showed an increased sensitivity to external Ca^{2+}. In addition, in histological analyses myocardial disarray, increase of interstitial fibrosis and calcification in the fibrotic areas were observed. The mice were bred on a C57BL/6J genetic background and were viable up to 30 weeks of age. C57BL/6J served as wild-type (WT) controls.

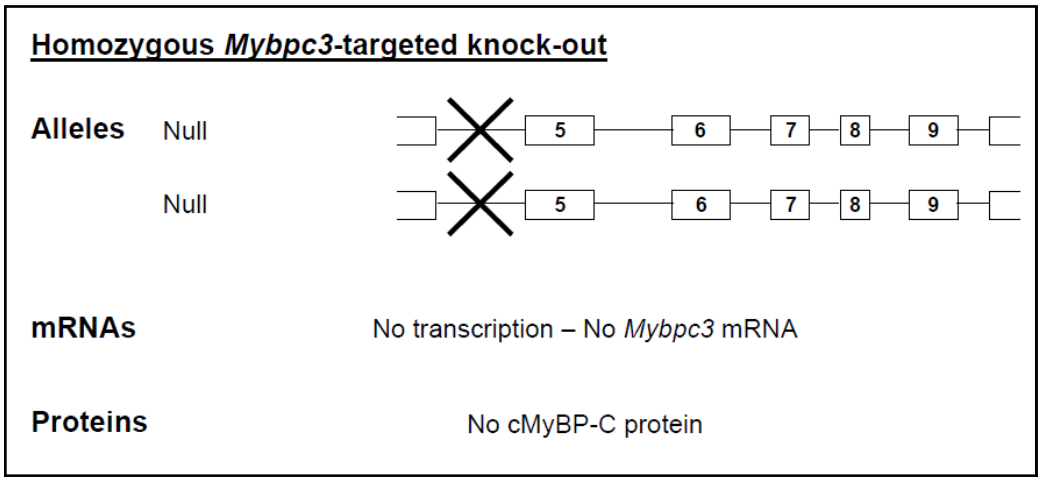

Figure 2.1: Schematic structure of alleles, mRNAs and proteins in homozygous *Mybpc3*-targeted knock-out (KO) mice. KO mice have 2 null alleles, in which the transcription initiation site and exons 1–2 have been replaced by a Neo resistance gene (Carrier et al. 2004). This results in the complete transcriptional inactivation of *Mybpc3*. Therefore, KO mice exhibit no *Mybp3* mRNA and no cMyBP-C protein (Figure was generated by Lucie Carrier).

2.1.1.2 The homozygous *Mybpc3*-targeted knock-in mouse model

The *Mybpc3*-targeted knock-in (KI) mouse model was developed as previously described (Vignier et al. 2009) and mice were kindly provided by Lucie Carrier. In these mice a G>A transition on the last nucleotide of exon 6 was introduced into the *Mybpc3* gene, which is encoding the cMyBP-C (Figure 2.2). This resembles a common human mutation and is associated with a severe phenotype and bad prognosis in human HCM patients. The mutation was introduced in mice by gene targeting with a Cre/lox system. Homozygous KI mice appeared normal and were viable for up to two years. At 3-4 months of age these mice exhibited myocyte and left ventricular hypertrophy, reduced fractional shortening and interstitial fibrosis. The level of total cMyBP-C mRNA was 50% and 80% lower in heterozygous and homozygous mice (Vignier et al. 2009). 3 different mutant mRNAs (missense, nonsense and deletion/insertion) were detected. The mice were bred on a Black Swiss genetic background. Black Swiss mice served as wild-type (WT) controls.

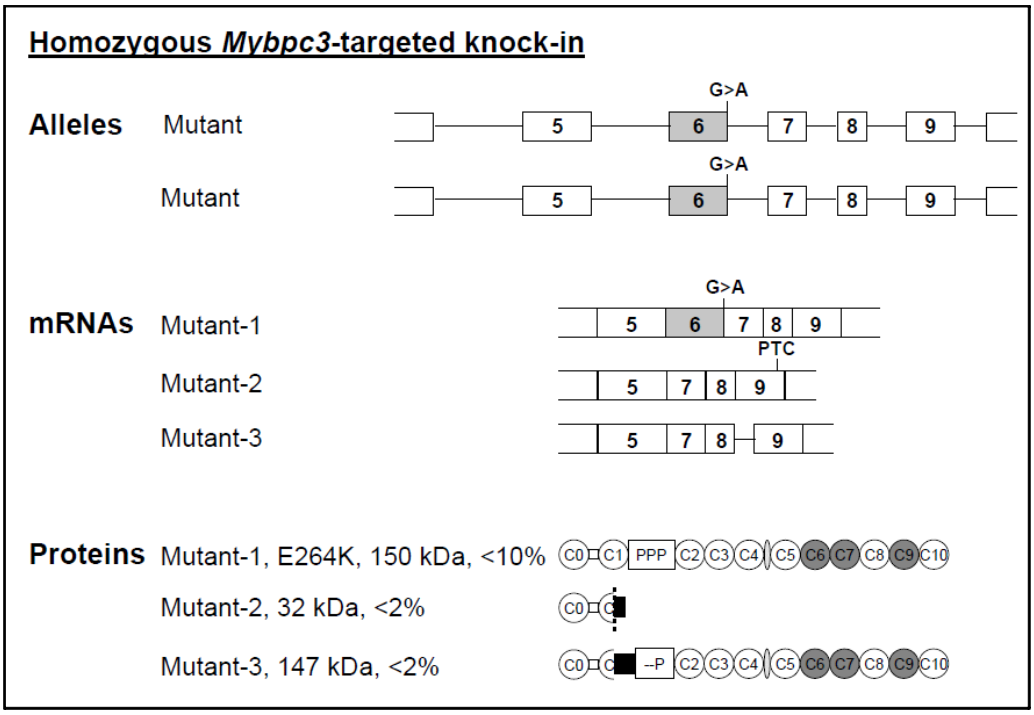

Figure 2.2: Schematic structure of alleles, mRNAs and proteins in homozygous *Mybpc3*-targeted knock-in (KI) mice. KI mice have 2 mutant alleles, each containing a G>A transition on the last nucleotide of exon 6 (Vignier et al. 2009). This results in 3 different mutant *Mybpc3* mRNA forms: 1) 20% of mutant-1 missense *Mybpc3* mRNA encoding a full-length 150-kDa E264K mutant-1 cardiac myosin-binding protein C (cMyBP-C) protein, which represents 10% of the wild-type cMyBP-C level in wild-type mice. 2) 5% of mutant-2 nonsense *Mybpc3* mRNA, which is deleted of exon 6 and results in a frameshift with a premature termination codon (PTC) in exon 9; it encodes a 32-kDa truncated mutant-2 protein (level <1%). 3) ~5% of mutant-3 *Mybpc3* mRNA, which is deleted of exon 6 and retains a part of intron 8 that restores the reading frame; it produces a 147-kDa mutant-3 cMyBP-C, which lacks the Ser-282 phosphorylation site (Figure was generated by Lucie Carrier).

2.1.2 Animal models used for angiogenesis screening

2.1.2.1 The BMX-Cre-ER^{T2}-Rosa26-LacZ and the VE-Cadherin-Cre-ER^{T2}-Rosa26-LacZ mouse model

The BMX-Cre-ER^{T2} (Florian Limbourg, unpublished) and the VE-Cadherin-Cre-ER^{T2} (Alva et al. 2006; Monvoisin et al. 2006) mice were kindly given by Florian Limbourg (MHH, Hannover). In our animal facility heterozygous Cre-positive mice were crossed to homozygous Rosa26R-LacZ reporter mice (Figure 2.3). These mouse models were generated for the purpose of specifically labeling endothelial cells *in vivo* or *in vitro* by LacZ gene expression. The Cre/lox system uses the Cre recombinase, which catalyzes site-specific recombination by the crossover between two distant Cre recognition sequences (*lox*P sites). Any DNA sequence introduced between the two *lox*P sequences (termed 'floxed'

DNA) is excised because of Cre-mediated recombination (Jaisser 2000). In Rosa26R reporter mice, a floxed stop codon is inserted between the promoter sequence and the cDNA of interest, in our case LacZ. Double transgenic mice do not express the LacZ gene until Cre is expressed, leading to excision of the floxed stop codon. Cre expression can be switched on at a certain time point either in the adult mouse *in vivo* or in the cell culture dish *in vitro* by the application of tamoxifen (*in vivo*) or *o*-hydroxytamoxifen (OHT, *in vitro*). Cre-ER^{T2} is a fusion protein of Cre recombinase and a specific ligand-binding domain, including a mutated estrogen-binding site termed ER^{T2}. ER^{T2} is highly sensitive to OHT and binding results in conformational changes of the fusion protein, which is associated with targeting of Cre recombinase to the nucleus (Indra et al. 1999; Monvoisin et al. 2006).

In general, this system provides control over the timing of Cre induction and limits the physiologic consequences of specific gene modifications in the animal to the timepoint of induction. The endothelial cell specificity of the system was obtained by placing the expression of the inducible Cre recombinase fusion protein under the control of specific promoters, in our case an arterial tyrosine kinase (BMX) or an endothelial cell specific surface protein (VE-Cadherin). LacZ expression can be easily monitored via X-Gal staining (2.7.1).

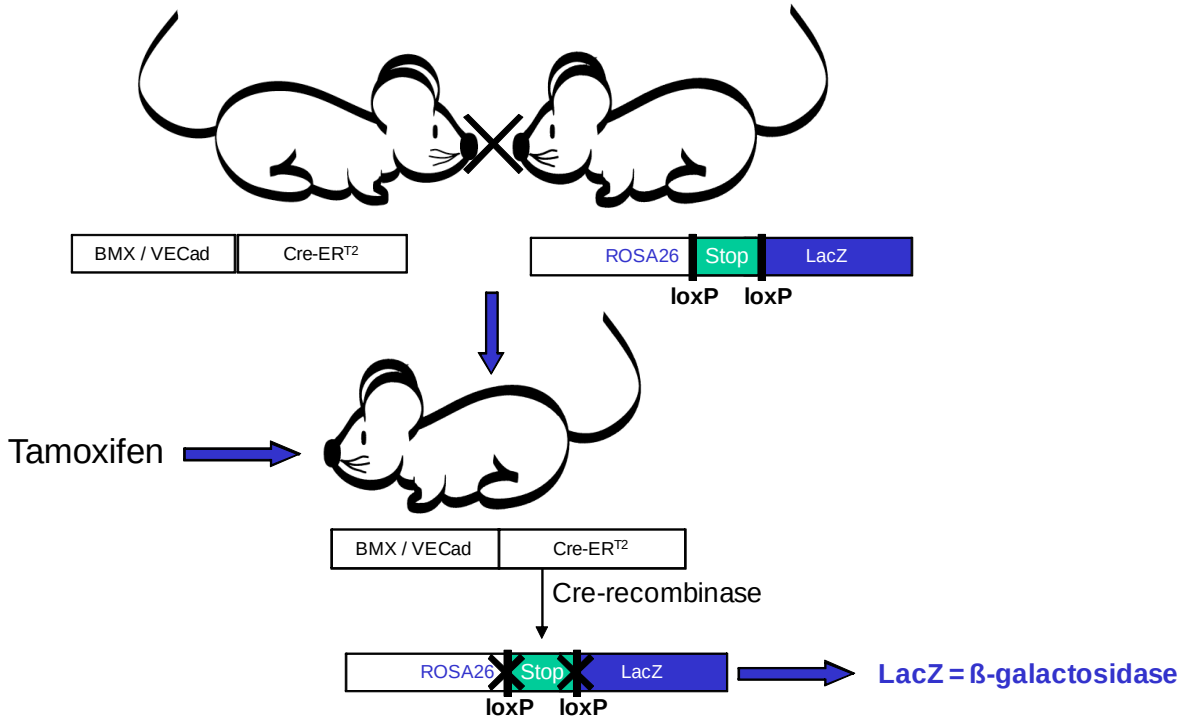

Figure 2.3: Mouse breeding scheme and induction of Cre expression. Double transgenic animals were identified by genotyping. Adult mice were either treated with tamoxifen i.p. (200µl, 10 mg/ml) and taken for analysis or used for further matings. The pups obtained from these matings served for EHT generation.

2.2 Genotyping

Genomic DNA was extracted and amplified from mouse tails according to the instruction manual of the Extract-N-Amp™ Tissue PCR Kit. Primers used are listed in the appendix (7.7). The PCR amplification was performed using the cycling parameters specified in Table 2.1. For VE-Cadherin-Cre-ER^{T2} PCR 10x Buffer #8 (500 mM KCl, 100 mM TrisHCl pH 8.5, 20 mM $MgCl_2$, 50% DMSO) was used instead of 10x PCR Qiagen buffer. The amplified DNA was loaded on a 1% agarose gel. The Gene Ruler™ 1 kb DNA Ladder was used as a molecular weight marker. Gel images were recorded with the Chemie Genius^2 Bio Imaging System.

Table 2.1: PCR cycling parameters for genotyping by PCR.

Mouse line	PCR step	Temperature (°C)	Time (min:s)	Cycles
Rosa26R	Initial denaturation	93	3:00	1
	Denaturation	93	0:30	38
	Annealing	58	0:30	38
	Elongation	72	1:00	38
	Final elongation	72	7:00	1
	Final hold	4	indefinitely	
BMX- Cre-ER^{T2}	Initial denaturation	94	3:00	1
	Denaturation	94	0:45	35
	Annealing	58	0:45	35
	Elongation	72	1:00	35
	Final elongation	72	7:00	1
	Final hold	4	indefinitely	
VE-Cadherin-Cre-ER^{T2}	Initial denaturation	94	3:00	1
	Denaturation	94	0:45	34
	Annealing	61	0:45	34
	Elongation	72	1:00	34
	Final elongation	72	7:00	1
	Final hold	4	indefinitely	

2.3 Induction of Cre expression in adult mice *in vivo*

For *in vivo* administration of tamoxifen in adult mice 100 mg tamoxifen was dissolved in ethanol (100%; 1 ml) and peanut oil was added for a final concentration of 10 mg/ml. For tamoxifen injection the mouse was hold by scruffing the neck and an insulin needle was used to inject a dose of 2 mg tamoxifen. The volume was injected into the right or left lower abdomen into the intraperitoneal space. Tamoxifen was injected daily for 5 days. A time period of 6 days was necessary to ensure the induction of Cre recombinase in the whole body. To detect LacZ gene expression mouse organs were fixed and stained as described in (2.7.1).

2.4 Methods of cell culture

2.4.1 Organ extraction

The organ extraction was authorized by the Behörde für Soziales, Familie, Gesundheit und Verbraucherschutz der Freien und Hansestadt Hamburg (Org 452). Neonatal mice (day 0-1, postnatal) were sacrificed by decapitation. Hearts were harvested and transferred to a dish with sterile Ca^{2+}- and bicarbonate free hanks buffer (CBFHH; in mM: 34.2 NaCl, 5.4 KCl, 0.81 $MgSO_4 \cdot 7\ H_2O$, 0.34 $NaH_2HPO_4 \cdot H_2O$, 5.6 glucose, 20 4-(2-hydroxyethyl)-1-piperazineethanesulfonic acid (HEPES), pH 7.4) at 4 °C.

2.4.2 Isolation of neonatal mouse heart cells with a trypsin-based digestion

After heart extraction the isolation of neonatal mouse cardiomyocytes was performed under sterile conditions. All solutions and the set of instruments were autoclaved. Neonatal heart cells were isolated by using an enzymatic dissociation based on methods to isolate neonatal rat cardiomyocytes (Webster et al. 1993). The hearts from 25 to 130 pups were washed in cold CBFHH (4 °C, 2.4.1). After removal of the vascular pedicle hearts were washed once more in 10 ml CBFHH. Then the hearts were minced in 1-2 ml CBFHH until tissue pieces reached a size of 1 mm^3 and subjected to a serial DNase/trypsin digestion to release single cells. Therefore, tissue pieces in CBFHH were transferred using a wide mouth pipette to a 50 ml falcon and an adapted amount of trypsin digestion solution was added. Trypsin digestion

solution (0.5 ml penicillin/streptomycin (pen/strep; Gibco), 1.3 ml trypsin stock solution, 0.6 ml DNase stock solution, 47.6 ml CBFHH; trypsin stock solution: 100 mg/ml in CBFHH; trypsin *crude extract* (Gibco), DNase stock solution: 2 mg/ml in PBS (w/o $MgCl_2$, w/o $CaCl_2$, Gibco); DNase II, type V, *bovine spleen* (Sigma-Aldrich)) was incubated for 10 min at room temperature on a rocker. After sedimentation of tissue the supernatant was discarded. Trypsin digestion solution was added and incubated on a rocker until supernatant dimed, immediately DNase working solution (0.5 ml pen/strep (Gibco), 0.6 ml DNase stock solution, 1.7 ml fetal calve serum (FCS, active; Gibco), 47.2 ml CBFHH) was added and triturated 20x with a 10 ml wide mouth pipette. After sedimentation of tissue pieces supernatant was transferred to a 50 ml falcon tube containing 5 ml active FCS on ice for inactivation of trypsin. This procedure was repeated until all tissue pieces were digested. Cell suspension was centrifuged (60 *g*, 15 min, 4 °C) and supernatant was discarded. The cell pellet was resuspended in a few ml of none cardiomyocyte medium (NKM, DMEM (Biochrom) including 10% FCS (inactive), 1% pen/strep, 1% L-glutamine; Gibco) and kept on ice. After pooling all cell suspensions DNase stock solution was added (250 µl per 30 ml cell suspension, incubation period 2 min). After final centrifugation supernatant was discarded, the cell pellet was resuspended in NKM and filtered (100 µm mesh size).

The trypsin-based method resulted in a cell yield of ~0.2-0.4x10^6 cells per heart.

Cells were counted in a Neubauer counting chamber. Therefore, the cell suspension was mixed and 50 µl was transferred to a fresh eppendorf tube. 125 µl trypane blue and 75 µl NKM was added (1:5 dilution). This suspension was used to fill the Neubauer counting chamber. After counting of the vital cells (not in blue) in 8 big squares the mean was calculated. The cell number could be determined according to this formula:

$$y \times 10^6 \times ml^{-1} = \bar{x} \times 5 \times 10.000$$

Abbreviations used in this formula:

y: calculated cell number
$\bar{x}$: calculated mean out of 8 big squares

After determination of the cell concentration cells were immediately taken for processing.

2.4.3 Isolation of neonatal mouse heart cells with a collagenase-based digestion

Unpurified heart cells were isolated from neonatal mouse hearts according to a procedure as previously described (Laugwitz et al. 2005). Mouse hearts were kept in a Ca^{2+}/Mg^{2+}-free Hank's balanced salt solution (HBSS; Gibco) on ice, washed, minced into small fragments in HBSS, and incubated over night at 4 °C in 0.5-mg/ml trypsin-HBSS. This trypsin (Gibco) predigestion was followed by five rounds of collagenase-based digestion. Therefore the cells were dissociated at 37 °C for 9 min with 240 U/ml collagenase type II (Worthington) in HBSS solution and collected in an equal volume of cold dark medium (DMEM:M199 (Gibco) 3:1, 10% horse serum (Gibco), 5% FCS (active; Gibco), 100 U/ml pen/strep (Gibco), 1 mM HEPES (2.4.1), pH 7.4). Collagenase digestion was repeated five times. The resulting mixture was centrifuged twice (8 and 5 min) at 60 *g* at room temperature and the cells were suspended in 20-25 ml of dark medium. The resulting cell population was counted as described above (2.4.2) and subjected to EHT generation immediately.

Using the collagenase-based digest resulted in a cell yield of 0.5-1.0x10^6 cells per mouse heart.

2.4.4 Preparation of chick embryo extract (CEE)

120 hatched eggs (9th day of hatch, animal facility, University Hospital Hamburg-Eppendorf; UKE) were disinfected with ethanol (70%). The eggs were carefully opened using scissors and the embryo was harvested with sterile tweezers. After decapitation the embryo head and body were transferred to 2 bottles containing 150 ml ice cold CBFHH (2.4.1) + 4% pen/strep (Gibco) each. After harvesting, the embryos in CBFHH were distributed to 4 flasks (150 ml) and homogenized (Polytron® homogenizer; 6 x 15 s; mode 11). After centrifugation (60 *g*, 15 min, 4 °C) the supernatant was collected. 300 ml of CBFHH was added to the pellets and homogenized again (6 x 15 s mode 11, 3 x 5 s mode 20). After centrifugation (60 *g*, 15 min, 4 °C) all supernatants were pooled and aliquots à 14 ml were stored at -20 °C. 360-460 ml extract could be collected from 120 hatched eggs. To exclude potential microbial contaminations a sample of CEE was analyzed in the Institut für Medizinische Mikrobiologie, Virologie und Hygiene (UKE). After confirmation of sterility, CEE was permanently added to the cell culture medium.

2.4.5 Generation of fibrin-based mini EHTs in a 24-well format

For generation of fibrin-based mini EHTs construct dimensions of silicone racks were established in our institute. After validation of this method the silicone racks were industrially produced by the company Siltec GmbH & Co. KG, Weiler-Simmerberg, Germany (Figure 2.4). Self-made Teflon spacers (Figure 1.8) were used to generate agarose casting molds (Figure 2.5). Silicone racks and Teflon spacers were boiled and autoclaved before sterile use.

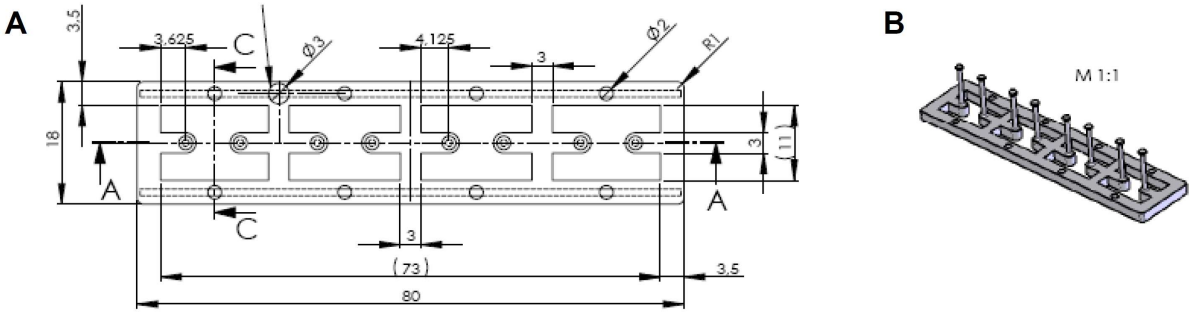

Figure 2.4: Illustration of a silicone rack from above. Dimensions of a silicone rack [**A**]: length x width: 80 mm x 18 mm; Dimensions of the silicone posts: length: 12 mm, diameter: 1 mm, diameter dish at the end of the post: 2 mm, distance between 2 posts: 8.5 mm. Silicone rack oblique view (**B**; rotated 180 degrees upside-down; from Siltec GmbH & Co. KG, 2009).

For the generation of EHTs molds were casted with sterile agarose (2%; Invitrogen) in PBS (w/o $MgCl_2$, w/o $CaCl_2$; Gibco) in a 24-well format culture dish by means of Teflon spacers. 20 min after the casting of agarose the Teflon spacers were removed carefully and the silicone racks were positioned on the agarose casting molds in a way, that one pair of silicone posts reached into each mold. During agarose solidification the EHT mastermix containing Matrigel (BD Bioscience) was pipetted on ice. After adding fibrinogen, the mastermix had to be mixed immediately until it was homogenous. Thrombin (3 U/ml) was kept in aliquots and a defined volume (100 or 150 µl) of mastermix was added, mixed by pipetting and casted into the agarose molds. After casting of all EHTs the 24-well plate was kept under cell culture conditions (2.4.6) for approximately 2 h. During this time the fibrin gel adhered to the silicone posts. At this point the silicone racks with fibrin gels were carefully transferred to new 24-well plates filled with EHT culturing medium (2.4.6).

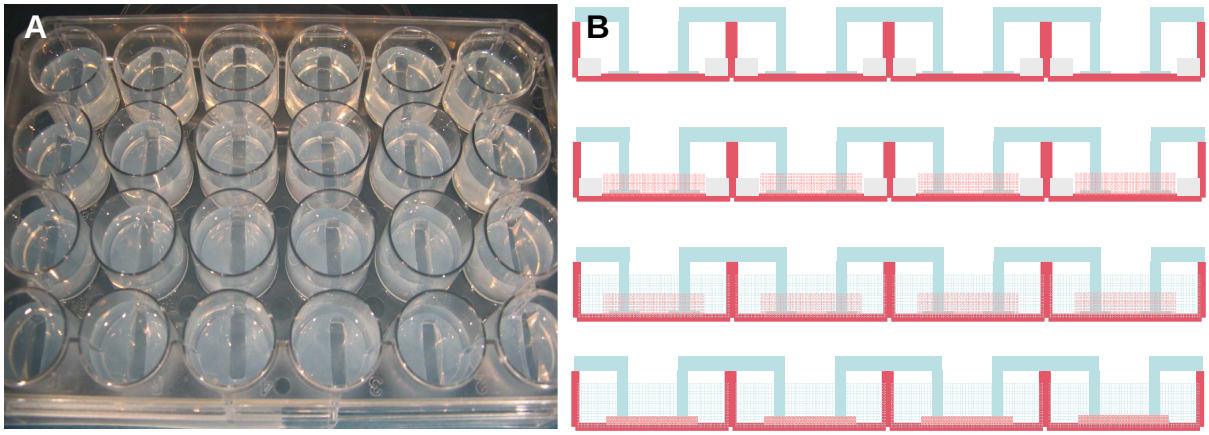

Figure 2.5: Items for EHT generation. 24-well plate with agarose casting molds [**A**]. Illustration of EHT generation scheme [**B**]: 1) Silicone rack is placed in casting molds, 2) Mastermix is pipetted into casting molds, 3) Polymerized EHTs are transferred into a fresh cell culture plate and 4) EHTs remodel during culturing period.

EHT mastermix:

$6.8x10^6$ cells

5 mg/ml Bovine fibrinogen (disease modeling) or 1.5-3.5 mg/ml human fibrinogen (angiogenesis screening)

2x DMEM according to combined volume of fibrinogen, thrombin and factor XIII

Matrigel, 10% (v/v)

ad to 1 ml NKM

2x DMEM:

10x DMEM, 20% (v/v; including 1 g/l D-glucose, 3.7 g/l $NaHCO_3$)

Horse serum, 20% (v/v; heat inactivated)

Pen/strep, 2% (v/v)

Chick embryo extract, 4% (v/v; CEE; 2.4.4)

in *aqua ad injectabilia*, sterile filtered

NKM:

DMEM (Biochrom)

Fetal calve serum, 10% (v/v; heat inactivated)

Pen/strep, 1% (v/v)

L-Glutamine, 1% (v/v)

2.4.6 EHT culture

EHTs were kept in a cell culture incubator (37 °C, 7% CO_2 and 20% or 40% O_2) in EHT culture medium.

EHT culture medium:
DMEM (including 1 g/l D-glucose, 3.7 g/l $NaHCO_3$)
Horse serum, 10% (v/v; heat inactivated)
Chick embryo extract, 2% (v/v; 2.4.4)
Pen/strep, 1% (v/v)
Insulin, 10 µg/ml
Aprotinin, 33 µg/ml

Aprotinin (Sigma) was used to avoid plasmin-induced degradation of the fibrin-matrix in the presence of horse serum (heat inactivated; Gibco) and CEE (Ahmed et al. 2007). Insulin (Sigma) was added to the culture medium to ensure survival of cardiomyocytes (Lv et al. 2011) and good force development (Zimmermann et al. 2006). The medium was changed 24 h after EHT generation. Subsequently, the medium was changed on Monday, Wednesday and Friday. Cytosine arabinoside (AraC, 25 µM; Sigma) was added on day 5 of culture to avoid an overgrowth of non-cardiomyocytes. Under these conditions, a few days after EHT casting contracting cell areas in the construct were detected. EHTs were cultured for up to 4 weeks.

2.4.6.1 Application of growth factors during EHT culture

In the context of the ongoing project *Angioscaff* (1.8) angiogenic effects of specific growth factors should be studied in artificial, three dimensional matrices. Soluble growth factors (VEGF-A_{165}, IGF-1 and PDGF-BB) were added supplementary to the EHT culturing medium from day 0 on. Modified growth factors with a transglutaminase (TG) binding domain (TG-$VEGF_{165}$, TG-IGF, TG-PDGF) were added directly to the EHT mastermix. The connection into the matrix was facilitated by the addition of factor XIII, which led to crosslinked binding. These substances were kindly provided by our cooperation partners Mikael Martino and Jeffrey Hubbell (Martino & Hubbell 2010). Used concentrations of growth factors or factor XIII were chosen according to recommendations from *Angioscaff*-working groups.

EHTs with growth factors were compared to control EHTs both generated with cells from the same cell isolation. EHTs were cultured either at 21% or at 40% oxygen, respectively. EHT culture was performed either under serum-free conditions or in serum-containing medium (10% horse serum, 2% chick embryo extract).

2.4.7 Transduction of murine EHT with an adenovirus

For the transduction of *Mybpc3*-targeted KO mouse EHTs a previously designed adenoviral vector was used (Sébillon et al. 2001; Flavigny et al. 1999). The adenoviral construct encoded the human WT-myc-cMyBP-C and EGFP in a bicistronic manner (Figure 2.6).

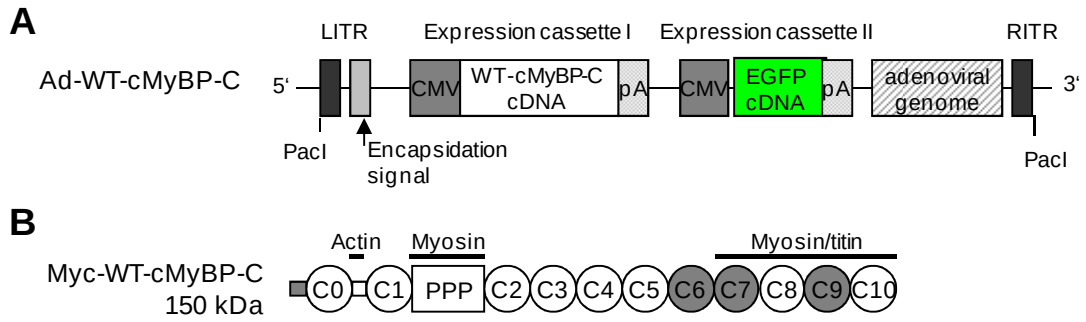

Figure 2.6: Adenoviral construct used for genetic therapy of KO EHTs and structural domains of the WT-cMyBP-C. Adenoviral construct encodes human WT-myc-cMyBP-C and EGFP in a bicistronic manner [**A**]. Structural domains of cMyBP-C protein, composed of 8 immunoglobulin, 3 fibronectin domains and a specific MyBP-C motif [**B**].

EHTs were transduced at 37 °C and 7% CO_2 for 48 h on day 3 of culture using a MOI of 75. Subsequently, EHTs were transferred to a fresh plate containing EHT medium (1.5.1; 2.4.6).

2.4.8 Transfection of murine EHT

Both pre-microRNAs (1.6), namely pre-microRNA-24 (miR-24) and a pre-scrambled microRNA (scr) were kindly provided by the laboratory of Thomas Thum, Hannover (Fiedler et al. 2011). MiR-24 and scr references are listed in the appendix (7.7). Transfection of VE-Cadherin EHTs was performed with Lipofectamine™ 2000 Reagent (Invitrogen) according to the manufacturers' instructions. Therefore, the amounts of microRNA and transfection agent were adapted to the use for EHT culture format. MiR-24 and scr were mixed separately and

incubated for 5 min with OptiMEM (Invitrogen), respectively. Lipofectamine was diluted in OptiMEM and incubated for 5 min. Subsequently, both solutions (miR-24 and Lipofectamine, scr and Lipofectamine, respectively) were mixed and incubated for 25 min. All incubation steps were done at room temperature. The transfection mix was given to wells including OptiMEM. After casting, EHTs were immediately placed into the wells including the transfection mix. EHTs were kept in the transfection mix at 37 °C and 7% CO_2 for 24 h. Subsequently, EHTs were transferred to a fresh plate containing EHT culture medium (2.4.6). Concentrations of miR-24 and scr were used in a range of 10–100 nM, respectively, as recommended by our cooperation partners.

2.5 EHT contraction analysis

2.5.1 Video-optical recording

The spontaneous contractile activity of EHTs was measured with a set-up for video-optical recording, which was established in the group (Hansen et al. 2010). The advantage of this system was that EHTs could be measured simply in the culture plate under sterile conditions. These measurements were used to evaluate contractile parameters over the whole culture period. A special software (Consulting Team Machine Vision, CTMV) was capable to measure contractile parameters such as force (mN), frequency (Hz), contraction (T1) and relaxation (T2) times (s) as well as contraction and relaxation velocities (mN/s) and fractional shortening (FS, %). For EHT measurement the 24-well plate was placed in a chamber with a glass roof that offered defined cell culture conditions (CO_2 = 7%, O_2 = 21%, N_2 = 72%, temperature = 37 °C and humidity >90%). A basler camera (type A 602f-2) was attached to a flexible x-, y-, z-device (IAI Corporation) which focused and recorded every single EHT. The camera was moved via a connected computer and the measured EHT was illuminated automatically. Permanent illumination was not performed to avoid warming of the medium. The software was able to recognize the silicone posts (Figure 2.7 B, green squares) due to a contour-recognition algorithm. Before measurement every single EHT was adjusted to find the perfect position of the camera and ensure sharpness. Duration of the measurement was determined before starting the software. The camera recorded all selected EHTs and generated a PDF document automatically. Contractility graphs of measured EHTs were recorded and contractile parameters were calculated according to the measured deflection of the silicone posts.

The fractional shortening of the EHT served for calculation of force. Based on silicone rack geometry and the silicone material (Sylgards 184, Young's modulus = 2.6 kPa) force was calculated by the use of a previous published formula (Vandenburgh et al. 2008):

$$\text{Force [mN]} = \frac{3 \text{ X } \textit{Young modulus} \text{ (Mpa) X } \textit{Pi} \text{ X Radius}^4 \text{ (mm)}^4 \text{ X } \Delta\text{post deflection (mm)}}{4 \text{ X Post length}^3 \text{ (mm)}^3}$$

Before analysis, parameters as the minimal force threshold, filter values or relaxation frames, interval and threshold could be defined. With this automated set-up a huge number of EHTs were measured and analyzed in a short time period. The software generated a PDF document including contractile parameters and contraction graphs at the end of each run. If this document indicated that settings were suboptimal, offline run documents with adapted settings could be generated to precisely optimize the calculation of contractile parameters.

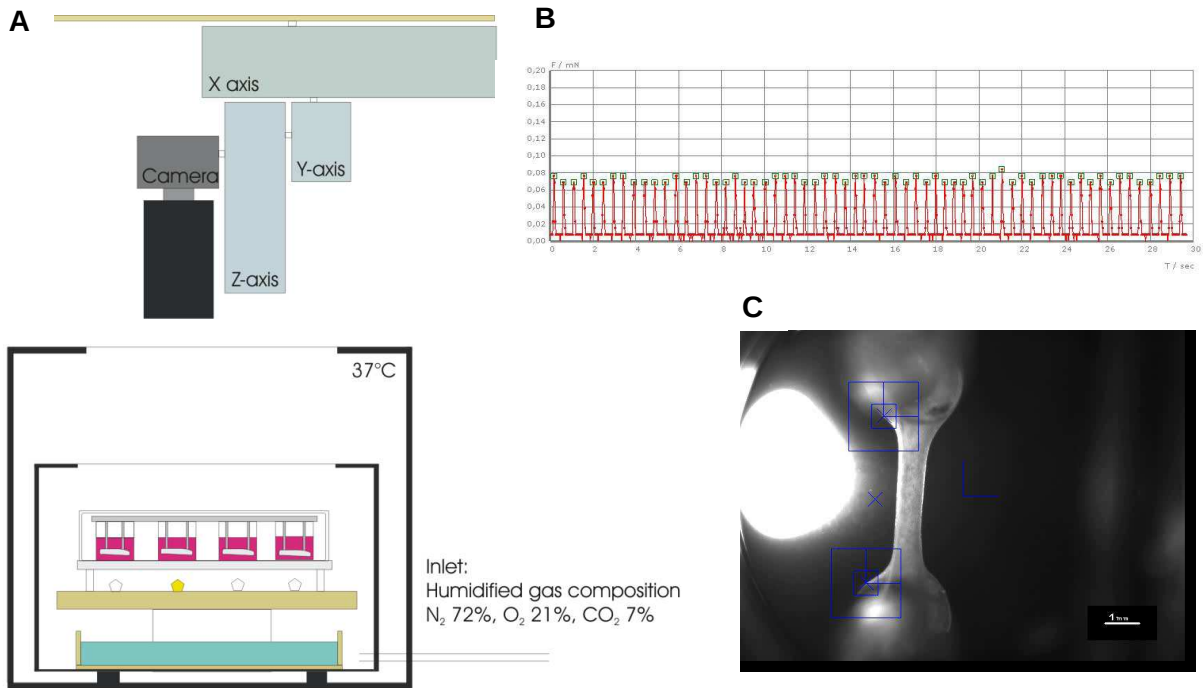

Figure 2.7: Video-optical recording. Set-up for EHT analysis (**A**; from Hansen et al. 2010). The 24-well plate is placed in the incubation chamber with a glass roof allowing the camera to focus a single EHT. A light source from below illuminates the recorded construct. Water is filled to the bottom to maintain humidity. The gas composition is delivered via flexible tubes. Recorded graph example of a mouse EHT with force (mN) on the y-axis and time (s) on the x-axis [**B**]. Recognized contraction peaks are marked by green squares. Depiction of a measured mouse EHT [**C**]. Blue squares on the edge of the silicone posts indicate a correct recognition and measurement.

2.5.2 Measurement in electrically stimulated and perfused EHT

2.5.2.1 Experimental set-up and procedure

To measure contractile function of EHTs under electrical pacing and continuous perfusion a novel microscope-based set-up was constructed. It consisted of a Zeiss Axiovert 200M (Carl Zeiss, Germany) inverted fluorescence microscope equipped with a 2.5x lens (Objective EC Plan-Neofluar 2.5x/0.12; Zeiss) and was connected to an IonOptix system (Figure 2.8). The movement of one EHT post was recorded by an IonOptix video camera (MyoCam^{TM}, Fluorescent System Interface) under red light and evaluated by IonOptix software (IonWizard 6.0 software). EHTs were positioned in 24-well glass bottom plates (IWAKI 090615) placed in a thermostatted and CO_2-controlled, custom-made incubation chamber, electrically paced by two platinum iridium electrodes connected to a field stimulator (MyoPacer, IonOptix Corporation, Milton, MA, USA) and continuously perfused by a custom-made system with 8 thermostatted (37 °C) and gassed (7%) glass reservoirs to switch perfusion buffers. If not otherwise indicated, electrical stimulation was performed at a frequency of 5–6 Hz and pulses of 30 V and 5 ms duration. Perfusion was done with Tyrode's solution (in mM: NaCl 120, KCl 5.4, $MgCl_2$ 1.0, $CaCl_2$ 0.2-1.8, NaH_2PO_4 0.4, $NaHCO_3$ 22.6, glucose 5.0, Na_2EDTA 0.05, ascorbic acid 0.3) with a flow rate of 6 ml/min. Tyrode's solution was gassed with carbogen (95% O_2, 5% CO_2) before and during measurement. At the beginning of EHT measurements the force-frequency relationship was evaluated at high extracellular Ca^{2+} (1.8 mM Ca^{2+}) and the stimulation was adjusted to 5 or 6 Hz, ensuring measurements of rhythmic contractions. To decrease external Ca^{2+} concentration EHTs were perfused with Tyrode's solution containing 0.2 mM Ca^{2+} for 20-30 min. Ca^{2+} concentrations were cumulatively increased to 1.8 mM in 8-15 min steps of 0.2 or 0.4 mM. Drug interventions were performed in Tyrode's solution containing 0.6 mM as indicated, after equilibration at that concentration for at least 15 min. Force development before addition of the respective compound was defined as baseline. The length of contraction experiments was 1-3 h. EHT post deflection was measured in µm and used to calculate force development in mN (2.5.1). Contractile function under the specific conditions was evaluated by averaging 50-100 peaks.

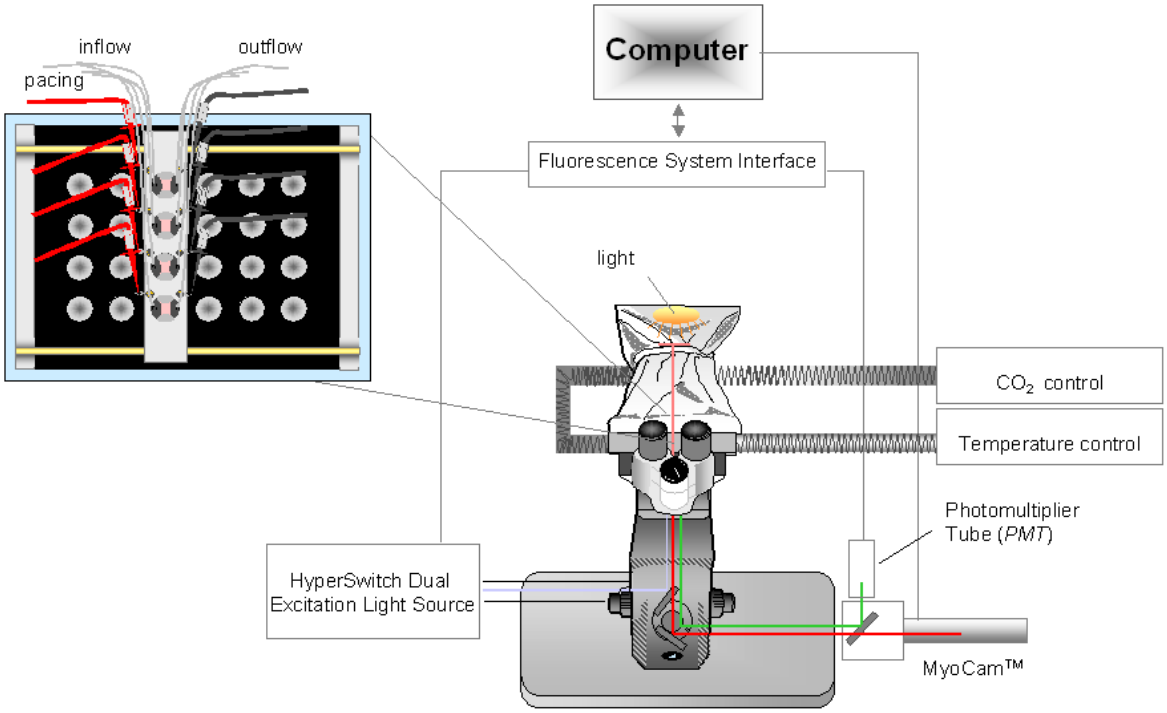

Figure 2.8: Novel-microscope based set-up for measurement of contractile force under electrical stimulation and continuous perfusion. The silicone rack with EHTs was placed in a special 24-well plate in the incubation chamber. A device was positioned on top containing the electrodes and the inflow and outflow track from the perfusion system. The EHT was focused via the microscope and the software was started. Pacing and perfusion were started autonomously. The HyperSwitch Dual, PMT and Fluorescence System Interface were used for Ca^{2+} transient measurements (2.5.2.3/4).

2.5.2.2 Measurement of contractile parameters with the IonOptix software

All measurements were performed under electrical stimulation and continuous perfusion (2.5.2.1). In the first years of my thesis EHT measurements were analyzed by the use of the IonOptix software. Single contractions of an EHT were recorded at one condition (Figure 2.9). The IonOptix MyoCam™ (IonOptix Corporation, Milton, MA, USA) recognized the silicone post of the EHT via phase-contrast. The black color of the silicone post depicted a contrast to the light structure of the EHT tissue. When analyzing the optical density, the density trace was recorded by the camera and subsequently transformed into a signal by the IonWizard 6.0 software. The program recorded and saved the EHT length as a function of time including also the stimulation marks which were necessary for the analysis (Figure 2.9). The camera was able to record 250 pictures per second. The calculated average peak served for calculation of contractile values as further indicated in the results part.

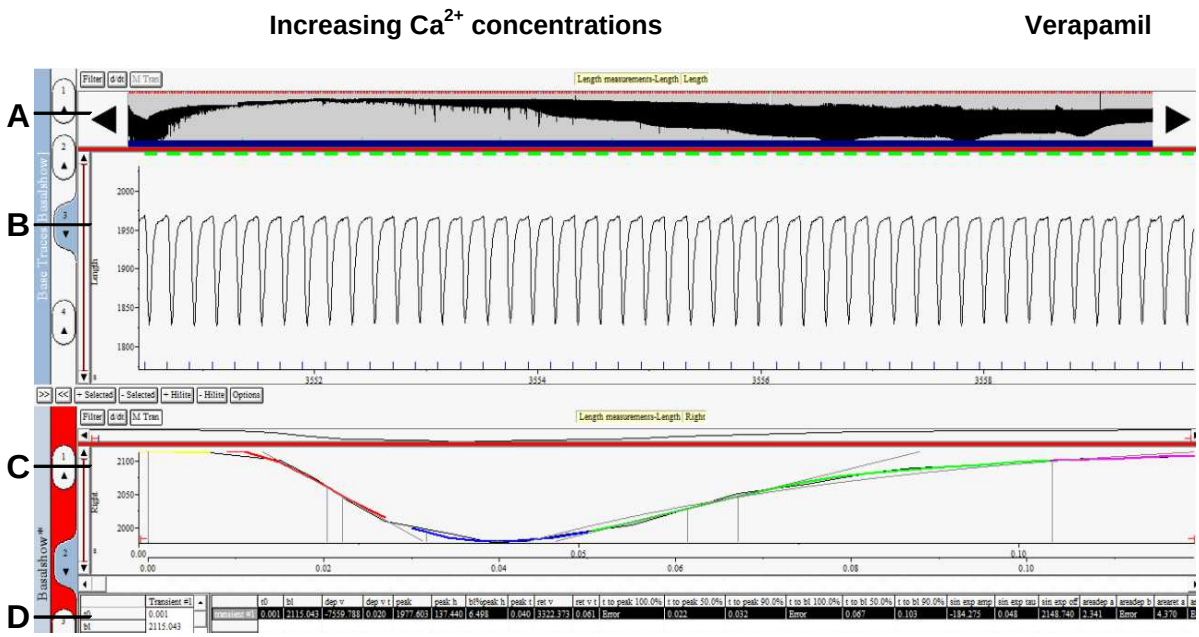

Figure 2.9: Surface of the IonWizard Software (6.0) during EHT measurement. The measurement was performed under electrical stimulation (5 Hz) and continuous perfusion. The upper panel shows the whole experiment (~3 h), seen as a mechanogram showing different contraction amplitudes from culture medium to low Ca^{2+} up to high Ca^{2+} and verapamil administration at the end [**A**]. The first middle panel shows the selected area of the recorded mechanogram, which should be used for analysis [**B**]. Blue ticks indicate the pacing signal. The second middle panel shows the calculation of an average peak from the selected area [**C**]. The different colors indicate the different stages of contraction and relaxation. Transient value from an average peak, giving contractile parameters as peak height, contraction and relaxation velocities and contraction and relaxation time values [**D**].

The length measurements were calibrated using a stage micrometer with a defined scale. Like this, the number of pixels/µm of the image from the IonOptix Myocam™ could be determined and entered as a defined parameter in the software. Force was calculated according to previously described formula (2.5.1).

2.5.2.3 Fura-2 staining of EHT

To record intracellular Ca^{2+} transients EHTs were loaded with the fluorescent Ca^{2+} chelator Fura-2 acetoxymethyl ester (Figure 2.10). Fura-2 is binding Ca^{2+}-ions and fluoresces after excitation with UV light (Grynkiewicz et al. 1985). The change in fluorescence emission is not unidirectional but twodirectional and depends on the wavelength of excitation. Ca^{2+} concentration dependent emission (510 nm) is increased at excitation wavelength below 370 nm with a maximum at 340 nm (Figure 2.10 B, blue arrow). However, excitation wavelength

above 370 nm results in a Ca^{2+} concentration dependent decrease in emission (Figure 2.10 B, brown arrow).

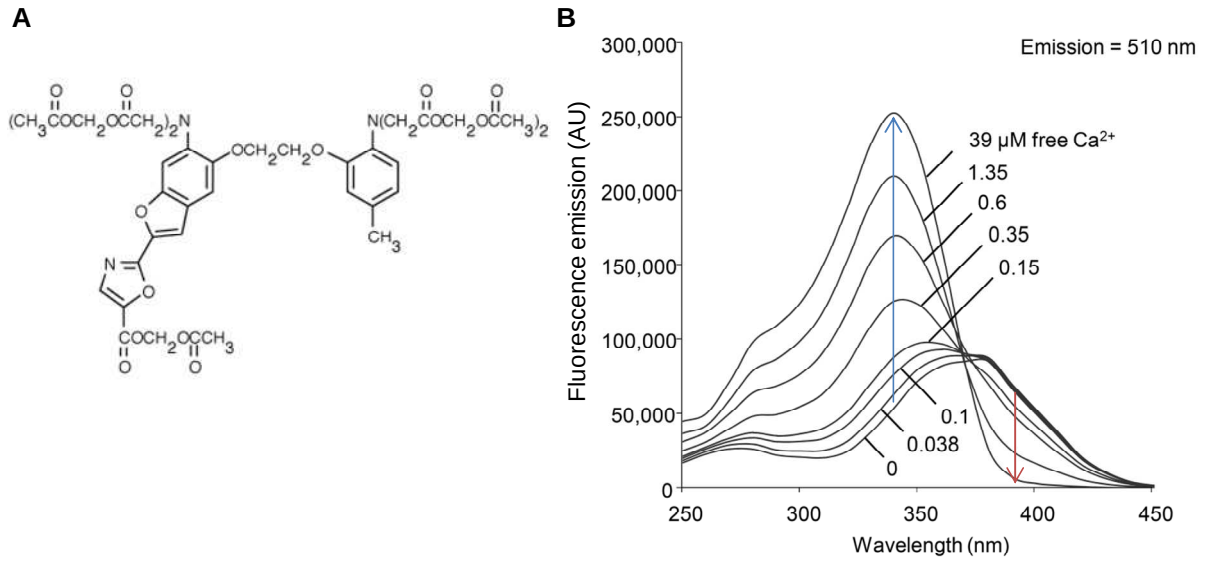

Figure 2.10: The chemical structure of Fura-2 acetoxymethyl ester and its fluorescence spectra. Fura-2 acetoxymethyl ester (**A**; Fura-2 AM). Fluorescence spectra of Fura-2 [**B**]. The emission of fluorescence from Fura-2 after excitation with increasing wavelength was recorded in eight calibrating solutions with different Ca^{2+} concentrations (0–39 µM).

The hydrophilic sodium and potassium salts of Fura-2 are cell-impermeable probes that cannot pass the membrane. The acetoxymethyl (AM) ester of Fura-2 can passively diffuse across cell membranes. Inside the cell, esters are cleaved by intracellular esterases to yield cell-impermeable Fura-2. Fura-2 AM (Molecular Probes) was used for all experiments.

Loading dye concentration should be high enough to overcome matrix inactivation while keeping cells alive. Serum in EHT culture medium is known to interact with Fura-2 AM causing cleavage of AM. Therefore, EHTs were stained in serum-free Tyrode's solution (2.5.2.1) at 1.8 mM external Ca^{2+}. Furthermore, the detergent Cremophor® EL (0.75%) was used to facilitate Fura-2 AM entering the cells (Tong et al. 2008). During loading (2 h), a temperature of 21 °C was recommended because it had been shown that cells actively extrude Fura-2 when incubated at 37 °C. Nevertheless, we observed that especially mouse EHTs stopped beating when they were kept in Tyrode's solution at room temperature. We had to ensure survival of the cells in the EHT and a beating activity of the cells during the staining process, thus EHTs were stained at 37 °C. In general, EHTs should be paced and gassed (95% O_2, 5% CO_2) during staining. However, this was technically challenging. We therefore decided to perform the Fura-2 (10 µM) staining at 37 °C in the cell incubator under

sterile conditions for 2 h in the presence of Cremophor® EL (0.75%). Before staining, EHTs were washed twice with Tyrode's solution (1.8 mM Ca^{2+}) to clear EHTs from serum. After staining, EHTs were washed twice before starting measurement experiments. Fura-2-stained EHTs were measured at a frequency of 1 or 2 Hz.

2.5.2.4 Simultaneous measurements of force and intracellular Ca^{2+} transient with the CTMV software

Parallel measurement of contractile force and Ca^{2+} transients was realized with an experimental set-up as shown in Figure 2.8. Important additional alterations included the exchange of the IonOptix Myocam^{TM} with a Basler camera (type A 602f-2) and the use of a second Basler camera in the frontport of the microscope. A second important addition was the use of two objectives: 1. A 1.25x lens (Objective EC Plan-Neofluar 1.25x/0.03; Zeiss) to monitor EHT contractile force and 2. A 10x lens (Objective EC Plan-Neofluar 10x/0.3; Zeiss) with high UV transmission to capture Ca^{2+} transients in center parts of the EHT.

To provide an alternate Fura-2 excitation with 340 and 380 nm UV light at a high rate an IonOptix HyperSwitch Dual Excitation Light Source (IonOptix Corporation, Milton, MA, USA) was used. The light from a 75 W Xenon arc bulb was formed into a converging beam and focused on a high-speed galvanometer driven mirror. This mirror directed the now diverging light to one of two collecting lenses. One path was sent straight into a dichroic cube where it encountered an emission filter and then passed through the dichroic mirror towards a liquid light guide to the microscope. In the second path the light was steered into the dichroic cube at a 90 degree angle where it encountered a second emission filter and was then reflected by the dichroic mirror towards the liquid light guide. Thus, two light beams with either 340 nm or 380 nm were alternatively sent to the EHT chamber on the microscope (Figure 2.11).

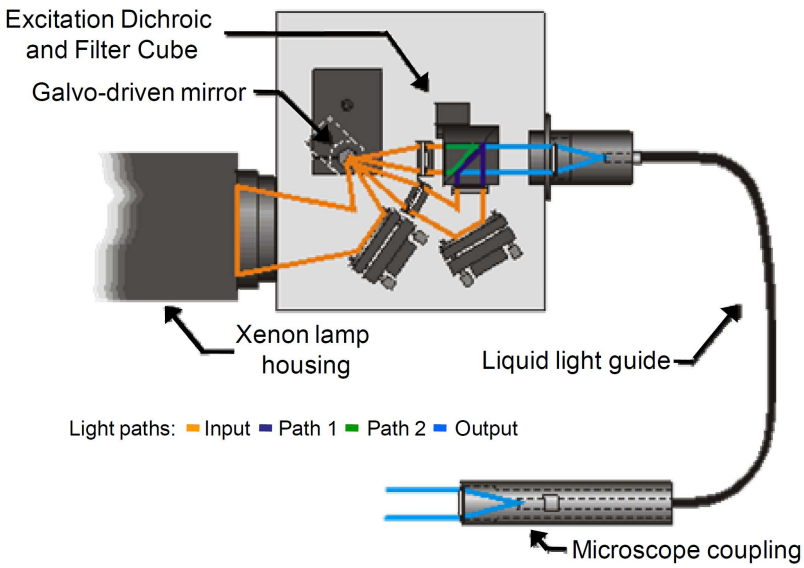

Figure 2.11: IonOptix HyperSwitch Dual Excitation Light Source

The excitation light reached the Fura-2 loaded EHTs through the objective (10x) with a frequency of 250 wavelength pairs per second which guaranteed an adequate time resolution to depict the intracellular Ca^{2+} transients. The emitted fluorescence light from the microscope was reflected by a dichroic mirror into a photo multiplier tube (PMT), which generated a little current for each sensed photon. The software formed the ratio of the fluorescence intensities at 340 and 380 nm excitation, plotted it and saved it as a function of time including the stimulation marks.

A customized software which was established in cooperation with CTMV GmbH was implemented to define x-, y-, z-coordinates for individual EHTs for measurement of contractile force (1.25x lens, front port camera) and Ca^{2+} transients (10x lens, PMT, camera attached to this was used to verify focus of EHT center parts) separately (Figure 2.12). Using this software measurements of both parameters were performed with high level of automation and standardisation in analogy to previously reported techniques (Hansen et al. 2010). The electrical pacing signals (IonOptix Myopacer) were visualized by vertical blue lines in the graphs for contractility and Ca^{2+} transients and allowed the calculation of parameters like force, contraction and relaxation times as well as Ca^{2+} transient amplitude and kinetics such as time to peak Ca^{2+} and time to 90% Ca^{2+} decay.

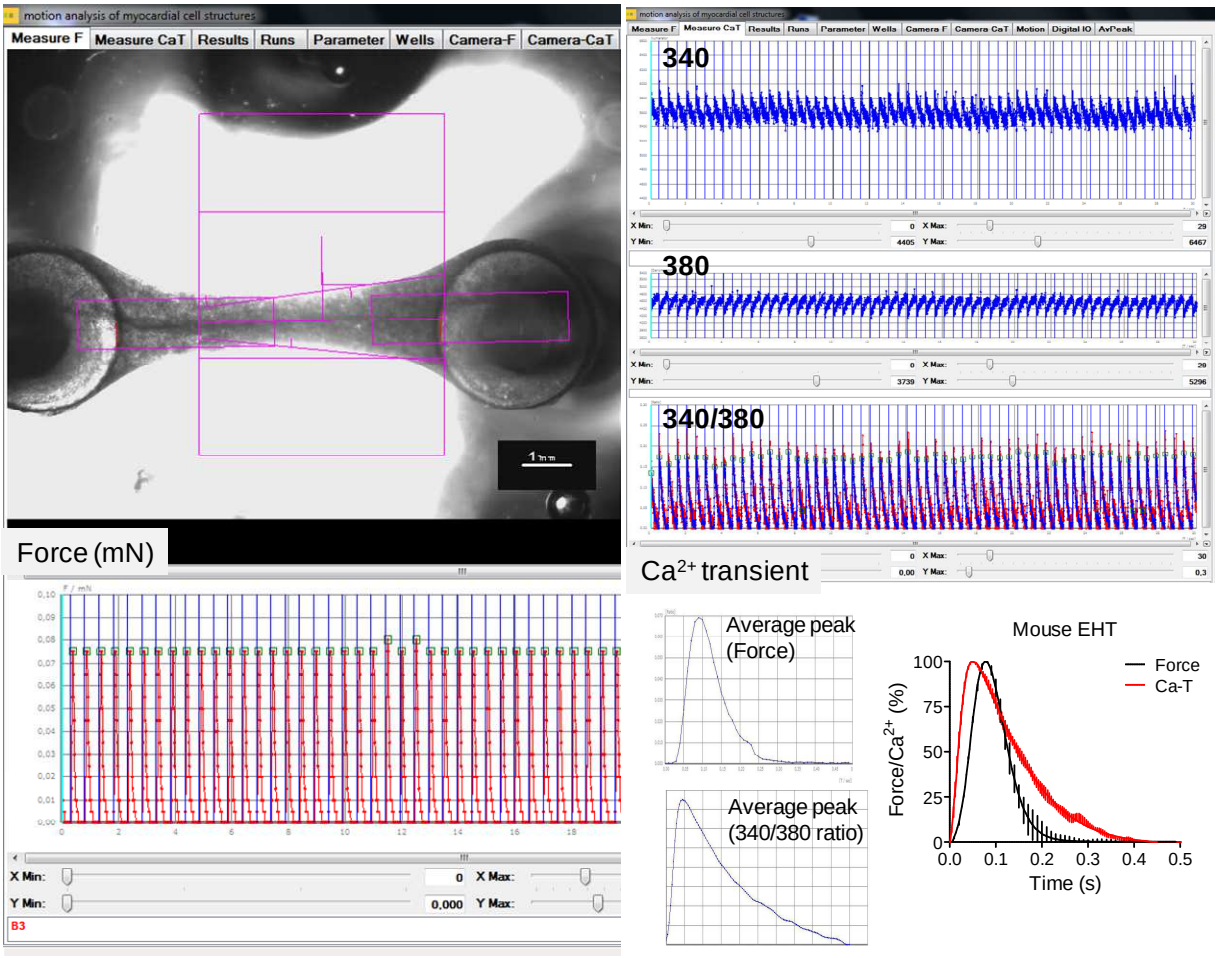

Figure 2.12: Force and Ca^{2+} transient measurements in a mouse EHT. EHTs were stained with 10 µM Fura-2 at 37 °C in 1.8 mM Tyrode's solution for 2 h at 37 °C. Depicted is the surface of the CTMV software, showing the nominator (upper right panel; 340) and the denominator (middle right panel; 380), the ratio (340/380) and generated average peaks (force and 340/380 ratio). Average force and 340/380 ratio peaks were blotted in one panel. Left panels: depicted EHT during measurement (upper panel). Pink marks indicate contour recognition. Recording of force (lower panel). Pacing signals were visualized by vertical blue lines. Electrical pacing was performed at 2 Hz. X-axis shows the time (10 s) and y-axis shows the force or Ca^{2+} transient amplitude (F340/380 ratio), respectively.

2.6 EHT as a graft for transplantation studies

2.6.1 Immunodeficient mouse models

Immunodeficient mice served for EHT-transplantation studies to avoid graft rejection and the need of pharmacological immunosuppression. In this context, different strains of immunodeficient mice were tested. First experiments were done with NMRI nu/nu mice (Figure 2.13). These mice are hairless and lack a thymus, thus resulting in absence of T-cells. Pfp/RAG2 double targeted mutation mice served for further experiments due to limited

disposability of NMRI nu/nu mice. These mice exhibit a severe depletion of NK-cell function through the disruption of the *Pfp* gene, and lack both mature T and B lymphocytes through disruption of the *Rag2* gene. Pfp/RAG2 mice often died early after cardiac surgery. Therefore NMRI nu/nu mice were preferably used for all implantation studies.

2.6.2 Implantation of EHT onto murine hearts

All surgical procedures were performed in adult NMRI nu/nu or Pfp/RAG2 mice in cooperation with the cardiac surgeons Lenard Conradi and Moritz Seiffert. The weight of mice ranged between 20–30 g. Xylazine/ketamine (Rompun® (Bayer): 12 mg/ml ketamine, 1.6 mg/ml xylazine in 0.9% NaCl; 10 ml/kg body weight) was chosen as an anesthetic because it provides an adequate depth of anesthesia for 20–25 min. First, the mouse was kept under isoflurane (3%) as a pre-anesthetic. Afterwards xylazine/ketamine was injected subcutaneously and the mouse sit for 7–10 min until anesthesia took effect. An adequate depth of anesthesia was verified by testing for toe-pinch reflex. Therefore the toe of the hindlimb was pinched firmly between the fingernails. When there was no response to the toe pinch, medium-deep anesthesia was attained. In the case of Pfp/RAG2 mice the animal's chest had to be prune of hairs, which were removed with hair removal mousse. Afterwards the mouse was positioned on an operating table for the subsequent intubation. The animal was fixed to the operating platform by tapping the forelimbs and the hindlimbs. For the endotracheal intubation it was important to ensure that the mouse was positioned in close proximity (5–10 mm) to the edge of the platform and the forelimbs were assured in place to the sides of the body. Noninvasive endotracheal intubation was performed as described in the literature (Tarnavski et al. 2004). For artificial ventilation a mouse ventilator (TOPO™ Dual Mode Ventilator, Kent Scientific) was used. The tidal volume and ventilation rate was between 120–180 breaths/min. The rhythmic movements of the chest synchronized with the ventilator were observed carefully. 0.5–0.8 l/min Oxygen was connected to the inflow of the ventilator. 2.5% Isoflurane was connected to the inflow for additive inhalational anesthesia.

After intubation, the legs were fixed to the platform with strands of tape. The mouse was kept on a warm plate (37 °C) during the operation. The operations were carried out under aseptic conditions and surgical tools were autoclaved before using. Before surgery, the operating field was disinfected with povidone-iodine solution (Betadine®; Mundipharma) and 70% ethanol. A transverse 5-mm incision of the skin was made with scissors 2 mm away from the left sterna border, 1-2 mm above the level of the armpit. The superficial thoracic vein should

be visualized which runs under the skin at the lateral corner of the incision. Both layers of thoracic muscles were cut, taking caution to avoid damaging the vein. The chest cavity was opened with scissors by a small incision (5 mm in length) at the level of the second intercostals space 2-3 mm from the left sterna border. It was important not to approach the sterna border any closer than this, because the internal thoracic artery (running along the sterna border of the inner surface of the thoracic cavity) could be easily damaged. While opening the chest wall, care was taken not to damage the underlying lung. The chest retractor was gently inserted to spread the wound 4-5 mm in width. With two forceps the pericardial sac was gently pulled apart. The heart could then be visualized. The EHT was washed in PBS (w/o $MgCl_2$, w/o $CaCl_2$; Gibco) for a few min. Then the EHT was removed from its silicone rack and threaded using a 6-0 suture with the help of a needle on its two edges. In this setting it was placed onto the left ventricle of the heart. Then the EHT was placed on the heart by stitching with the needle into the EHT and heart tissue carefully about 1 mm in depth. Double knots were made on each side of the EHT to keep it fixed onto the heart. Cotton applicators were used to stop eventual bleeding. PBS (w/o $MgCl_2$, w/o $CaCl_2$; Gibco) was put into the wound to avoid the EHT to stick together with the chest wall after surgery.

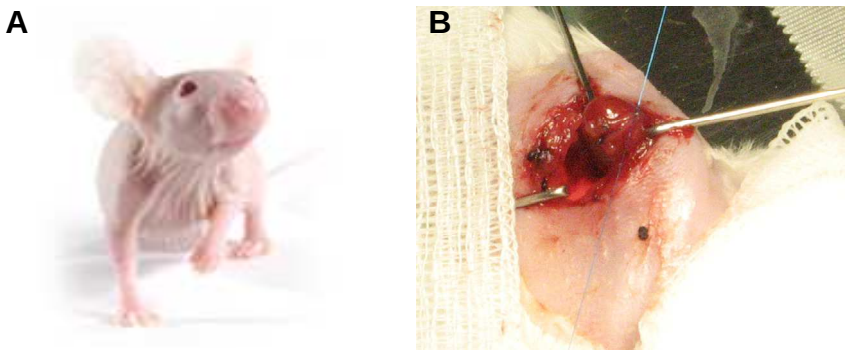

Figure 2.13: NMRI nu/nu mouse and fixation of an EHT onto a mouse heart. NMRI nu/nu mouse (immunodeficient) were used for cardiac surgery [**A**]. After chest-opening, the graft was implanted onto the left ventricle of the heart [**B**].

After implantation of the EHT the chest retractor was removed. Since the lungs were partially compressed by the retractor, they had to be reinflated by shutting off the outflow of the ventilator for 1-2 s using a finger. This was important since collapse of the lungs would have resulted in respiratory distress and poor recovery after surgery. The chest cavity was closed by bringing together the second and third ribs with one 6-0 nylon suture. All layers of muscles and skin were closed with 6-0 continuous absorbable and nylon sutures, respectively.

Isoflurane inflow was stopped and 100% oxygen was connected to its inflow. After 15-25 min the mouse started to breathe spontaneously. Then the ventilation was stopped and the mouse was extubated. Finally, an analgesic (buprenorphine hydrochloride (Sigma), 0.1 mg/kg, s.c.) was given subcutaneously. After surgery, the mouse recovered for a few min on the warm plate. The mouse was placed in a clean cage with a sterile filter on top. Metamizole sodium solution (Novaminsulfon-ratiopharm®, 500 mg/ml metamizole sodium; Ratiopharm) was added to the drinking water (1.3 mg/ml). The subsequent postoperative care (food and drinking water supply) was done in our animal facility.

2.6.3 Mouse heart extraction

Organ extraction was authorized by the Behörde für Soziales, Familie, Gesundheit und Verbraucherschutz der Freien und Hansestadt Hamburg (G10/079_3-D EHT). Mice were anesthesized in light CO_2. Then a 50 ml Falcon tube was filled with pieces of tissue and moisturized with a few drops of diethyl ether. The head of the mouse was placed inside to ensure anesthesia. The animal was fixed with taps on an operating plate. Median thoracotomy was performed, afterwards the hearts were extracted and steadily held with forceps (heart should be beating at this point). The hearts were taken for perfusion fixation through the heart according to Langendorff (2.6.4) immediately.

2.6.4 Perfusion fixation through the heart according to Langendorff

A uniform fixation is usually obtained if the fixative solution is perfused via the vascular system, either through the heart or through the abdominal aorta. The following procedures provide fixation with a fixative solution containing paraformaldehyde and glutaraldehyde (2.7.1). First, the perfusion pump was set up and the perfusion set and needle were attached (Figure 2.14). 100 ml of *aqua ad injectabilia* was used to clean the system. Then the place open end of the perfusion tube in the beaker was filled with cold 4% fixative solution (2.7.1). The volume needed was usually ~100 ml per heart. The valve was opened and adjusted to a slow steady drip, and then the valve was closed. Then a needle was directly inserted into the protrusion of the left ventricle of the beating heart (~5 mm depth). This needle was assured by clamping in place near the point of entry. The valve was released to allow a slow and steady flow of 0.9% saline solution. When the blood was cleaned from the heart a change to fixative solution was performed (100 ml per heart). The hearts were perfused for 5–10 min,

then the perfusion was stopped and the hearts were transferred to a dish with PBS (w/o $MgCl_2$, w/o $CaCl_2$; Gibco). Hearts were further X-gal stained and a post fixation was performed (2.7.1).

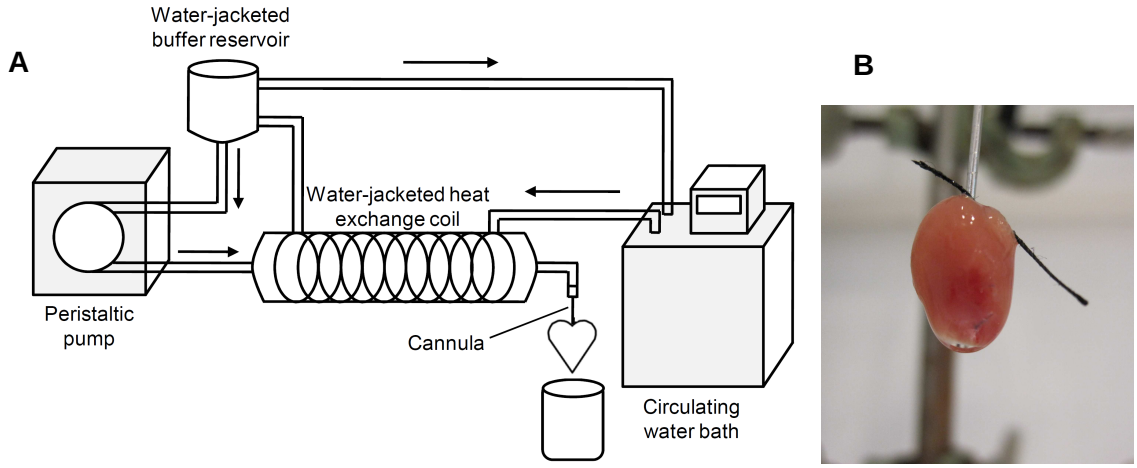

Figure 2.14: Perfusion fixation of the heart. Schematic depiction of the perfusion system used in our laboratory [**A**]. A mouse heart during perfusion fixation [**B**].

2.6.5 Implantation of EHT into the dorsal mouse skin

To test the effect of different EHT culturing conditions (serum-containing, serum-free culture or growth factor application) on the vascularization *in vivo* first pilot studies were performed in the dorsal skin of NMRI nu/nu mice. 4-6 EHTs of different conditions were implanted in the dorsal skin according to the shown scheme (Figure 2.15). The inner part of the skin offers a good vessel network, allowing a potential good EHT survival *in vivo*.

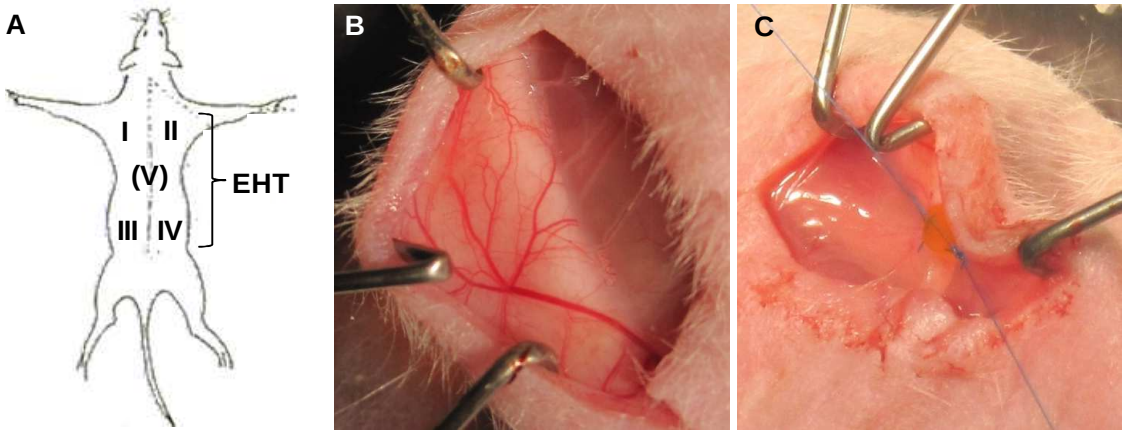

Figure 2.15: EHT implantation scheme and inner view of a mouse dorsal skin. Schematic depiction of a mouse, showing labeling of implanted EHT grafts [**A**]. Inner view of the vessel network in mouse dorsal skin [**B**]. Implantation of the graft into the dorsal skin [**C**].

The preparations before surgery including the surgical equipment, ventilation and leg taping were performed as described for mouse cardiac surgery (2.6.2). Taped mice were anesthesized with 2.5% isoflurane. After skin opening the EHT was washed for a few min in PBS (w/o $MgCl_2$, w/o $CaCl_2$; Gibco), subsequently removed from the silicone rack and fixed onto the inner part of the dorsal skin (Figure 2.15). EHTs were fixed at both edgeds with sutures. After this process, some drops of PBS (w/o $MgCl_2$, w/o $CaCl_2$; Gibco) were added into the wound and the skin layer was sutured with 6-0 continuous absorbable and nylon sutures, also used for EHT fixation. Isoflurane inflow was stopped and 100% oxygen was connected to the inflow. After 15-25 min the mouse started to breathe spontaneously. Finally, an analgesic (buprenorphine (Sigma), 0.1 mg/kg, s.c.) was injected subcutaneously. The mouse was placed in a clean cage with a sterile filter on top. Metamizole sodium solution (Novaminsulfon-ratiopharm®, 500 mg/ml metamizole sodium; Ratiopharm) was added to the drinking water (1.3 mg/ml). The subsequent postoperative care (food and drinking water supply) was done in our animal facility.

2.7 Histological analysis

2.7.1 X-gal staining

EHTs (whole-mount) or EHT-grafted mouse organs were transferred to a clean dish containing PBS (w/o $MgCl_2$, w/o $CaCl_2$; Gibco). The tissue was washed 2 times with PBS for 10 min. Then the samples were transferred to a dish containing the fixation solution for 45 s. The pre-fixation solution was discarded immediately in 2 times PBS washing steps for 10-20 min. A dish was filled with staining solution containing 0.4 mg/ml X-gal and the tissue was added. The staining procedure was done at 37 °C over night. The X-gal-positive cells could be detected by the blue staining of the resulting adduct (Figure 2.16). After staining, samples were washed in PBS for 2-3 min and post-fixed with Histofix® (Roth) for 30 min. The samples were kept in PBS plus sodium azide (Sigma) for further histological analyses (2.7.2).

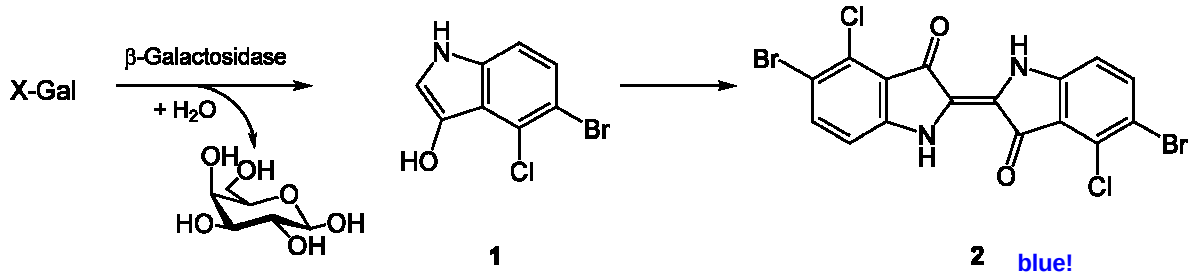

Figure 2.16: Chemical reaction resulting in the blue X-gal reaction product. The enzymatic activity of the expressed LacZ (β-galactosidase) removes the sugar residue from the X-gal substrate. The resulting indole reaction product will further create a mesomeric stabilized adduction product.

Fixation solution:

20x PBS (64 mM Na_2HPO_4, 10 mM KH_2PO_4, 26 mM KCl, 2.7 M NaCl, pH 7.4), 5% (v/v)

37% Formaldehyde, 5% (v/v)

25% Glutaraldehyde, 0.2% (v/v)

in *aqua ad injectabilia*

Stain solution:

20x PBS (64 mM Na_2HPO_4, 10 mM KH_2PO_4, 26 mM KCl, 2.7 M NaCl, pH 7.4), 5% (v/v)

Potassium ferricyanide crystalline (500 mM), 1% (v/v)

Potassium ferricyanide trihydrate (500 mM), 1% (v/v)

Magnesium chloride (1 M), 0.2% (v/v)

in *aqua ad injectabilia*

X-Gal:

40 mg/ml in DMSO

2.7.2 Paraffin embedding

After the X-gal staining (2.7.1) and post fixation with Histofix® (Roth) the paraffin embedding process was initiated. EHTs in culture were washed with PBS (w/o $MgCl_2$, w/o $CaCl_2$; Gibco) 2 times for 10 min and subsequently fixed with Histofix® (Roth) at 4 °C over night before paraffin embedding. Organs and EHTs were pre-embedded in agarose (Invitrogen; 4% in PBS; w/o $MgCl_2$, w/o $CaCl_2$; Gibco) to ensure an appropriate position of the tissue. The hot

agarose (60 °C) was put into the wells containing EHTs or organs. After the hardening of agarose the blocks were cut and a process of dehydration pursued according to table 2.2.

Table 2.2: Process of dehydration

Step	Reagent	Time (min)	Temperature (°C)
1	Isopropanol 70%	30–60	RT
2	Isopropanol 80%	30–60	RT
3	Isopropanol 96% I	30–60	RT
4	Isopropanol 96% II	30–60	RT
5	Isopropanol 100% I	30–60	RT
6	Isopropanol 100% II	30–60	RT
7	Isopropanol 100%	30–60	60
8	Isopropanol paraffin (1:1)	30–60	60
9	Paraffin I	60	60
10	Paraffin II	60	60
11	Paraffin III	over night	60

After dehydration the samples were transferred to casting molds and positioned. Paraffin was added and the blocks were cooled at 4 °C for 48 h. A microtom (Leica RM 2125 RT, Leica) was used to generate 4 µm thin sections which were then transferred to a water bath at 55 °C. The sections were stretched and mounted on a slide (Superfrost, HistoBond®; Hecht Assistant).

2.7.3 Hematoxylin and Eosin staining

This staining method involves the application of hematoxylin, which colors the nuclei of cells in blue. It is followed by counterstaining with eosin, which colors the cytosol in pink. The paraffin sections were cleaned of paraffin with xylol 2 times for 10 min each. Subsequently, the sections were rehydrated in different dilutions of ethanol (2 x 100%, 2 x 96%, 80% and 70%) for 5 min each and hematoxylin staining (dilution 1:5, hemalum 1%, $NaJO_3$ 0.2%, $KAI(SO_4)_2$, chloral hydrate 50%, citric acid 1%; Roth) was done for 5 min. The samples were brought to HCl 1% in ethanol for a few seconds. Then the sections were washed in *aqua ad injectabilia* and rinsed in piped water for 10 min. Eosin staining (0.3% Eosin G, aqueous; Merck) was performed for 0.5–3 min and the slides were rinsed in water. In a row of different

dilutions of ethanol (96%, 100%, 2 x 2 min each) the slides were dehydrated, incubated in xylol for 3–5 min and embedded in Eukitt® (O. Kindler). Photographic images were done with a microscope (Zeiss-Axioplan IM-35) and the suitable software (Zeiss-Axiocam).

2.7.4 Eosin staining of X-gal-stained EHT cross sections

X-gal-stained EHT and organ sections were rehydrated as mentioned in 2.7.2. For these sections eosin staining was performed for two seconds only without hematoxylin staining to avoid an overlay of the LacZ-signal with the blue color of the nuclei. For each sample, a native section was generated without any staining. The dehydration process and the eosin staining of these samples was performed by the HEXT core facility mouse pathology (http://www.uke.de/medizinische-fakultaet/core-facilities/index_ENG_75082.php).
Photographic images of the slides were done with a microscope (Zeiss-Axioplan IM-35) and the suitable software (Zeiss-Axiocam).

2.7.5 Immunohistochemistry

Paraffin sections of EHTs or organs (2.7.2) were kept at 4 °C until the staining procedure started. The staining was performed by the HEXT core facility mouse pathology (http://www.uke.de/medizinische-fakultaet/core-facilities/index_ENG_75082.php).
Photographic images of the slides were done with a microscope (Zeiss-Axioplan IM-35) and the suitable software (Zeiss-Axiocam). Antibodies were used as listed in the appendix (7.6).

2.7.6 Immunofluorescence staining

For whole-mount immunofluorescence analysis EHTs were washed with PBS (w/o $MgCl_2$, w/o $CaCl_2$; Gibco) for 10 min twice. Subsequently, EHTs were fixed over night in Histofix® (Roth). Afterwards EHTs were quickly washed in TBS (in mM: 50 tris base ultra pure, 150 NaCl, 1 N HCl was used to adjust to pH 7.2-7.4). EHTs were transferred to 2 ml tubes containing 500 µl of blocking solution (TBS 0.05 M, pH 7.4, 10% FCS, 1% BSA, 0.5% triton X-100). After blocking solution, EHTs were immediately brought into the antibody solution (TBS 0.05 M, pH 7.4, 1% BSA, 0.5% triton X-100), containing the primary antibody for 24 h.

The EHTs were washed under continuous movement in TBS. The washing solution was changed 3 times in 24 h. After washing, the EHTs were transferred to the antibody solution containing the secondary antibody and the counter staining for 24 h under light protection. EHTs were washed in TBS for 3-4 h, during that time the solution was changed 3 times. After the last washing step EHTs were transferred to slides (26 x 76 mm, two molds; Thermo Scientific) and subsequently fixed with Mowiol 4-88 (Hoechst). Confocal images were obtained with a Zeiss LSM 510 META System. Antibodies were used as listed in the appendix (7.6). All staining steps were performed at 4 °C on a shaker.

2.8 Molecular analysis

2.8.1 RNA analysis

2.8.1.1 RNA isolation

Total RNA was extracted from 1 EHT using TRIzol® (Invitrogen) reagent (300 µl/EHT) according to the manufacturers' instructions. EHTs were homogenized by the use of a TissueLyser® (Qiagen) at a vibration frequency of 30 Hz. RNA concentration was determinded by measuring the absorbance at a wavelength of 260 nm with a spectrophotometer (NanoDrop® ND-1000, PeqLab). Absorbance was also determined at the wavelength of 280 nm, and the ratio A_{260}/A_{280} was calculated to test for purity. RNA samples were stored at -80 °C for further use.

2.8.1.2 Reverse transcription (RT)

A total amount of 500 ng RNA was reverse transcribed into cDNA using the High Capacity cDNA Reverse Transcription Kit (Applied Biosystems) according to manufacturers' instructions. The samples were stored at -20 °C for further analysis.

2.8.1.3 Quantitative RT-PCR

The concentration of mRNA was determined by real-time polymerase chain reaction (quantitative RT-PCR, qRT-PCR), which was performed on the TaqMan® ABI Prism® 7900HT sequence detection system (Applied Biosystems) using SYBR® Green (Figure 2.17) according to the instruction manual.

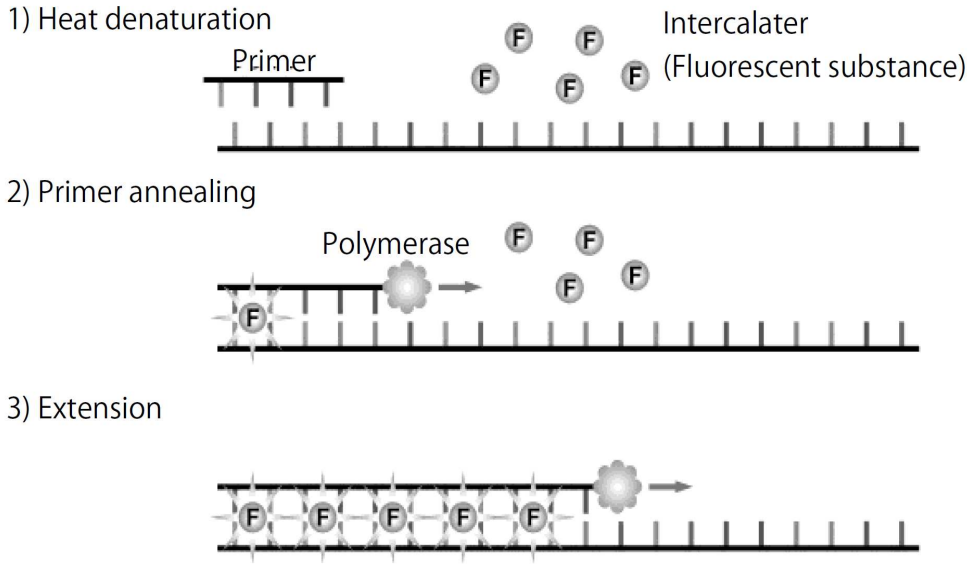

Figure 2.17: Quantitative RT-PCR using SYBR® Green. SYBR® Green is a dye that unspecifically intercalates in double-stranded DNA. This intercalation induces a fluorescent emission. After the PCR reaction, a melting curve analysis is required to differentiate between mismatched PCR products (e.g. primer dimers) and perfectly matched fragments (from the Takara Bio USA website).

For all qRT-PCRs, either Gsalpha or 18S ribosomal RNA (18S rRNA) were used as endogenous controls to normalize the quantification of the target mRNAs for difference in the amount of cDNA added to each reaction (Table 2.3). cDNAs (2.8.1.2) were diluted 1:20 with nuclease free water and amplified using the primer pairs and the TaqMan® Universal PCR Master Mix (Applied Biosystems). All primer pair sequences used are listed in the appendix (7.7). All measurements were performed in triplicates and analyzed with the ABI Prism 7900HT Sequence Detection System Software, Version 2.3. The mRNA amount was quantified according to the comparative Ct method with the $2^{-\Delta\Delta Ct}$ formula. The Ct values of the endogenous control were substracted from the Ct values of the target gene (ΔCt). The mean of ΔCt of the reference was then substracted from each single ΔCt resulting in the ΔΔCt value. The formula $2^{-\Delta\Delta Ct}$ provides the relative amount of mRNA in every sample.

Table 2.3: PCR program for qRT-PCR using the relative quantification method and the TaqMan® Universal PCR Master Mix.

Stage	Temperature (°C)	Time (min:s)	Cycles
Stage 1	50	2:00	1
Stage 2	95	10:00	1
Stage 3	95	00:15	40
	60	1:00	40
Stage 4	95	0:15	1
	60	0:15	1
	95	0:15	1

2.8.2 DNA analysis

2.8.2.1 Isolation of DNA

To isolate genomic DNA from EHTs TRIzol® reagent (Invitrogen) was used. The phenol phase obtained in 2.8.1.1 was used to isolate DNA according to manufacturers' instructions. The concentration of genomic DNA was measured photometric at 260 nm by Nanodrop (ND-100; Spectrophotometer). The purity of the samples was controlled by measuring the ratio of the absorbance (A_{260}/A_{280}). The samples were stored at -20 °C for further use.

2.8.3 Protein analysis

2.8.3.1 Protein extraction

EHTs were washed in a 24-well plate filled with PBS (w/o $MgCl_2$, w/o $CaCl_2$; Gibco) for 10 min on a rocker. Subsequently, EHTs were removed from the silicone racks and immediately frozen in liquid nitrogen. The frozen EHTs were powdered with a steel mortar in liquid nitrogen. The powder was stored at -80 °C for further analysis. The powder was dissolved in 75 µl Kranias buffer (30 mM Tris, 5 mM EDTA, 30 mM NaF, 3% SDS, 10% glycerol) and stored at -20 °C.

2.8.3.2 Trizol based isolation of proteins

TRIzol® reagent (Invitrogen) was used for protein isolation from EHTs. Therefore, the phenol-ethanol supernatant was used after precipitation of DNA with ethanol (2.8.2.1). The protein was precipitated and cleaned according to the instruction manual of TRIzol®. The protein pellet was dissolved in 75 µl Kranias buffer (30 mM Tris, 5 mM EDTA, 30 mM NaF, 3% SDS, 10% glycerol) and stored at -20 °C.

2.8.3.3 Determination of the protein concentration

The protein concentration was determined by the Bradford protein assay, which is a dye-binding assay in which a differential color change of a dye occurs in response to various concentrations of protein (Bradford 1976). The color change is due to a shift of the absorption maximum of 465 to 595 nm, which occurs in dependence of protein binding. To measure the concentration of proteins according to Lambert-Beer's law a standard (bovine IgG, γ-globuline; Sigma Aldrich I-5506) curve was created. 10 mg of IgG was dissolved in *aqua ad injectabilia*. This stock solution (3.4 mg/ml) was diluted 1:10 in 0.1 M NaOH. The standard curve was pipetted according to table 2.4.

Table 2.4 Bradford standard curve

Protein concentration [mg/ml]	0	85	170	340	510	680	850	1020
BSA standard (1:10) [µl]	0	5	10	20	30	40	50	60
NaOH (0.1 M) [µl]	800	795	790	780	770	760	750	740

5 µl of pre-diluted (1:10) protein samples were added to 795 µl 0.1 M NaOH. For determination, a total volume of 800 µl (either standard or protein sample) was added to 200 µl Bradford reagent (Bio Rad, Roth) and vortexed. After 10 min of incubation at room temperature, the absorbance at 595 nm was measured in a cuvette (Sarstedt) with a spectrophotometer (Smart Spec® 3000, Bio Rad). Subtraction of the blank value (800 µl 0.1 M NaOH plus 200 µl Bradford reagent) and comparison to the standard curve provided an indirect measurement of absolute protein concentrations. Each protein concentration determination was performed in duplicates.

2.8.3.4 SDS-PAGE

SDS-PAGE (Sodium dodecyl sulfate polyacrylamide gel electrophoresis) is a method used to separate proteins according to their size. Since different proteins with similar molecular weights may migrate differently due to their differences in structure, SDS, an anionic detergent, is used to reduce proteins to their linearized structure and coat them with uniform negative charges. SDS-PAGE was performed following the Laemmli method (Cleveland 1983). The protein samples were adjusted to 6x Laemmli buffer composition in a ratio of 6:1 and denaturated using heat (95 °C) for 5 min. Subsequently, the samples were separated on 8% or 15% (depending on the target protein size) polyacrylamide gels by gel electrophoresis first at 80 V for 10 min and then at 120 V in the *Mini Protean 3* electrophoresis system (Bio Rad) in electrophoresis buffer. On each gel the Precision Plus Protein Standard™ was used as molecular weight marker.

6x Laemmli buffer composition:
SDS, 2% (v/v)
Glycerol, 10% (v/v)
Tris base, 10 mM, pH 6.8
DTT, 100 mM
Bromphenol blue, 0.01% (v/v)

Running gel composition:
Tris base, 375 mM, pH 8.8
Acrylamide/bis solution (29:1), 8% or 15% (v/v)
SDS, 0.1 % (v/v)
APS, 0.1 % (v/v)
TEMED, 0.03% (v/v)

Loading gel composition:
Tris base, 125 mM, pH 6.8
Acrylamide/bis solution (29:1), 5% (v/v)
SDS, 0.1 % (v/v)
APS, 0.1 % (v/v)
TEMED, 0.08% (v/v)

Electrophoresis buffer:
Tris base, 25 mM
Glycine, 192 mM
SDS, 0.1 % (v/v)

2.8.3.5 Western blot analysis

After electrophoretic separation, the proteins were transferred onto a nitrocellulose membrane (Protan®, Whatman) or a PVDF membrane (PLB; Amersham Hybond^{TM}-P, GE Healthcare) in the *Mini Trans-Blot Cell System* (Bio Rad) in an electrical field. This was done at 400 mA for 90 min in transfer buffer I or II, according to the protein size. Afterwards, the membrane was stained with Ponceau S (Sigma) to visualize the transferred proteins. After 3 times washing with TBS-T buffer until the color vanished, the membrane was blocked in 5% milk solution for 1 h at room temperature to block unspecific antibody binding regions. Then, after repeated washing, incubation with the primary antibody (7.6) was done over night at 4 °C. After 3 times 10 min washing with TBS-T buffer, the membrane was incubated with the secondary antibody (HRP conjugated; 7.6) for 1 h at room temperature. After a final washing with TBS-T buffer (3 times) to remove unbound antibody, the membrane was incubated with a detection reagent according to the instruction manual of the ECL Plus Western blotting detection system for tissue preparations or the SuperSignal® West Dura (Thermo Scientific) extended duration substrate for cell preparations. The kit provided a substrate, which is transformed by the horseradish peroxidase into a luminescent product. The produced chemiluminescent signal was detected by photographic film. The films were then fotographed by means of the Chemie Genius^2 Bio Imaging System and quantified with the Gene Tools software.

Transfer buffer I:
Tris base, 25 mM
Glycine, 190 mM
Methanol, 20 % (v/v)

Transfer buffer II (used for proteins>80-100 kDa):
Tris base, 50 mM
Glycine, 380 mM
SDS, 0.1 % (v/v)
Methanol, 20% (v/v)

Ponceau S solution:
Ponceau S, 0.1% (v/v)
Acetic acid, 1% (v/v)

TBS-T buffer:
Tris base, 100 mM, pH 7.5
Tween 20, 0.1% (v/v)
NaCl, 150 mM

5% Milk solution:
Milk powder in TBS-T buffer, 5% (w/v)

2.9 Statistical analysis

Results are presented as means±SEM. All statistical tests were performed in GraphPad Prism version 5.02. In detail, one-way ANOVA with Tukey's, Dunnett's or Bonferroni's multiple comparison post tests (to compare to control group or condition) or two-way ANOVA and Bonferroni's multiple comparison post test (to compare between more groups or different conditions) were used for more than 2 groups, student's unpaired t-test for 2 groups (different genotype) or student's paired t-test for 2 groups (same genotype, different condition). $P<0.05$ or less was considered statistically significant. P-values are displayed graphically as follows: $*P<0.05$, $**P<0.01$, $***P<0.001$. Quantitative PCR data analyses were carried out using the ΔΔ-Ct method. Curve fittings and transformations were performed with GraphPad Prism5.

3 Results

The first goal of this thesis was the establishment of coherently beating mouse engineered heart tissue (EHT) for cardiac disease modeling and angiogenesis screening. Several years ago, collagen-based EHTs from neonatal mouse cardiomyocytes have already been generated (unpublished data). However, this technique turned out to be technically challenging and biotechnological standardisation insufficient. An important first part of this thesis was to answer the question whether fibrin-based mini EHT format (Hansen et al. 2010) is better suited to constitute EHTs from neonatal mouse heart cells.

3.1 Basic observations

First experiments indeed suggested that the fibrin-based mini EHT format was suitable to generate beating mouse EHTs in a robust and reproducible manner. For the successful generation of beating mouse EHTs a pup number between 20–60 was necessary. The ideal age of the pups was between day 0–1 after birth. Entire hearts were harvested to obtain atrial and ventricular cardiomyocytes in the cell suspension. Murine EHTs lacking atrial cardiomyocytes did not develop coherent contractions. Furthermore, the cell suspension after cell isolation had to be taken immediately without any steps to omit non-cardiomyocytes. Preplating of the cell suspension to decrease the number of fibroblasts resulted in absence of coherent contraction.

After casting of the EHTs, cells were evenly distributed in the matrix as single cells and the fibrin blocks were shaped according to the geometry of the Teflon spacer. Only few days after casting the fibrin matrix was remodelled and large areas of beating cells were detected (day 3–5). Between day 5 and day 7 almost all EHTs of one batch developed coherent contraction with movement of the silicone posts (Figure 3.1). Around day 14 EHTs developed a maximum of force, which was accompanied by a reduction in width by ~60%. Width was further reduced up to day 23, as seen in light microscopic analysis, but force decreased in comparison to day 14. The frequency was stable between day 7–14 of culture and was higher on day 21 in comparison to day 7. Contraction (T1) and relaxation (T2) times did not significantly change over the culture period.

Taken together, these results indicated that the fibrin-silicone post method was principally suited to generate mouse EHTs and that contractile analyses of EHTs as drug tests or comparisons between different mouse lines should be done best around day 14, as seen by

video-optical recordings (3.2.2). Experiments under electrical stimulation and continuous perfusion (3.2.3) were performed in a range between day 12-21 since many days were needed to measure a sufficient number of biological replicates.

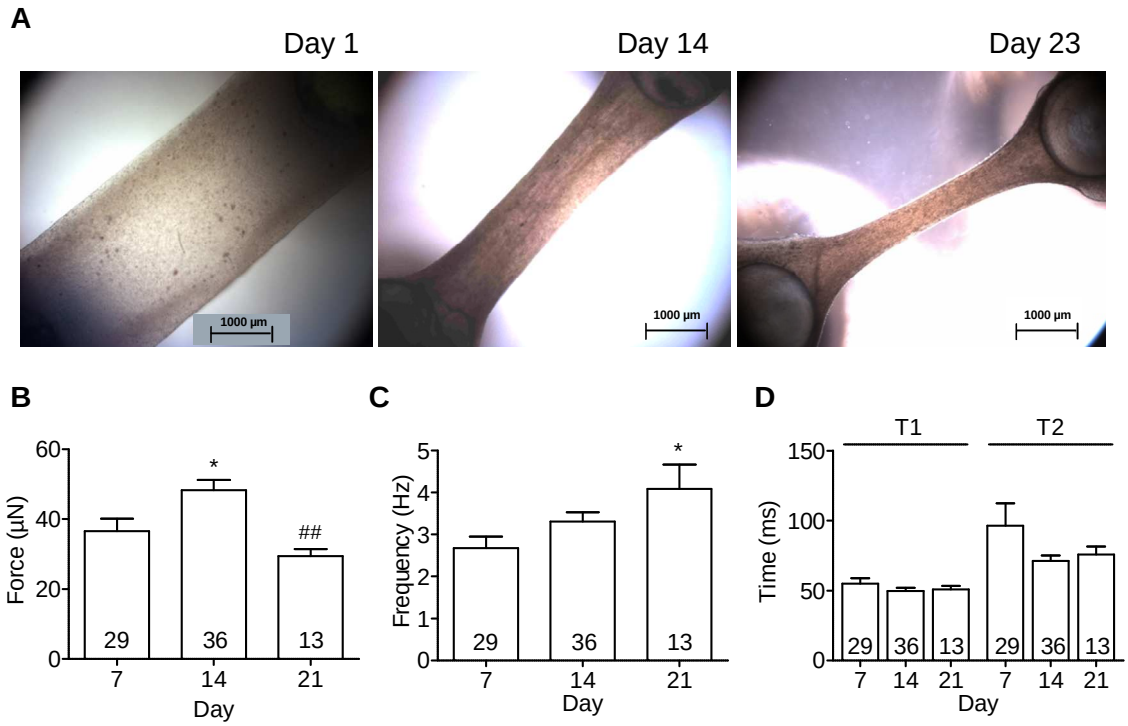

Figure 3.1: Development of mouse EHTs over time. Representative light microscopic images of EHTs on day 1, 14 and 23 of culture [**A**]. Contractile parameters such as force [**B**], frequency [**C**] and contraction (T1) and relaxation (T2) times [**D**] were recorded over a culture period of 21 days. Number of analyzed EHTs is indicated in the bars. Data are expressed as means±SEM. **P*<0.05 vs. day 7 and $^{\#\#}$*P*<0.01 vs. day 14 (one-way ANOVA plus Bonferroni posttests).

To establish a robust protocol for the generation of force-developing mouse EHTs a number of different parameters needed to be optimized including cell concentration, EHT volume and media supplements.

3.1.1 Cell concentration in mouse EHT

The best cell concentration in mouse EHTs was determined by histological analyses and video-optical recording of force development. Initially, cell concentrations were adjusted according to rat fibrin-based mini EHTs ($0.41x10^6$ cells/EHT). In immunofluorescence analysis of mouse EHTs ($0.41x10^6$ cells/EHT) large numbers of loose single cells were detected and almost no cell bundle formation was observed (Figure 3.2), indicating insufficient cell concentration. To improve the development of a tissue-like structure,

characterized by a dense cellular network, higher cell concentrations were tested. A cell concentration of 0.68x10^6 cells/EHT turned out to be sufficient to improve formation of densely packed cell bundles. Complexes of longitudinally oriented cell strands of α-actinin-positive cardiomyocytes were detected frequently throughout the EHT matrix.

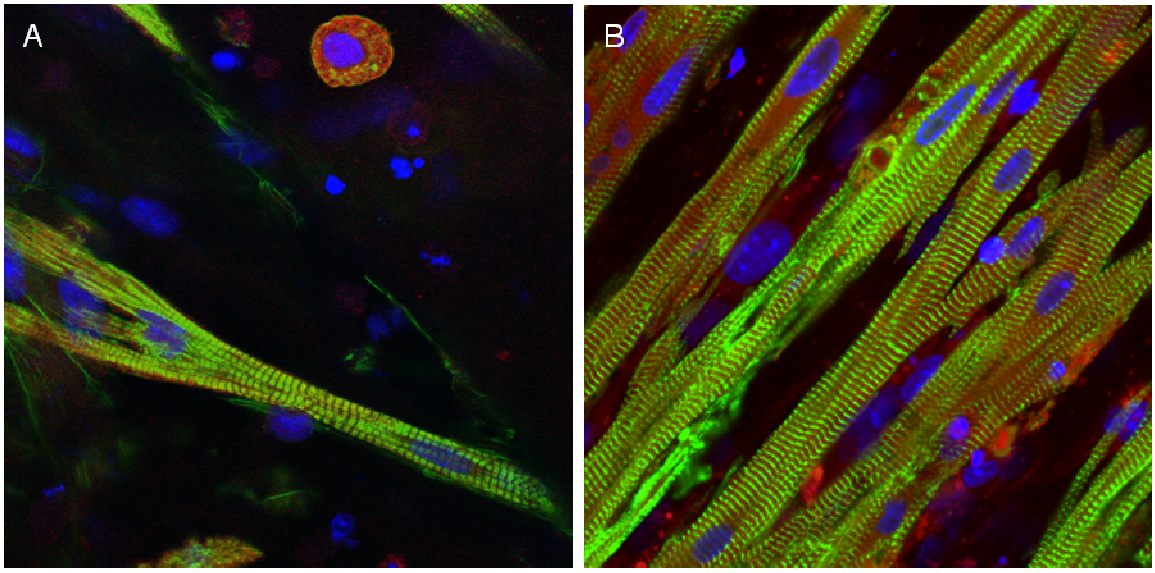

Figure 3.2: Effect of different cell concentrations on mouse EHT morphogenesis. Immunofluorescence staining for α-actinin (green), cMyBP-C (red) and nuclei with DRAQ5 (blue) of an EHT with a cell concentration of 0.41x10^6 cells/EHT [**A**] and image of a cell strand in an EHT with a cell concentration of 0.68x10^6 cells/EHT [**B**].

High cell concentrations of 1.0x10^6 cells/EHT resulted in an earlier onset of coherent beating in comparison to EHTs with a cell concentration of 0.68x10^6 cells/EHT (Figure 3.3). However, this condition resulted in a high degree of variability in force development between day 12-14. Furthermore, an earlier stagnation of the coherent contraction at later time points of culture (day 20) was observed, potentially caused by a higher number of non-cardiomyocytes.

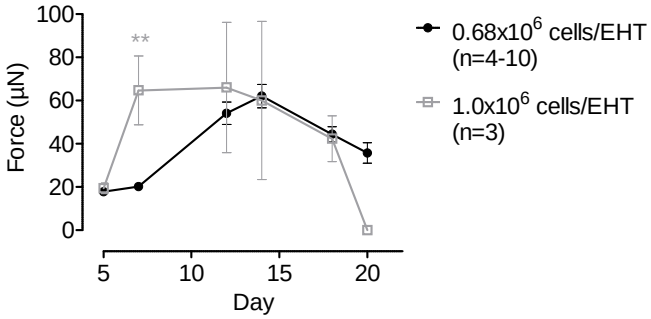

Figure 3.3: Effect of different cell concentrations on force development. Force was measured in EHTs over a culturing period of 20 days and compared. Data are expressed as means±SEM. **P<0.01 vs. 0.68x10^6 cells/EHT, same day (two-way ANOVA plus Bonferroni posttests).

On the basis of these results it was decided to use a cell concentration of $0.68x10^6$ cells/EHT. Paraffin sections were stained with hematoxylin/eosin to study cell distribution. The cytosol of the cell was stained in intense pink with eosin, fibrin in light pink with eosin, and nuclei in blue with hematoxylin. Sections of mature EHTs on day 18 revealed an appropriate cell density and longitudinally cell alignment (Figure 3.4). Muscle-like cell bundles were frequently detected at the lateral free edges, as seen by intense staining with eosin. Up to day 25 eosin staining was more intense which was accompanied by a clearly visible reduction in width, as already seen in light microscopic images of EHTs (3.1). Cell bundles in 25-day-old EHTs were densely packed, thus closely resembling a tissue-like structure. Interestingly, the cells in EHT edges were longitudinally orientated to a higher degree than cells in the inner region of the EHT.

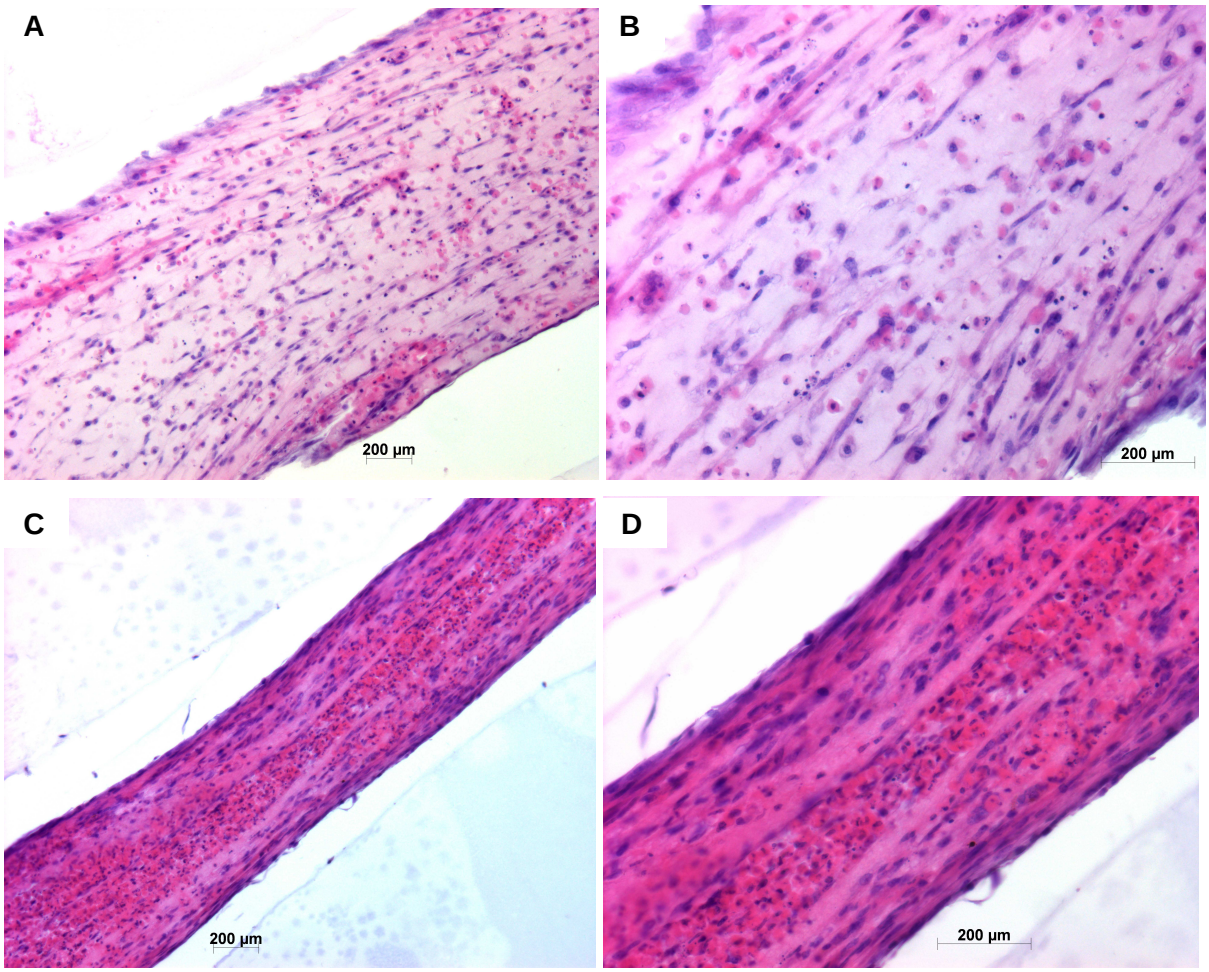

Figure 3.4: Hematoxylin/eosin-stained paraffin sections. Longitudinal sections of EHTs were stained either after 18 days [**A**, **B**] or after 25 days [**C**, **D**] of EHT culture. Light microscopic images were taken in a 10x [**A**, **C**] and a 20x [**B**, **D**] magnification. Eosin stained the cytosol of all cells in the EHT (intense pink) and the fibrin matrix (light pink). Hematoxylin stained the cell nuclei in blue.

3.1.2 EHT volume

To increase the number of biological replicates per cell preparation the volume of each EHT was decreased. EHTs were generated either with 100 or with 150 µl of mastermix. The total cell concentration was $6.8x10^6$ cells/ml in both cases, yielding equal cell densities. Low-volume EHTs showed good force development and a more stable frequency during a culturing period of up to nearly 3 weeks (Figure 3.5). Therefore EHT constructs were casted with a volume of 100 µl in further experiments.

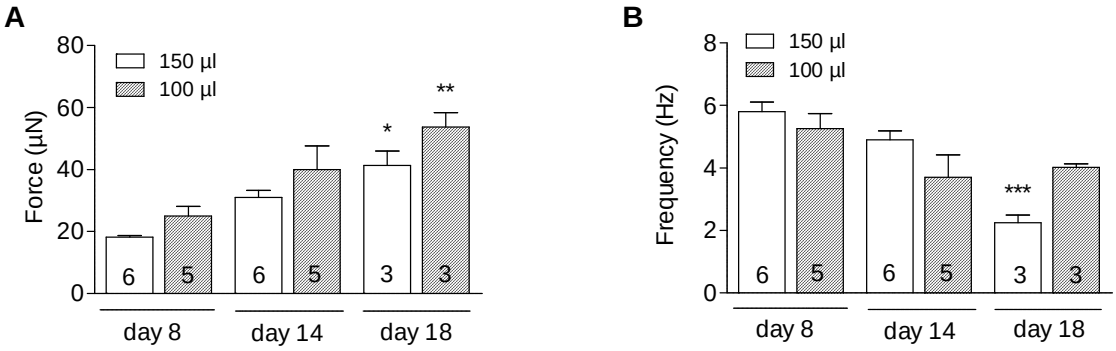

Figure 3.5: Effect of different EHT volumes on contractility. Force [**A**] and frequency [**B**] were measured in 150 and 100 µl EHTs at different days of culture and compared. Number of EHTs is indicated in the bars. Data are expressed as means±SEM. **P*<0.05, ***P*<0.01 and ***P*<0.001 vs. day 8, same condition (one-way ANOVA plus Bonferroni posttests).

3.1.3 Medium supplements

When the mouse EHT technology was established, the culture medium for rat EHTs consisted of DMEM, horse serum, chick embryo extract, penicillin/streptomycin and aprotinin (2.4.6). For mouse EHTs based on collagen I media supplements such as ITS+1 (insulin, transferrin, selenium and α-linoleic acid) and triiodthyronine (T3; 9 nM) were already tested and considered as beneficial for mouse EHT development (unpublished data). In previous studies it has been shown that insulin addition to the culture medium ensured a better survival of cardiomyocytes (Lv et al. 2011) and enhanced the force development in rat EHTs (Zimmermann et al. 2006), which was induced by myocyte hypertrophy via binding to the insulin-like growth factor receptor. Therefore media supplements were tested such as ITS+1 and T3, which were added to the medium during the whole culturing period. Analyses were done on day 8, day 14 and in the presence of isoprenaline (ISO; 100 nM). Under ITS+1 or ITS+1 plus T3 supplementation high percentages of beating EHTs were detected. In contrast, 75-80% of T3-only supplemented EHTs failed to develop coherent contractions (Figure 3.6). Measurements of contractile parameters such as force, frequency, T1 and T2

were performed with video-optical recording. Force development in the presence of ITS+1 was higher than in the presence of both ITS+1 and T3. Parameters such as frequency and T1 did not significantly differ between the groups. Only EHTs in the ITS+1 group showed the expected positive lusitropic effect in the presence of ISO. Thus, T3 had no beneficial effect and was omitted in further experiments.

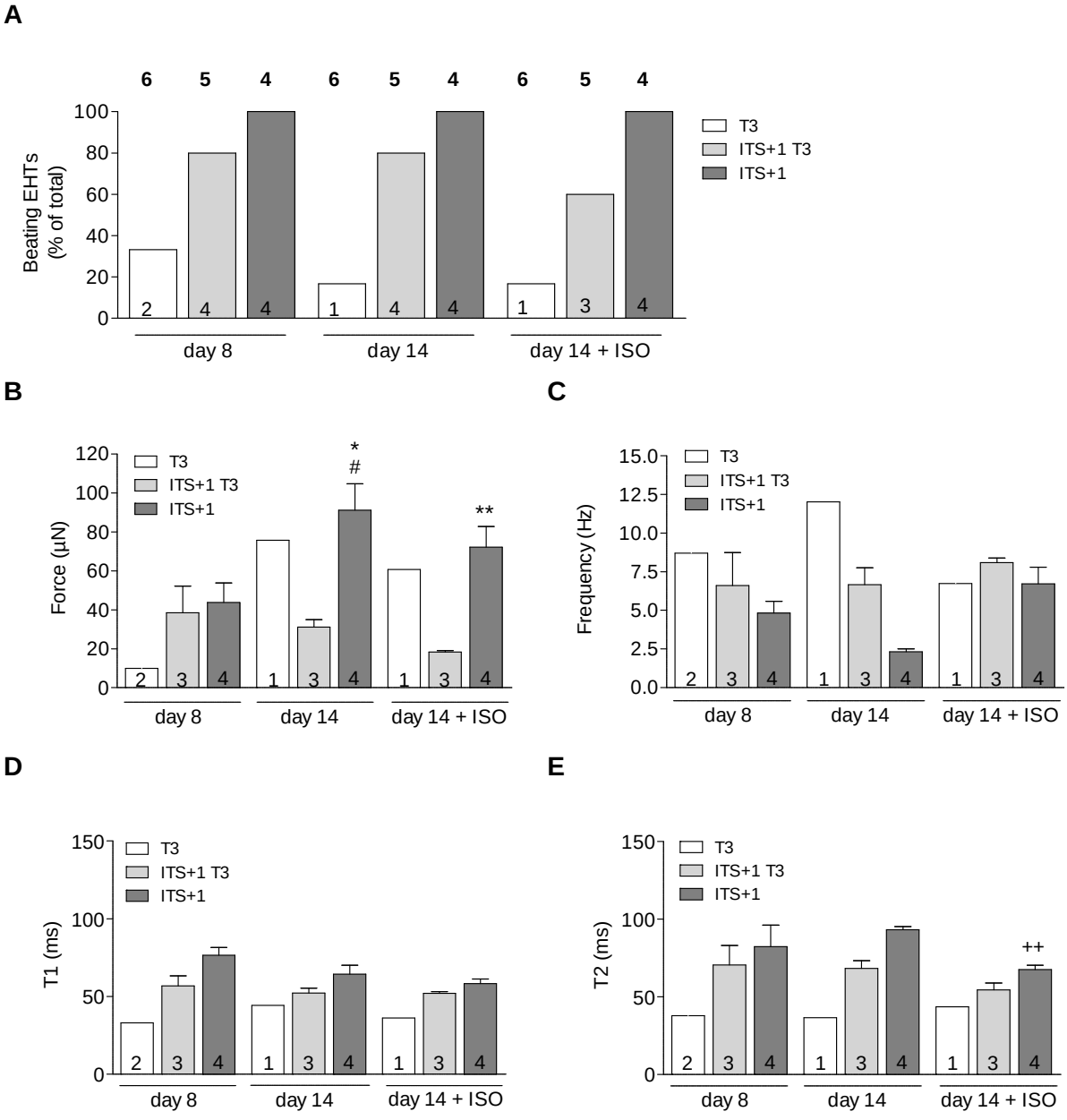

Figure 3.6: Percentage of beating EHTs and contractile parameters under different medium supplements. Percentage of beating EHTs [**A**]. Contractile parameters such as force [**B**], frequency [**C**], contraction [T1; **D**] and relaxation [T2; **E**] times were measured with video-optical recording on day 8, 14 and in the presence of isoprenaline (ISO; 100 nM; 1.8 mM Ca^{2+}). Number of analyzed EHTs is indicated in the bars. Red numbers indicate total numbers of EHTs. Data are expressed as means±SEM. **P*<0.05 and ***P*<0.01 vs. corresponding ITS+1 T3 (two-way ANOVA plus Bonferroni posttests); $^{\#}$*P*<0.05 vs. ITS+1 day 8 (one-way ANOVA plus Bonferroni posttests); $^{++}$*P*<0.01 vs. ITS+1 day 14 (paired student's t-test).

Further experiments revealed that insulin added to the medium had the same beneficial effect as ITS+1. Therefore insulin (10 µg/ml) was supplementary added to the mouse EHT medium during the culturing period.

Mouse EHTs were incubated with the cell cycle inhibiting drug cytosine arabinofuranoside (AraC; 2.4.6). This was necessary to prevent a potential fibroblast overgrowth, which could have induced an increase in stiffness of the EHTs, thereby inhibiting a coherent contraction. A lack of AraC treatment often resulted in an earlier stagnation of a coherent contraction and reduced force development (data not shown). Therefore, different concentrations of AraC were tested in a range of 12.5–50 µM. A continuous treatment with 12.5 µM AraC starting on day 0 of culture resulted in impaired force development. To avoid toxic effects EHTs were incubated with AraC (25 µM) on day 5 for 48 h in further experiments, based on the observation that this concentration did not impair force development.

Taken together, insulin (10 µg/ml), AraC (25 µM; day 5–7), a volume of 100 µl and a cell concentration of $0.68x10^6$ cells/EHT were used in further experiments. Under these conditions contractile forces reached up to 170 µN (mean ~50 µN), spontaneous beating frequency ranged between 1.0 and 10 Hz (mean 4 Hz).

3.2 Modeling HCM: Results of *Mybpc3*-targeted KO and KI mouse EHTs

To model hypertrophic cardiomyopathy, EHTs of *Mybpc3*-targeted knock-out (KO) and knock-in (KI) mice were generated and compared to their corresponding WT control. C57BL/6J and Black Swiss WT served as controls for KO and KI, respectively. Overall, cardiomyocytes in EHTs generated from KO, KI and both WT mouse lines matured similarly. The fibrin matrix was remodelled over time, visible as a reduction in width and thickness compared to the rectangular cell-fibrin block directly after casting in all lines to the same extent (Figure 3.7). During this process EHTs of all groups created a muscle-like structure with deflection of the silicone posts.

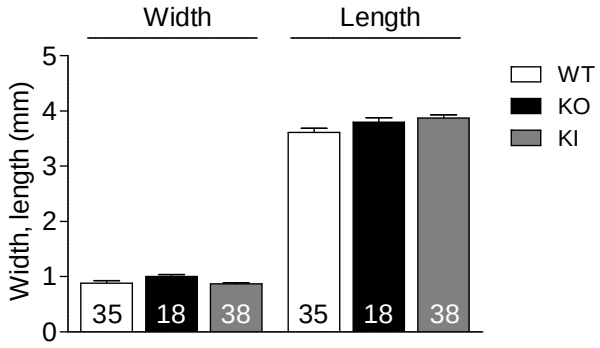

Figure 3.7: Dimensions of mouse EHTs. Construct width and length (free muscle between posts) were measured after 14 days of culture. Number of EHTs is indicated in the bars. C57BL/6J and Black Swiss WT were pooled. Data are expressed as means±SEM.

3.2.1 Histological analysis

3.2.1.1 Hematoxylin/eosin staining

In hematoxylin/eosin-stained paraffin sections of 18-day-old EHTs cells were evenly distributed and aligned along the force lines in all EHTs (Figure 3.8). There were no obvious differences between WT, KO and KI. Muscle-like cell bundles were detected throughout the EHT, as seen by intense staining with eosin, but preferably localized closed to the lateral free edges. Generally, it was observed that the cell density as visualized in the sections was dependent on the depth of cut. Inner parts of the EHT showed lower cell densities than the border zones.

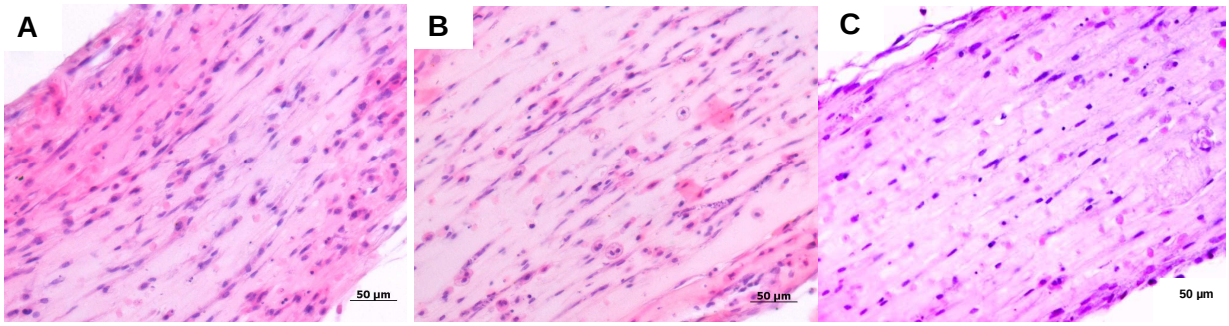

Figure 3.8: Hematoxylin/eosin-stained paraffin sections. WT [**A**], KO [**B**] and KI [**C**] EHT longitudinal sections were stained on day 18 of culture and light microscopic images were taken with a 20x objective. Eosin stained the cytosol of all cells in the EHT (intense pink) and the fibrin matrix (light pink). Hematoxylin stained the cell nuclei in blue.

3.2.1.2 Immunofluorescence staining

Immunofluorescence staining of 18-day old EHTs showed a dense network of longitudinally orientated cell strands of α-actinin-positive cardiomyocytes with distinct cross striation (Z-disk) and characteristic A-band staining of cMyBP-C in WT and KI EHTs (Figure 3.9). cMyBP-C was arranged in doublets in the sarcomeric organization. In all force-developing EHTs cell bundles were detected as shown here, independent of the genotype. KO EHTs showed longitudinally orientated α-actinin-positive cardiomyocytes lacking cMyBP-C. No systematic differences between genotypes were observed.

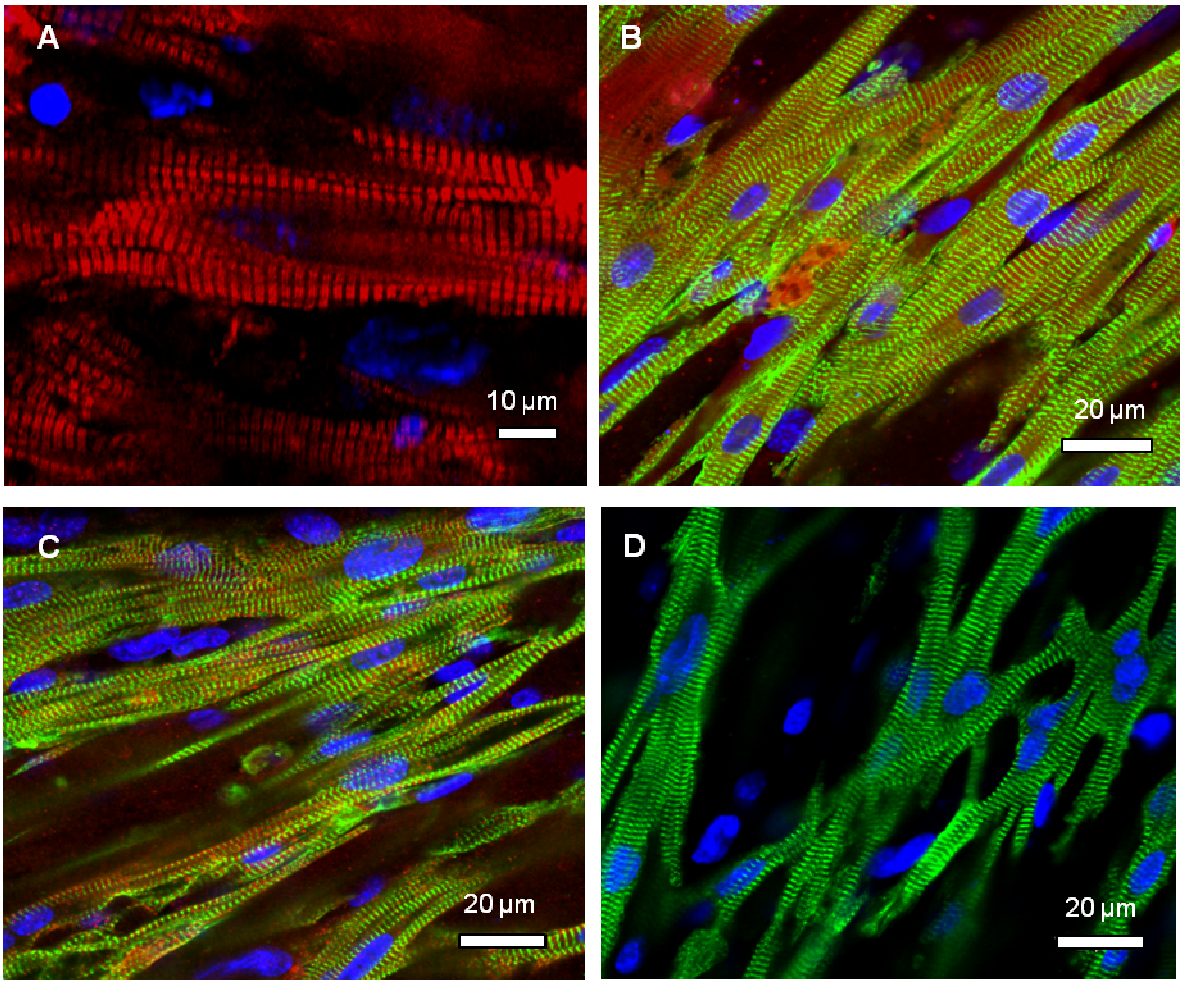

Figure 3.9: Immunofluorescence staining of whole mount EHTs. Immunofluorescence staining for cMyBP-C (red) and nuclei with DRAQ5 (blue) in WT EHT [**A**]. Merged immunofluorescence analysis of cardiomyocytes with staining for α-actinin (green), cMyBP-C (red) and nuclei with DRAQ5 (blue) in WT [**B**], KI [**C**] and KO [**D**] EHTs.

3.2.2 Video-optical recording

3.2.2.1 Contractile analysis under standard culture conditions

To answer the question whether there are phenotypic differences in the contractile behaviour of WT, KO and KI spontaneous activity, EHTs were monitored on day 14 of culture via video-optical recording. Spontaneous measurements were performed in EHT culture medium (1.8 mM Ca^{2+}). Examples of original recordings are shown in Figure 3.10. Recorded contraction peaks were analyzed for force, frequency, T1 and T2, as shown in a hand-drawn peak example.

Original recording graphs revealed a high degree of spontaneous activity in EHTs of all lines. KO and KI EHTs showed higher peak amplitudes than EHTs of both WT lines. Interestingly, about 15% of KI EHTs and none of WT or KO showed tetanic contractions, which occurred spontaneously between day 12–14 of culture. These EHTs were excluded from frequency, T1 and T2 basal measurements.

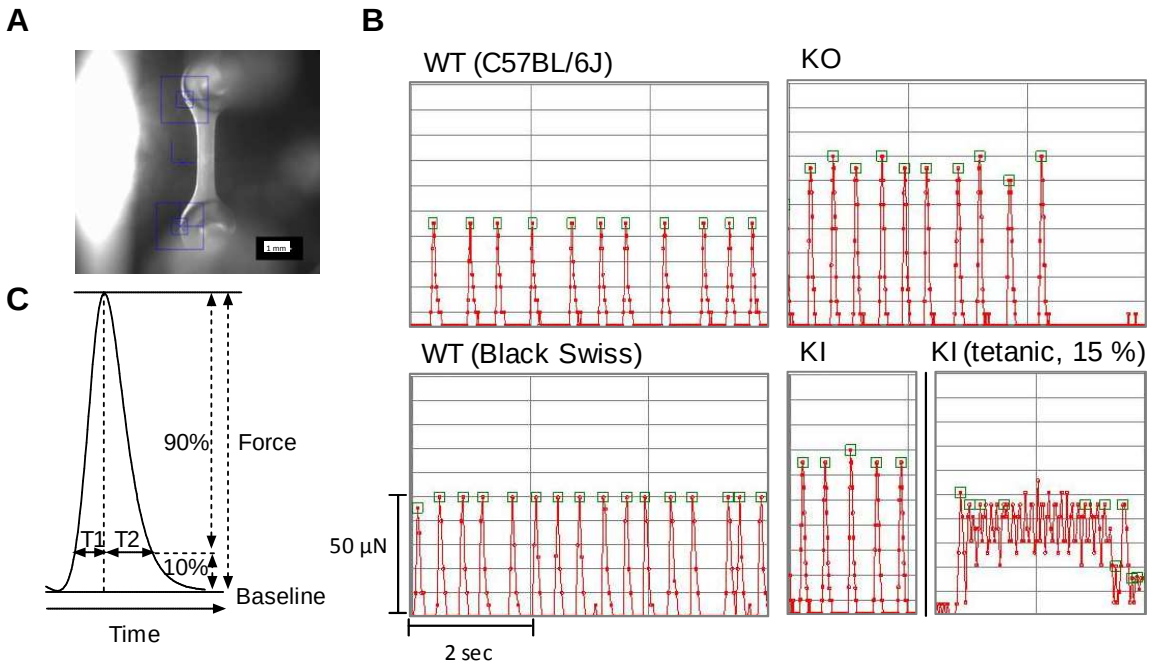

Figure 3.10: Spontaneous activity of mouse EHTs, measured with video-optical recording. Representative picture of EHT as viewed by the video camera and evaluated by automated contour recognition (**A**; blue squares). Original recordings of spontaneous contractile activity in EHT from C57BL/6J and Black Swiss WT, KO and KI (**B**; 1.8 mM Ca^{2+}). Note that 15% of KI EHTs showed tetanic contractions. Modeled contraction peak with the evaluated parameters of contractile function [**C**].

The analysis of contractile parameters showed that total force was 42% and 32% higher in KO and KI, respectively, in comparison to corresponding WT control after 14 days of culture (Figure 3.11). Regarding frequency, the two groups of WT-derived mouse strains (C57BL/6J and Black Swiss WT) differed and were therefore not grouped together in video-optical analyses. Basal frequency measured in WT (Black Swiss) was 46% higher than in WT (C57BL/6J). KO and WT (C57BL/6J) did not show differences in frequency, but frequency in KI was 30% lower than WT (Black Swiss). T1 and T2 values did not differ between EHT lines in video-optical recording (30–100 frames/s).

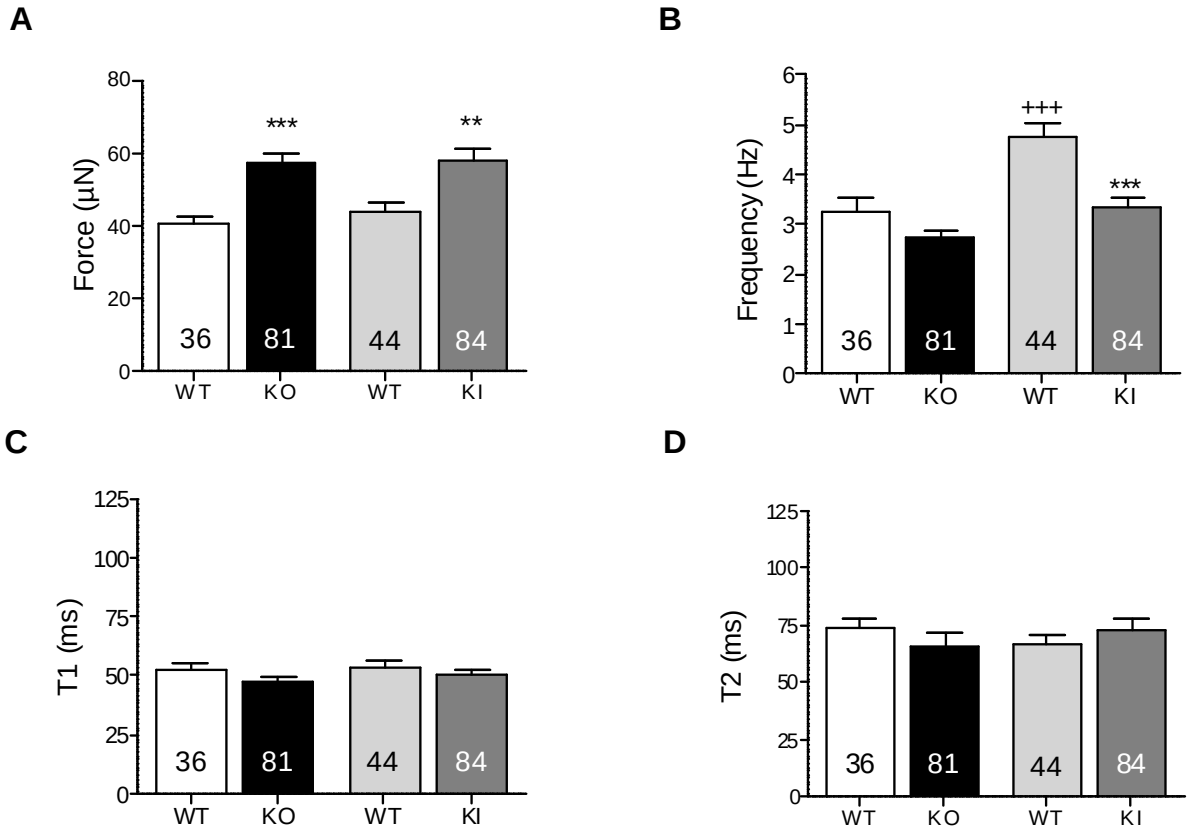

Figure 3.11: Contractile parameters of mouse EHTs, measured with video-optical recording. Parameters of contractility (force [**A**], frequency [**B**], contraction time T1 [**C**] and relaxation time T2 [**D**]) were measured at day 14 in culture medium containing 1.8 mM Ca^{2+}. Number of EHTs is indicated in the bars. Data are expressed as means±SEM. ***P*<0.01 and ****P*<0.001 vs. corresponding WT (one-way ANOVA plus Bonferroni posttests); $^{+++}$*P*<0.001 vs. C57BL/6J WT (one-way ANOVA plus Bonferroni posttests).

Contractile parameters of tetanic contractions could hardly be evaluated in KI EHTs since the figure recognition mode was not capable to correctly analyze these contractions, indicated by incorrect position of green squares (Figure 3.12). Force and frequency of arrhythmic KI did

not differ in comparison to coherently beating KI, but kinetic values such as T1 and T2 differed significantly.

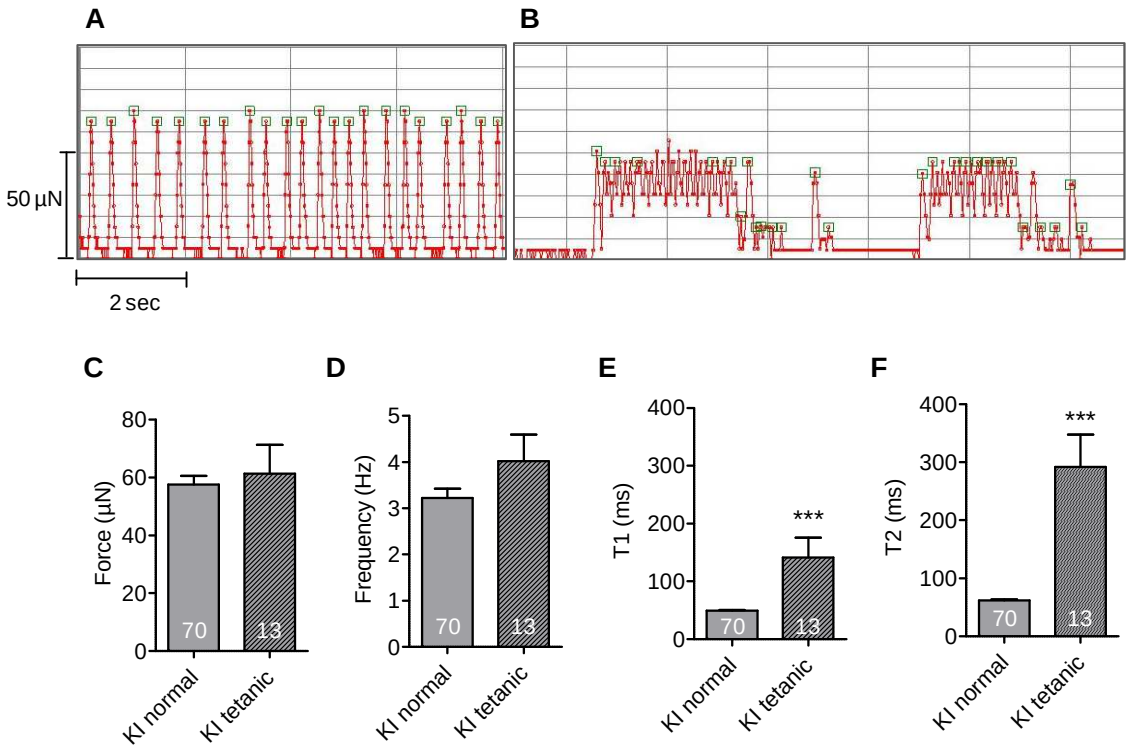

Figure 3.12: Normal and tetanic contracting KI EHTs, measured via video-optical recording. Contraction graphs of a normal [**A**] and a tetanic contracting [**B**] KI were recorded. Main contractile parameters such as force [**C**], frequency [**D**], contraction time [T1; **E**] and relaxation time [T2; **F**] were analyzed. Spontaneous measurements were performed at day 14 in EHT culture medium (1.8 mM Ca^{2+}). Number of EHTs is indicated in the bars. Data are expressed as means±SEM. ****P*<0.001 vs. KI normal (student's t-test).

KI EHTs were cultured in the absence of chick embryo extract and horse serum (2.4.6) for the purpose of investigating a potential effect of animal serum on the development of tetanic contractions. Serum-free culture medium was comprised of a mixture of different medium supplements (Ingra Vollert, unpublished data). In a mature status after 14 days, serum-free cultured KI developed lower force than KI's under standard conditions (10% horse serum, 2% chick embryo extract; Figure 3.13). Under serum-free conditions, T1 and T2 tended to shorten. Furthermore, serum-free cultured KI developed a more homogenous contraction pattern, which was determined simply by counting the normal and the erratic contracting KI EHTs (*P*<0.05; Fisher's exact test). Interestingly, in this experiment only 30% of serum-free cultured KI developed coherent contractions at all in comparison to 100% under serum-containing conditions.

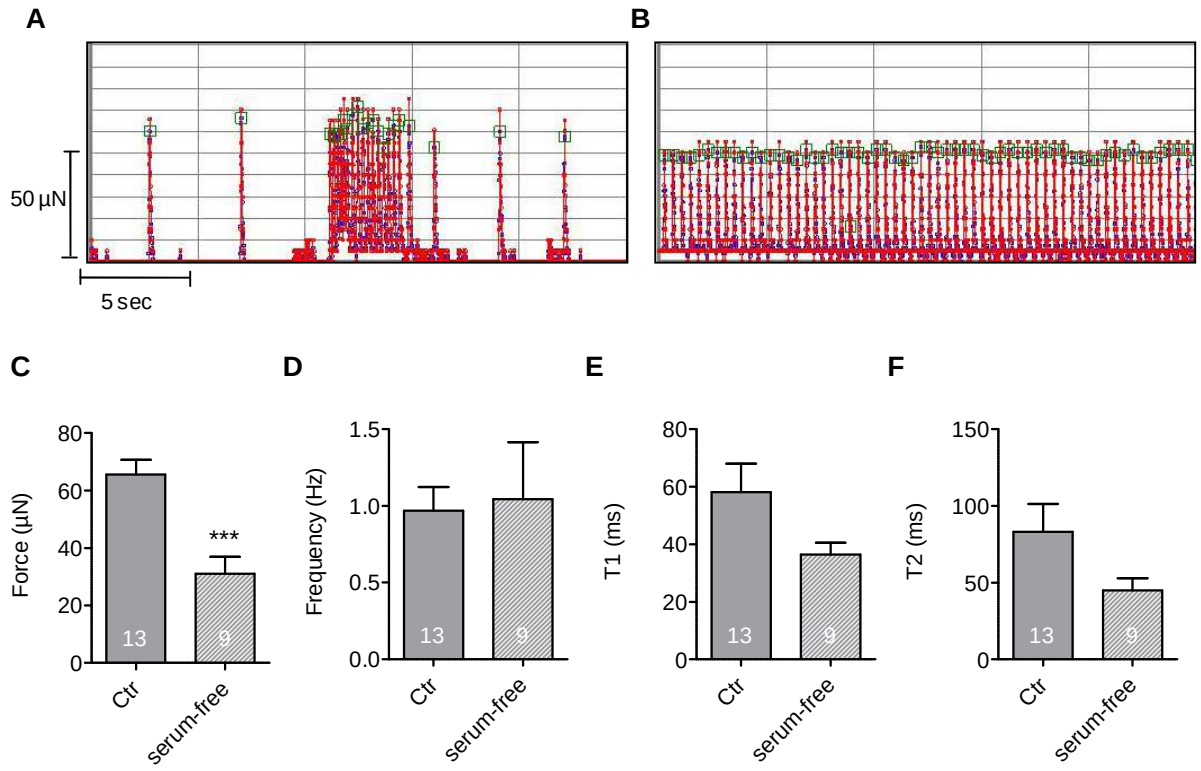

Figure 3.13: KI EHTs were cultured in the presence or in the absence of animal serum and measured via video-optical recording. Contraction graphs of a serum cultured KI [**A**] and a KI cultured under serum-free conditions [**B**] were recorded. Main contractile parameters such as force [**C**], frequency [**D**], contraction time [T1; **E**] and relaxation time [T2; **F**] were analyzed. Spontaneous measurements were performed in EHT culture medium (1.8 mM Ca^{2+}). Number of EHTs is indicated in the bars. Data are expressed as means±SEM. ****P*<0.001 vs. ctr (student's t-test).

3.2.2.2 The Ca^{2+}-sensitizing drug EMD 57033

The effect of EMD 57033 (EMD), which is a well-characterized Ca^{2+}-sensitizing drug (Tsutsui et al. 2001), was investigated on spontaneous contractility. First, this drug was used for the purpose of provoking potential arrhythmia in KI or KO. EMD (10 µM in DMSO) induced under basal conditions, namely culture medium (1.8 mM Ca^{2+}) without pacing, an increase in force of C57BL/6J and Black Swiss WT EHTs (+43% and 33%, respectively; Figure 3.14). In contrast, EMD increased force in KI by only 9% and even decreased force in KO EHTs by ~25%, which was unexpected. Force changes were accompanied by a decrease in frequency in WT (Black Swiss, -30%) but not in KO or KI. EMD increased T1 in all groups to a similar degree (~+50%). T2 was markedly increased in WT and KO (~+130%) and less so in KI (~+60%). However, tetanic contractions were not provoked in KI or KO by EMD.

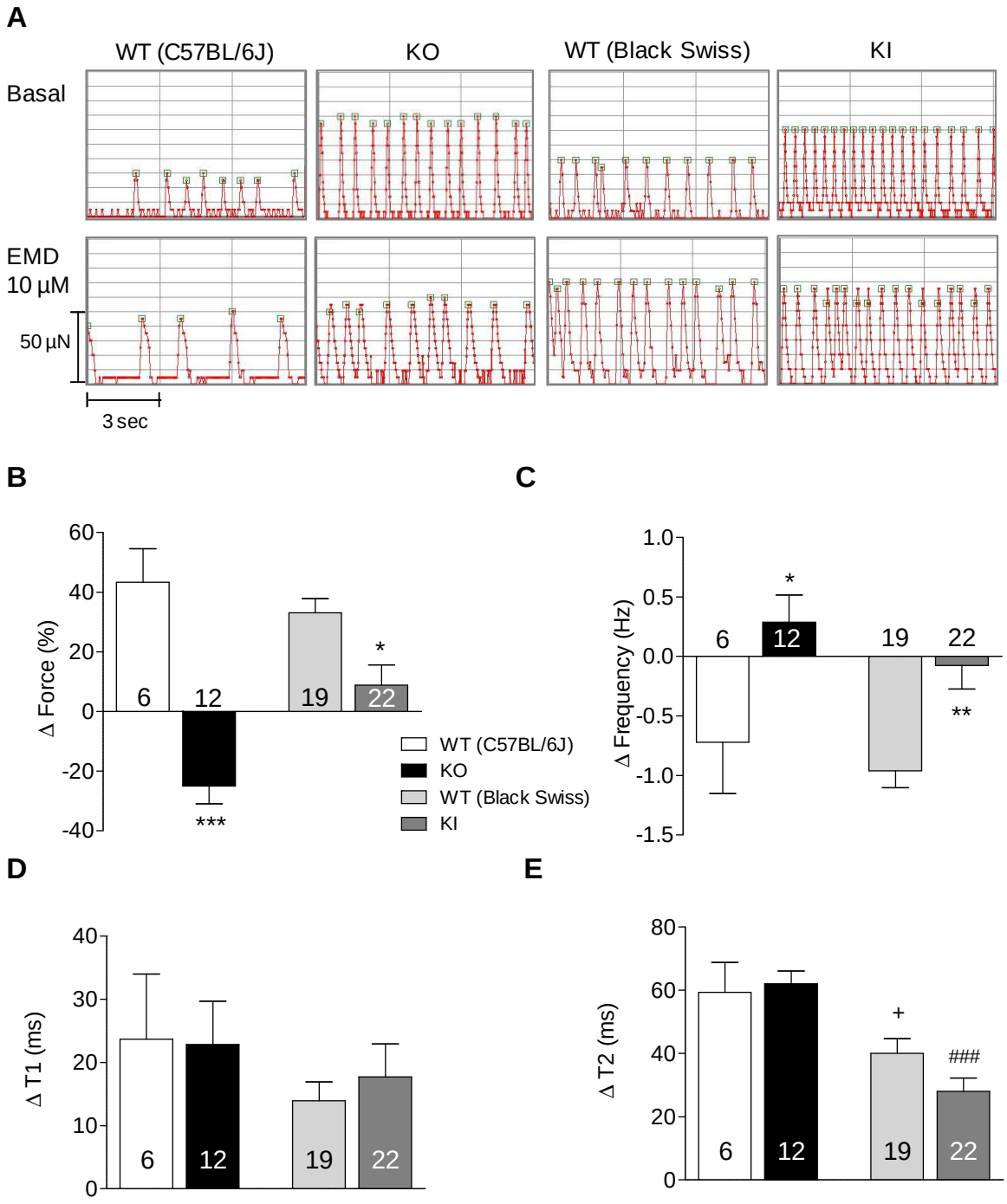

Figure 3.14: Effect of EMD 57033 (EMD) on EHT contractility, measured with video-optical recording. Contraction peak recordings of KO, KI and WT [**A**]. Contractile parameters (delta values for EMD-induced changes in force [**B**], frequency [**C**], contraction time T1 [**D**] and relaxation time T2 [**E**]) in KO, KI and both WT were measured in culture medium (1.8 mM Ca^{2+}) before and 20 min after addition of EMD (10 µM). Force is displayed in % of pre-drug condition. Number of EHTs is indicated in the bars. Data are expressed as means±SEM. **P*<0.05, ***P*<0.01 and ****P*<0.001 vs. corresponding WT (one-way ANOVA plus Tukey posttests); $^{+}$*P*<0.05 vs. C57BL/6J WT and $^{\#\#\#}$*P*<0.001 vs. KO (one-way ANOVA plus Tukey posttests).

In these experiments, basal force in KO and KI was higher than in WT, as expected (Figure 3.15). To evaluate potential time-dependent effects of EMD, EHTs were additionally measured repeatedly after 20, 40 and 60 min of EMD incubation. As seen previously, EMD decreased force in KO, had no major effects in KI and increased force by ~30% in both WT at 20 min. Force and frequency values did not markedly change from 20 to 60 min incubation for all EHT lines. A long-term EMD incubation for 48 h resulted in a strong decrease in force in all EHTs to a low level of 15–20 µN.

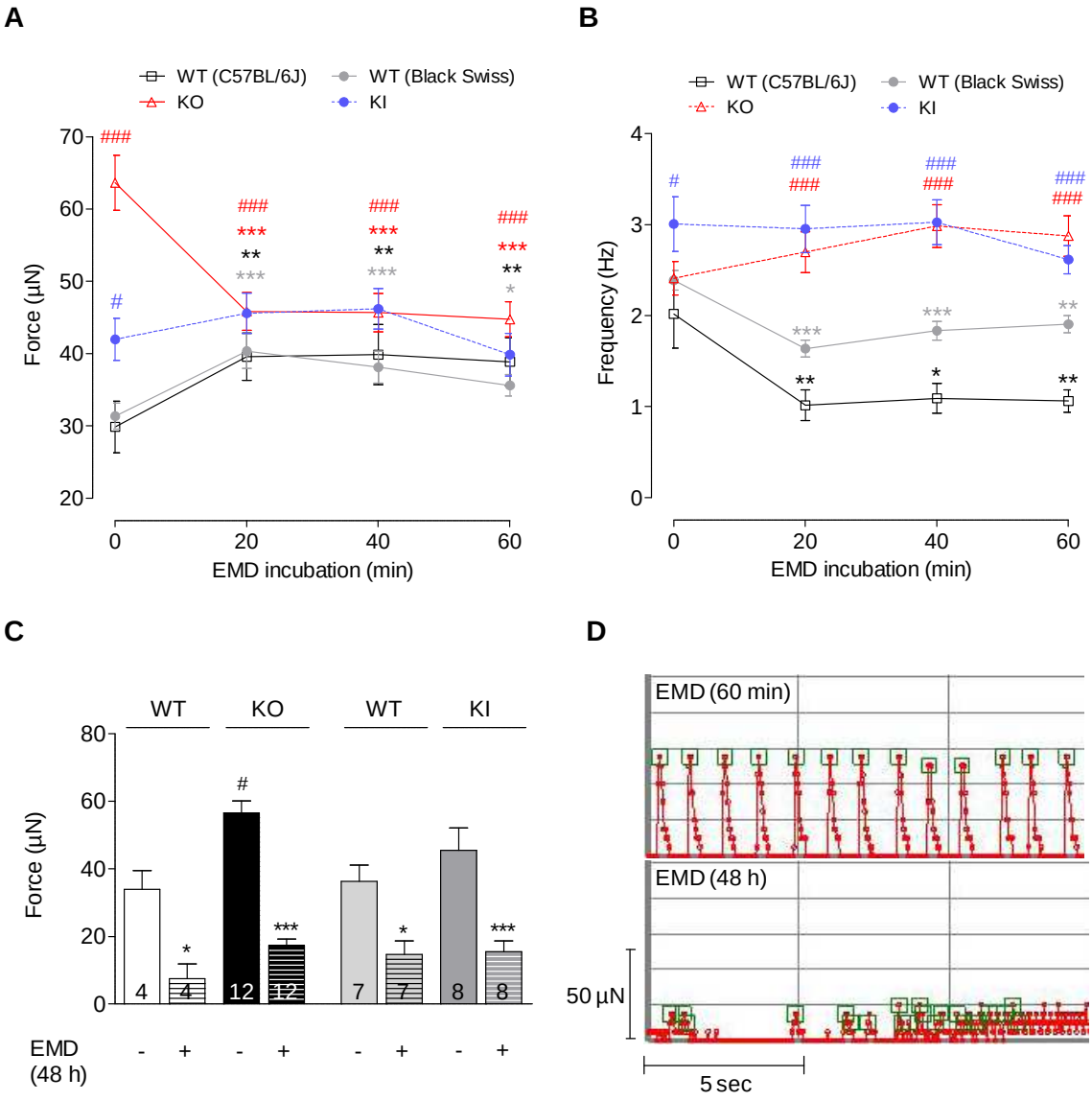

Figure 3.15: Effect of EMD 57033 (EMD) incubation duration. Force [**A**] and frequency [**B**] were measured repeatedly up to 60 min under EMD (10 µM in DMSO; n=7-23 per group). Total force development before and after EMD incubation for 48 h [**C**]. Number of EHTs is indicated in the bars. Contraction peak recordings of WT after EMD incubation for either 60 min or 48 h, as indicated in the panels [**D**]. Data are expressed as means±SEM. **P*<0.05, ***P*<0.01 and ****P*<0.001 vs. baseline, same genotype (one-way ANOVA plus Bonferroni posttests); $^{\#}P$<0.05 and $^{\#\#\#}P$<0.001 vs. corresponding WT, same condition (two-way ANOVA plus Bonferroni posttests).

3.2.3 Measurements of electrically stimulated EHTs

To analyse the contractile phenotype under more defined experimental conditions, measurements were performed under near physiological conditions, i.e. 37 °C, electrical pacing and continuous perfusion with Tyrode's solution.

3.2.3.1 Effect of stimulation frequency

Here, we evaluated the effect of beating rate on force development at 1.8 mM external Ca^{2+} by using the IonOptix software and a set-up that allowed continuous pacing and perfusion. WT, KO and KI EHTs were stimulated at different pacing frequencies, ranging from 1–10 Hz as shown in Figure 3.16. As seen in the representative mechanogram, an increase in pacing frequency led to a decrease in the contraction amplitude. The baseline value at the beginning of the contraction is called 'resting tension' (RT) and represents the diastolic force. The peak force represents the systolic force.

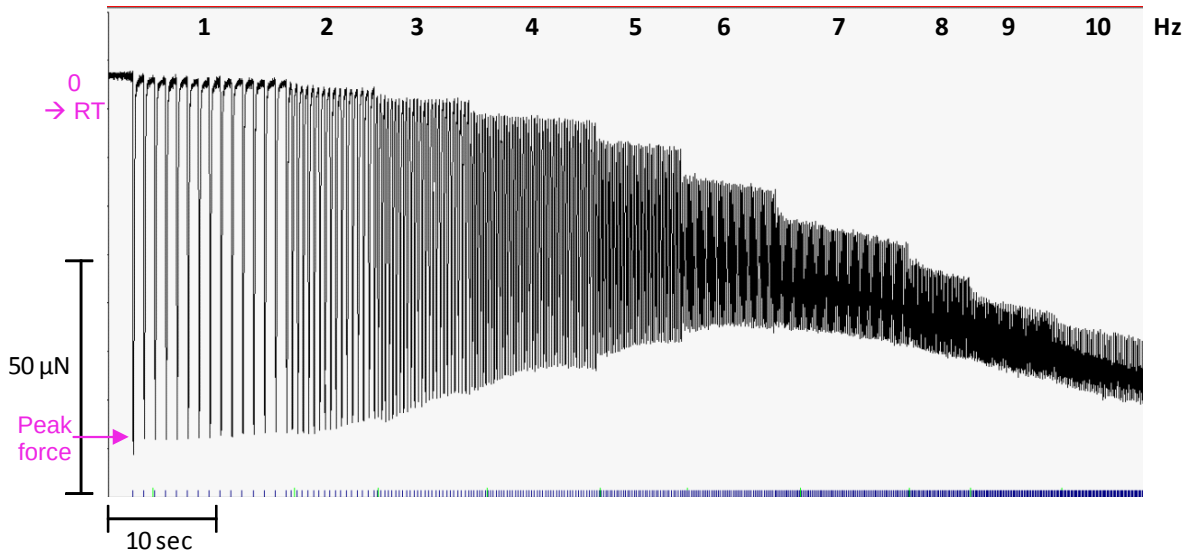

Figure 3.16: Representative mechanogram of force development with increasing frequencies. Original recording of a KI EHT stimulated with 1–10 Hz and 30 V, in 1.8 mM extracellular Ca^{2+}. The blue marks represent the stimulation events. In pink, the value 0 stands for the baseline and RT stands for resting tension. The peak force describes the maximal developed systolic force.

For analyses, the software generated average peaks to calculate contractile parameters such as force, contraction or relaxation velocities, and contraction or relaxation times. A representative peak is shown in Figure 3.17.

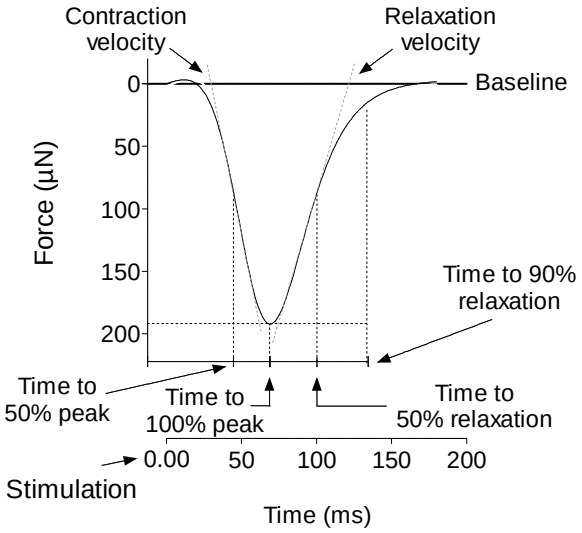

Figure 3.17: Representative average peak. Representative average peak was generated to depict contractile parameters calculated by the IonOptix software. Analyzed values were force, time to 50% peak (TTP 50), time to 100% peak (TTP), time to 50% or 90% relaxation (TTR 50 and TTR 90, respectively) and contraction as well as relaxation velocity.

In general, we could not detect differences in WT EHTs according to the genetic background (C57BL/6J and Black Swiss) under electrical stimulation and continuous perfusion, as shown in detail in 3.2.3.2. Therefore C57BL/6J and Black Swiss WT EHTs were pooled in all further experiments.

In WT and KI EHTs increasing pacing frequency decreased the amplitudes of twitch (Figure 3.18). At lower frequencies from 1–4 Hz EHTs in all groups often beat faster in their own rhythm, especially when Ca^{2+} was washed out (3.2.3.2). In a range of 5–6 Hz EHTs beat regularly without arrhythmia according to the stimulation. Beginning with a frequency of 7 Hz the contraction amplitude in EHTs was strongly diminished, as seen in absolute and normalized force development (Figure 3.18). With higher frequencies (10–12 Hz) of stimulation the EHTs were no longer able to adequately respond to the stimulation rhythm (data not shown). This failure of capture was observed independently of the genetic background or genotype. Diastolic force increased with increasing pacing frequencies, as seen in increasing baseline values (Figure 3.16). Increasing pacing frequencies from 1 to 9 Hz decreased maximal twitch amplitude in WT and KI by ~75%, in KO by only 51%,

respectively. This implies that the negative force-frequency relationship was blunted in KO EHTs. At a frequency of 6 Hz, where most experiments were performed, WT and KI lost approximately 40% of their initial contraction amplitude and KO 25%, respectively.

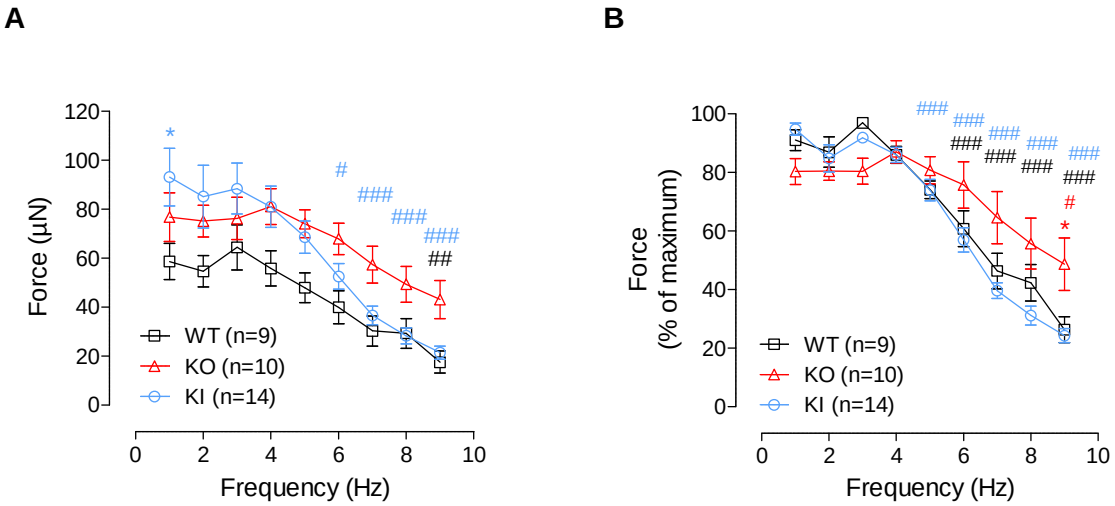

Figure 3.18: Effect of pacing frequency on EHT force, measured with the IonOptix software. Measurements were performed under 30 V-stimulation in 1.8 mM extracellular Ca^{2+} (1–9 Hz). Absolute force development was measured with increasing pacing frequencies [**A**]. Force was normalized to the maximal developing force of every EHT [**B**]. Number of EHTs is indicated in the panel. Data are expressed as means±SEM. **P*<0.05 vs. WT, same condition (two-way ANOVA plus Bonferroni posttests). $^{\#}P$<0.05, $^{\#\#}P$<0.01 and $^{\#\#\#}P$<0.001 vs. 1 Hz, same genotype (one-way ANOVA plus Bonferroni posttests).

Increasing pacing frequencies resulted in reduced contraction velocities in WT and KI from 1 to 9 Hz, but not in KO. KO showed 3-fold and 2.5-fold higher contraction and relaxation velocities than WT with increasing pacing frequencies, respectively, which matched with the higher force at 9 Hz (Figure 3.19). In all EHTs contraction (time to 100% peak, TTP) and relaxation times (time to 90% relaxation, TTR 90) shortened from 1 to 9 Hz by ~35 ms and ~90 ms, respectively. Relative changes (expressed as delta) in TTP and TTR 90 did not significantly differ between EHT lines.

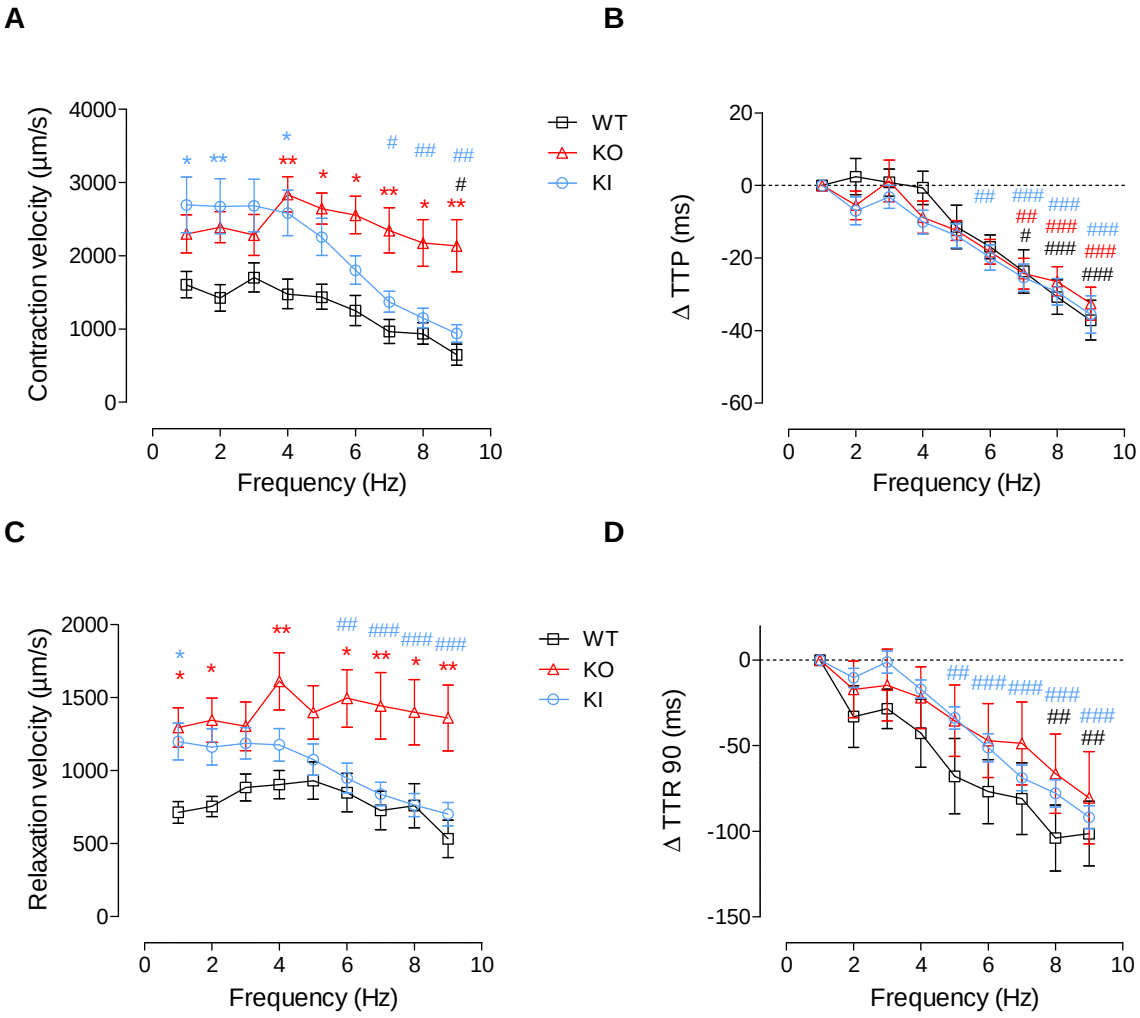

Figure 3.19: Effect of pacing frequency on EHT contraction kinetics. Contraction velocity [**A**], time to 100% peak [TTP; **B**], relaxation velocity [**C**] and time to 90% relaxation [TTR 90; **D**] were measured with increasing pacing frequencies. TTP and TTR 90 values are expressed as delta of starting condition (1 Hz). Measurements were performed under 30 V-stimulation at 1.8 mM extracellular Ca^{2+} (1–9 Hz) in WT (n=10), KO (n=9) and KI (n=14) EHTs. Data are expressed as means±SEM. **P*<0.05 and ***P*<0.01 vs. WT, same condition (two-way ANOVA plus Bonferroni posttests). $^{\#}$*P*<0.05, $^{\#\#}$*P*<0.01 and $^{\#\#\#}$*P*<0.001 vs. 1 Hz, same genotype (one-way ANOVA plus Bonferroni posttests).

Since all EHTs were adequately controlled at stimulation frequencies of 5–6 Hz and still developed good forces, these frequencies were chosen for further experiments. All measurements were analyzed with the IonOptix software based on average peaks as shown in 3.17.

At basal conditions (1.8 mM Ca^{2+}) EHTs were analyzed at 6 Hz and 9 Hz, mimicking *in vivo* condition for rest and physical stress. Interestingly, at 6 Hz, the early phase (TTP 50) and the late phase (TTP) of contraction were 17-23% shorter in KO and KI than in WT (Figure 3.20). The early time of relaxation (TTR 50) was also shorter in KO and KI (35.5% and 23%), but only KO showed a shorter late time of relaxation (TTR 90; 19.8%) than WT. These altered

contraction kinetics resulted in average peaks, which were shifted to the left in KO and KI in comparison to WT. Interestingly, these differences faded away in KI at a frequency of 9 Hz. In contrast, KO EHTs still showed shorter TTP (-13%) and TTR 50–90 (-20%) even at 9 Hz, indicating that these changes could play an important role *in vivo*. The analyzed EHTs did not significantly differ in total force development, excluding potential confounding influence of maximal peak height on contraction kinetics.

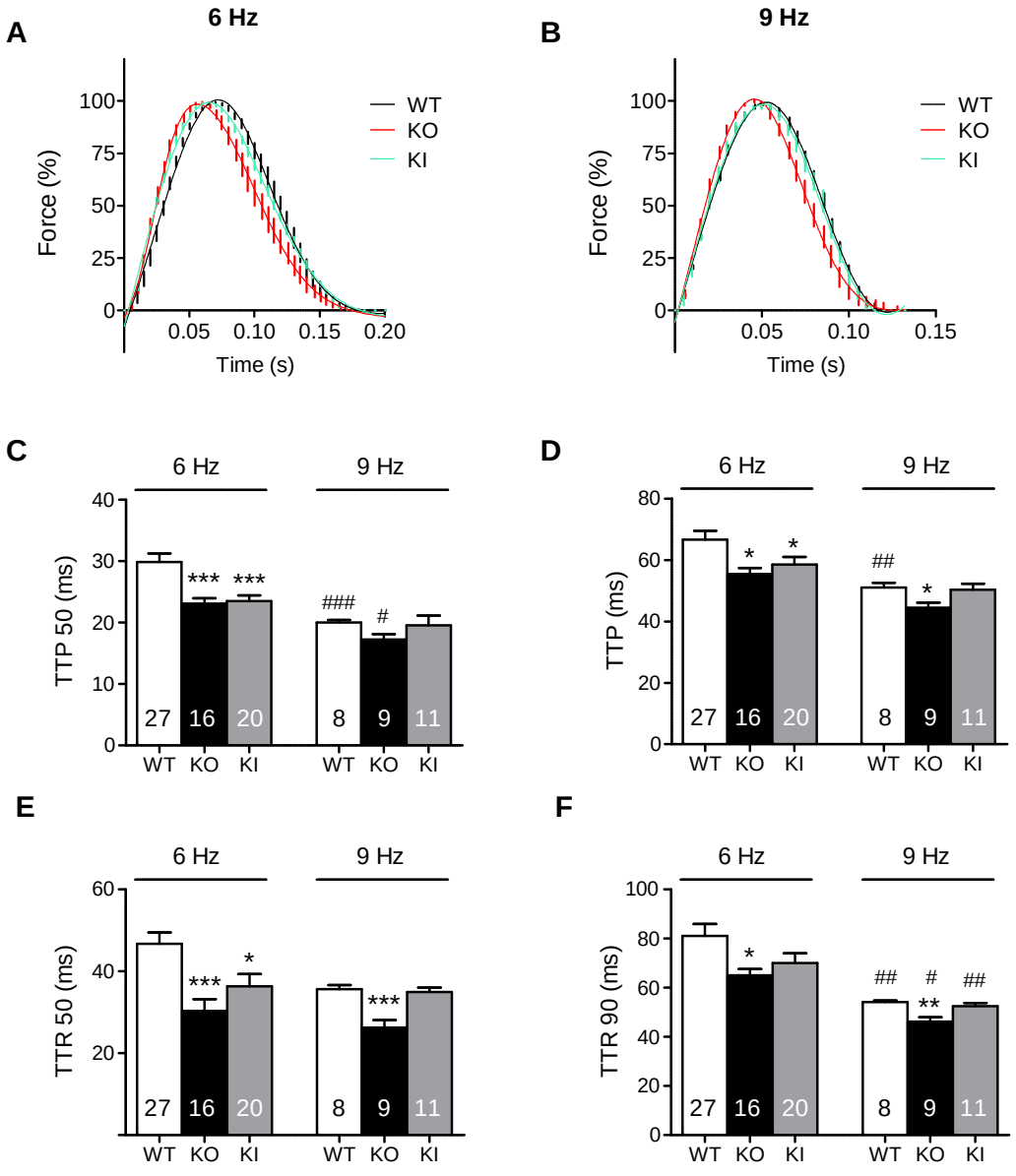

Figure 3.20: Contractile phenotype of WT, KO and KI EHTs under electrical stimulation and continuous perfusion. KO and KI EHTs were compared to pooled C57BL/6J WT and Black Swiss WT. Representative average peaks were generated from KO and KI versus WT at 6 Hz [**A**] and 9 Hz [**B**] pacing frequency, respectively. Contractile parameters (TTP 50 [**C**], TTP [**D**], TTR 50 [**E**] and TTR 90 [**F**]) in KO, KI and both WT were measured at 1.8 mM Ca^{2+}. Number of EHTs is indicated in the bars. Data are expressed as means±SEM. **P*<0.05, ***P*<0.01 and ****P*<0.001 vs. WT control (two-way ANOVA plus Bonferroni posttests); $^{\#}P$<0.05, $^{\#\#}P$<0.01 and $^{\#\#\#}P$<0.001 vs. 6 Hz, same genotype (one-way ANOVA plus Dunnett posttests).

3.2.3.2 Response to external Ca^{2+}

To investigate the contractile response to different external Ca^{2+} concentrations EHTs were continuously perfused with increasing Ca^{2+} concentrations (0.2 to 1.8 mM) in Tyrode's solution. Frequencies of 5–6 Hz were chosen for electrical stimulation. All measurements were analyzed with the IonOptix software based on average peaks as shown in 3.17. All EHTs showed increasing contraction amplitude with rising extracellular Ca^{2+}, as seen in the representative mechanogram image (Figure 3.21). For these measurements EHTs were chosen with a sufficient force development under culturing conditions (>20 µN).

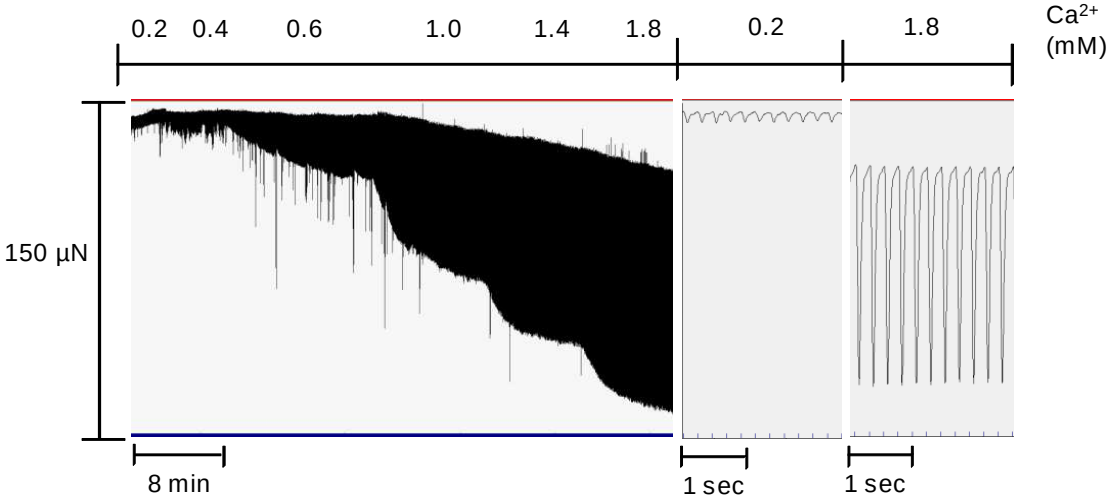

Figure 3.21: Contraction amplitude with rising extracellular Ca^{2+}. Representative mechanogram of a KI EHT, showing the positive inotropic effect of cumulative increases in extracellular Ca^{2+} concentrations ranging from 0.2 to 1.8 mM.

C57BL/6J and Black Swiss WT EHTs did not differ with regard to force (Figure 3.22) or Ca^{2+} sensitivity (EC_{50}: 0.38 mM in C57BL/6J and 0.41 mM Ca^{2+} in Black Swiss) and were therefore pooled for all experiments under pacing. Contractile parameters were calculated from averaged single twitches. At low external Ca^{2+} (0.2, 0.4 and 0.6 mM) twitch force was 2-fold higher in KO than in WT, examples of mechanograms are shown in 3.22. To substantiate differences in Ca^{2+} handling every EHT was normalized to its maximal contraction amplitude (1.8 mM Ca^{2+}), which was already reached at 0.6 mM Ca^{2+} in KO, but at 1.0 mM Ca^{2+} in WT and KI, indicating a higher sensitivity to external Ca^{2+} in KO. Calculated EC_{50} values were 0.41, 0.24 and 0.41 mM in WT, KO and KI, respectively. Under these conditions, at high Ca^{2+} concentrations (1.4 and 1.8 mM) force development was similar in KO and KI as in WT. An increase in extracellular Ca^{2+} concentration from 0.2 to 1.8 resulted in a rise in force in WT, KO and KI by 400%, 225% and 570%, respectively. Contractile kinetics did not change with increasing Ca^{2+} concentrations (data not shown).

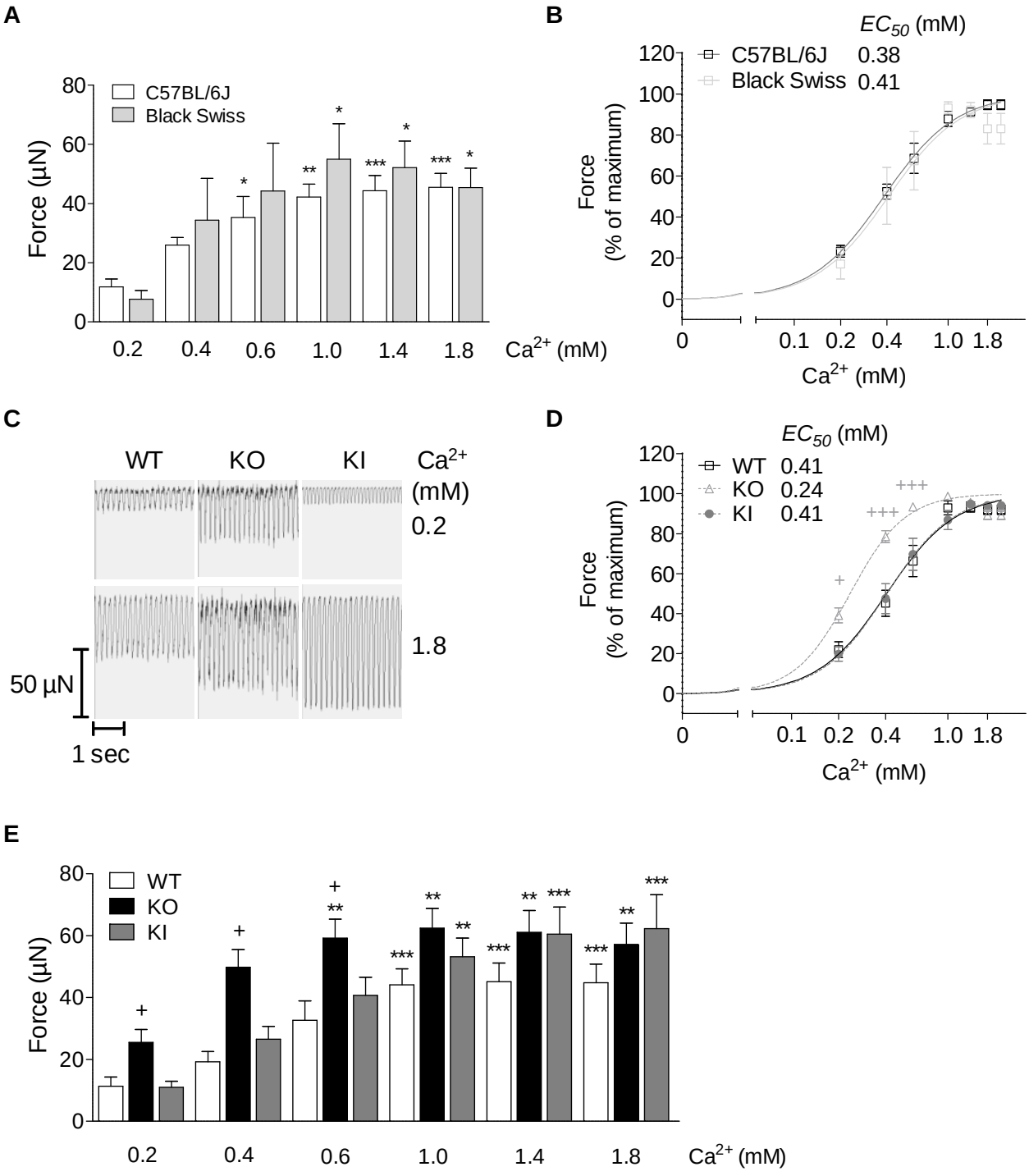

Figure 3.22: Contractile phenotype of electrically stimulated C57BL/6J WT, Black Swiss WT, KO and KI EHTs under continuous perfusion. Total force development in C57BL/6J and Black Swiss WT, analyzed separately (n=3-8 per group; **A**) and normalized relation of force to external Ca^{2+} at different external Ca^{2+} concentrations (0.2-1.8 mM; **B**). Representative force traces of pooled WT, KO and KI at 0.2 and 1.8 mM Ca^{2+} [**C**]. Note the high residual activity in KO EHT at low Ca^{2+}. Normalized relation of force to external Ca^{2+} in pooled WT (n=10), KO (n=9) and KI (n=9) EHTs at different external Ca^{2+} concentrations (0.2-1.8 mM; **D**). **E**, Same data as [**D**], total force development in all EHTs at different external Ca^{2+} concentrations (0.2-1.8 mM; n=9-10 per group). Data are expressed as means±SEM. **P*<0.05, ***P*<0.01 and ****P*<0.001 vs. 0.2 mM Ca^{2+}, same genotype (one-way ANOVA plus Bonferroni posttests); ^{+}P<0.05 and ^{+++}P<0.001 vs. WT, same condition (two-way ANOVA plus Bonferroni posttests).

3.2.3.3 Pharmacological provocation test

3.2.3.3.1 Verapamil

The first drug of interest was the L-type Ca^{2+}-channel blocker verapamil since it targets Ca^{2+}-handling. The goal of this experiment was to investigate whether WT, KO and KI show differences in the contractile response to verapamil. This could also help to better understand the phenotype in general and to learn something about treatment strategies of diseased EHTs. WT, KO and KI EHTs were perfused with different verapamil concentrations at high external Ca^{2+} (1.8 mM) and force development was measured. Interestingly, verapamil was more potent to decrease force of contraction in WT than in KO and KI EHTs, as seen in calculated IC_{50} values, which were higher in KO and KI (IC_{50}: 1397 nM in KO and 1269 nM in KI versus 255.8 nM verapamil in WT; Figure 3.23). Average peaks showed shortened twitch kinetics in KO and KI at 1.8 mM Ca^{2+}, as expected under basal conditions. Under increasing verapamil concentrations, the accelerated kinetics persisted. Under basal conditions, TTP values were 14.8% and 9.8% shorter in KO and KI than in WT, respectively, whereas in the presence of verapamil (1 µM) TTP values were 23.2% and 9.2% shorter in KO and KI. In the relaxation phase, TTR 90 values were 30.3% and 15.5% shorter in KO and KI than in WT under basal conditions, respectively, whereas in the presence of verapamil (1 µM) TTR 90 values were 37.3% and 26.9% shorter in KO and KI.

Thus, the phenomenon of accelerated kinetics in KO and KI is independent of the Ca^{2+} influx via the L-type Ca^{2+}-channel.

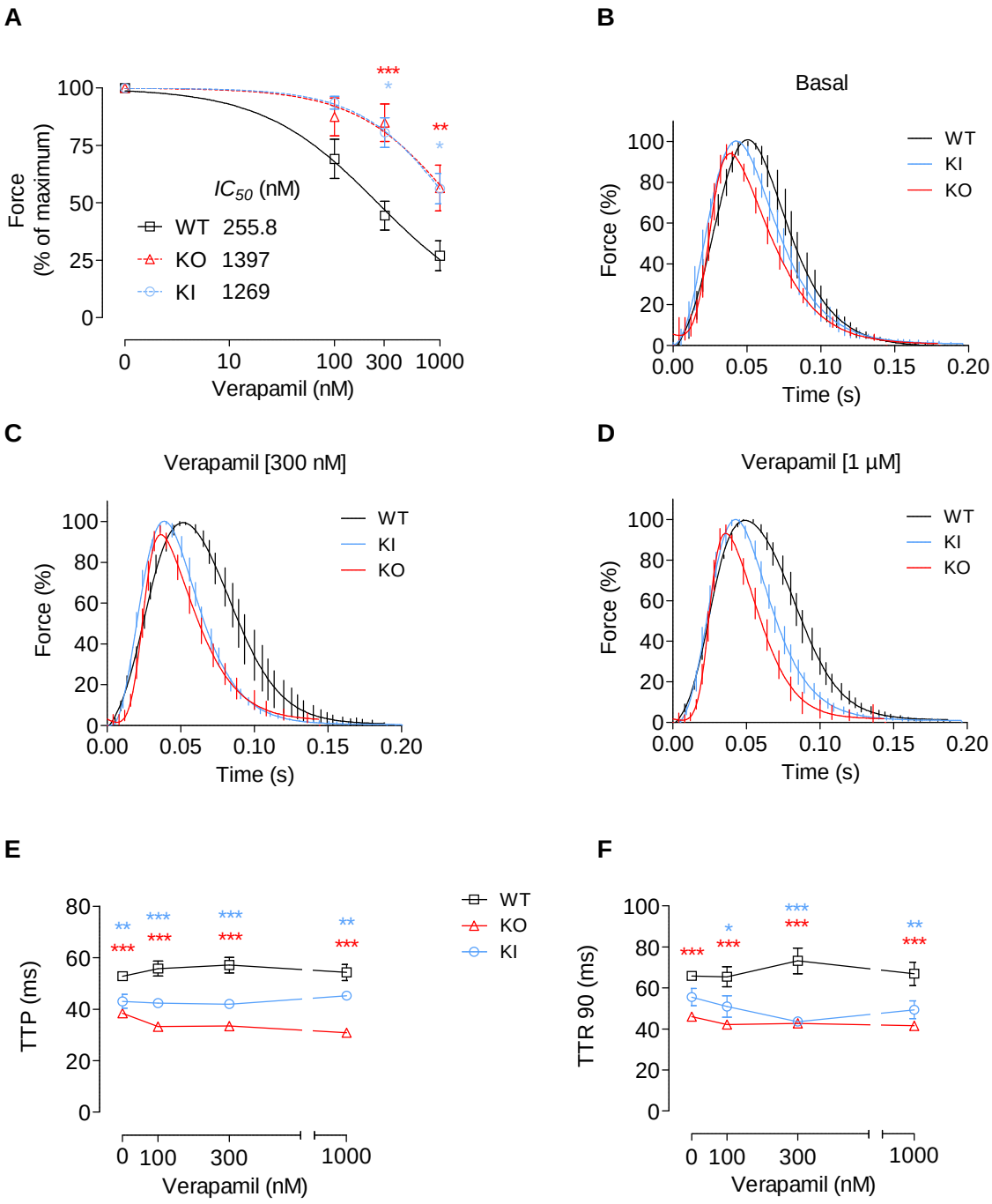

Figure 3.23: Effect of verapamil on EHT contractility. Force in % of maximum (basal condition) with increasing verapamil concentrations (100–1000 nM) in WT, KO and KI [**A**]. Average contraction peaks were generated under basal conditions [**B**], verapamil 300 nM [**C**] and verapamil 1 µM [**D**]. Kinetic parameters such as TTP [**E**] and TTR 90 [**F**] were measured with increasing verapamil concentrations in WT, KO and KI. Measurements were performed under 30 V-stimulation in 1.8 mM extracellular Ca^{2+} (5–6 Hz) in WT (n=4), KO (n=7) and KI (n=5). Data are expressed as means±SEM. **P*<0.05, ***P*<0.01 and ****P*<0.001 vs. WT (two-way ANOVA plus Bonferroni posttests).

3.2.3.3.2 EMD 57033 in WT EHT

To characterize EMD (3.2.2.2) in terms of potency, measurements of force were performed in the presence of different EMD concentrations (0.1–10 µM) under electrical stimulation (5 Hz) and continuous perfusion. The dose-response curve for EMD was measured in WT EHTs, showing an EC_{50} of 1.52 µM for EMD (Figure 3.24). The force in the presence of EMD (10 µM) was 1.5-fold higher than under baseline conditions in these EHTs. The measurement was performed at 0.6 mM external Ca^{2+}. EMD increased the contraction (T1) and the relaxation (T2) times as expected (3.2.2.2).

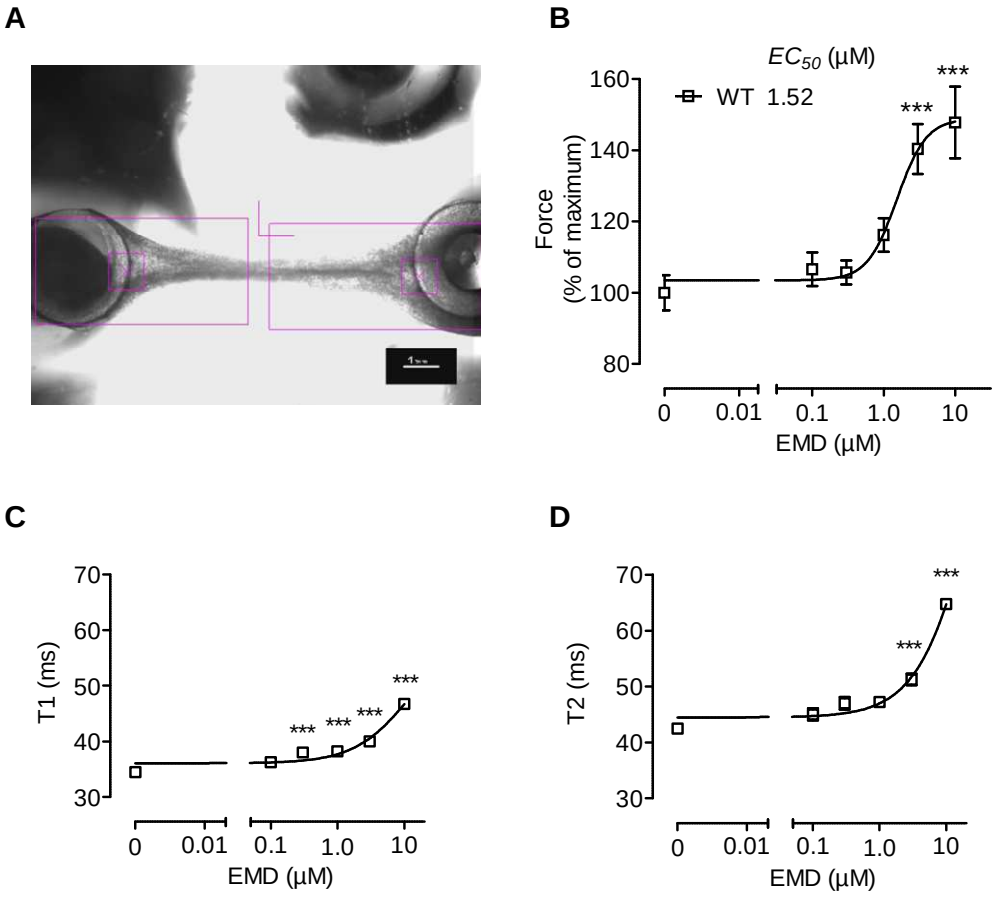

Figure 3.24: Effect of EMD 57033 on contractile parameters of WT EHT, measured with the CTMV software. Contour recognition figure of an EHT under perfusion and electrical stimulation [**A**]. Normalized force in % of maximum (baseline condition; **B**), contraction time T1 [**C**] and relaxation time T2 [**D**] were measured in WT EHTs (n=4) under increasing EMD concentrations (0-10 µM) at 0.6 mM Ca^{2+}. EHTs were paced at 5 Hz. Data are expressed as means±SEM. ***P<0.001 vs. baseline (one-way ANOVA plus Bonferroni posttests).

3.2.3.3.3 Effect of Ca^{2+} sensitization versus β-adrenergic stimulation

We also assessed the effect of EMD (10 µM) in comparison to the β_1-adrenergic agonist isoprenaline (ISO; 100 nM) under electrical pacing (5-6 Hz) at 0.6 mM external Ca^{2+}. As seen in Figure 3.25, ISO increased the systolic (increase in peak force) and slightly decreased the diastolic force (decrease in baseline values), whereas EMD preferably increased the systolic force and slightly increased the diastolic force.

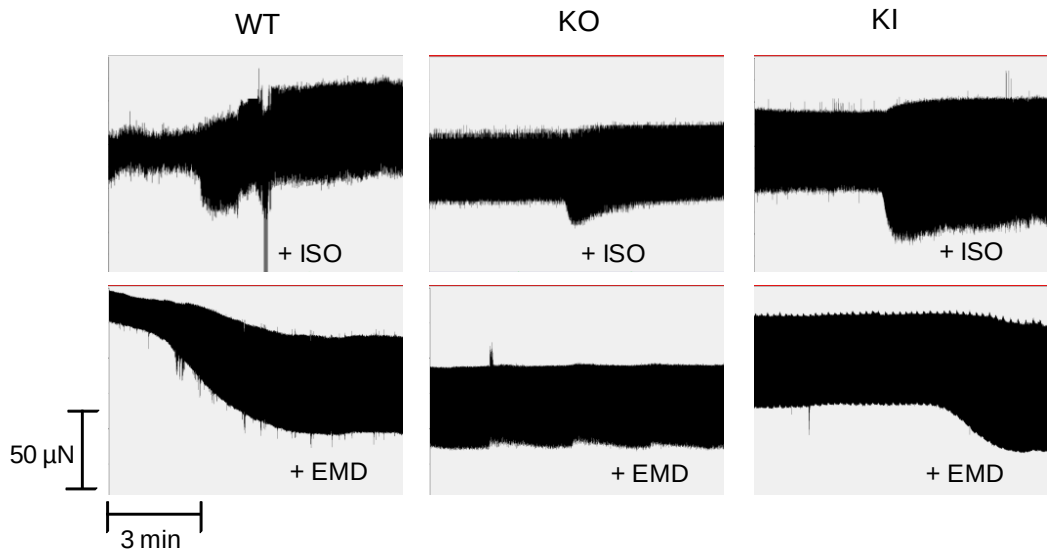

Figure 3.25: Effect of isoprenaline in comparison to EMD 57033, measured in electrically stimulated WT, KO and KI EHTs with the IonOptix software. Measurements were done at 0.6 mM external Ca^{2+}. Representative mechanograms of KO, KI and WT EHTs showing the effect of isoprenaline (ISO, 100 nM, upper panels) and EMD 57033 (EMD, 10 µM, lower panels). EHTs were paced at 5 or 6 Hz.

Average peaks showed that ISO, as expected for cardiac muscle, accelerated twitch kinetics in WT, particularly by abbreviating the contraction and relaxation phases, the classical positive klinotropic and lusitropic effects of β-adrenergic stimulation (-6 ms in TTP and -23 ms in TTR 90, respectively). These effects were not seen in KO (+4 ms in TTP and -1 ms in TTR 90) and only minor in KI (+2 ms in TTP and -12 ms in TTR 90; Figure 3.26). In contrast, EMD decelerated twitch kinetics in all EHTs, as seen in prolonged contraction (+11, +0.5 and +5 ms in TTP in WT, KO and KI, respectively) and relaxation (+24, +20 and +12 ms in TTR 90 in WT, KO and KI, respectively) phases. As seen before in spontaneously beating EHTs at 1.8 mM Ca^{2+}, EMD markedly increased twitch force in WT (+110%), but nearly did not affect force in KO (+2%) and had only a minor positive inotropic effect in a fraction of KI (+32%). In contrast, all EHTs responded to ISO. Force in WT increased by 160% in the presence of ISO, whereas it increased by only 36% in KO. KI showed a tendency towards a reduced positive inotropic response to ISO (+90%) in comparison to WT.

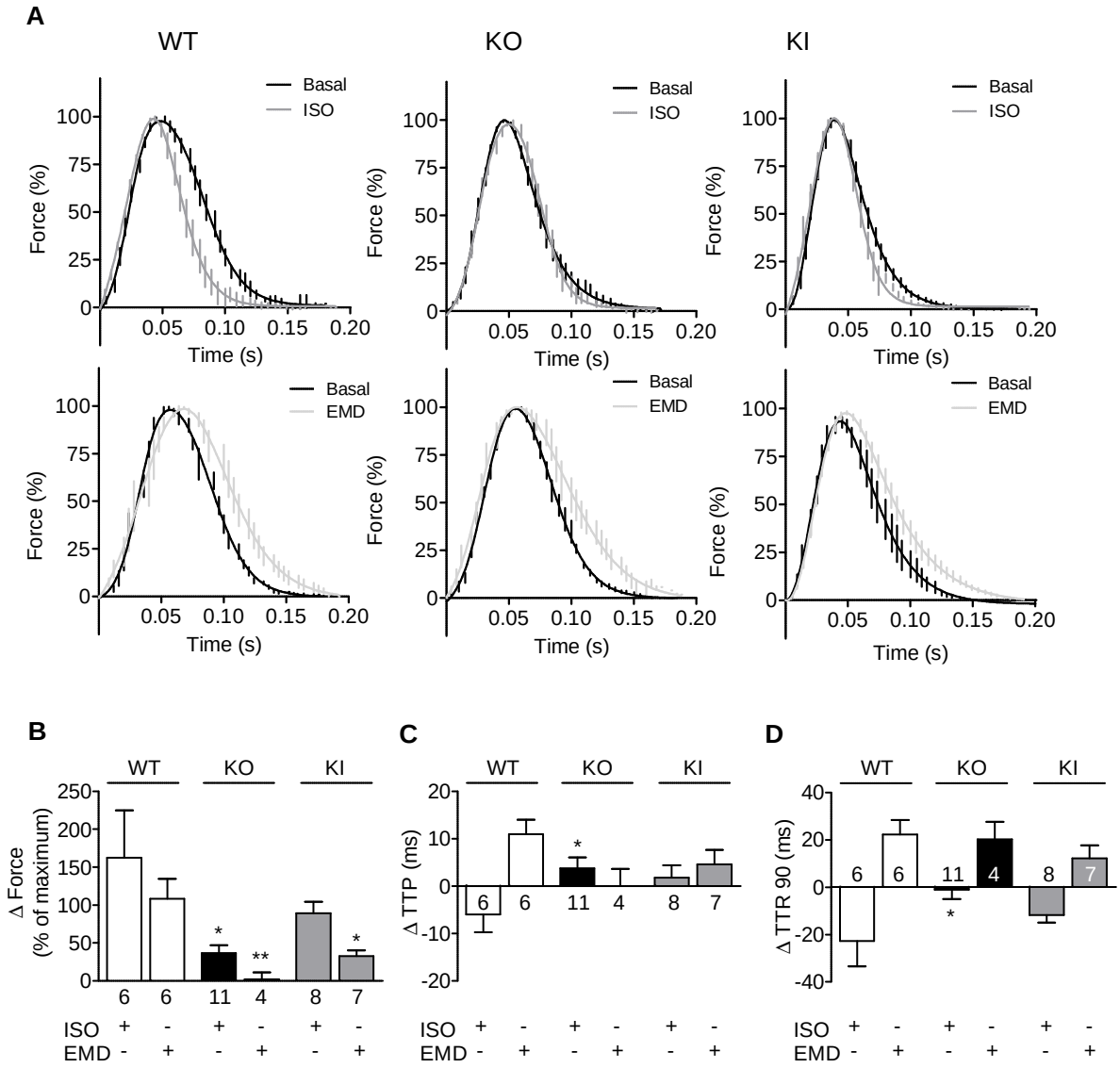

Figure 3.26: Effect of isoprenaline in comparison to EMD 57033 on kinetics, measured in electrically stimulated WT, KO and KI EHTs. All measurements were performed at 0.6 mM external Ca^{2+}. Average peaks were generated [**A**] and delta values of contractile parameters (force in % of basal [**B**], TTP [**C**] and TTR 90 [**D**]) were analyzed in KO, KI and both WT in the following conditions: basal and ISO or basal (DMSO, 1:1000) and EMD (dissolved in DMSO). Number of EHTs is indicated in the bars. C57BL/6J and Black Swiss WT were pooled. EHTs were paced at 5 or 6 Hz. Data are expressed as means±SEM. **P*<0.05 and ***P*<0.01 vs. WT (one-way ANOVA plus Dunnett posttests).

3.2.3.3.4 Ca^{2+} desensitization to rescue KO's phenotype

To answer the question whether the lack of a positive inotropic effect of EMD in KO was due to the absence of cMyBP-C directly or due to an already high Ca^{2+} sensitivity and therefore already high force in KO EHT, we used the actin-myosin interaction-inhibitor blebbistatin to decrease twitch force in KO EHTs to a level similar to WT. At micromolar concentrations, blebbistatin almost completely abolished force in KO EHTs, the calculated IC_{50} value was 116 nM (Figure 3.27). When EHTs were perfused with blebbistatin (100 nM), force decreased by 36%. Under this condition, EMD (3 µM) increased contraction amplitude by 40%. This demonstrates that Ca^{2+} desensitizing effects of blebbistatin can rescue the phenotype in KO EHT and that cMyBP-C is not required for EMD action. Contraction (T1) and relaxation (T2) times remained stable under blebbistatin and tended to increase under the combination of blebbistatin and EMD.

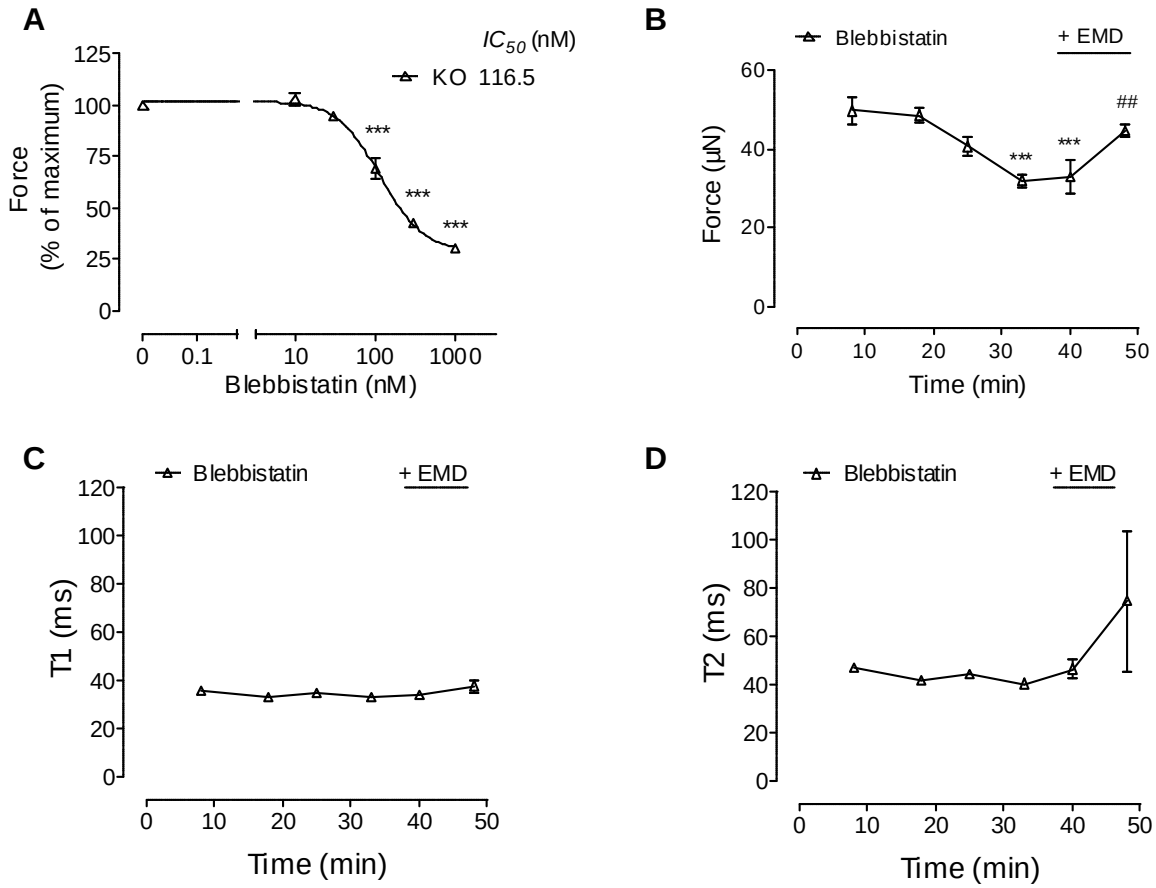

Figure 3.27: Effect of EMD 57033 (EMD) under blebbistatin in KO EHT, measured with the CTMV software. Concentration-response curve for blebbistatin in KO EHTs (n=7) at 0.6 mM Ca^{2+} [**A**]. KO EHTs (n=7) were perfused with blebbistatin (100 nM), EMD (3 µM) was added supplementary after 35 min of perfusion at 0.6 mM Ca^{2+} and force [**B**], T1 [**C**] and T2 [**D**] were measured. Data are expressed as means±SEM. ***P<0.001 vs. basal condition (one-way ANOVA plus Bonferroni posttests); $^{\#\#}P$<0.01 vs. blebbistatin perfusion after 35 min (one-way ANOVA plus Bonferroni posttests).

3.2.3.4 Simultaneous force and Ca^{2+} transient measurements in EHT

Simultaneous force and Ca^{2+} transient measurements were performed to determine intracellular Ca^{2+} concentrations during contraction and relaxation phases. The goal was to detect potential alterations of intracellular Ca^{2+} transients in KO or KI EHTs. Measurements were performed with a customized system, which was established dedicated to measure force and Ca^{2+} transient simultaneously (CTMV software; 2.5.2.4). For every EHT force and subsequent Ca^{2+} transient (F340/380 ratio) were measured, both for 30 sec. PDF files were generated for parameters of contractility and Ca^{2+} transient. Fura-2 (10 µM) staining of EHTs was performed at 1.8 mM external Ca^{2+} in Tyrode's solution. After staining, the pacing frequency was adjusted to 2 Hz for measurement, which was lower than under Fura-free conditions (5 Hz). Since Fura-2 has a Ca^{2+} buffering effect, less Ca^{2+} is available at the myofilaments, thus causing decreases in force development and frequency. Mouse EHTs, which developed average forces between 40–50 µN prior to Fura-2 staining, lost almost 70-80% of their initial force under Fura-2. Ca^{2+} transient values reached up to 0.12. After 60 min of continuous perfusion the F340/380 ratio decreased progressively, as seen in Figure 3.28, which was caused by washing out processes of Fura-2. After 75 min of perfusion EHTs became arrhythmic at a pacing frequency of 2 Hz, which was due to washing out processes of Ca^{2+} buffering Fura-2. To avoid arrhythmia, pacing frequency had to be adjusted to 5 Hz at this point. Meanwhile force development was recovering to almost starting conditions. After 200 min of perfusion, merely baseline noise was recorded. To generate reliable results the length of a perfusion experiment was limited to the duration of 1 hour.

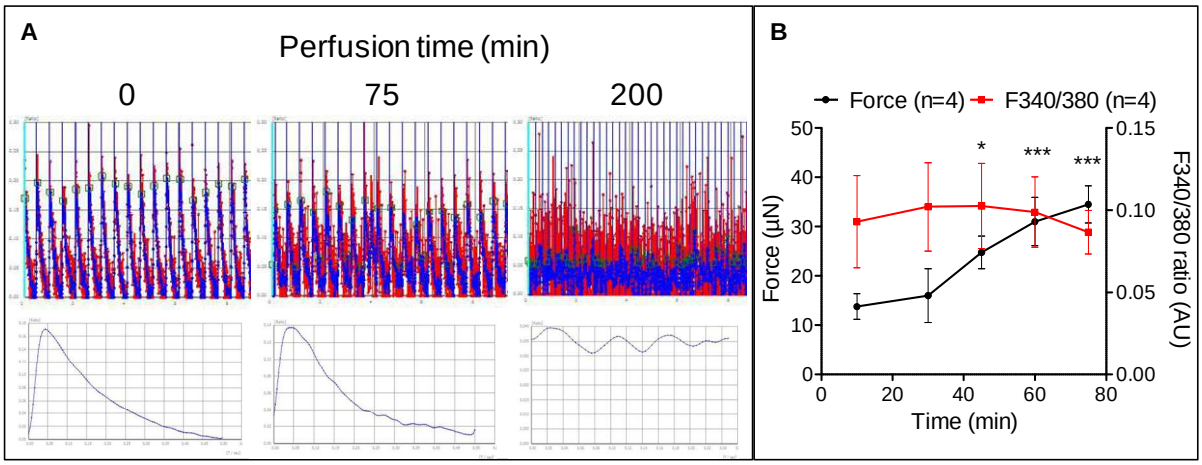

Figure 3.28: Simultaneous force and Ca^{2+} transient measurements in mouse EHT. EHTs were stained with 10 µM Fura-2 in 1.8 mM Tyrode's solution for 2 h at 37 °C. Electrical pacing was done at 2 Hz. EHTs were perfused with Tyrode's solution (1.8 mM Ca^{2+}) for up to 200 min and average peaks of F340/380 ratios were generated [**A**]. Force and F340/380 ratio were measured for 75 min [**B**]. Number of EHTs is indicated in the panel. Data are expressed as means±SEM. **P*<0.05 and ****P*<0.001 vs. force directly after staining (one-way ANOVA plus Bonferroni posttests).

Initially, the Fura-2 staining protocol had been established for rat EHTs, since rat EHTs are available in large amounts and develop high contractile forces. To investigate the effect of our common drugs isoprenaline (ISO) and EMD 57033 (EMD) on intracellular Ca^{2+} transients, Fura-2-stained rat EHTs raised for measurements. Ca^{2+} (1.8 mM) was washed out to an external Ca^{2+} concentration of 0.2 mM. ISO or EMD was added to Tyrode's solution (0.2 mM Ca^{2+}) and Ca^{2+} transients were measured after 15 min of perfusion, respectively. As already shown in previous studies in adult rat cardiomyocytes, ISO significantly increased the Ca^{2+} transient (F340/380) amplitude (+60%; Tamura et al. 1992), whereas EMD only minor changed the Ca^{2+} transient (+18%), supporting the hypothesis that it preferably acts on the myofilaments (Tsutsui et al. 2001) as seen in Figure 3.29. Under both substances force significantly increased at a low external Ca^{2+} concentration (0.2 mM Ca^{2+}). Generated phase plane diagrams, which characterize the relationship between Ca^{2+} transient and force, showed increasing F340/380 ratio at low forces in the presence of ISO. F340/380 ratio did not markedly increase in the presence of EMD. Force remained high with decreasing F340/380 ratio in the presence of EMD.

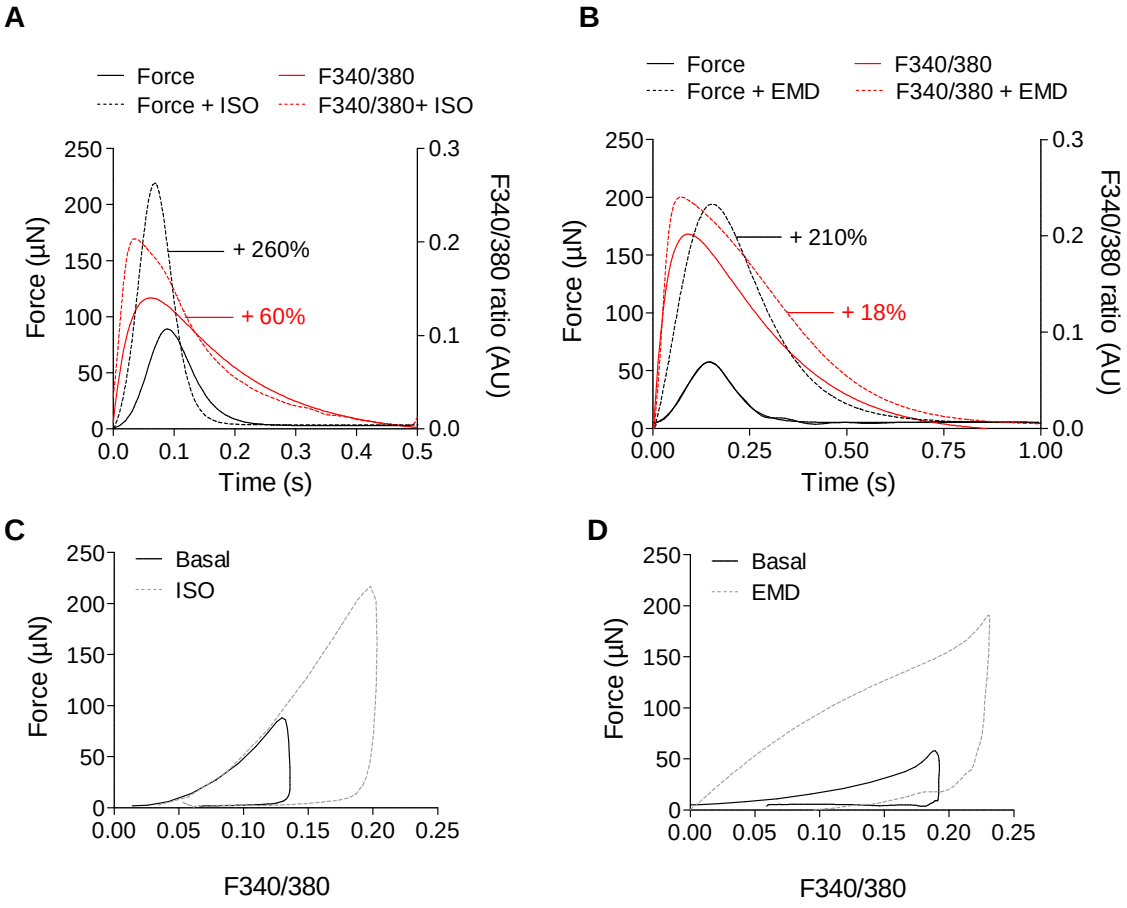

Figure 3.29: Simultaneous force and Ca^{2+} transient measurements in rat EHTs. Measurements were done at 0.2 mM external Ca^{2+}. Effect of isoprenaline (ISO) on force and Ca^{2+} transient at a pacing frequency of 2 Hz [**A**]. Effect of EMD 57033 (EMD) on force and Ca^{2+} transient at a pacing of 1 Hz [**B**]. Phase plane diagrams for ISO [**C**] and EMD [**D**] were generated for both experiments (n=3-4).

3.2.3.4.1 Ca^{2+} transient and force measurements in WT, KO and KI

After Fura-2 staining, Ca^{2+} transients and force development were measured in WT, KO and KI EHTs at an external Ca^{2+} concentration of 1.8 mM. All values were analyzed after 35 min of perfusion (1.8 mM Ca^{2+}) to ensure an appropriate force development and Ca^{2+} transient amplitude. The CTMV software (2.5.2.4) was used for measurements. Average peaks were generated for force and Ca^{2+} transients as depicted in Figure 3.30. Values were normalized to 100% to better detect potential differences in average peak kinetics.

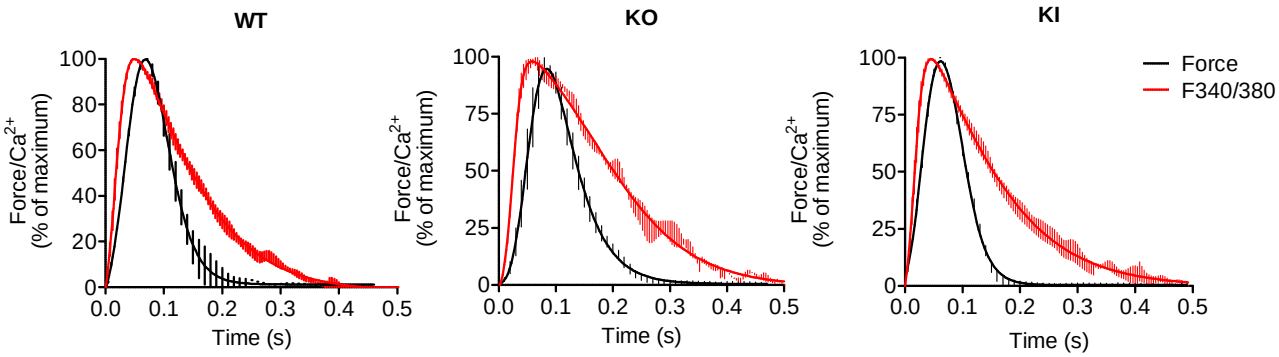

Figure 3.30: Average peaks of simultaneous force and Ca^{2+} transient measurements in Fura-2 stained WT, KO and KI EHTs. Measurements were performed at 2 Hz electrical stimulation (1.8 mM Ca^{2+}) after Fura-2 staining (2 h, 37 °C). Force and Ca^{2+} transient values (F340/380) were normalized to 100% for every EHT. Data are expressed as means±SEM.

KO EHTs exhibited higher force than WT and KI after Fura-2 staining (Figure 3.31). Since the decrease in force is a result of Ca^{2+} buffering capacity of Fura-2, this observation is indirectly supporting the Ca^{2+} hypersensitivity in KO. KO EHTs showed a strong tendency towards lower Ca^{2+} transient amplitude in comparison to KI and WT, as also seen in generated phase plane diagrams (Figure 3.31). As a consequence, cytoplasmatic Ca^{2+} concentrations in KO cardiomyocytes might not reach values as high as they are in KI or WT cardiomyocytes, expressed as lower F340/380 values.

In the presence of Fura-2 contraction and relaxation phases were prolonged in comparison to Fura-free conditions (3.2.3.1). Interestingly, in the presence of Fura-2 kinetics were not accelerated in KO and KI in contrast to Fura-free conditions (3.2.3.1), suggesting that the Ca^{2+} buffering effect of Fura-2 may mask accelerated kinetics. Average peaks were used to determine kinetics of Ca^{2+} transient amplitudes. There were no significant differences in time to peak Ca^{2+}, but KO tended to be longer and exhibited prolonged time to 90% Ca^{2+} decay, suggesting a slower extrusion of Ca^{2+} (Figure 3.31).

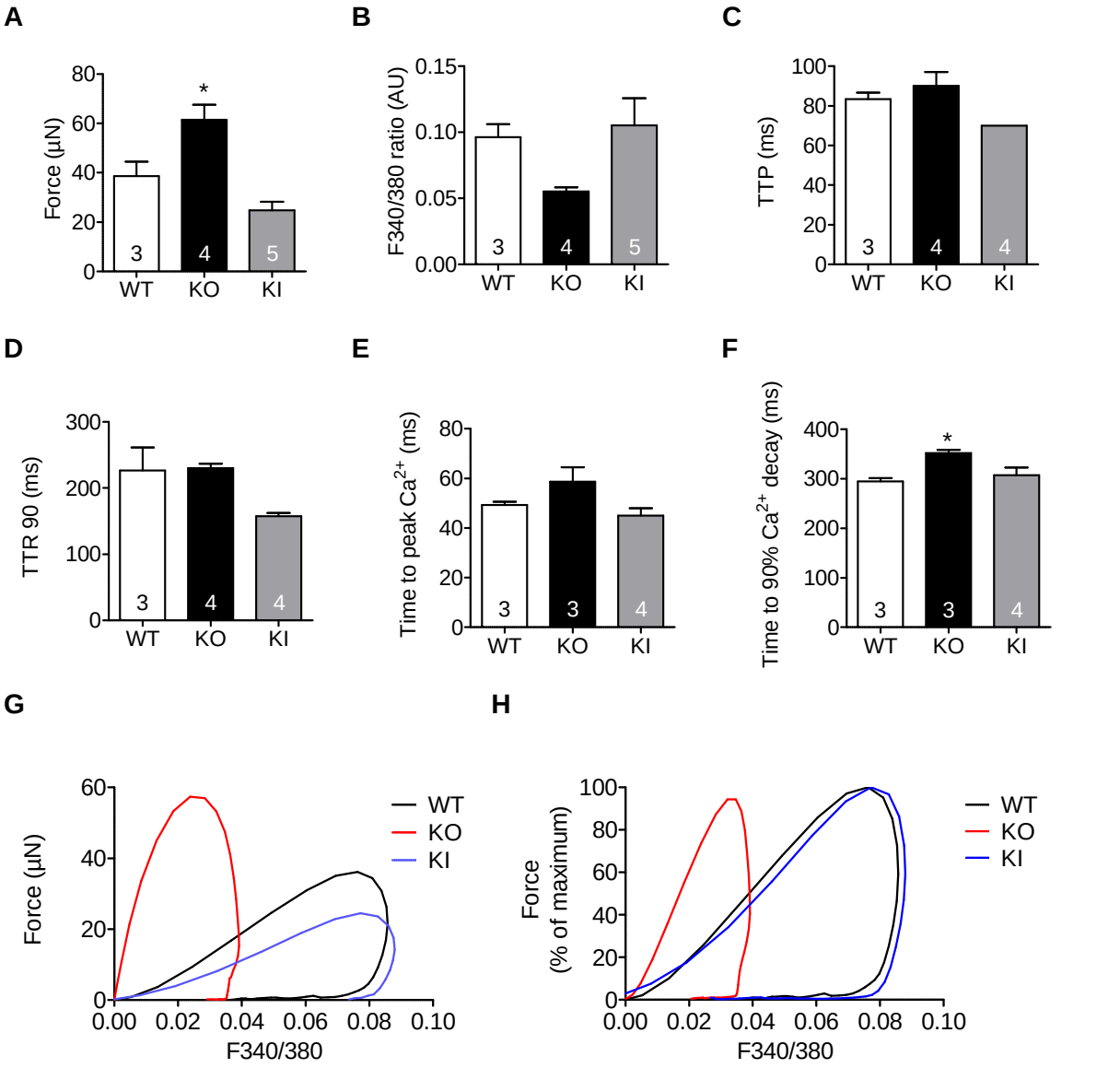

Figure 3.31: Simultaneous measurements of force and Ca^{2+} transient in Fura-2-stained WT, KO and KI EHTs. Measurements were performed at 2 Hz electrical stimulation (1.8 mM Ca^{2+}) after Fura-2 staining (2 h, 37 °C). Contractile parameters such as force [**A**], Ca^{2+} transient amplitude [F340/380 ratio; **B**], time to 100% peak [TTP; **C**], time to 90% relaxation [TTR 90; **D**] as well as time to peak Ca^{2+} [**E**] and time to 90% Ca^{2+} decay [**F**] were measured in WT, KO and KI. Number of EHTs is indicated in the panel. Phase plane diagrams were generated to show the relation between force and F340/380 ratio in absolute values [**G**] and normalized on maximal force [**H**]. Data are expressed as means±SEM. **P*<0.05 vs. WT (one-way ANOVA plus Bonferroni posttests).

3.2.3.4.2 Effect of EMD 57033 on Ca^{2+} transient and force in Fura-2-stained KO EHT

EMD is known to have strong Ca^{2+}-sensitizing, but also weak inhibitory effects on phosphodiesterases (Endoh 2008). The second is expected to increase intracellular Ca^{2+} levels. To assess this question, the effect of EMD on intracellular Ca^{2+} transients was measured in KO EHTs. We therefore performed a basal measurement 5-10 min after Fura-2

staining and started perfusion for 15 min with Tyrode's solution (1.8 mM Ca^{2+}). Perfusion with 0.6 mM Ca^{2+} was initiated and measurements were done after 10 and 15 min to ensure a stable baseline. Force in KO did not significantly decline between 1.8 and 0.6 mM external Ca^{2+}, as expected. EMD (3 µM) was perfused for 11 min at 0.6 mM Ca^{2+} (Figure 3.32). Interestingly, Fura-2-stained KO EHTs showed a positive inotropic response to EMD, which was not observed before (3.2.2.2 and 3.2.3.3.3). This suggested that Fura-2 Ca^{2+} buffering capacity induced similar contractile responses as seen under Ca^{2+} desensitization with blebbistatin (3.2.3.3.4). EMD had no effect on Ca^{2+} transient amplitude (Figure 3.32) or kinetics (data not shown). Prolonged contraction and relaxation times after Fura-2 staining were significantly decreased already after 15 min of perfusion. Fura-2 abolished the previously observed prolongation in contraction and relaxation times under EMD (3.2.2.2; 3.2.3.3.2 and 3.2.3.3.3).

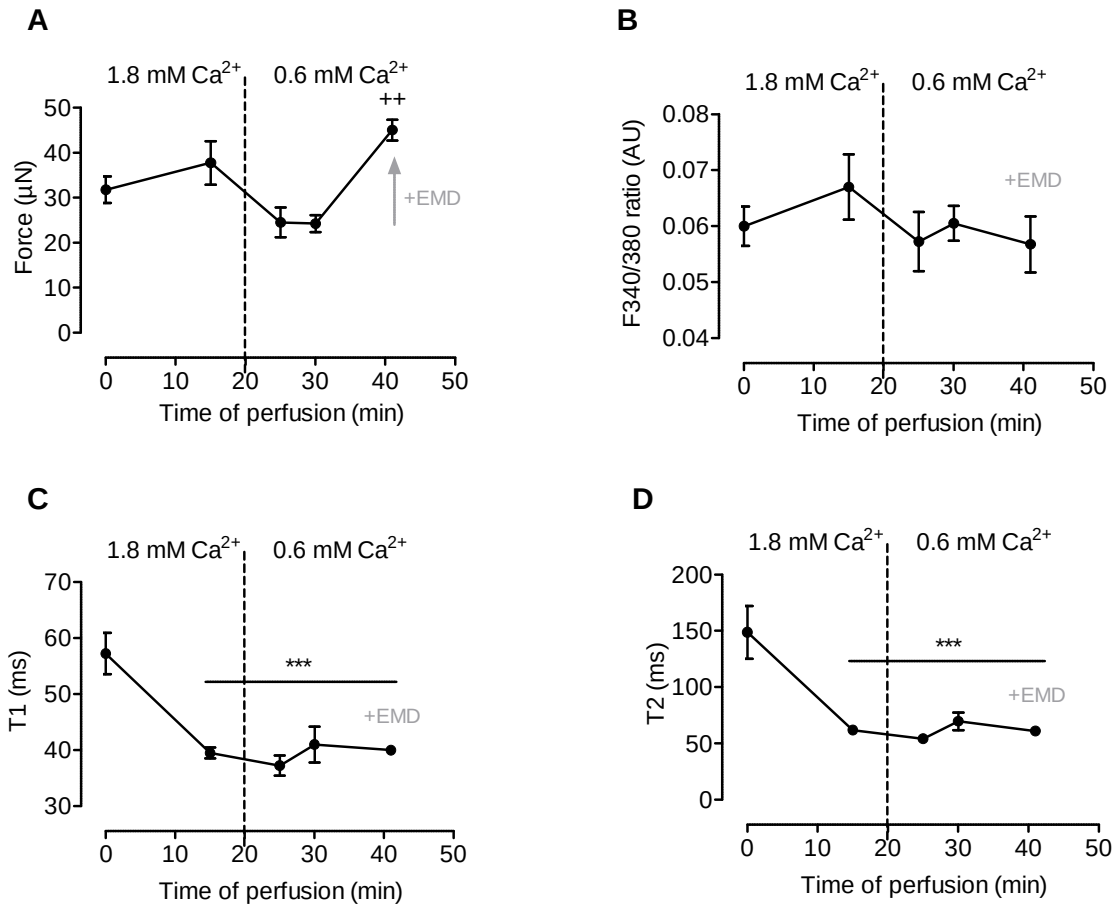

Figure 3.32: Effect of EMD 57033 (EMD) on Fura-2-stained KO EHTs. After preincubation of KO EHTs (n=4) with 10 µM Fura-2 for 2 h, measurements were performed at 2 Hz electrical stimulation. Parameters such as force [**A**], Ca^{2+} transient [**B**], contraction time T1 [**C**] and relaxation time T2 [**D**] were measured. $^{++}P<0.01$ vs. 0.6 mM Ca^{2+} and $^{***}P<0.001$ vs. basal (one-way ANOVA plus Bonferroni posttests).

3.2.4 Molecular analysis of WT, KO and KI EHT

3.2.4.1 Determination of cMyBP-C and hypertrophic gene markers

For genotype confirmation the amount of cMyBP-C protein was determined in EHTs by Western blot. As expected, cMyBP-C protein could not be detected in KO, and levels were ~70% lower in KI than in WT (Figure 3.33). The band was migrating at the same apparent molecular weight as in WT. Interestingly, a slower migrating band of unknown origin above the cMyBP-C band was detected in WT (28.6%), KO (80%) and KI (75%) EHTs. This band was present in mature EHTs in most cases, but not in neonatal heart tissue.

To study hypertrophy in EHTs, amounts of the proteins β-myosin heavy chain (fetal isoform of the myosin heavy chain; β-MHC) and atrial natriuretic peptide (ANP) were determined by Western blot with specific antibodies. Therefore ‘neonatal’ EHTs at the beginning of culture (day 0; after casting) were compared to mature EHTs on day 20 of culture. β-MHC was highly expressed in all EHTs on day 0, as expected. β-MHC protein amount decreased from day 0 to day 20 significantly in all EHTs, which may be a result of maturation. β-MHC protein level was ~20-fold higher in KO and in KI than in WT at day 20, respectively.

ANP protein level only showed a tendency towards an increase in KO and KI on day 0 of culture. Furthermore, ANP protein expression tended to increase during EHT culture period. This could be a consequence of either silicone-post-induced stretch or animal sera in the culture medium, which are known to be hypertrophic stimuli. During culture, ANP protein expression did not differ significantly between WT, KO and KI, suggesting an incomplete activation of the hypertrophic gene program in KO and KI.

Thus, during EHT culture cell maturation, stretch, serum effects and genotype, of course, can alter and change the expression of genes, which are known to be upregulated in hypertrophy.

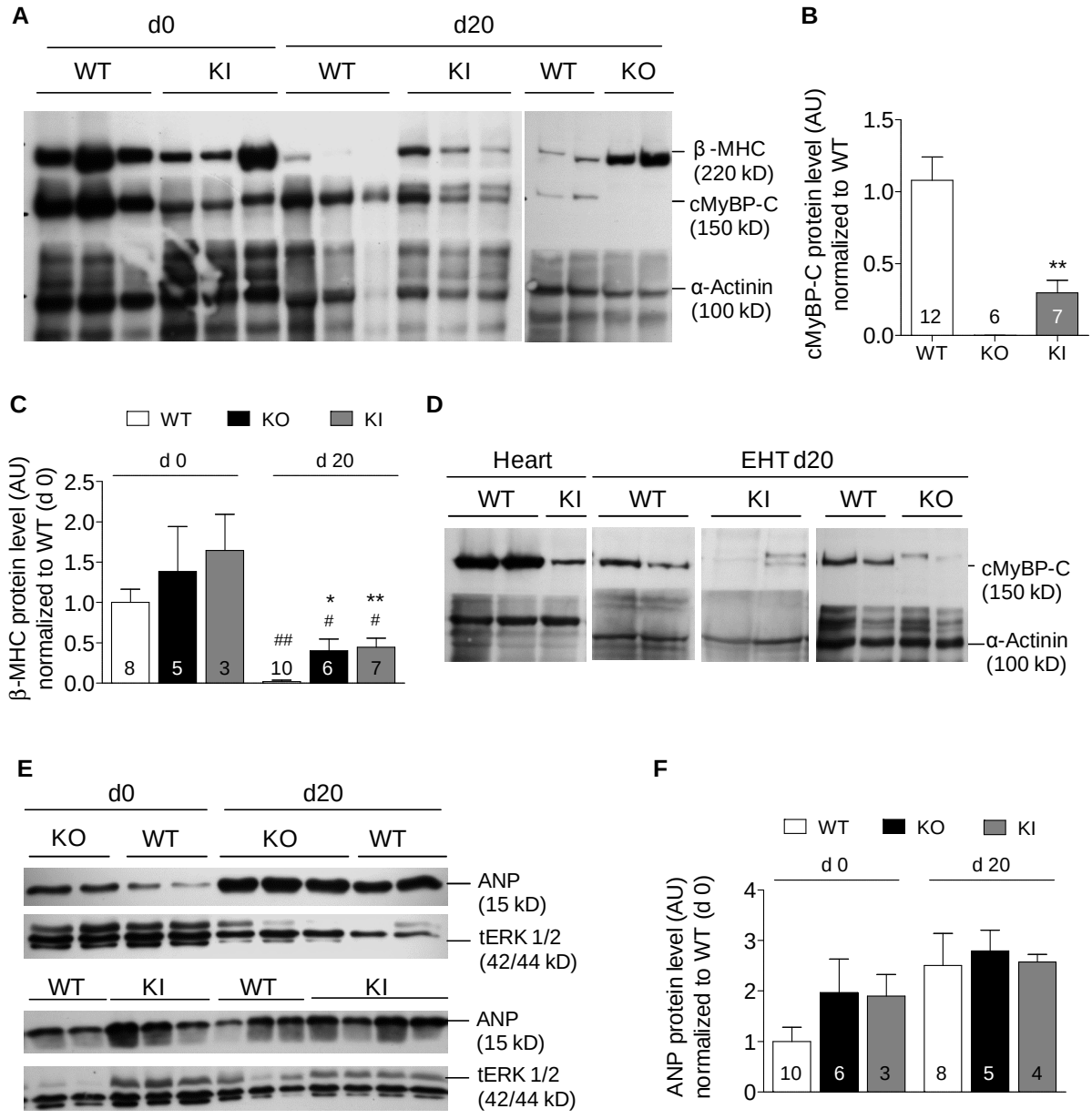

Figure 3.33: Molecular analysis of WT, KO and KI EHTs. A, D and E: Representative Western blots of cMyBP-C, β-MHC and ANP, α-actinin or total ERK 1/2 served as loading controls. Statistical analysis of cMyBP-C [**B**, day 20], β-MHC [**C**] and ANP [**F**] protein levels. Number of EHTs is indicated in the bars. Note that an unspecific band above the cMyBP-C band was detected in 28.6%, 80% (P<0.001) and 75% (P<0.01) of WT, KO and KI EHTs, respectively (Fisher's exact test). Data are expressed as means±SEM. *P<0.05 and **P<0.01 vs. WT (two-way ANOVA plus Bonferroni posttests); $^{\#}P$<0.05 and $^{\#\#}P$<0.01 vs. d0 (one-way ANOVA plus Bonferroni posttests).

Additionally, transcript concentrations of cMyBP-C, alpha myosin-heavy chain (α-MHC), β-MHC, alpha skeletal actin (α-skAct), ANP, SERCA, NCX, cTn-C (cardiac troponin C), cTn-I (cardiac troponin I), LTCC (L-type Ca^{2+}-channel) and β_1-AR (β_1-adrenoceptor) were analyzed by RT-qPCR in 20-day-old EHTs. In KO, α-MHC mRNA was lower (40%), while β-MHC, α-skAct and ANP transcript levels were 3-fold higher than in WT. In KI, β-MHC and α-skAct transcript levels were similarly higher, but α-MHC and ANP mRNA levels did not differ from WT, confirming the overall milder phenotype of KI than KO (Figure 3.34). SERCA and cTn-I transcript levels were lower and β_1-AR mRNA was higher in KO than in WT. Interestingly, KI showed different expression patterns regarding SERCA, NCX, cTn-C, cTn-I, LTCC and β_1-AR levels than KO, which cannot be explained at this time. In KI, NCX, cTn-C and cTn-I transcript levels were higher than in WT.

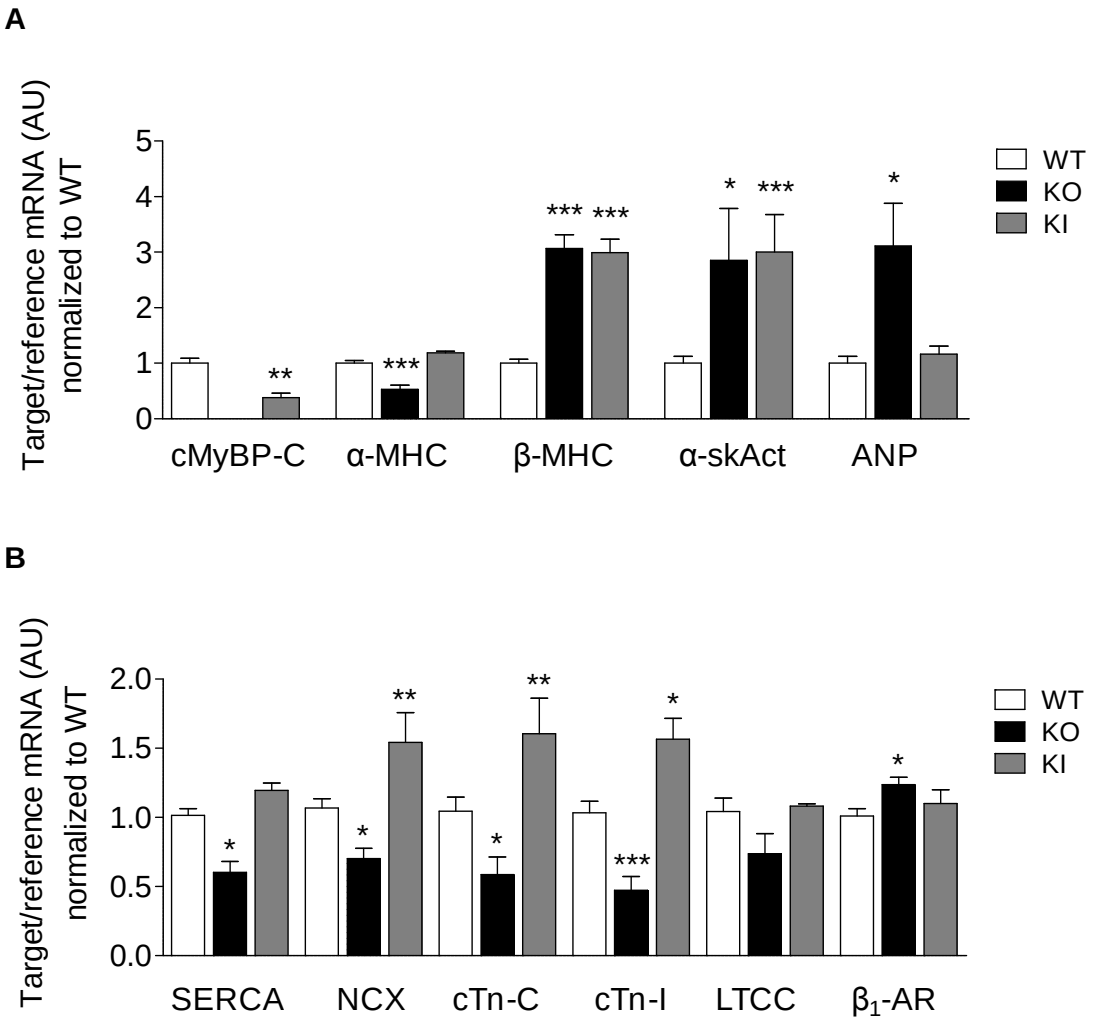

Figure 3.34: RT-qPCR analysis of WT, KO and KI EHTs. cMyBP-C, α-MHC , β-MHC, α-skAct, ANP [**A**] and SERCA, NCX, cTn-C, cTn-I, LTCC, β_1-AR [**B**] mRNA amounts (n=7-21 per group) were analyzed on day 20 of EHT culture. Data are expressed as means±SEM. **P*<0.05, ***P*<0.01 and ****P*<0.001 vs. WT (one-way ANOVA plus Tukey posttests).

Furthermore, qRT-PCR analysis was performed to precisely address the question whether neonatal cardiomyocytes from KO and KI express hypertrophic marker genes on day 0 after cell isolation prior to EHT generation. Therefore, EHTs from day 0 were compared to neonatal hearts on day 0 and on day 2 postnatal. Interestingly, in neonatal hearts (day 0) mRNA levels of hypertrophic marker genes such as β-MHC, α-skAct or BNP were not higher in KO than in WT hearts. When the heart weight to body weight ratio was measured there were no differences in genotype and gender in pooled neonatal hearts (day 0-3). Unfortunately, we had no hearts (day 0) from KI mice in these experiments. In contrast to day 0, neonatal hearts analyzed on day 2 after birth showed higher levels of β-MHC and BNP in KO and KI in comparison to WT. In EHTs on day 0 mRNA amounts of α-MHC, β-MHC, α-skAct or NCX were unchanged between WT, KO and KI (Figure 3.35). This may be explained by the fact that EHTs were mainly composed of heart cells from day 0 postnatal. Therefore, the expression pattern reflected the unhypertrophic gene program of hearts on day 0. These results suggested that KO and KI cardiomyocytes likely developed overexpression of hypertrophic molecular markers such as β-MHC in EHT culture similar to *in vivo* conditions.

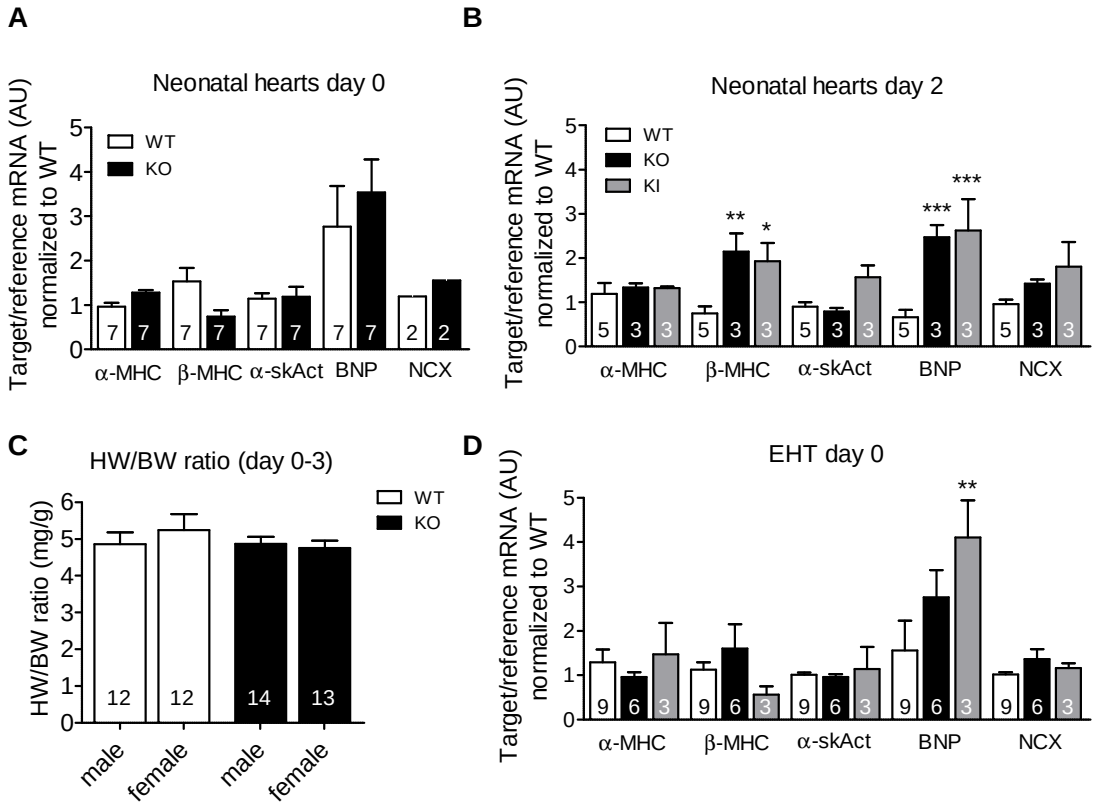

Figure 3.35: Analyses of WT, KO and KI hearts or EHTs. α-MHC , β-MHC, α-skAct, BNP and NCX mRNA levels were measured in neonatal hearts on day 0 postnatal [**A**], on day 2 postnatal [**B**] or in EHTs on day 0 [**D**]. Heart weight to body weight ratio was measured in pooled (day 0-3) WT and KO hearts [**C**]. Number of samples is indicated in the bars. Data are expressed as means±SEM. **P*<0.05, ***P*<0.01 and ****P*<0.001 vs. WT (one-way ANOVA plus Bonferroni posttests).

3.2.4.2 DNA and RNA content

To get an impression of cell survival in the EHT matrix over the culturing period and to characterize metabolic activity DNA and RNA contents were measured in EHTs at day 0, 20 and 30 of culture. In all EHTs DNA content decreased over culture without significant differences between WT, KO and KI. The drop in DNA amounted to approximately 60% between day 0 and day 20 and was minor between day 20 and day 30. On day 0 RNA content was 96% and 119% higher in KO and in KI, respectively (Figure 3.36). Difference between the groups remained, but got smaller over time. This argued for a high apoptosis rate of cells in the first 20 days of EHT culture.

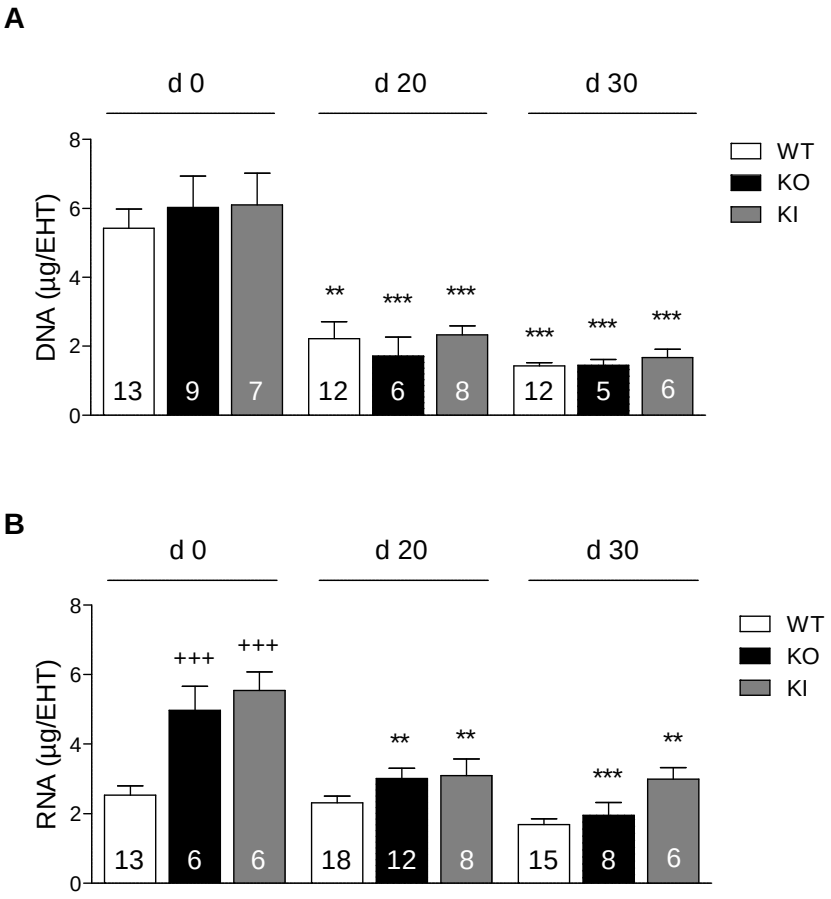

Figure 3.36: DNA and total RNA content of murine EHTs. DNA content of WT, KO and KI over time [**A**]. Total RNA content [**B**]. Number of EHTs is indicated in the bars. C57BL/6J and Black Swiss WT were pooled. Data are expressed as means±SEM. ***P*<0.01 and ****P*<0.001 vs. d0, same genotype (one-way ANOVA plus Bonferroni posttests); ^{+++}P<0.001 vs. WT (two-way ANOVA plus Bonferroni posttests).

3.2.5 First attempts for gene therapy in KO EHT

3.2.5.1 Wild-type cMyBP-C adenovirus transduction

KO EHTs were transduced with an adenovirus encoding the human wild-type cMyBP-C (2.4.7) to induce a genetic rescue. EHTs were transduced with cMyBP-C adenovirus in comparison to GFP adenovirus, both with a MOI of 75 on day 3 of culture. First, the adenovirus was added to the EHT mastermix on day 0, which resulted in cell death in EHTs. On day 3 of culture cells in the EHT survived the adenovirus transduction substantially better. EHTs were cultured for up to 3 weeks.

3.2.5.1.1 UV-light images

UV-light images of transduced KO EHTs served for analyzing transduction efficiency on day 7 of culture. Live imaging (UV light) revealed that the majority of cells seemed to fluoresce (Figure 3.37). Single cell analysis was not possible since no protocol for efficient dissociation of fibrin constructs into single cells could be established.

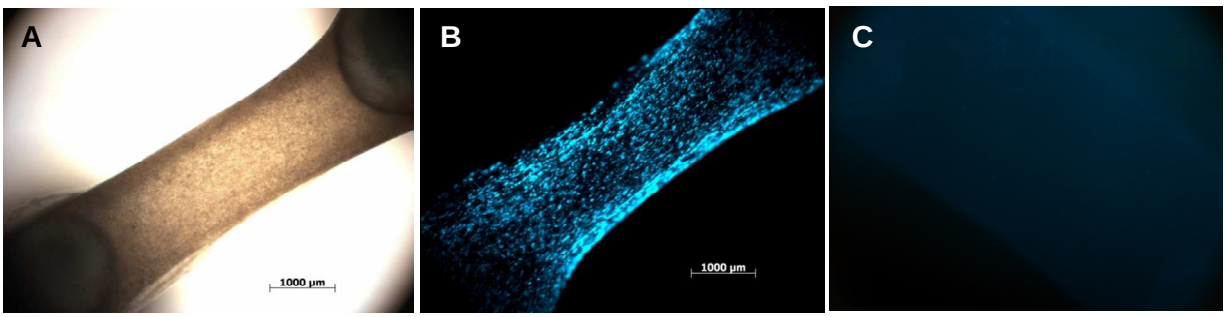

Figure 3.37: KO EHT after transduction with an adenovirus encoding GFP. Transduction was performed on day 3 with a MOI of 75. Phase contrast image [**A**], UV-light images of KO with adenovirus [**B**] and KO without adenovirus [**C**]. Pictures were taken on day 7 of EHT culture.

3.2.5.1.2 Video-optical recording

Under spontaneous beating conditions in culture medium, cMyBP-C adenovirus-transduced KO (v) did not show significant differences in force development in comparison to GFP adenovirus transduced KO (cv) or KO native (Figure 3.38). Since KO EHTs were hypercontractile in previous video-optical recording analysis (3.2.2.1), we would have expected a lower force in KO (v) in comparison to GFP. This was not the case and argued

for an absent curative effect of the cMyBP-C adenoviral gene therapy. Also frequency, contraction and relaxation times were unchanged between the groups.

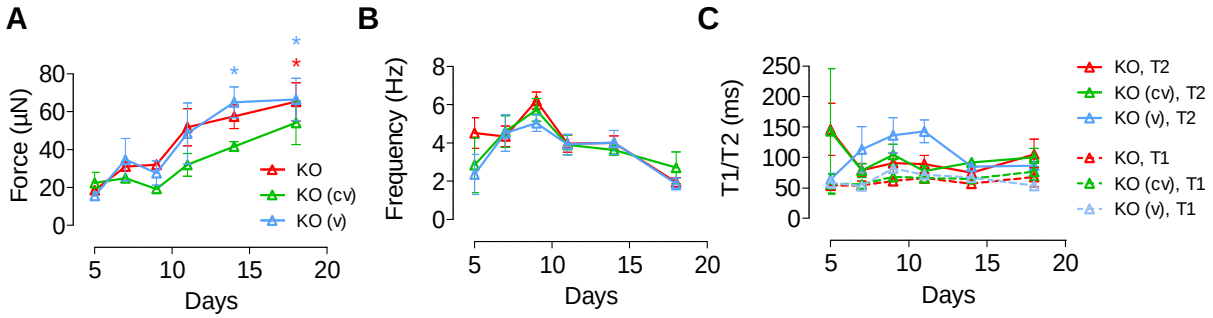

Figure 3.38: Contractile analysis under standard culture conditions of native, cMyBP-C (v) or GFP (cv) adenoviral transduced KO EHTs, measured with video-optical recording. Parameters of contractility (force [**A**], frequency [**B**], contraction time T1 and relaxation time T2 [**C**]) were measured repeatedly over EHT culturing period (day 5–18; 1.8 mM Ca^{2+}) in KO (n=8-12), KO (v; n=5-9) and KO (cv; n=5-7). Data are expressed as means±SEM. **P*<0.05 vs. day 5, same genotype (one-way ANOVA plus Bonferroni posttests).

3.2.5.1.3 Measurements under electrical stimulation and perfusion

Force and parameters of kinetics were measured in KO (v) and KO (cv) under electrical stimulation (6 Hz) and continuous perfusion. The force development was measured at different external Ca^{2+} concentrations. In these experiments, no decrease in the Ca^{2+} sensitivity in KO (v) could be detected in comparison to KO (cv). Furthermore, there were no differences in kinetics such as TTP and TTR 90, which underlined the hypothesis that a cMyBP-C adenovirus treatment of KO was inefficient (Figure 3.39).

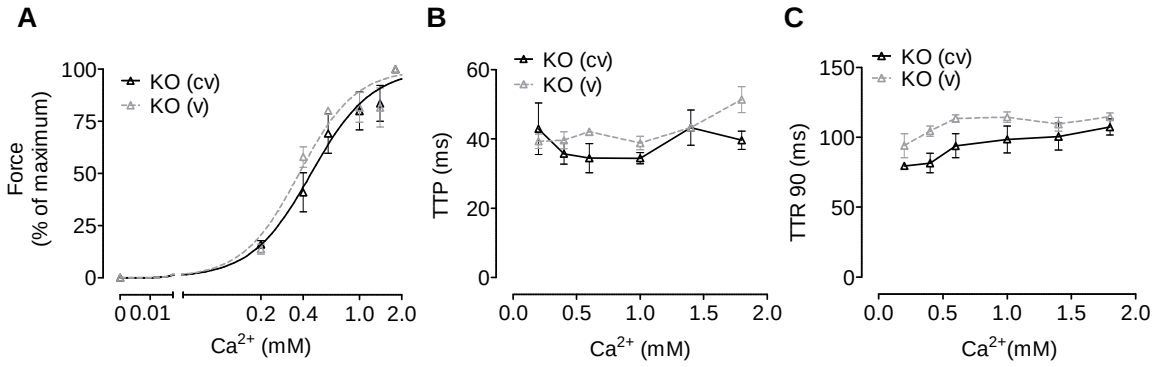

Figure 3.39: Measurement of electrically stimulated KO EHTs, transduced either with cMyBP-C or GFP adenovirus. Measured contractile parameters (force [**A**], time to peak [TTP; **B**] and time to 90% relaxation [TTR 90; **C**]) in KO, either transduced with cMyBP-C (v; n=3) or with GFP (cv; n=3) adenovirus, under increasing extracellular Ca^{2+} (0.2–1.8 mM) concentrations. EHTs were paced at 6 Hz. Data are expressed as means±SEM.

3.2.5.1.4 Immunofluorescence analysis

To explain the lack of functional improvement in KO (v) versus KO (cv), immunofluorescence staining of KO (v) EHTs as whole mounts was performed to visualize cMyBP-C. cMyBP-C could be detected in approximately 30% of α-actinin positive cardiomyocytes and was incorporated into the sarcomeric organization. Immunofluorescence images showed that cardiomyocytes which did not express cMyBP-C lacked specific staining for cMyBP-C (Figure 3.40).

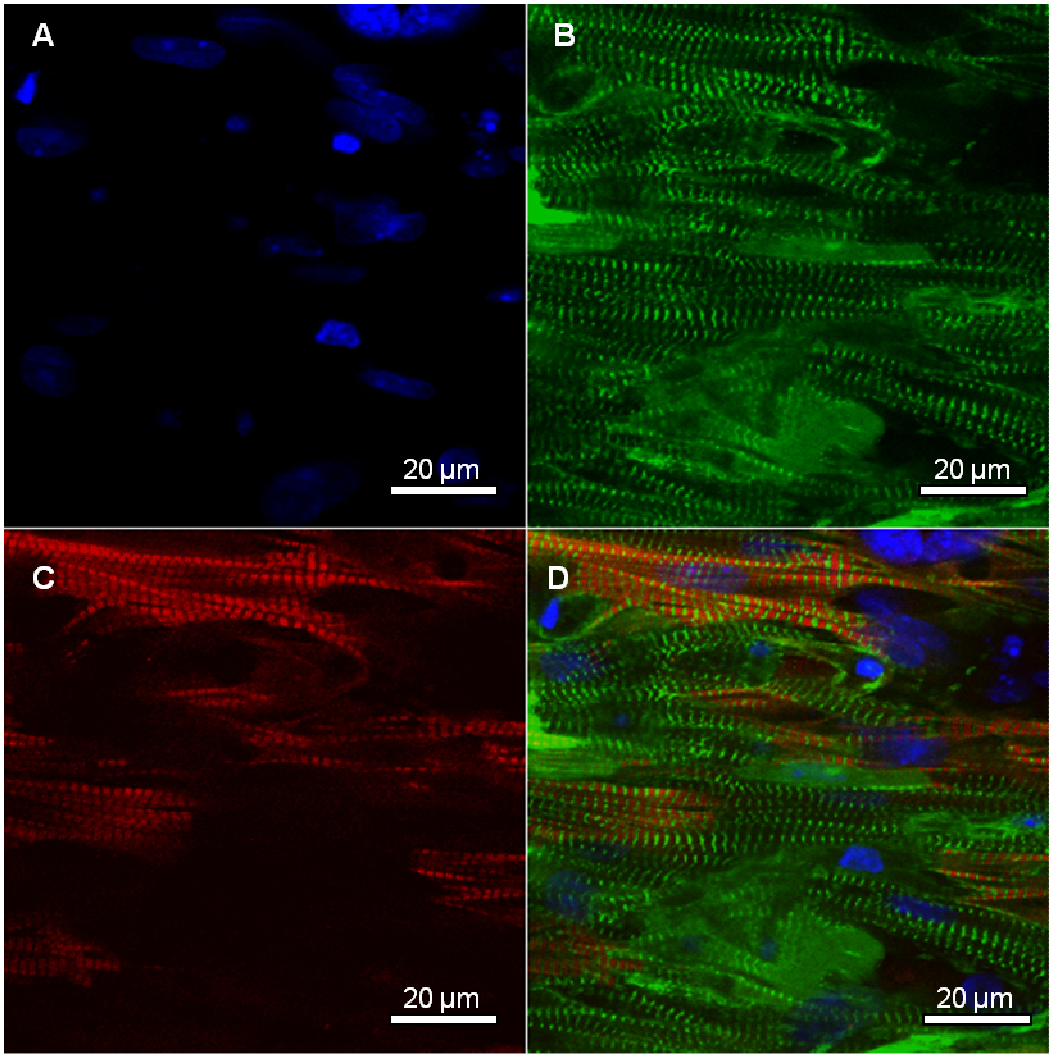

Figure 3.40: Immunofluorescence staining of whole mount cMyBP-C adenovirus-transduced KO EHT. Split image of immunofluorescence staining for nuclei with DRAQ5 [blue; **A**], α-actinin [green; **B**] and cMyBP-C [red; **C**]. Merged immunofluorescence image [**D**].

3.2.5.1.5 Molecular analysis

cMyBP-C protein levels were analyzed in KO, KO (v), KO (cv) and WT EHTs by Western blot. WT EHTs showed a cMyBP-C band, as expected. In KO and KO (cv) no cMyBP-C band could be detected. KO (v) EHTs showed a band in the size of cMyBP-C, which was quantified (Figure 3.41). The thin band right above the cMyBP-C band (150 kD) was the slower migrating band of unknown origin, which was already seen before (3.2.4.1), and was not included in the quantification. This unknown band was not observed in KO (v) and KO (cv). The cMyBP-C protein amount in WT was considered as 100%. In KO (v) only 25% of the wild-type cMyBP-C could be detected in comparison to WT. This manifested the results of the immunofluorescence analysis (3.2.5.1.4), suggesting poor transduction efficiency. Interestingly, the mRNA level of cMyBP-C in KO (v) was not lower than in WT, suggesting that the cMyBP-C protein may have been partially degraded by intracellular quality control systems (Carrier et al. 2010).

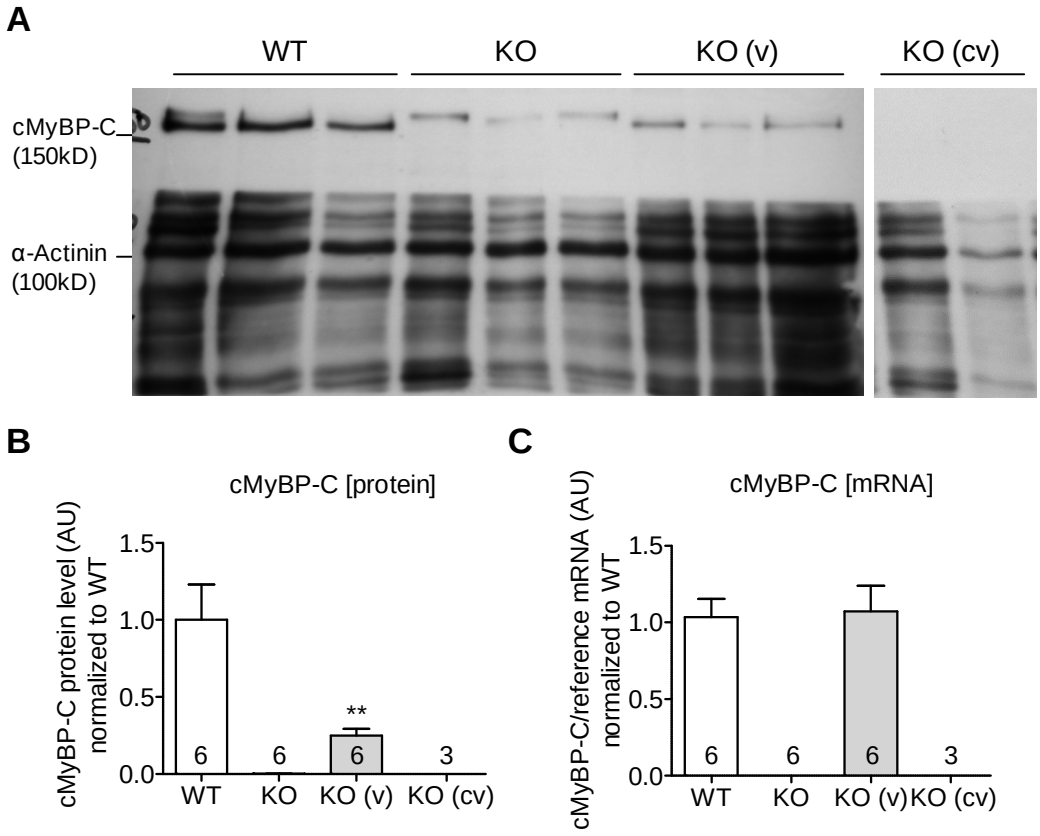

Figure 3.41: Molecular analysis of cMyBP-C adenovirus-transduced KO EHT. Representative Western blot image of cMyBP-C, α-actinin served as loading control [**A**]. Quantitative analysis of cMyBP-C protein level [**B**]. Quantitative analysis of cMyBP-C mRNA level [**C**]. Number of EHTs is indicated in the panel. Data are expressed as means±SEM. ***P*<0.01 vs. WT (one-way ANOVA plus Bonferroni posttests).

Furthermore, protein and mRNA levels of β-MHC were measured in KO, KO (v), KO (cv) and WT EHTs by Western blot. This was done to answer the question whether a gene therapy with cMyBP-C is able to prevent the activation of the fetal gene program in KO (3.2.4.1). A reduced expression of β-MHC would be another indication for a molecular rescue of the phenotype of KO EHTs. β-MHC protein levels were significantly higher in KO and KO (cv) in comparison to WT EHTs, as expected. Transduction of KO with the cMyBP-C adenovirus resulted in β-MHC protein levels which were not significantly higher than in WT (Figure 3.42). However, β-MHC protein levels in KO (v) and KO (cv) did not reach significant differences.

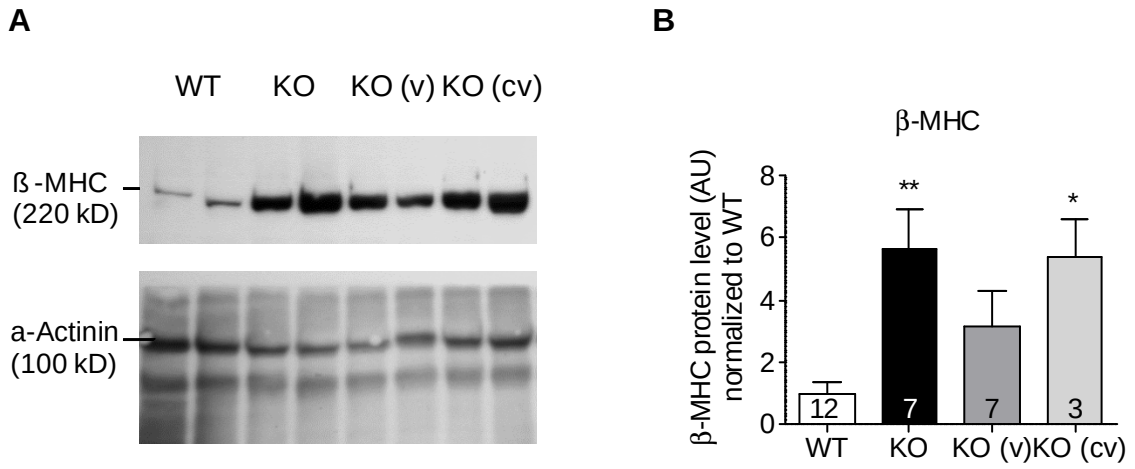

Figure 3.42: Western blot analysis for β-MHC of cMyBP-C adenovirus-transduced KO EHTs. Representative Western blot image of β-MHC, α-actinin served as loading control [**A**]. Quantitative analysis of β-MHC protein level [**B**]. Data are expressed as means±SEM. **P*<0.05 and ***P*<0.01 vs. WT (one-way ANOVA plus Bonferroni posttests).

Overall, these results indicate that the adenovirus-mediated rescue was insufficient. Since an increase in MOI is limited by adenovirus toxicity, the development of adeno-associated viruses (AAV) can be an option. AAVs have been shown to be less toxic and can be used for transduction during EHT casting (day 0; unpublished data; Müller et al. 2006).

3.3 Visualization of endothelial cells in EHT

3.3.1 Establishment of BMX- and VE-Cadherin-Cre-ER^{T2}-Rosa26-LacZ mouse matings

BMX- and VE-Cadherin-Cre-positive male mice were used to establish two mouse lines in the animal facility of the UKE (2.1.2.1). In these mouse lines Cre expression was driven either by an arterial endothelial cell specific promoter (BMX) or by an endothelial cell specific promoter (VE-Cadherin), in both cases only in the presence of tamoxifen. Genotyping of offspring was performed to select individuals for breeding (red marked offspring, figure 3.43). However in case of preparing heart cells for EHTs all neonates were included without genetic preselection due to limited time (pups should be taken on day 0-1 for EHT generation). The rate of unlabeled endothelial cells was lower than expected (50%, rule of Mendel), respresentative analysis of 11 mouse litters revealed that 87% of offspring were positive for Cre.

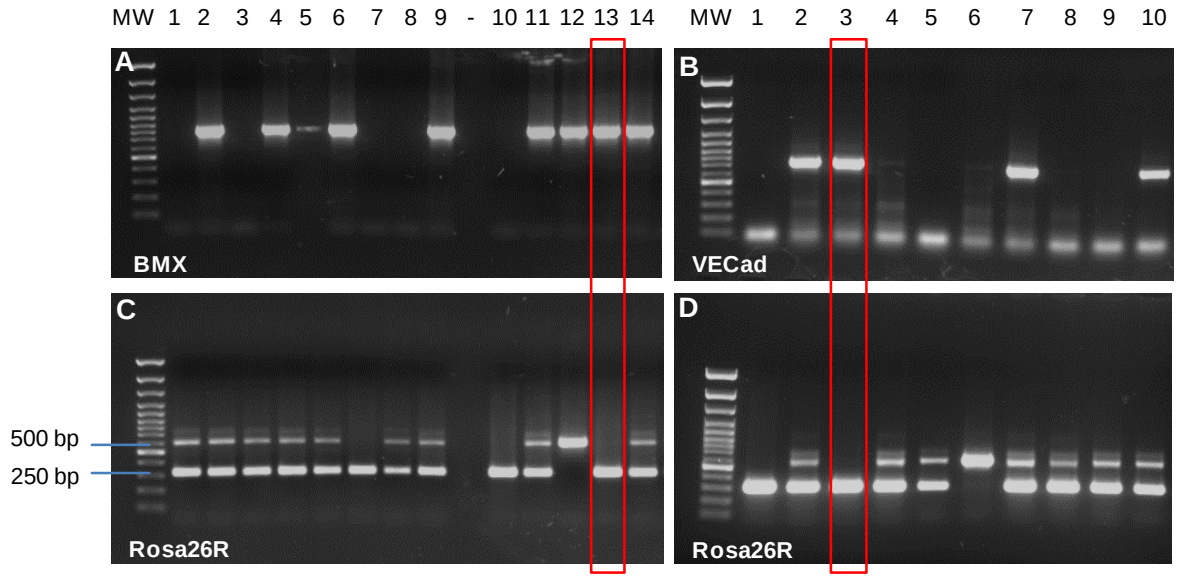

Figure 3.43: Genotyping of BMX and VE-Cadherin mice by PCR. PCR was performed on genomic tail DNA from BMX and VE-Cadherin mice. As a negative control (-) water was added instead of DNA. Sample number characterizes the analyzed mouse tail. MW stands for the 1000-bp molecular weight marker. Red marked samples were taken for further matings. BMX [**A**] and VE-Cadherin [**B**]: One band on the gel stands for Cre-positive sample. Rosa26R [**C** and **D**]: One band (250 bp) means homozygous floxed and one band (500 bp) means wild-type; two bands means heterozygous floxed.

To confirm the endothelial cell specific β-galactosidase expression, a BMX-Cre-ER^{T2}-Rosa26-LacZ mouse was treated for 5 days with tamoxifen i.p. to induce Cre and resulting β-galactosidase expression. The mouse was kept in the cage until 6 days after the last

tamoxifen injection to ensure Cre expression in all organs. The animal was sacrified, the organs were harvested and underwent X-gal staining (2.7.1). X-gal-positive vessels could be detected in the lung, kidney, liver and the heart (Figure 3.44), indicating successful induction of Cre expression.

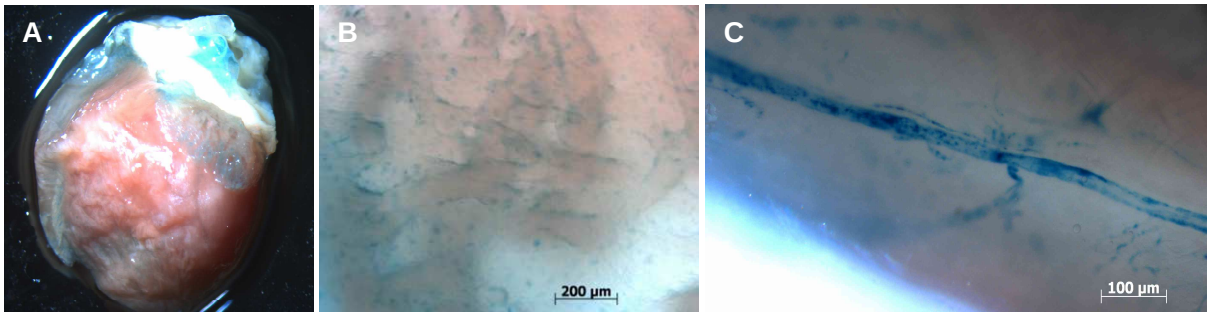

Figure 3.44: X-gal-positive regions in a tamoxifen-treated BMX mouse. Mouse heart after X-gal staining [**A**]. Blue endothelial cells in the heart [**B**] and in the lung [**C**]. Pictures were taken after X-gal staining of whole mount organs. Picture [**A**] was taken with a binocular microscope where no scale was adjusted.

3.3.2 Visualizing endothelial cells in EHT: VE-Cadherin versus BMX EHT

3.3.2.1 Characterization of BMX EHT

Cell suspension of neonatal BMX mice was used for EHT generation. In general, these EHTs served more for investigations of endothelial cells than for contractile analysis in the context of the described *Angioscaff* project (1.8). Human fibrinogen was used for EHT generation, which was purified from serum-derived growth factors. To analyze endothelial cell (EC) distribution, alignment and proliferation in EHT during culture, EHTs were cultured either for 17 or for 30 days. Two days before X-gal staining, Cre expression in EHT was induced by adding *o*-hydroxytamoxifen (1 nM) to the culture medium. After 48 h EHTs underwent a short fixation with fixation solution, washing and subsequent X-gal staining (2.7.1). After 24 h, X-gal-stained EHTs were analyzed with a light microscope, postfixed and embedded in paraffin or used for immunofluorescence analysis. As expected, BMX EHTs showed X-gal-positive ECs scattered within the EHT as seen in blue in Figure 3.45. There were no complete vessel-like structures in the EHT matrix visible. The density of X-gal-positive cells was higher after 30 days than after 17 days of EHT culture on the first view.

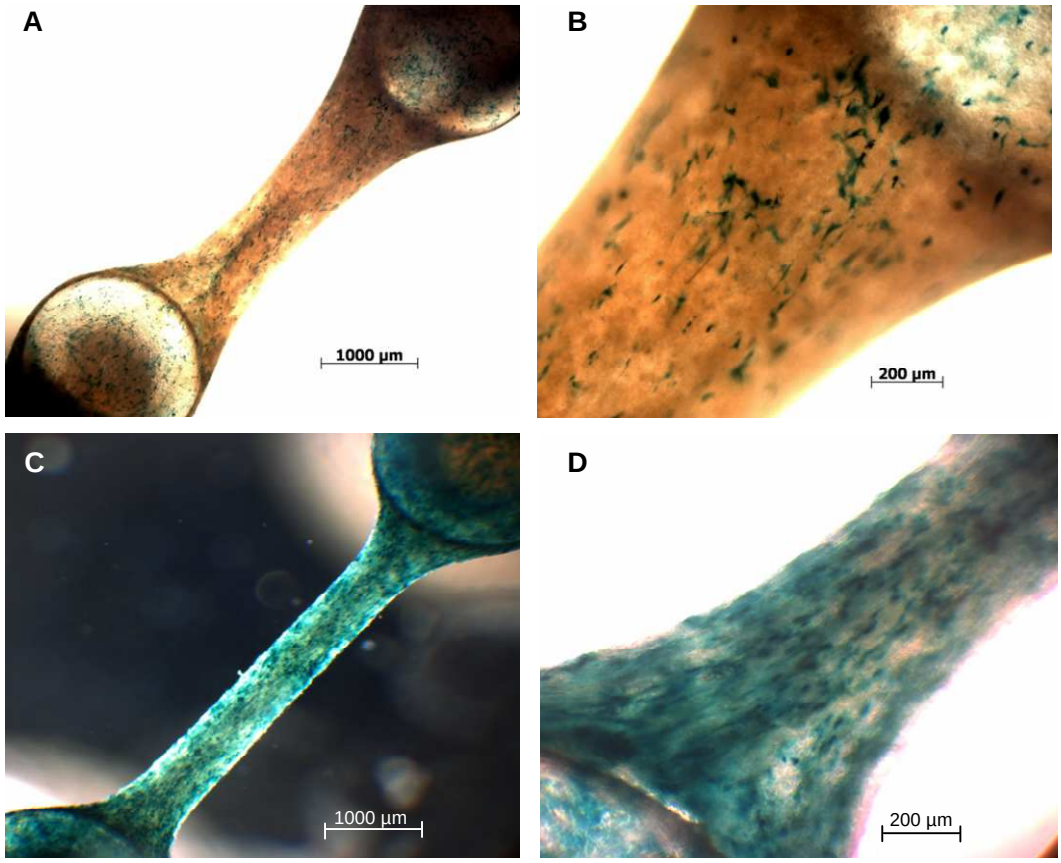

Figure 3.45: Light microscope images of X-gal-stained BMX EHTs. BMX EHTs cultured for 17 [**A** and **B**] or 30 days [**C** and **D**]. Pictures were taken in a 2.5x [**A**; **C**] or in a 10x [**B**; **D**] magnification.

To analyze EC distribution and potential vessel formation, EHTs underwent paraffin-embedding and paraffin sections were investigated histologically. Eosin-stained longitudinal sections of different EHT depths ranging from the surface to the middle part showed that X-gal-positive cells were preferably localized in EHT border zones (Figure 3.46). Immunofluorescence staining was performed of whole mount EHT analysis for β-galactosidase and α-actinin. A homogenous distribution of cardiomyocytes could be detected in BMX EHTs as well as longitudinally orientated and interconnected X-gal-positive ECs.

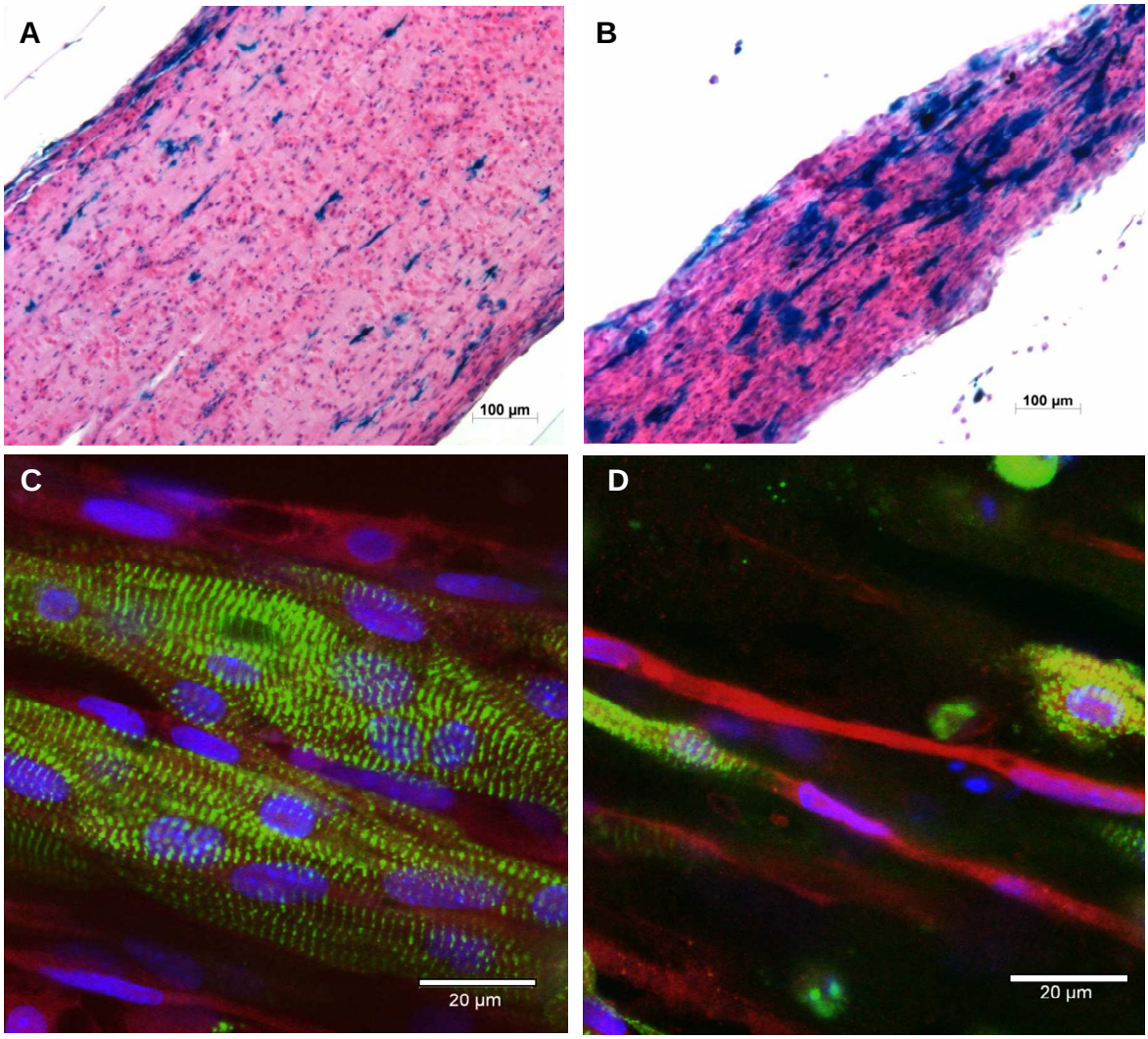

Figure 3.46: Histological and immunofluorescence analyses of BMX EHTs (day 17 of culture). Eosin-stained paraffin section from the inner part of the EHT [**A**] and from the border zone [**B**]. Merged immunofluorescence analysis with staining for β-galactosidase (red), α-actinin (green) and nuclei with DRAQ5 (blue) in BMX EHT [**C** and **D**].

3.3.2.2 Characterization of VE-Cadherin EHT

EHTs were generated from heart cell suspension of neonatal VE-Cadherin mice as described for BMX mice (3.3.2.1) and cultured for up to 18 days. Purified human fibrinogen served for VE-Cadherin EHT generation. On day 15 of culture *o*-hydroxytamoxifen (1 nM) was added for 48 h to the culture medium. EHTs underwent a short fixation (45 s) and subsequent X-gal staining (2.7.1). After 24 h, X-gal-stained EHTs were analyzed via light microscope and post-fixed (30 min). Interestingly, in VE-Cadherin EHTs interconnected ECs

formed a network, as seen in Figure 3.47. This was the first solid evidence for a primitive, longitudinally orientated vessel-like network in 24 well EHTs.

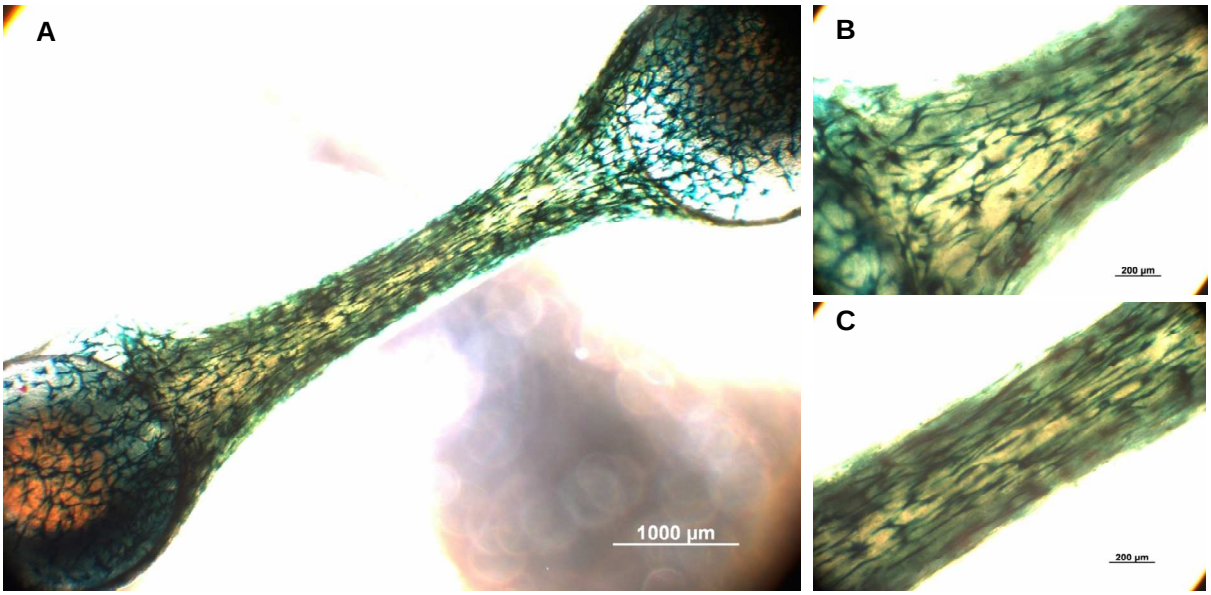

Figure 3.47: Light microscope images of X-gal-stained VE-Cadherin EHTs. VE-Cadherin EHTs were cultured for 18 days. Pictures were taken in a 2.5x [**A**] or in a 10x [**B**; **C**] magnification, depicting the area near the silicone post [**B**] and the middle part of the EHT [**C**].

Interestingly, the vessel-like structure seemed to be dependent on matrix properties. EHTs with a concentration of 3.5 mg/ml human fibrinogen showed less vessel-like structures, especially in the center zone of the EHT, than EHTs with a concentration of 1.5 mg/ml human fibrinogen (Figure 3.48). In contrast, the development of coherent contractions seemed to be better in EHTs with 3.5 mg/ml human fibrinogen (data not shown). This suggests that the best fibrinogen concentration is between 1.5–3.5 mg/ml for the generation of VE-Cadherin EHTs.

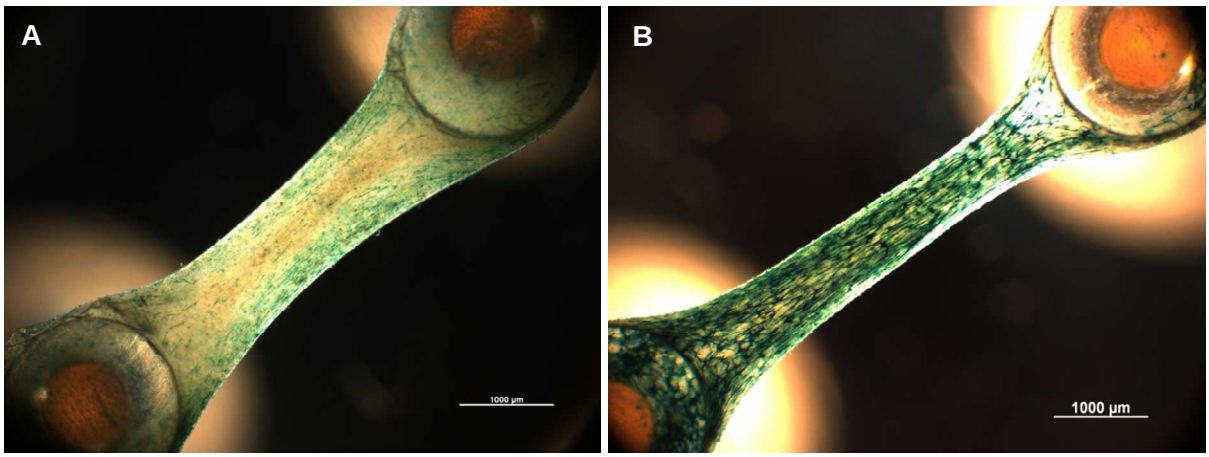

Figure 3.48: VE-Cadherin EHTs after 18 days of culture. Concentration of human fibrinogen was 3.5 mg/ml [**A**] or 1.5 mg/ml [**B**].

In this context, vessel-like network grow and alignment was investigated over time. VE-Cadherin EHTs underwent X-gal staining after 7 or 12 days of culture. Already at day 7 primitive vessel-like and longitudinally orientated cells were scattered in the EHT matrix. At day 12 elongation alignment and density of X-gal-positive cells were superior (Figure 3.49).

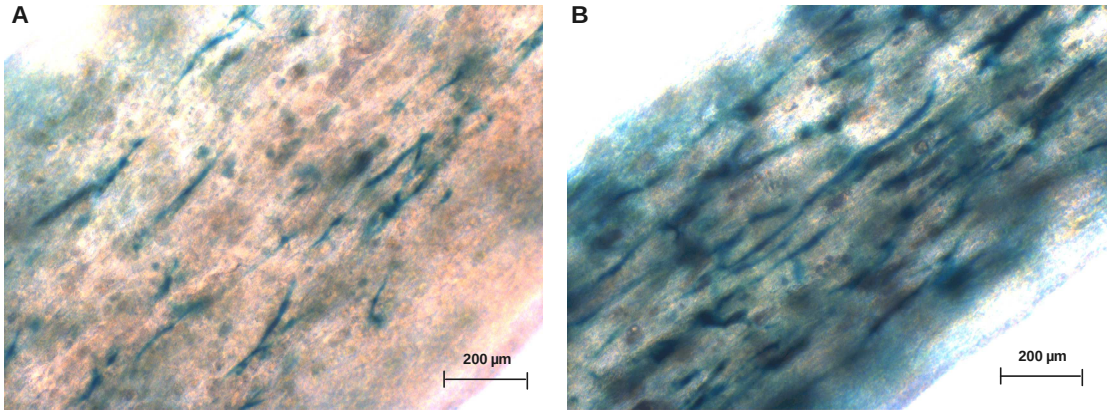

Figure 3.49: X-gal-stained VE-Cadherin EHTs. Light microscopic images (10x magnification) were taken at day 7 [**A**] and at day 12 of culture [**B**].

3.3.2.3 Effect of different oxygen concentrations on endothelial cell density

VE-Cadherin EHTs served for answering the question how oxygen concentration can influence the EC density during culture. EC density was the highest in 21% oxygen. There were no obvious visible differences in EHTs cultured under 21% or 40% of oxygen. In contrast, a reduction of oxygen concentration to 3% led to a reduction in EC density (Figure 3.50). This was unexpected, since low oxygen concentration is considered to enhance EC density through an induction of HIF-1α (1.6). Interestingly, this lack of EC vessel-like network at low oxygen concentration was accompanied by reduced matrix remodeling, suggesting a potential slower maturation of hypoxic EHTs.

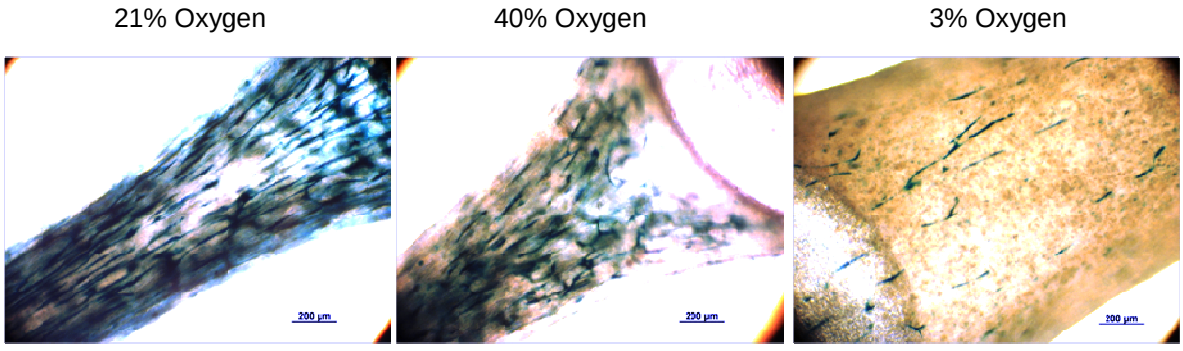

Figure 3.50: X-gal-stained VE-Cadherin EHTs (day 17). Light microscopic images of EHTs cultured at different oxygen concentrations, as indicated in the panel (21, 40 and 3% oxygen).

3.3.3 Quantification of endothelial cells in EHT

To quantify X-gal-stained ECs in EHTs for investigation of angiogenesis-modifying substances such as growth factors, drugs or microRNAs, a special protocol was established. X-gal-stained, post-fixed EHTs were embedded in paraffin and sectioned in 3 levels of depth with a distance of 200 µm, as depicted in Figure 3.51. For every EHT three cross sections were analyzed with the Axiovision Zeiss software either unstained or slightly eosin-stained. These sections were considered as three technical replicates per EHT. Three technical replicates were averaged to generate the biological replicate for the respective EHT. The software recognized blue cell areas and calculated parameters such as blue area in μm^2 and number of blue regions (Figure 3.51). BMX or VE-Cadherin EHTs of different conditions were analyzed and compared to control EHTs of the same batch.

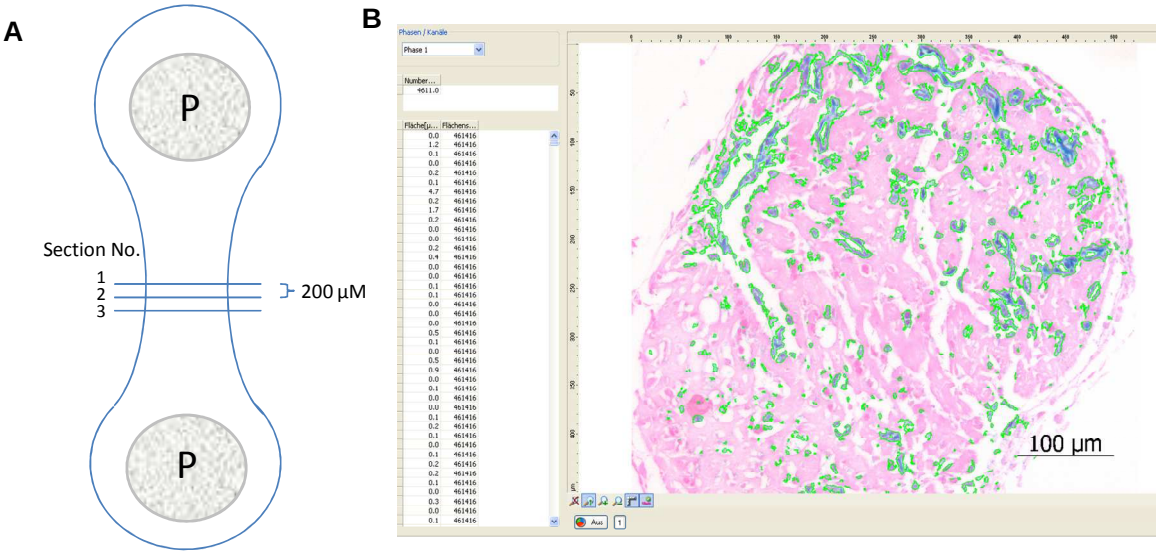

Figure 3.51: EHT section scheme and screenshot of the Axiovision Zeiss software with blue cell quantification of a VE-Cadherin EHT cross section. Modeled EHT shows 3 section levels in a distance of 200 µM each [**A**]. P means silicone post. In this example an eosin-stained paraffin section was used for analysis [**B**]. The green marked areas indicate which areas the software recognized as X-gal-positive.

3.3.3.1 Effect of growth factors on endothelial cell proliferation or migration

Within the European project *Angioscaff* (1.8) the overall goal was to study the influence of growth factors on EC density and the formation of primitive tube-like structures in EHT. It was investigated whether EC density can be modified in the presence of soluble- (1) or matrix-bound (2) proangiogenic growth factors such as VEGF, PDGF and IGF. In short, the following results were obtained:

(1) Soluble growth factors such as VEGF (10 µg/ml), PDGF (10 µg/ml) and IGF (20 ng/ml) did not increase EC density in BMX EHTs cultured in serum-containing medium (10% horse serum, 2% chick embryo extract). Detailed graphs and analysis are shown in the appendix (7.8). In these series EHTs were incubated with AraC according to the established protocol (3.1.3), which could have inhibited EC proliferation.

(2) Matrix-bound growth factors such as TG-PDGF (40 or 4 ng/ml), TG-VEGF (40 or 4 ng/ml) and TG-IGF (31 or 3.1 ng/ml) did not increase EC density in VE-Cadherin EHTs (Figure 3.52). In these experiments EHTs were cultured in the presence of serum (10% horse serum, 2% chick embryo extract) and incubated with AraC (3.1.3). To omit confounding effects of AraC incubation we performed an experiment in the absence of AraC. However, AraC absence did not result in increased EC density in VE-Cadherin EHTs in the presence of TG-VEGF (200 ng/ml).

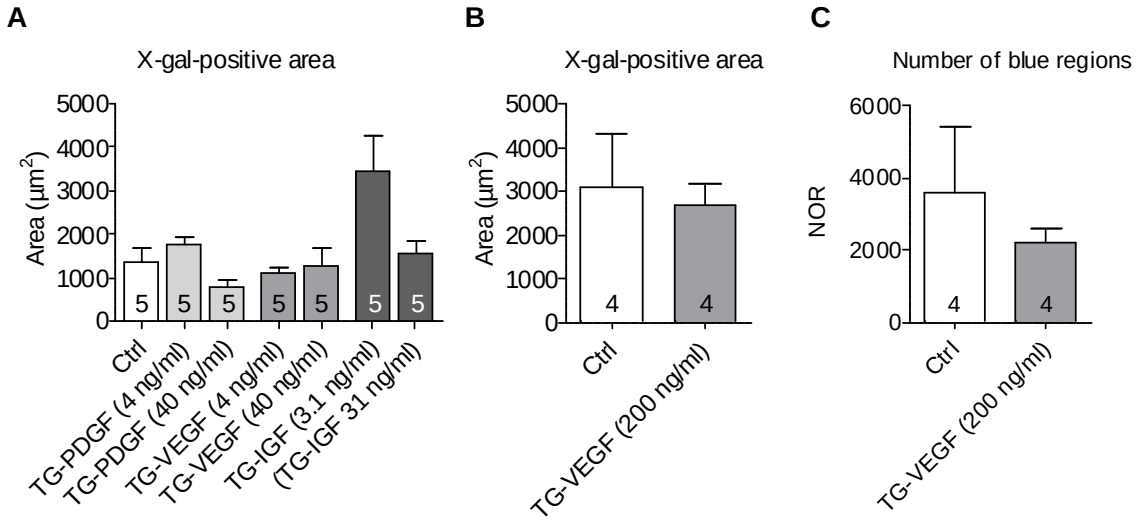

Figure 3.52: Effect of matrix-bound growth factors on endothelial cell density in VE-Cadherin EHTs, measured with the Axiovision Zeiss software. X-gal-positive area, measured in EHT cross sections in the presence of AraC [**A**]. X-gal-positive area [**B**] and number of blue regions [NOR; **C**], measured in EHT cross sections in the absence of AraC.

3.3.3.2 Effect of serum on vessel-like structure in VE-Cadherin EHT

Since no beneficial effect of growth factor application was detected in previous experiments, the influence of growth factors in normal EHT culture medium was investigated, which are present in animal sera such as horse serum and chick embryo extract. Therefore, VE-Cadherin EHTs were cultured either under serum-containing or under serum-free conditions and in all conditions without AraC. Serum-free cultured EHTs revealed a dramatically

reduced EC density as depicted in Figure 3.53, indicating that animal serum contained large amounts of proangiogenic growth factors.

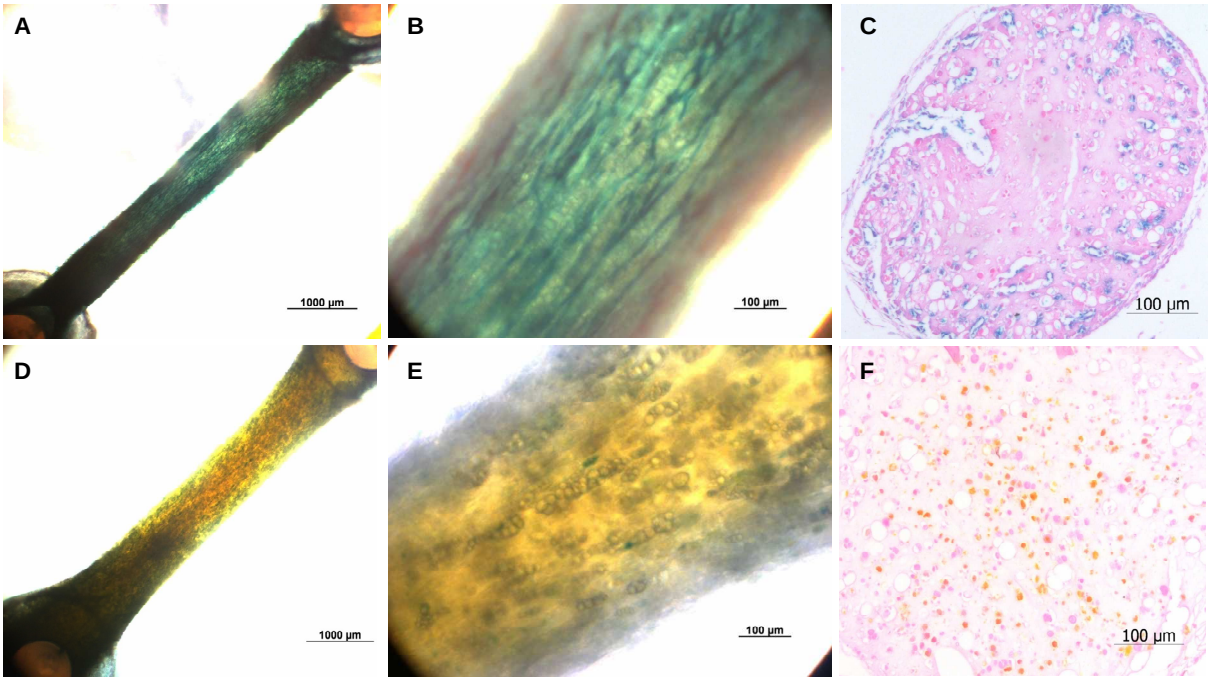

Figure 3.53: Histological analysis of VE-Cadherin EHTs under serum-containing or serum-free conditions. Light microscopic images showed a vessel-like network in serum-containing cultured EHTs [**A** and **B**] and absent vessel-like structures in serum-free cultured EHTs [**D** and **E**]. Eosin-stained paraffin cross sections of serum-containing cultured [**E**] or serum-free cultured VE-Cadherin EHTs [**F**].

In short, serum in the EHT culture medium was essential for a good vessel-like structure in EHT. Next, proangiogenic growth factors were bound in the EHT matrix to rescue the lack of vascularization under serum-free conditions. The low EC density under serum-free conditions could not be increased in the presence of matrix-bound growth factors such as TG-VEGF (100 ng/ml), TG-VEGF plus TG-PDGF (100 ng/ml each) or TG-IGF (3.1 ng/ml; Figure 3.54).

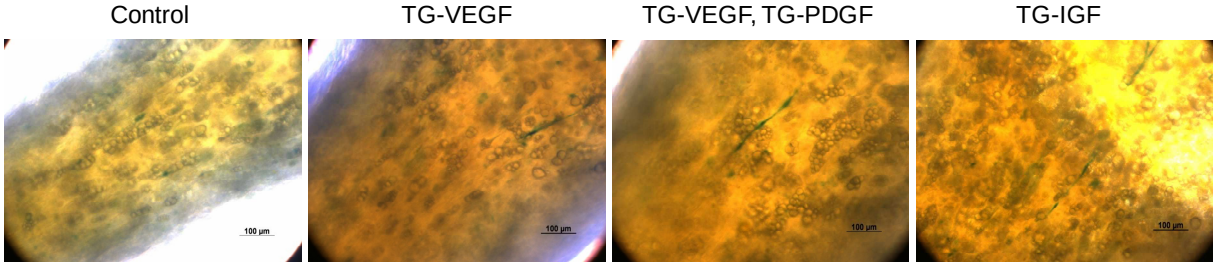

Figure 3.54: Morphological analysis of serum-free cultured VE-Cadherin EHTs. Light microscopic images (10x magnification) of EHTs in the presence of matrix-bound growth factors such as TG-VEGF, TG-VEGF plus TG-PDGF or TG-IGF.

For quantification EHTs were embedded in paraffin, cross sections were generated and analyzed. Serum-free cultured EHTs showed a 1,000-fold reduced EC density in comparison to serum control (Figure 3.55). Matrix-bound growth factors such as TG-VEGF, TG-VEGF plus TG-PDGF or TG-IGF could not significantly enhance EC density under serum-free conditions.

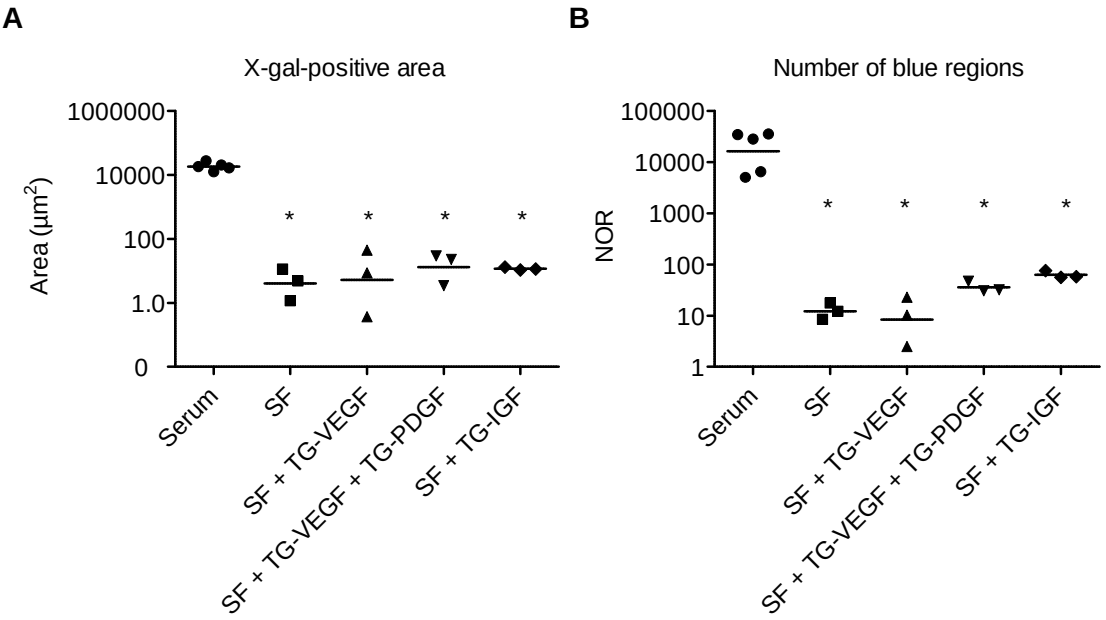

Figure 3.55: Effect of matrix-bound growth factors on endothelial cell density in serum-free (SF) cultured VE-Cadherin EHTs. Axiovision Zeiss software was used for quantification. Identified X-gal-positive area, measured in EHT cross sections [**A**]. Detected number of X-gal-positive regions, measured in EHT cross sections [**B**]. The single dots represent biological samples. **P*<0.001 vs. serum (one-way ANOVA plus Bonferroni posttests).

3.3.3.3 Effect of microRNA-24 on endothelial cell density

MicroRNA-24 has been shown to inhibit EC proliferation (Fiedler et al. 2011). This effect could be confirmed in the VE-Cadherin EHT model. EHTs were transfected directly after casting (day 0; 2.4.8) with pre-microRNA-24 (miR-24) or scrambled pre-microRNA (scr). Prior to this transfection, protocols were optimized using a Cy3-labeled pre-miR (50 nM). EHTs were cultured for up to 15 days and Cre expression was induced on day 13. X-gal staining and morphological analysis were performed via light microscope and the established EC quantification method. A decrease in the X-gal-positive area and in the number of blue regions was observed in the presence of miR-24 (Figure 3.56). Cross sections showed less tube-like structures in miR-24-transfected EHTs than in scr at a concentration of 100 nM.

This was supported by longitudinal histological sections, which also suggested that EC density showed a concentration-dependent defect between 10–100 nM.

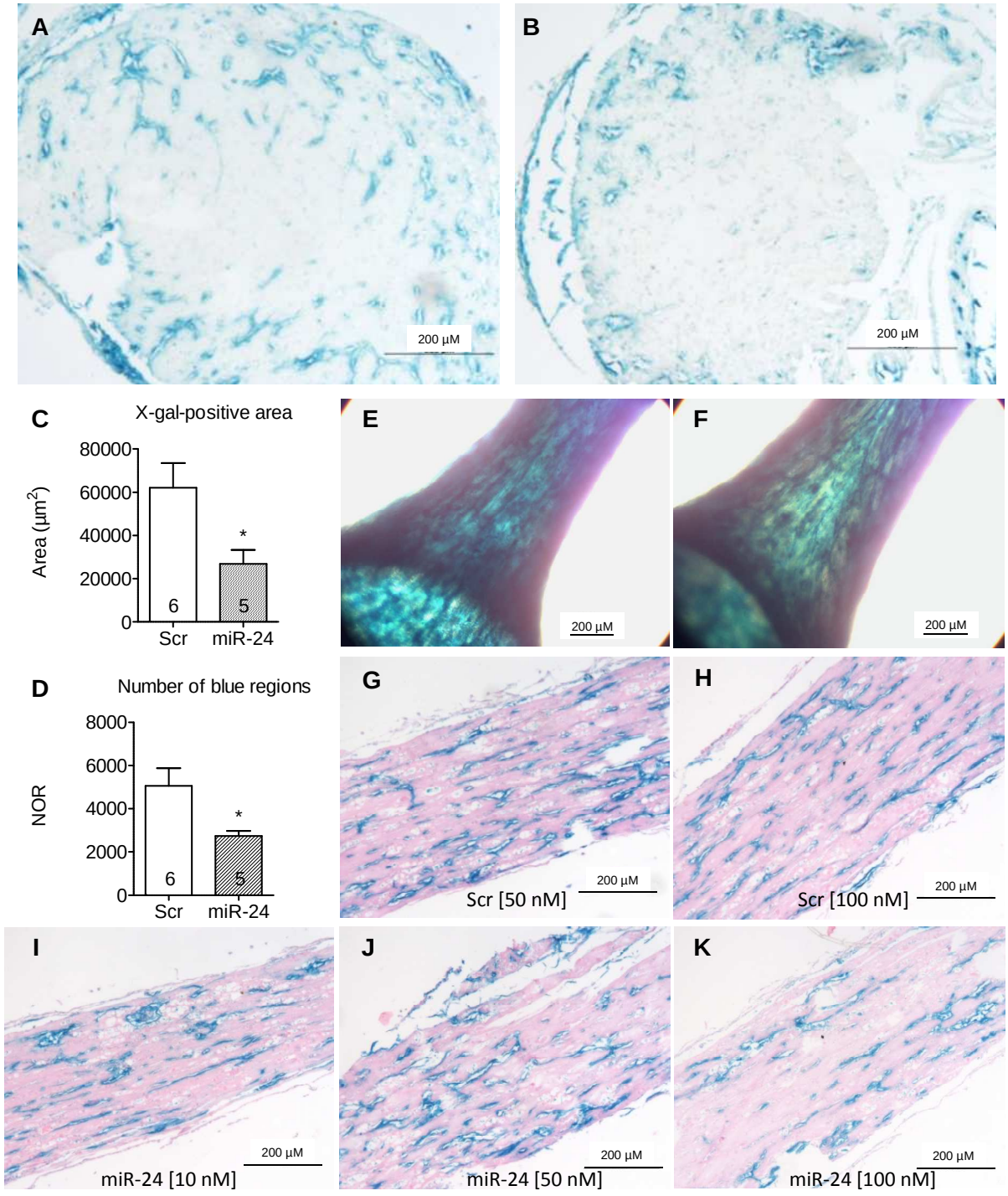

Figure 3.56: Endothelial cell quantification and morphological aspects of miR-24-transfected VE-Cadherin EHTs. Native paraffin cross sections after X-gal staining of control [**A**] and miR-24-transfected EHTs [**B**], 100 nM. Identified X-gal-positive area [**C**] and detected number of X-gal-positive regions, measured in EHT cross sections [**D**]. Light microscopic images of X-gal-stained control (scr) EHT [**E**] and miR-24-transfected EHT [**F**], 100 nM. Eosin-stained longitudinal EHT paraffin sections of miR-scr (50 [**G**] and 100 nM [**H**]) and miR-24 (10 [**I**], 50 [**J**] and 100 [**K**] nM) as indicated in the panels. **P*<0.05 vs. scr (student's t-test).

To confirm transfection efficiency our cooperation partner Jan Fiedler analyzed miR-24 mRNA levels in miR-24-transfected EHTs in comparison to scr-miR-transfected EHTs. The highest miR-24 mRNA level was detected 1 day after transfection (5-fold of the miR-24 mRNA levels in scr EHTs), further decreasing over day 4 (2-fold) up to day 11 (1-fold), indicating that the effect of miR-24 is most pronounced in the first days of EHT culture (data not shown).

3.4 EHT as a graft

To study whether mouse EHTs can serve as grafts and to answer the question whether growth factors can enhance vascularization of EHTs *in vivo* in further studies, WT or VE-Cadherin EHTs were implanted onto the heart or into the dorsal skin of immunodeficient mice (2.6). For these studies either NMRI nu/nu (no T-cells) or Pfp/RAG2 (no B, T- and NK-cells) immunodeficient mice were used, depending on availability.

3.4.1 Implantation of VE-Cadherin EHT into the dorsal skin

To identify angiogenic growth factors *in vivo*, VE-Cadherin EHTs were cultured in the presence of serum (as control) or fibrin-bound growth factors (serum-free conditions) and were subsequently implanted into the dorsal skin of NMRI nu/nu immunocompromised mice. The dorsal skin of the mouse has a dense capillary network, offering the possibility for vessel ingrowth. Before implantation Cre expression was induced *in vitro*. After 4 weeks dorsal mouse skins with EHTs were explanted and analyzed. First, it was challenging to detect the EHTs in the inner skin, which was potentially due to degradation processes *in vivo*. Dorsal skin parts with EHTs were cut and embedded in paraffin for further histological analysis (Figure 3.57). EHTs cultivated in the presence of serum showed clusters of X-gal-positive cells which integrated into host tissue structures suggestive for small vessels, preferably in regions where the needle entered the tissue. In explants with EHTs containing bound growth factors, cultivated in the absence of serum, no similar clusters of X-gal-positive cells were identified.

In conclusion, the inner surface of the dorsal mouse skin is not perfectly suitable for vessel graft analysis, since the histology did not offer a detailed view of vessel growth or formation. Furthermore, growth factor application to serum-free cultured EHTs did not enhance EC proliferation *in vivo*. Thus, EHTs were implanted on the hearts of immunodeficient mice in

further grafting experiments. Nevertheless, this study gave the first hint that ECs tended to concentrate along suture zones.

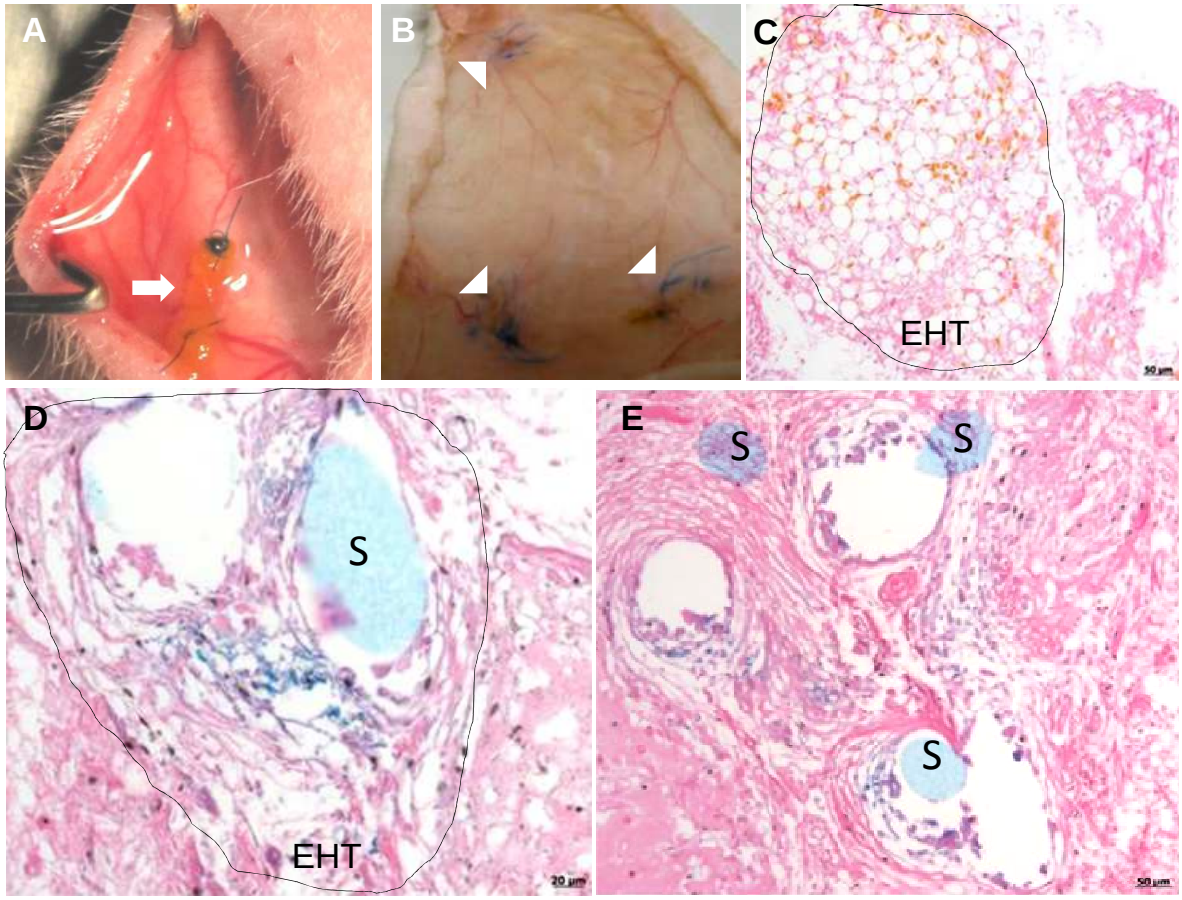

Figure 3.57: Morphological analysis of mouse dorsal skin with VE-Cadherin EHT grafts after 4 weeks *in vivo*. Implantation of EHT into the dorsal skin [**A**]. View on the inner surface of the skin after X-gal staining [**B**]. White arrows indicate EHT. Sutures are visible in blue. Histological sections underwent eosin staining for the following conditions: serum-free [**C**] and serum-containing [**D, E**]. **D:** Upper right corner: suture (S). **E:** 3 Sutures (S) are visible in light blue. NMRI nu/nu immunodeficient mice served for EHT implantation.

3.4.2 Implantation of mouse EHT onto the heart

Mouse cardiac surgery was performed as described in the materials and methods (2.6.2). In a first series of experiments, WT EHTs (C57BL/6J) were implanted onto the left ventricle of NMRI nu/nu mouse hearts. Two weeks later histological analyses were performed. Hematoxylin/eosin-stained longitudinal sections showed the EHT on top of the left ventricle. In the myocardium, eosin staining was more intense than in the EHT, which may be due to lower cell density or less differentiation of cardiomyocytes in the EHT (Figure 3.58). Eosin staining of cells in the EHT region near the myocardium was often more intense than that of cells in the periphery. Furthermore, cells from the EHT seemed to have migrated to the host.

Immunohistochemistry for connexin-43 showed positive areas in the myocardium, in the EHT itself and in the connection zone between EHT and myocardium in brown (Figure 3.58), indicating potential electromechanical coupling.

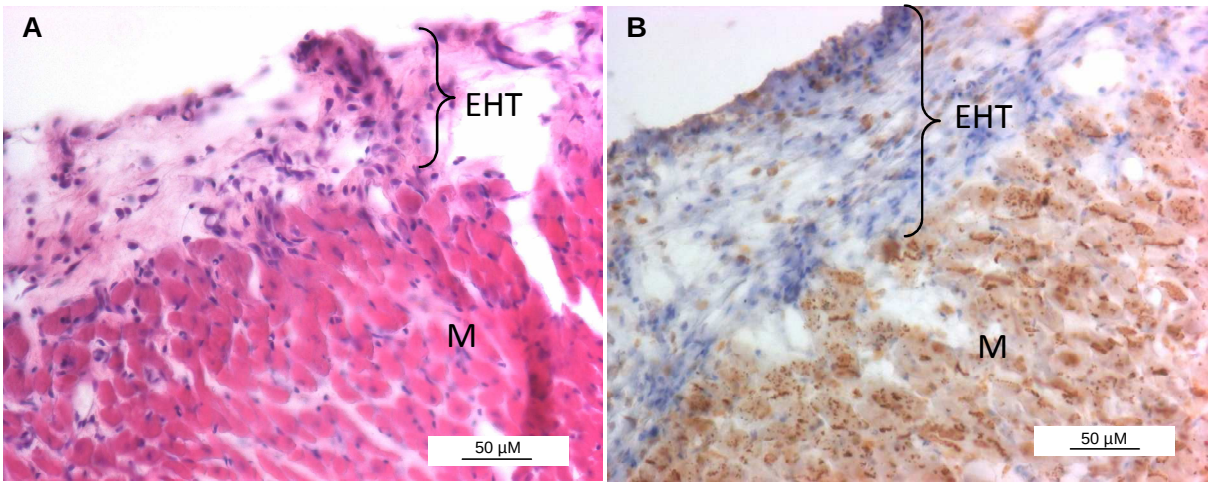

Figure 3.58: Histological analysis of implanted WT EHT on the left ventricle of a mouse heart. Hematoxylin/eosin-stained paraffin sections of the myocardium plus EHT on top [**A**]. M indicates myocardium. Immunohistochemical analysis of [**B**]: Connexin-43 (brown), light blue counterstaining with hematoxylin, showing the EHT on top of the myocardium in a typical shape. Images were taken in a 20x magnification. NMRI nu/nu immunodeficient mice served for EHT implantation.

In series of pilot experiments, mature WT and VE-Cadherin EHTs were implanted (day 26 of culture, serum-containing medium, Cre expression) onto the left ventricle of Pfp/RAG2 mouse hearts. After 2 weeks the hearts were explanted and analyzed macroscopically and microscopically after X-gal staining. Cells derived from the EHT were traced by X-gal staining and covered the whole heart. This suggests that X-gal-positive cells from EHT may have proliferated *in vivo*. Histological analysis revealed that X-gal-positive cells primarily formed a multicellular layer (Figure 3.59). In the heart and in EHT regions many α-actinin-positive cardiomyocytes were detected in immunohistochemical analysis.

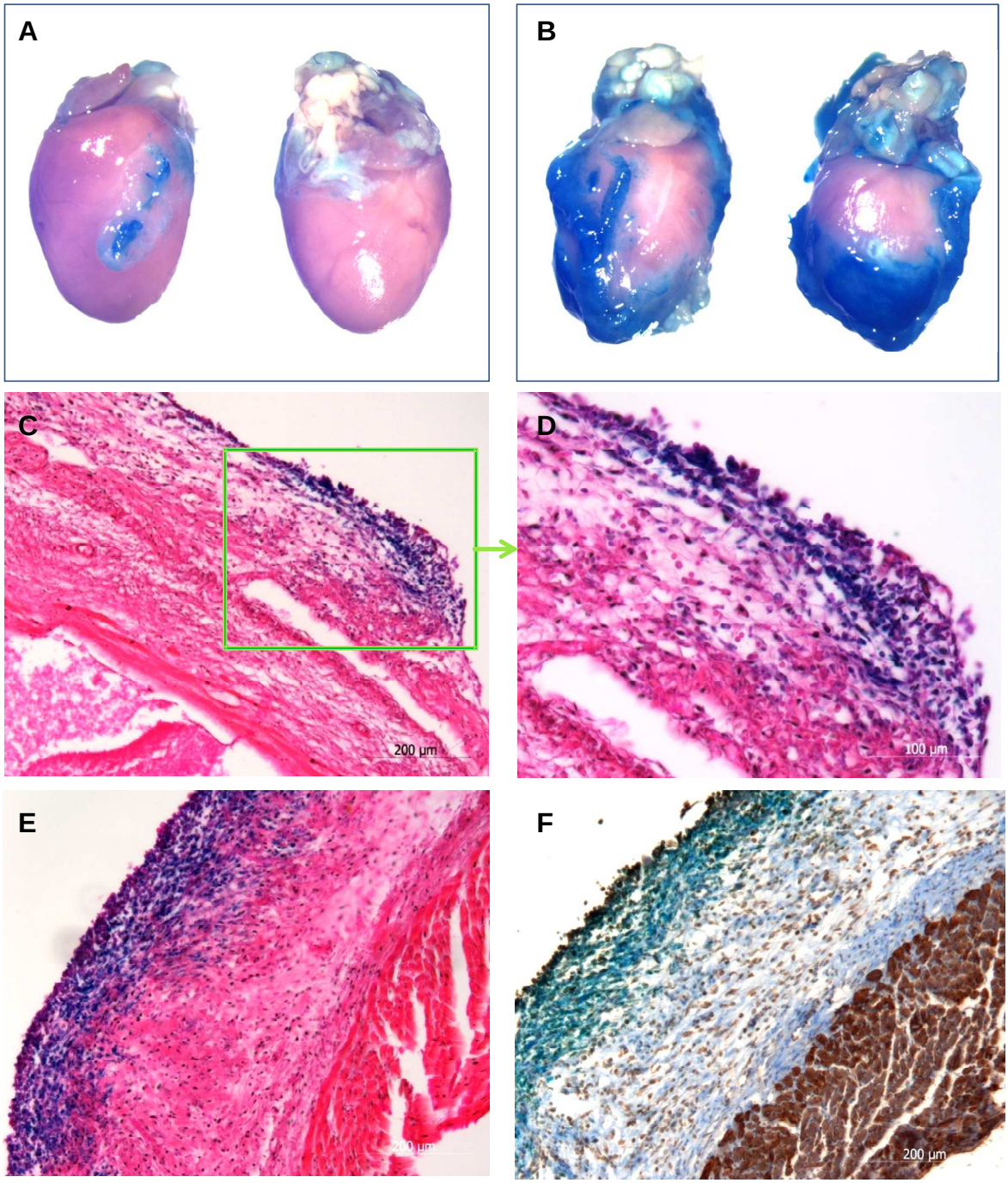

Figure 3.59: Morphological analysis of VE-Cadherin EHT transplanted heart. Whole mount X-gal staining of recipient hearts was performed two weeks after transplantation of wild-type control [**A**] or VE-Cadherin EHT [**B**]. Eosin-stained paraffin sections of heart with VE-Cadherin EHT in a longitudinal view [**C**, **D** and **E**]. Immunohistochemistry for α-actinin (brown) and light blue counterstaining with hematoxylin [**F**].

4 Discussion

Substantial progress has been made in cardiac tissue engineering over the last 15 years. Many studies have been published using 3-dimensional cardiac tissue constructs generated from neonatal rat and chick cardiomyocytes (Eschenhagen et al. 1997; Carrier et al. 1999; Eschenhagen & Zimmermann 2005). Interestingly, in all these years only one paper used neonatal mouse cardiomyocytes as a cell source for cardiac tissue engineering (de Lange et al. 2011). The present study aimed at using neonatal mouse heart cells of different mouse lines for engineered heart tissue (EHT) generation for the following purposes: (1) Establishment of murine fibrin-based mini EHTs with solid contractility and a highly differentiated tissue-like structure. (2) Evaluation if EHT is a format suitable to detect a phenotype of genetically determined cardiac diseases. To answer this question, EHTs from two mouse models of hypertrophic cardiomyopathy were studied. (3) Establishment of a genetic model that allows for the labeling of endothelial cells in EHT to study angiogenesis *in vitro* and *in vivo.*

The principle findings of this study are as follows:

1. Contractile murine fibrin-based mini EHTs could be generated in consideration of some key prerequisites:

    a) A minimum of 20-60 neonatal mouse pups was required for cell isolation.

    b) The ideal age of neonatal mouse pups was between day 0 and day 1 postnatal.

    c) Whole mouse hearts, including both atrial and ventricular cardiomyocytes, were necessary for the generation of contractile EHTs.

    d) Matrigel was beneficial in the EHT mastermix.

    e) ITS+1 or insulin had to be present in the EHT culture medium.

    f) Transient cell-cycle inhibition with AraC was necessary between day 5–day 7

2. Murine EHTs displayed features of intact cardiac muscle, namely a pronounced spontaneous beating activity and positive inotropic responses to external Ca^{2+}, to the Ca^{2+} sensitizing drug EMD 57033 and to isoprenaline. Murine EHTs showed a negative inotropic response to the Ca^{2+} channel blocker verapamil.

3. Cardiomyocytes in murine EHTs developed an interconnected, longitudinally orientated network, which consisted mainly of highly differentiated cardiomyocytes.

4. EHTs generated from two different mouse models of hypertrophic cardiomyopathy (*Mybpc3*-targeted KO and KI mice) reproduced important features observed earlier in these mice and led to the discovery of new aspects. KO and KI EHTs were macroscopically and histologically undistinguishable from WT-derived EHTs, but showed spontaneous hypercontractility, attenuated (KI) or absent (KO) positive inotropic responses to the Ca^{2+}-sensitizing drug EMD 57033 and decreased sensitivity towards the negative inotropic effect of the L-type Ca^{2+}-channel blocker verapamil. KO EHTs exhibited increased sensitivity to external Ca^{2+}. Furthermore contraction and relaxation kinetics were accelerated in both KO and KI. Accordingly, the positive lusitropic effect of isoprenaline was blunted. Quantification of protein and mRNA levels revealed partial activation of the fetal gene program in KO and KI, e.g. overexpression of β-MHC.

5. EHTs generated from VE-Cadherin- or BMX-ER^{T2}-Rosa26-LacZ mice allowed, for the first time, simple and definite labeling of endothelial cells in EHTs and therefore represent a new, versatile angiogenesis model. It showed that endothelial cells in murine EHTs develop extensive vessel-like interconnected vascular structures with lumina.

6. Murine EHTs could serve as grafts for implantation studies *in vivo*.

4.1 Establishment of murine fibrin-based mini EHT

The present study was based on a fibrin-based EHT technology which was recently developed in our institute (Hansen et al. 2010). Fibrin-based mini-EHTs offer a robust, reproducible and simple way to cast and assess EHTs under sterile conditions in a 24-well format with a limited amount of cells. This miniaturized format appeared to be a well suited platform for the use of neonatal mouse cardiomyocytes, since it has been shown in the past that murine circular EHTs based on a collagen I matrix showed comparably few cell-cell contacts and poor cell alignment along the force lines (unpublished data). We therefore hoped that using fibrin as a matrix would improve the generation of force-developing mouse EHTs due to potential differences in matrix properties such as altered stiffness or faster polymerization in comparison to collagen I (Janmey et al. 2009), allowing for a more homogenous cell distribution in the construct.

4.1.1 Mouse matings and neonatal pups

One of the most important requirements for the successful generation of murine EHTs was the good organization of mouse matings to ensure a sufficient birth rate of pups. To reach a pup number between 20–60, 8–18 mouse matings (one male and two females) were started in parallel. It took approximately 6–12 months in small mouse lines (<15 adult mice) to recruit enough mice for matings, and storing spaces of mating cages in the animal facility were limited. A synchronous start of mouse matings was of extreme importance to ensure birth of pups in a range of 2 days, since pups were only suitable for EHT generation between day 0–1 postnatal. This required fast decisions and extreme flexibility of all persons who were involved in cell isolation and EHT generation. The young age was necessary in order to obtain coherently, spontaneously beating mouse EHTs. These observations were confirmed by recent findings from another group, developing engineered cardiac tissues (ECTs) from neonatal mouse heart cells (de Lange et al. 2011).

4.1.2 Cell population and concentration

Murine EHTs were generated from unpurified neonatal mouse heart cells. Entire hearts were harvested for digestion, which resulted in a mixture of various subtypes of cells such as both atrial and ventricular cardiomyocytes, cells from sinus nodes and the conduction system as well as non-cardiomyocytes such as fibroblasts, endothelial cells and smooth muscle cells. These cell types maintain the electrical, chemical, and biomechanical nature of the heart as well as the three-dimensional structure via autocrine, paracrine, and cell-cell interactions (Katz & Katz 1989). The mixture of cells was of particular importance for sufficient force development and regular maturation of murine EHTs. In this respect the presence of both ventricular and atrial cardiomyocytes also turned out to be beneficial. Murine EHTs generated only from ventricular cardiomyocytes did not develop coherent contractions (data not shown). One reason may be that atrial cardiomyocytes have a higher spontaneous beating activity and act as *in vitro* pacemakers in EHTs.

In an artificial *in vitro* environment, cardiomyocytes from heart cell mixtures are rapidly overgrown by proliferating fibroblasts, smooth muscle cells and endothelial cells. To decrease the fraction of non-cardiomyocytes, cell suspensions are normally preplated (45–75 min) under cell culturing conditions. During preplating, non-cardiomyocytes quickly attach to the bottom of a culture dish while cardiomyocytes preferably stay in the supernatant (Blondel et al. 1971). Preplating technology can yield up to 97% of cardiomyocytes in the cell suspension (Brooks et al. 1997). However, murine EHTs generated from preplated cell

suspensions did not develop coherent contractions. One reason might be that fibroblasts have been shown to secrete growth factors such as PDGF, TNF-α, FGF or TGF-β (Long et al. 1991), which could facilitate cardiomyocyte survival and growth and thereby act as important players for the maturation of murine EHTs.

Another important issue was the final cell concentration in murine EHTs. The optimal cell concentration in murine EHTs was higher than in EHTs from rat hearts ($0.68x10^6$/100 µl versus $0.41x10^6$/100 µl, respectively). A cell concentration below $0.68x10^6$/100 µl resulted in a lack of coherent force development and in cell death. Cell concentrations above $0.68x10^6$/100 µl resulted in an early onset of post deflection but also in an early stagnation of coherent contractions. This may be due to a high number of non-cardiomyocytes which overgrow the cardiomyocytes, thereby increasing the stiffness of the matrix. At $0.68x10^6$/100 µl murine EHTs showed a high density of longitudinally orientated cell bundles as discussed below.

In almost all EHT regions non-vital cells were detected. Indeed, measurements of DNA content showed that only ~40% of the cells survived a culture period of 20 days in the EHT matrix. Reasons for cell death could be enzymatic overdigestion during cell isolation or cell death in the matrix due to shortage of oxygen or nutritive supply. The latter hypothesis is supported by the observation that cell concentrations were higher and muscle-like cell bundles were preferably localized at the lateral free edges of the EHT.

4.1.3 Murine EHT culture

The addition of Matrigel to the cell mastermix proved to be of likewise importance for the constitution of contractile murine EHTs, as was previously described for rat EHTs (Zimmermann et al. 2000; Hansen et al. 2010). It has been shown that the formation of spontaneously and coherently beating rat EHTs was dependent on Matrigel and was further improved by adding chick embryo extract (Zimmermannet al. 2000). Matrigel is a commercially available biological product extracted from the extracellular matrix of the murine Engelbreth-Holm-Swarm tumor. It consists of basal membrane fragments such as collagen and proteoglycans, a mixture of different growth factors and glycoproteins such as laminin and entactin. These compounds could provide a physiological environment necessary for matrix formation and stimulate growth and differentiation. Extracellular matrix-based 3D cell cultures allow for a higher degree of differentiation than cultures on plastic or glass dishes. Soluble compounds in Matrigel are most likely growth factors, which can

influence the degree of differentiation or cell survival. According to the information of the manufacturing company (Becton Dickinson) Matrigel contains growth factors such as EGF, PDGF, IGF-1 and TGF-β. The beneficial effect of Matrigel on murine cardiomyocytes could either result from the combination of all factors or from one or two key factors. It has been shown that IGF-1 had a cytoprotective effect on cardiomyocytes by promoting survival under conditions of serum deprivation in a dose-dependent manner (Fujio et al. 2000). TGF-β is known to be a powerful and essential immune regulator, capable of modulating inflammatory events. It promotes or inhibits cell proliferation and induces fibrotic processes and extracellular matrix production in numerous cell types (Rosenkranz et al. 2002). Furthermore, mice overexpressing TGF-β developed cardiac hypertrophy, suggesting that TGF-β can increase the size of cultured cardiomyocytes. Increased cell size imposing rather pathological on the first view, could potentially promote the development of cell-cell contacts in a three-dimensional matrix and thereby lead to an improved tissue-like structure. However, this speculation has not been proven yet. An additional source of growth factors are animal sera such as horse serum and chick embryo extract. Culture under serum-containing conditions is known to induce cardiomyocyte hypertrophy (Simpson et al. 1982).

Murine cardiomyocytes in fibrin-based EHT format were cultured under continuous stretch which was induced by silicone posts and led to an alignment of cells along the force lines. Former studies examined the influence of chronic stretch on the functional behavior of cardiomyocytes either in 2D or in 3D culture (Fink et al. 2000; Frank et al. 2008). In both systems stretch induced cardiomyocyte hypertrophy. Additionally, stretched EHTs exhibited improved organization of cardiomyocytes into parallel arrays of rod-shaped cells, increased cell length and width, longer myofilaments, and increased mitochondrial density (Fink et al. 2000). The main finding of this study was that stretch of EHTs induced cardiomyocyte hypertrophy, which was accompanied by a marked improvement of contractile function. In this regard, murine EHTs are similar to the previously developed fibrin-based EHT model in which rat cardiomyocytes were also cultured under auxotonic stretch (Hansen et al. 2010). Insulin, which was also present in the EHT culture medium, activates a variety of metabolic and anabolic pathways in cardiomyocytes and is known to prevent apoptosis by activation of PI3K (Aikawa et al. 2000; Lv et al. 2011). Similar to IGF-1, insulin binds to the insulin-like growth factor receptor and is thereby inducing myocyte hypertrophy.

Transient cell-cycle inhibition with AraC was performed in murine EHTs to prevent an overgrowth by non-cardiomyocytes between day 5–7 of culture. This method was successful for the establishment of collagen-based murine EHTs several years ago (unpublished data). 2D cultures of murine cardiomyocytes exhibited 40-65% less fibroblasts in the presence of

AraC than without cell-cycle inhibition (Ollinger & Brunmark 1994). However, the presence of AraC in the culture medium on day 0 resulted in an inhibition of coherent EHT contraction (data not shown). To avoid cardiotoxic effects EHTs were incubated with AraC for 48 hours beginning on day 5. Under these conditions murine EHTs were coherently contracting until approximately day 30. A second treatment with AraC later in culture (day 12–14) was not beneficial (data not shown).

4.2 Histological and physiological characterization of murine EHT

Histological analyses of murine EHTs showed a well developed tissue-like structure. Cells were evenly distributed in the matrix, which was probably caused by the fast polymerization of fibrinogen and a homogenous EHT mastermix. Hematoxylin/eosin-stained longitudinal sections showed a dense, longitudinally orientated cell network. Immunofluorescence analysis confirmed that longitudinally oriented cell bundles were mainly composed of α-actinin-positive cardiomyocytes, which could be detected throughout the EHT. Cardiomyocytes were also characterized by connexin-43 positive gap junctions on the cell membrane in immunofluorescence analysis. Connexin-43 positive structures were detected between the α-actinin positive cell bundles (data not shown), suggesting electromechanical connection between the cardiomyocytes. The fibrin matrix was remodelled over time, macroscopically visible as a reduction in width and thickness compared to the rectangular cell-fibrin block directly after casting. Final dimensions were approximately 0.9x3.8 mm. Fibrin remodelling and degradation were likely caused by enzymes such as metalloproteinases (MMP-2, MMP-3) and plasmin (Ahmed et al. 2007).

The maximally developed force of EHTs is generally lower than that of myocardial tissue. Murine EHTs with a minimal diameter of 0.2 mm under cell culture conditions in video-optical analysis only reached up to 0.12 mN (3.8 mN/mm^2). This is low in comparison to forces developed by murine papillary muscle. Murine papillary muscles reach between 5-40 mN/mm^2, human papillary muscles reach between 44-56 mN/mm^2 (Hasenfuss et al. 1991). Rat fibrin-based mini EHTs with a minimal diameter of 0.2 mm under cell culture conditions in video-optical recording analysis reached up to 0.3 mN (9.5 mN/mm^2) and even up to 0.9 mN (28.7 mN/mm^2) under maximal preload and isometric conditions (Hansen et al. 2010). Under isometric conditions, EHTs were stretched up to the length of the maximal force development, according to the law of Frank-Starling (for review see de Tombe et al. 2010). The calculated force values under cell culture conditions may be attributable to a systematic error but are more likely attributable to the absence of electrical pacing and preload

optimization. We could not measure the force of murine EHTs with standard force transducers and optimal preload and isometric conditions because of size limitations. Thus, 'real' force development could be higher than the calculated values, but values are certainly lower than in rat EHTs and much lower than in native murine heart muscle preparations. Force of fibrin-based murine EHTs could be optimized (1) by reducing the construct diameter and matrix fraction, (2) increasing the number and density of the cardiomyocyte fraction or (3) better maturation of cardiac myocytes, i.e. thicker, higher-force-generating myocytes. It is also possible that the large amount of non-cardiomyocytes in the EHT matrix has to be reduced since they increase EHT stiffness and resting tension.

4.3 Murine EHT for modeling HCM

Mouse EHT technology was used to address the question whether the complex phenotype of an inherited cardiomyopathy can be modeled in EHTs and whether this approach provides new insights into the pathogenesis of the disease. Two mouse models of HCM were selected, namely *Mybpc3*-targeted KO and KI mice. *Mybpc3*-targeted KO mice were introduced in 2004 and developed asymmetric septal hypertrophy associated with fibrosis in the heterozygous state, which is a phenotypic key feature of HCM (Carrier et al. 2004). Homozygous KO mice developed eccentric left ventricular hypertrophy with decreased fractional shortening at 3-4 months of age and markedly impaired relaxation after 9 months. This was associated with myocardial disarray and interstitial fibrosis. Isolated cells from KO exhibited lower diastolic sarcomere length, indicating residual actin-myosin interaction in diastole (Pohlmann et al. 2007). Isolated KO left atria exhibited a marked increase in sensitivity to external Ca^{2+}. *Mybpc3*-targeted KI mice, carrying a point mutation which is associated with a severe phenotype in humans, exhibited myocyte and left ventricular hypertrophy, reduced fractional shortening, and interstitial fibrosis, but only in the homozygous state (Vignier et al. 2009). In homozygous KI mice higher myofilament Ca^{2+} sensitivity in skinned ventricular trabeculae was described. Heterozygous KI mice showed no major phenotype *in vivo*, despite increased myofilament Ca^{2+} sensitivity *in vitro* (Fraysse et al. 2012). In this study, homozygous neonatal mice of both lines served for EHT generation. Cell concentrations in WT, KO and KI EHTs were similar. Cardiac cells from both disease models generated spontaneously beating, force-developing EHTs that were macroscopically and histologically undistinguishable from WT-derived EHTs.

4.3.1 Contractile analysis under standard culture conditions

Video-optical recording was used to analyze spontaneous contractility of fibrin-based murine EHTs. This technique had been developed prior to this study in our group and turned out to be simple, robust and time-efficient (Hansen et al. 2010). Murine EHTs in large series could be repetitively measured under cell culture conditions. Monitoring of EHTs was performed during the whole culturing period and effects of maturation on contractile parameters could be studied. Since force decreased in murine fibrin-based EHTs between day 14–21 of culture, contractile parameters of disease-specific EHTs were mainly evaluated on day 14. Between day 14–20 unsterile measurements under electrical stimulation and perfusion were performed and EHTs were frozen for further analysis. This protocol was newly developed and turned out to be reproducible and reliable. The custom software, developed for video-optical recording, was capable to automatically recognize the silicone posts using a contour-recognition algorithm. This helped to precisely adjust the optimal position of the EHT for measurement. Video-optical evaluation of contractile force superseded the manual transfer and force evaluation of EHTs under non-standardized and non-sterile conditions and allowed for simple repeated measurements.

Compared to WT, KO and KI EHTs showed higher spontaneous force development and attenuated (KI) or absent (KO) positive inotropic responses to the Ca^{2+}-sensitizing drug EMD 57033. KI showed spontaneous dramatic prolongations of relaxation in 15% of the cases, which was not seen in the other genotypes. These first results indicated that EHTs might be useful to model a disease *in vitro* and that phenotypic differences can be detected. Indeed, hypercontractility is a common phenotype in patients with HCM, despite the fact that some patients develop severe systolic dysfunction, dilatation and heart failure late in life (Olivotto et al. 2010). In fact, an early hypothesis on the pathogenesis of HCM suggested a hyperactive sympathetic nervous system as a cause of HCM, because the main features recognized clinically were hyperdynamic left ventricular contraction, reduced coronary flow reserve, a propensity for ventricular and atrial arrhythmias, and amelioration of symptoms by β-adrenoceptor blocking agents (Laks & Morady 1976). Hypercontractility was also observed in cardiac muscle fibers in which cMyBP-C was extracted by chemical means (Kunst et al. 2000) and in young homozygous cMyBP-C KO (Cazorla et al. 2006; Carrier et al. 2004). In this case as well as in KO and KI EHTs, hypercontractility could have been caused simply by higher cardiac muscle mass. Several results argue against this idea. On day 0, KO and KI mouse hearts do not overexpress hypertrophic markers. The higher total RNA concentrations in day 0 EHTs indicate induction of hypertrophy, but not its establishment. Histological analyses did not show apparent evidence of cardiomyocyte hypertrophy in KO or KI.

Dystrophin staining of cell membranes should be done in future experiments to assess myocyte size in a more quantitative manner. Furthermore, KO showed complete, KI partial absence of positive inotropic responses to EMD 57033, arguing for a qualitative change of myocyte function rather than a quantitative difference in muscle mass. KI mouse hearts, though hypertrophic and hypocontractile under basal conditions, also lacked a response to EMD (data not shown). These data suggest that the phenotypes seen in *Mybpc3*-targeted KO and KI EHTs as well as in the according respective mice, rather than being secondary to myocyte hypertrophy, are the direct consequence of the primary defect in myofilament function. Increased myofilament Ca^{2+} sensitivity has been demonstrated earlier (Pohlmann et al. 2007; Fraysse et al. 2012; Cazorla et al. 2006) and could well explain higher force generation and higher ATPase activity under unstimulated conditions. How this primary abnormality leads to the anatomic features of HCM (hypertrophy, myofibre disarray, fibrosis) remains unknown. But recent data suggest that increased Ca^{2+} sensitivity could be a direct cause for arrhythmias by altering the Ca^{2+}-buffering capacity of the myofilament compartment of the cell (Schober et al. 2012). An increase in the cytosolic Ca^{2+} binding activity results in increased end-diastolic Ca^{2+} and enhanced sarcomplasmatic reticulum Ca^{2+} content and release after pauses, and action potential prolongation, thus provoking arrhythmias. The fact that we observed spontaneous tetanic contractions only in KI, but not in KO or WT EHTs suggest, however, that factors specific for the KI model are responsible. This could be the expression of mutant cMyBP-C proteins (Vignier et al. 2009).

4.3.2 Measurements under electrical stimulation and perfusion

Force of contraction in heart muscle depends on beating rate (force-frequency relationship), which, in EHTs, varied under spontaneous beating conditions. Measurements under continuous electrical pacing and perfusion showed that in a range of 1 up to 9 Hz, the force of fibrin-based murine EHTs decreased with increasing pacing frequencies. Specifically, force remained more or less stable between 0.5 and 4 Hz and decreased above these values. This finding is in line with some studies on small rodents (Bers 2000), but not with others, showing a positive force-frequency relationship in rat myocardium under physiological conditions (Janssen et al. 2002). Rabbit and human heart muscle preparations show a positive force-frequency relationship (Pieske et al. 1995; Maier et al. 2000). Explanations for these differences include higher SR Ca^{2+}-load (and lower intracellular Na^{+} concentrations) in rabbits and humans with increasing frequencies. During a shorter relaxation phase less Ca^{2+} would be extruded via the NCX, inducing a Ca^{2+} overload of the SR along with higher SERCA activity. In mice the NCX contributes relatively little to the Ca^{2+} decline during the

repolarization phase (Bers 2000). Therefore a potentially decreased SR Ca^{2+}-load may play only a minor role in the negative force-frequency relationship in rodents (Bluhm et al. 2000). Interestingly, there is a study showing that the force-frequency relationship in mouse papillary muscle varies with differences in temperature and in extracellular Ca^{2+}. At low temperature and low Ca^{2+} the force-frequency relation was strongly positive whereas at high temperature and high Ca^{2+} it turned negative (Redel et al. 2002). Force-frequency relation of murine EHTs was measured at 37 °C (1.8 mM Ca^{2+}). We weren't yet able to investigate whether the negative relation could be 'cured' simply by decreasing the temperature. In contrast, another study showed that the force-frequency relationship measured in ultrathin rat cardiac trabeculae was slightly negative at 22.5 °C, but became clearly positive at 37.5 °C (Janssen et al. 2002). Interestingly, the group showed that the frequency optimum for electrical stimulation decreases with increasing muscle thickness. At high frequencies, diffusion of nutrients and oxygen on one hand, and removal metabolites like phosphate on the other hand, can become limiting for muscle function. This would indicate that generation of contractile force at high frequencies may be hampered at diffusion distances exceeding ~75 µm, as it is the case for fibrin-based EHTs with a diameter of ~1 mm. The use of thinner fibrin-based mini EHTs could be beneficial to overcome diffusion limitations that may distort contraction in thicker muscles under physiologically meaningful conditions.

Interestingly, KO EHTs showed higher force than WT or KI at a high pacing frequency of 9 Hz. At 9 Hz, which reflects the situation *in vivo*, KO EHTs showed higher velocity of contraction than WT. This argues for the fact that increased contraction velocity and a higher level of actin-myosin interaction is caused by the ablation of cMyBP-C, which causes higher forces, even at high frequencies. Mutated full-length cMyBP-C in KI EHTs or other mutants seem to take over the regulatory function of cMyBP-C under these conditions. In general, it is hypothesized that the diversity in KI EHTs could be due to incorporation of different mutants (truncated, mutated and frame-shift) into the sarcomeric organization (Vignier et al. 2009), which could potentially modulate the contractile response depending on which mutants dominate in the measured EHT. Under physiological conditions, a mouse heart is contracting at a frequency of 600 beats per minute (10 Hz). Murine EHTs could hardly be paced with a frequency of 10 Hz since this resulted in a failure of capture, strong arrhythmia development and diminished force values. Therefore the pacing frequency was adjusted to 5-6 Hz for most experiments, allowing sufficient contraction amplitude and no arrhythmia development, even at low external Ca^{2+} concentrations (0.2 mM).

An interesting novel finding in the EHT model was the abbreviation of basal twitch kinetics. At 6 Hz early and late contraction times (T1 50% and T1 90%) and the early phase of relaxation

were shorter in KO and KI than in WT. This indicates that the absence of cMyBP-C or the expression of a full-length mutant cMyBP-C at a low level in EHT resulted in accelerated contractile kinetics without compromising twitch force amplitude. These results were well compatible with results from another group, where cMyBP-C-null ECTs exhibited characteristic acceleration of contraction kinetics (de Lange et al. 2011). In their model, ECTs are measured under mechanical loading for which they are stretched to the original (spacer) length. This length, determining resting tension ("preload"), is increased stepwise until no further increase or a decrease in twitch amplitude is seen, according to the mechanism of Frank-Starling. In their following experiments the length of the construct is fixed and the tension is variable, resulting in isometric contraction. In contrast, we performed measurements under auxotonic conditions, meaning that muscle length and tension are changing simultaneously but obtained similar results. Taken together, the altered kinetics in KO and KI seem to be an important phenotype, which is seen independently of the method of force measurement.

4.3.2.1 The effect of Ca^{2+} and pharmacological provocation tests

Since it had been shown previously in our institute that in mouse left atria the sensitivity to external Ca^{2+} was increased in KO compared to WT (Pohlmann et al. 2007), we tested the effect of different external Ca^{2+} concentrations in order to explore in more depth the role of Ca^{2+} in HCM and to test potential therapeutic options. The following results were obtained: (I) KO EHTs exhibited increased sensitivity to external Ca^{2+} concentrations. (II) KO and KI EHTs showed a lack or attenuated response to the Ca^{2+} sensitizer EMD 57033. (III) Both KO and KI EHTs showed decreased sensitivity towards the negative inotropic effect of the L-type Ca^{2+} channel blocker verapamil.

(I) KO EHTs developed higher force of contraction at low external Ca^{2+} concentrations (0.2-0.6 mM) in comparison to WT. This phenotype underlined the theory of myofilament hypersensitivity in KO (Pohlmann et al. 2007). The higher force at low Ca^{2+} concentrations in KO was accompanied by high contraction and relaxation velocities (data not shown). This argued for faster cross-bridge formation under cMyBP-C ablation, which has already been shown in older studies in rabbit skeletal muscle fibers at low Ca^{2+} levels (Hofmann et al. 1991) or in murine skinned myocardium (Stelzer et al. 2006).

(II) A novel finding was the complete loss of positive inotropic effects of a Ca^{2+} sensitizer. The absence of the EMD-effect in KO could theoretically indicate that the drug, of which the

mechanism of action is not clearly established, needs cMyBP-C as a target. However, this possibility could be ruled out since EMD markedly prolonged contraction and relaxation times not only in WT and KI, but also in KO. This prolongation was observed mainly in spontaneous recordings, since in measurements under electrical stimulation the EHTs were 'forced' to contract again, even if they were still in the relaxation phase. Moreover, EMD also increased force of contraction in KO in the presence of a concentration matching the IC_{50} of the myosin-actin inhibitor blebbistatin, which decreased force by approximately 40% in KO. These data suggest that the lack of EMD sensitivity in KO simply reflects the already maximally activated myofilaments at an external Ca^{2+} concentration (0.6 mM) which, in WT and KI, induces only ~70% of maximal force generation. This would underline the theory of an increased Ca^{2+} sensitivity in KO, and to a lesser extent in KI as well. Interestingly, the lack of EMD response in KO was independent of EHT age. Neither 14-day-old nor 33-day-old KO EHTs showed a positive inotropic response to EMD under different external Ca^{2+} concentrations (0.6 and 1.8 mM), which argues for an age-independent phenomenon. Furthermore, EMD had no inotropic effect in homozygous KI mice *in vivo*. KI exhibit a dilated and hypocontractile heart when investigated by transthoraric echocardiography (data not shown, Felix Friedrich and Frederik Flenner). This state of KI mice is similar to late stages of HCM in patients (with most frequently heterozygous sarcomeric gene mutations), when longstanding severe hypertrophy, small ventricular cavity and diastolic dysfunction passed the transition to a dilated phenotype with systolic dysfunction and low output failure (Vignier et al. 2009). The present data suggest that the use of a Ca^{2+} sensitizer would not be effective. Moreover, EMD, under spontaneous beating conditions and also under pacing, increased time of relaxation, suggesting that it may even adversely affect diastolic function. These results rather argue for a strategy of decreasing the myofilamental Ca^{2+} sensitivity in HCM patients as a therapeutic intervention. However, no pure Ca^{2+} desensitizers have been developed so far.

(III) Another important novel finding was the decreased sensitivity of KO and KI EHTs to the Ca^{2+}-channel blocker verapamil. Both KO and KI reacted to verapamil with 5-fold less sensitivity. Our data suggest that the blunted response to verapamil in KO and KI is due to the myofilaments already working at the maximum of the pCa-force relation. Verapamil is currently contraindicated in heart failure patients with low ejection fraction for its negative inotropic effect. Our results indicate that it could in fact exert beneficial effects even in terminal stages of HCM. Ca^{2+}-channel blocker-induced reductions of intracellular Ca^{2+} levels would favor diastolic relaxation. Moreover, the risk for negative inotropic effects and an aggravation of output failure should be lower than in normal patients due to the abnormally

high myofilament Ca^{2+} sensitivity. Indeed, Ca^{2+}-channel blockers are drugs of choice for the treatment of HCM and early studies in humans have shown that intravenous verapamil improves relaxation and early rapid diastolic filling in patients with HCM (Hanrath et al. 1980; Bonow et al. 1985; Tendera et al. 1993). The present data suggest that, at least in *MYBPC3*-related HCM, higher doses of verapamil would be needed to achieve such effect.

One remaining question is how spontaneous hypercontractility, abbreviated contraction and relaxation times, increased sensitivity to external Ca^{2+} and decreased sensitivity to EMD and verapamil in the EHT model or in isolated myocytes of the KO/KI mice (Pohlmann et al. 2007; Vignier et al. 2009) fit to decreased fractional area shortening (FAS) observed by echocardiography in whole mice (Harris 2002; Carrier et al. 2004; Vignier et al. 2009) or to the HCM phenotype in humans. One explanation could be that the hypercontractile phenotype in EHTs represents a primary defect, which is only seen in very early stages and dissipates later (Ferrans & Rodríguez 1983). However, in previous work from our institute, myocytes and atrial tissue were isolated from mice of similar age (6-10 weeks) and also showed signs of hypercontractility and increased Ca^{2+} sensitivity (Pohlmann et al. 2007; Fraysse et al. 2012). Normally, an increase in Ca^{2+} sensitivity leads to an increase in ejection fraction and slowing of relaxation (see effect of EMD 57033 in WT). This and former studies clearly show that ablation of cMyBP-C does not have the same consequences. Instead, the lack of cMyBP-C appears to favor weak actin-myosin-interactions (Lecarpentier et al. 2008). This seems sufficient to cause shortened diastolic sarcomere length of isotonically contracting cardiomyocytes (Fraysse et al. 2012; van Dijk et al. 2012), increased sensitivity to external Ca^{2+} in isolated right atria (Pohlmann et al. 2007) and auxotonically contracting EHT (this study), respectively, as well as decreased sensitivity to verapamil and EMD (this study), and diastolic dysfunction *in vivo* (Fraysse et al. 2012). On the other hand, ablation of cMyBP-C also reduces the number of strong, high force-generating cross bridges (Lecarpentier et al. 2008) and accordingly the time of systolic force development (Palmer et al. 2004). This is well compatible with abbreviated contraction and relaxation times seen in the present study and could lead to reduced ejection fraction. The inability to eject will be accentuated under conditions of increased (hemodynamic) demand and likely less seen under low pre- and afterload as in our EHTs that beat against low resistance. Low fractional area shortening (FAS) in homozygous KI mice does in fact not indicate low output failure, but, on the basis of the dilated LV, establishes a normal cardiac output. Even physiological cardiac hypertrophy induced by physical exercise is accompanied by a slight increase in the diastolic left ventricular inner diameter (LVIDd) and a decrease in FAS (own unpublished finding). Moreover *Mybpc3*-targeted KO mice exhibited high-normal systolic and decreased

diastolic function (Carrier et al. 2004). This seems to contrast with results from a recent study on human heart muscle biopsies demonstrating that skinned myocytes from patients with HCM exhibit decreased maximal force development compared to normal controls (Carrier et al. 2010). However, the decrease in maximal myofilament force generation is likely not seen in isolated, unloaded myocytes or in EHTs that are not stretched to the length of maximal force development.

Taken together, the results obtained in KO and KI EHTs recapitulate and extend key findings obtained in isolated myocytes and intact heart preparation from the same mouse models, indicating that EHTs are useful to model a *Mybpc3*-related HCM-phenotype *in vitro* (Korte et al. 2003; Carrier et al. 2004; Pohlmann et al. 2007; Vignier et al. 2009; Fraysse et al. 2012). They also strengthen the concept that increased sensitivity to Ca^{2+} is a consequence of the absence or marked reduction in cMyBP-C levels and one of the possible disease mechanisms in HCM.

4.3.2.2 Effects of β-adrenergic stimulation

Since β-adrenergic stimulation is the predominant extrinsic modulator of cardiac contractile performance the effect of isoprenaline was assessed in WT, KO and KI EHTs. This should help to characterize differences in comparison to the mentioned positive inotropic effect of the Ca^{2+} sensitizer EMD and to better understand how phosphorylated wild-type or mutated cMyBP-C modulates contractility. We used isoprenaline (ISO) at a concentration of 100 nM, which was shown to be sufficient to induce full phosphorylation of cMyBP-C (El-Armouche et al. 2006). To see a positive inotropic effect of ISO in the EHT model the external Ca^{2+} concentration had to be decreased to a level leading to approximately 40–50% of the maximal contraction amplitude of WT EHTs. This was the case for 0.6 mM, since at lower Ca^{2+} WT EHTs repeatedly failed to beat according to the stimulation frequency or the peak height did not sufficiently exceed the noise. Under these conditions WT EHTs exhibited the strongest positive inotropic response to ISO, reflected by an increase of about 160% of basal force development. In contrast, KO EHTs already reached 100% of their maximal contraction amplitude at 0.6 mM Ca^{2+}. Thus, the ISO-induced increase in force in KO EHTs was only 36%, which was significantly lower than in WT. KI EHTs also showed a tendency to a milder positive inotropic response to ISO (+90%). These results fit to those, which were previously seen in left atria and Langendorff perfused KO hearts (unpublished data, Lutz Pohlmann). For these measurements, the tissues were stretched, according to the Frank-Starling mechanism to obtain maximal basal force. Here, ISO had a weaker effect on force in KO

than in WT. This was in contrast to isolated KO myocytes, which even showed an increased response to ISO in comparison to WT. This argues for the fact that EHTs are more similar than isolated cells to the respective phenotype observed in native tissue, such as isolated left atria or the whole heart, despite the fact that EHTs were measured under auxotonic conditions. Taken together, KO left atria as well as KO EHTs were sensitized to Ca^{2+} and were contracting already at more than half-maximal force at 0.6 mM Ca^{2+} (Pohlmann et al. 2007; own data). Therefore KO EHTs were not capable to increase their force to the same extent as WT EHTs. In KI, this could also be an explanation. However, at 0.6 mM Ca^{2+}, only a tendency towards a higher force development could be observed for KI, suggesting a milder hypersensitivity to Ca^{2+} than KO. In KI, a tendency towards a decreased positive inotropic response to ISO was observed. In general, since KI cardiomyocytes only contain ~10% of mutant cMyBP-C (Vignier et al. 2009), the model can be considered as a partial knock-out of cMyBP-C, which could explain the similarities to KO. For the occurring differences, however, it has to be taken into account that the full-length protein expressed is a mutant, which might act as a poison peptide and exert a significantly altered function. In KI EHTs the level of full-length mutant was even ~30%, which argues for the fact that under EHT culture conditions the proportions of the different expressed mutants can vary.

KO EHTs exhibited a slightly prolonged contraction and unchanged relaxation time in response to 100 nM ISO, which is in contrast to the common positive klinotropic and lusitropic effect of ISO in WT. It is generally assumed that the positive lusitropic effect of β-adrenergic stimulation is mainly mediated by phosphorylation of cTn-I and PLB, resulting in accelerated Ca^{2+}-dissociation from Tn-C. Yet, the exact contribution of cTnI, PLB and cMyBP-C phosphorylation in this context is not clear since they are all targets of PKA (Bers 2002; de Tombe 2003). Skinned fibers from cMyBP-C KO mice showed hypersensitivity to Ca^{2+} and a blunted desensitizing response to *in vitro* phosphorylation by PKA (Cazorla et al. 2006). This suggests that cMyBP-C plays a role in the acceleration of relaxation mediated by β-adrenergic stimulation and may explain the blunted response to ISO in our KO EHTs. Another explanation could be that accelerated contraction and relaxation kinetics in KO and KI leave only a minimal additional kinetic reserve for a change to ISO.

4.3.2.3 Evaluation of Ca^{2+} transient measurements in EHTs and the effect of Fura-2

To measure Ca^{2+} transients EHTs were loaded with the Ca^{2+}-sensitive dye Fura-2-AM. Fura-2-AM is an intracellularly trapped Ca^{2+}-binding fluorescent indicator, which was developed in the 1980s (Grynkiewicz et al. 1985). The acetoxymethyl (AM) ester of Fura-2 can passively

diffuse across cell membranes. Inside the cell these esters are cleaved by intracellular esterases to yield cell-impermeant Fura-2. Fura-2 has the advantage that it can be evaluated ratiometrically by computing the ratio of the fluorescence at two wavelengths (2.5.2.3). The measured Fura-2 ratio is therefore independent of the cell geometry and the intracellular dye concentration. Since Fura-2 as a Ca^{2+} chelator binds Ca^{2+} intracellularly (Ca^{2+} buffer), the Ca^{2+} concentration at the myofilaments decreases and force declines. For this reason a minimum extracellular Ca^{2+} concentration is required to ensure adequate myocyte/EHT beating under Fura-2 staining. It was observed that an extracellular Ca^{2+} concentration of 1.8 mM is enough to ensure suitable force values for initial measurements after staining, at least in rat EHTs. Mouse EHTs showed a stronger decrease in force under Fura-2 staining at 1.8 mM Ca^{2+}. Indeed, shortening amplitude was lower at any concentration of extracellular Ca^{2+} in single cardiomyocytes loaded with Fura-2 than those not loaded (own findings). Contraction and relaxation kinetics were prolonged in the presence of Fura-2, which is likely also due to the buffering features of this compound and led us to decide to pace mouse EHTs at a lower frequency (2 Hz).

When force and Ca^{2+} transient amplitudes were measured in WT, KO and KI EHTs, KO exhibited higher force than KI or WT, similar to the measurements without Fura-2. Ca^{2+} transient amplitudes tended to be lower in KO with poor signal to noise ratios. This could argue either for a distinct ‘competition’ for Ca^{2+} between KO myofilaments and Fura-2 or a diminished Ca^{2+} transient amplitude to compensate myofilament Ca^{2+} hypersensitivity. In any case, it indicates that hypercontractility in KO EHTs was not due to more Ca^{2+} (or cardiac cell mass, see above), but to a higher myofilament response to Ca^{2+}, i.e. increased Ca^{2+} sensitivity. Interestingly, in the presence of Fura-2 at 0.6 mM Ca^{2+} EMD was able to increase the force not only in WT and KI, but also in KO EHTs. This argues again for the buffering effect of Fura-2, lowering the free cytosolic Ca^{2+} to a degree which allowed for the positive inotropic response to EMD. As expected, EMD did not alter Ca^{2+} transients in KO EHTs, which is in line with only minor PDE3 inhibitory effects as described earlier (Neumann et al. 1996; Tsutsui et al. 2001).

4.3.3 Molecular characterization of disease-specific EHT

As already mentioned, a potential myocyte hypertrophy in KO and/or KI EHTs can influence the contractile phenotype by confounding remodeling events, e.g. altered cytoskeletal architecture, Ca^{2+} handling, and energy metabolism. The hallmark feature of a hypertrophied cardiomyocyte is its increased size (Dorn et al. 2003). This is associated with increased

sarcomerogenesis and increased expression of both natriuretic peptides (ANP and BNP) and the fetal isoform of the myosin heavy chain (β-MHC), which is part of the 'hypertrophic gene program'. Additionally, most studies of hypertrophied or failing hearts have shown decreased expression of SERCA (Hobai & O'Rourke 2001; Hasenfuss & Pieske 2002). In our model, an activation of the hypertrophic gene program was detected in KO adult cardiomyocytes and EHTs, including overexpression of β-MHC, and on a mRNA-level, increased ANP and α-skeletal actin expression and lower SERCA expression (own data; Pohlmann et al. 2007). Interestingly, neonatal hearts of KO mice on day 0 did not show an activation of the hypertrophic gene program in comparison to WT. However, when hearts were analyzed on day 2 postnatal, β-MHC and BNP mRNA levels were already higher in KO and in KI, suggesting that KO and KI hearts become hypertrophic between day 0 and day 2 postnatal. When we consider that in our model cardiomyocytes have an average age of day 0–1, they should not be hypertrophic in this state. This was confirmed by measurements of mRNA isolated from EHTs on day 0, which did not show any differences in β-MHC. This would underline findings of another group, showing that cardiomyocytes of their *Mybpc3*-targeted knock-out mouse model are not hypertrophic at day 0, in contrast to day 10 (de Lange et al. 2011). In other studies KO and KI mice are thought to be already born with cardiac hypertrophy (increase in heart weight-to-body weight ratio by ~30%, when born in the homozygous state; Cazorla et al. 2006; Schlossarek et al. 2012). However, here the exact age of the pups used is not declared.

In EHTs after 20 days of culture, β-MHC mRNA and protein levels were higher in both KO and KI. In contrast to our data, *Mybpc3*-targeted KO ECTs (de Lange et al. 2011) did not show an activation of the hypertrophic gene program on a molecular level (ANP, β-MHC and α-MHC) when investigated over day 10 of culture. Differences in culture conditions and matrix properties might explain these differences. ECTs have a collagen I-based matrix and are cultured under phasic stretch. In our case, EHTs are based on a fibrin-matrix and are cultured under auxotonic stretch. In this model tension remains unchanged while the length of the muscle changes. In contrast, ECTs were fixed to fibrin tabs and kept in culture. Interestingly, mechanical manipulation of tissue can induce the activation of the hypertrophic gene pattern even by itself (own findings). This means that this procedure could have resulted in elevated ANP and β-MHC expression in WT ECT, which served for normalization. This circumstance could have masked higher values in KO.

Levels of β-MHC were lower in 20-day-old EHTs than in hearts of newborn mice or in young EHTs (day 0), which is likely related to maturation processes during EHT culture *in vitro*. Interestingly, β-MHC protein levels rebounded from day 20 up to day 30 in EHT culture

independently of the genotype (data not shown). Aging under stretch or serum-containing culture conditions may have provoked this, since it is known that stretch and serum components can induce cardiomyocyte hypertrophy (Simpson et al. 1982; Fink et al. 2000; Frank et al. 2008).

4.3.4 Gene therapeutic approach

In the fibrin-based EHT model a clear phenotype was detected in KO EHTs. In this context it was interesting to investigate whether this pathological phenotype could be reversed by drugs (as mentioned above) or gene therapy. Gene therapy is becoming a promising field for the treatment of heart failure or genetic diseases such as HCM. For this purpose the development of vectors and delivery methods are important to effectively transduce the majority of cardiomyocytes (Ishikawa et al. 2011). However despite the simple concept, gene transfer is complex. The major issues of successful gene therapy approaches are the design of the vector, mode of delivery, transduction efficiency, and organ tropism (in an organism) and the expression of the gene to obtain the therapeutic effect. The cytomegalovirus (CMV) promoter to drive protein expression is of viral origin and known to be a ‘strong’ promoter in cardiac cells (Maass et al. 2003).

Using the EHT technology, approaches of gene therapy can be tested quickly within a time window of 2 weeks, which is an advantage in comparison to long-lasting and complicated procedures in the animal model. In our study, an adenovirus encoding the human *MYBPC3* gene served for the transduction of KO EHTs. The multiplicity of infection (MOI) in the EHTs was 75, which is relatively high in comparison to 2D culture (MOI~1). We decided to use this viral concentration referring to previous studies of our institute, where an MOI of 50-100 was sufficient to infect almost all neonatal rat cardiomyocytes in collagen-based EHTs (Zimmermann et al. 2000). In this study, adenovirus (AV)-mediated gene transfer of β-galactosidase into rat EHTs reached 100% efficiency. AV addition to the fibrin-based EHT mastermix immediately before casting resulted in cell death in our study, indicating AV-induced toxicity (Ishikawa et al. 2011). In contrast, cardiomyocytes in 3-day-old EHTs tolerated the AV transduction well. However, protein concentrations of cMyBP-C were low in the transduced KO EHTs, as confirmed by immunofluorescence and Western blot analyses. Interestingly, AV-transduced KO EHTs showed normal levels of cMyBP-C mRNA, suggesting sufficient transduction efficiency. An explanation for the low protein amount of cMyBP-C could be that transgenic human cMyBP-C may have been degraded by protein degradation mechanisms (Carrier et al. 2010). Another study showed that the mRNA and protein level

can be completely uncorrelated in single cells (Taniguchi et al. 2010). Furthermore, it has been shown for contractile proteins that increases observed at the mRNA level are not necessarily translated into absolute increases in protein (Sanbe et al. 2005). In our study, the low level of cMyBP-C protein also explains the lacking curative effect of AV transduction in KO EHTs (e.g. increased Ca^{2+} sensitivity or total spontaneous force development). In 2011, de Lange et al. transduced heart cells of neonatal KO mice during a preplating procedure with an AV encoding murine *Mybpc3* and successfully rescued the KO ECT phenotype (de Lange et al. 2011). This suggested that the AV addition to the culture medium during the preplating process was beneficial. Preplating of the cell suspension may have resulted in a selection of transduced and vital cardiomyocytes, which served for ECT generation. Another explanation could be that the murine cMyBP-C may not have been degraded by protein degradation mechanisms. However, the report does not state how reliable this method was, how many ECTs could be rescued and whether they performed a selection. Furthermore, the AV transduction during preplating requires high AV amounts and yields low amounts of surviving transduced cardiomyocytes. For the future, the use of less toxic adeno-associated viruses (AAVs; Müller et al. 2006) is a promising option. AAVs can be added simply to the EHT mastermix. This technique turned out to be successful to transduce the majority of cardiomyocytes, which was confirmed by histological and molecular analyses (unpublished data, Christiane Neuber). One reason for the very good transduction rate in fibrin-EHTs may be that the fibrin matrix captures AAV particles during the polymerization. The persisting AAV in the EHT matrix could therefore also transduce cardiomyocytes during EHT culture, thus promoting increased transduction efficiency and long-term transgene expression.

4.4 Endothelial cell labeling in mouse EHT

To specifically label endothelial cells in EHT, two mouse models were established in our animal facility, during about 1 year. The original mice were kindly provided by Florian Limbourg (MHH, Hannover). The first model was the BMX-Cre-ER^{T2} mouse model (Florian Limbourg, unpublished). BMX is a bone marrow tyrosine kinase which was identified in human bone marrow and is known to be highly expressed in human heart (Ekman et al. 1997). Growth and differentiation of endothelial cells are regulated by tyrosine protein kinases signal transduction. BMX mRNA is specifically expressed in the endocardium of the developing heart as well as in the endocardium of the left ventricle and in the endothelium of large arteries in adult mice. BMX may be involved in signal transduction in endocardial and arterial endothelial cells. The second mouse model, the VE-Cadherin-Cre-ER^{T2} model is a

widely known model (Alva et al. 2006; Monvoisin et al. 2006). VE-Cadherin (vascular endothelial cadherin) is also known as CD-144 and cadherin-5 and is a transmembrane protein involved in endothelial homotypic cell adhesion (Lampugnani et al. 1995). VE-Cadherin has been localized to adherens junctions in endothelial cells (Alva et al. 2006). Complete absence of VE-Cadherin in mice results in embryonic lethality due to vascular abnormalities. In addition, VE-Cadherin has been implicated in modulation of flow, VEGF signalling, and vascular permeability within a variety of organs in adult mice. In our mice, the inducible Cre recombinase fusion protein was expressed under regulatory control of the mouse BMX or VE-Cadherin specific gene promoter regions. Inducible control of Cre activity has been achieved by fusing sequences from the Cre gene with sequences encoding a mutant form of the estrogen receptor ligand-binding domain (ER^{T2}; Metzger & Chambon 2001). ER^{T2} functions as a specific receptor for tamoxifen and is unresponsive to natural estrogens or other physiological steroids. Cre-ER^{T2} brings Cre activity under control of tamoxifen or the synthetic ligand *o*-hydroxytamoxifen (OHT). In the absence of tamoxifen or OHT, Cre-ER^{T2} protein remains locked in the cytoplasm by hsp90 (Mattioni et al. 1994), preventing Cre-mediated recombination events in the nucleus. Binding of the ligand to the receptor disrupts the interaction with hsp90, allowing the translocation of Cre to the nucleus where it can initiate *lox*P-specific recombination. With this technique genetic experiments targeting the endothelium can be temporally controlled and physiologic consequences of specific gene modifications are limited. Specificity and efficiency of Cre activity was documented by crossing heterozygous VE-Cadherin-Cre-ER^{T2} mice with homozygous Rosa26R reporter mice, in which a floxed stop cassette has been placed upstream of the β-galactosidase gene. In the Cre/lox system the Cre recombinase catalyzes site-specific recombination by the crossover between two distant Cre recognition sequences (*lox*P sites), leading to the excision of the floxed stop codon. Cre expression can be switched on or off at a certain time point either in the adult mouse *in vivo* by the injection of tamoxifen or in the cell culture dish *in vitro* by OHT.

In EHTs generated from the BMX- or VE-Cadherin mouse lines endothelial cells (ECs) were detected by X-gal staining. In BMX EHTs ECs were homogenously distributed as single cells or small branched cell complexes throughout the matrix, showing incipient stages of vessel formation. EHT cross sections showed tubular ‘lumina’, surrounded by X-gal-positive cells. This was the first solid evidence that ECs in fibrin-based EHTs formed lumina by themselves during EHT standard culture conditions. In contrast to BMX EHTs, VE-Cadherin EHTs showed an extensive, continuous network of LacZ-positive ECs, indicating the formation of complex vascular structures, oriented along the force lines. Structures of these primitive EC

networks were dependent on the presence of animal serum in the culture medium. Interestingly, vasculature structure appeared the better the ‘thinner’ the EHT construct was, depending on the fibrinogen concentration (1.5 mg/ml). In thick constructs (3.5 mg/ml) the inner part of the EHTs almost completely lacked X-gal-positive cells, which argued for the fact that ECs were mostly provided with nutrition by diffusion processes (Frerich et al. 2001). It is consensual that there is a critical size limit of a tissue that cannot be surpassed without active perfusion of nutrients and oxygen (Eschenhagen et al. 2007). This is even more important since beating cardiomyocytes in EHTs have a very high metabolic activity. Therefore different approaches in our group are evaluated in order to improve the oxygen and nutritive supply in inner EHT regions. One could have expected the EC density to rather increase in regions with low oxygen saturation, since it has been shown that low oxygen concentration induces HIF-1α, thereby inducing EC proliferation (1.5.3; Pugh and Ratcliffe 2003). However, in our study low oxygen concentrations (3%) during EHT culture clearly decreased EC density in VE-Cadherin EHTs. VE-Cadherin EHTs at 3% oxygen showed greater width than EHTs cultured at 21 or 40%, indicating less remodeling and less maturation. Furthermore, increased rate of cell apoptosis due to insufficient oxygen and nutritive supply may explain the low EC and cardiomyocyte densities in inner EHT regions.

Neither matrix-bound nor free soluble growth-factors (IGF-1, PDGF-BB, VEGF) modified EC density in EHTs. This disappointing finding was likely due to the fact that EHTs were cultured in the presence of animal sera, which contains large amounts of angiogenesis-modifying growth factors (Brown et al. 1996). Thus, vascularization was likely already maximal and further growth factor application could not enhance EC proliferation. Under serum-free conditions, vessel-like structures were ~1,000-fold reduced and could be not or only marginally rescued by free or matrix-bound VEGF, PDGF or IGF. Angiogenesis is driven by numerous mediators produced by many cells under a variety of conditions. VEGF is one of the most potent proangiogenic factors (Senger et al. 1983) and is secreted by tissues in response to ischemic and inflammatory stimuli and results in endothelial migration, proliferation, and increased vascular permeability (Pandya et al. 2006). Other factors such as PDGF, TGF-β and FGF are also known to contribute to angiogenesis in healing wounds. One clear explanation for our negative results is the concentration of the respective growth factor. Former studies suggested that VEGF has a ‘threshold dose’ to significantly affect angiogenesis in *in vitro* assays such as the widely known CAM (chorio-allantoic membrane) model (Ehrbar et al. 2004). The CAM assay is based on the implantation of a membrane containing the compound of interest on the chick CAM through a hole cut in the egg shell (Jakob et al. 1978). We decided to use a concentration of 100 ng/ml according to previously

established *in vitro* angiogenesis assays. *In vitro* angiogenesis assays for endothelial cell migration showed that most endothelial cells migrated under the combination of VEGF and bFGF (basic fibroblast growth factor) in a concentration of 10-100 ng/ml each (Staton et al. 2004). Growth factor concentrations above 100 ng/ml resulted in decreased EC migration. Additionally, it has been shown that too high concentrations of VEGF can result in malformed vessels. However, studies of our cooperation partners indicate that growth factor concentration in our model might have been too low. In their study fibrin-implants with matrix-bound TG-VEGF in a concentration of 50 µg/ml displayed more vascularization than fibrin-implants with soluble VEGF after a time period of 4 weeks *in vivo* (Ehrbar et al. 2008). This argues for the fact that matrix-bound TG-VEGF should be applied in higher concentrations than plain, soluble VEGF. Our established fibrin-based miniaturized EHT model provides the opportunity to test various concentrations and combinations of pro-angiogenic growth factors, which will be exerted in the future using VE-Cadherin mice. The combination of soluble growth factors in a defined concentration could help to optimize EC survival and vessel-like network formation of VE-Cadherin EHTs in *in vitro* and in *in vivo* studies.

4.5 EHT as graft for implantation studies

Compared to current treatment options like drugs, devices, transplantation, prostheses or cell therapy, cardiac repair with tissue-engineered myocardial patches appears still very ambitious (Isenberg et al. 2006; Eschenhagen et al. 2007). To bioengineer 3-dimensional heart muscle equivalents for cardiac regeneration the grafts should be composed of heart cells in an extracellular matrix, should have a myocardium-like structure without inducing arrhythmias and should be vascularized. In our study we also focused on the analysis of graft vascularization *in vivo*. A good vascularization of the graft is an important parameter to ensure graft longevity *in vivo*. The questions we considered most important were the following: Can murine fibrin-based mini EHTs serve as grafts? Does the vessel-like network in VE-Cadherin EHTs connect to the vessels of the host myocardium after implantation? Do endothelial cells from the EHT migrate into the host myocardium or *vice versa*?

WT and VE-Cadherin mini-EHTs were suitable in size to cover the left ventricle of an adult murine heart. In a pilot study we implanted VE-Cadherin EHTs cultured for 26 days onto the healthy heart and analyzed the heart plus graft after 14 days *in vivo*. On first sight, the surprisingly extensive blue staining across the entire heart indicated strong proliferation of EHT-derived ECs over the whole heart. However, it should be noted that expression of Cre in ECs had been induced in EHTs *in vitro* by the addition of OHT to the culture medium,

inducing permanent expression of the LacZ gene. In this experiments, we could therefore not distinguish between ECs and cells that derived from them after the period *in vivo*. ECs can undergo an 'endothelial–mesenchymal transition' (Krenning et al. 2010). Specifically, they can acquire a fibroblast-like phenotype and loose characteristics of ECs under pressure of pro-fibrotic stimuli (e.g. TGF-β or hypoxia). This can contribute to cardiac fibrosis both by fibroblast accumulation and microvascular rarefication (Zeisberg et al. 2007). In general, the endothelial-mesenchymal transition pathway can be activated in the adult heart to recruit fibroblasts to perivascular areas during injury, as the cardiac surgery procedure in our case. This would explain the large number of detected X-gal-positive cells in the epicardial layer of recipient hearts as well as the absence of X-gal-positive blood vessels.

EHT grafting studies in mouse dorsal skin consistently showed that X-gal-positive cells (ECs) were localized primarily in regions of stitching, suggesting that the tissue injury associated with stitches stimulated inflammation and the local production of endogenous growth factors. In healing wounds rising levels of VEGF induce a period of robust angiogenesis (Gosain et al. 2006). We therefore hope that fibrin-bound VEGF in the EHT matrix will help to improve vessel connection between EHT and the host myocardium.

4.6 Outlook

4.6.1 EHT for cardiac disease modeling

So-called monogenic cardiovascular disease are associated with an increasing number and variety of gene mutations (see for example Schlossarek et al. 2011). In human HCM, genotype-phenotype-correlations are poor, because the effect of likely disease-causing mutations are largely affected by modifier gene mutations and environmental factors. Thus, the simple knowledge of a mutation does not predict the course of the disease. This is one of the reasons why disease modelling with stem cells has gained much public attendance. Our studies based on mouse EHTs served as pilot experiments, since the goal for the future is to model human disease. The breakthrough in this field was the development of human induced pluripotent stem (iPS) cells. The first iPS cells from human dermal fibroblasts were reprogrammed by the use of 4 retrovirally transduced transcription factors (*Oct3/4*, *Sox2*, *Klf4* and *c-Myc*; Takahashi et al. 2007) and were differentiated into functional cardiomyocytes in 2009 (Zhang et al. 2009; Lau et al. 2009). For patient-specific disease modeling the underlying hypothesis is that cardiomyocytes generated from iPS exhibit a phenotype that is the integrated consequence of a specific gene mutation and all modifier gene variants. Recent studies provide first evidence for this concept in the cardiac diseases LQT syndrome

(Moretti et al. 2010; Itzhaki et al. 2011), Timothy syndrome (Paşca et al. 2011) or dilated cardiomyopathy (DCM; Sun et al. 2012).

An important limitation of all these studies is that cardiomyocytes derived from iPS cells *in vitro* exhibit a fetal status. Moreover, the functional readout in isolated cells or embryoid bodies is very limited. At this point, our EHT technology can serve both to prolong the duration of cardiomyocyte culture and to improve the maturation of cardiomyocytes and to allow a much higher content analysis of function as shown in the present study. 3D muscle construct resembles the muscle tissue of the patient more closely than isolated cells. In the future, EHTs of disease-specific cardiomyocytes will be generated and analyzed in contractile experiments. EHTs based on iPS-cell derived cardiomyocytes from DCM and HCM patients will be analyzed with regard to force development, sensitivity to external Ca^{2+} and response to stress. Furthermore, Ca^{2+}-desensitizing drugs will be tested.

4.6.2 EHT for angiogenesis studies

BMX and VE-Cadherin EHTs turned out to be an excellent model for angiogenesis screenings *in vitro* and *in vivo*. Effects of animal serum and the anti-angiogenic miR-24 could be detected successfully. In the future, the development of vessel-like structures in EHT will be optimized by adding defined combinations of angiogenesis-inducing growth factors to the culture medium. Improvement of serum-free culture conditions is another goal for the future. If the tissue-engineering strategy is to enter the clinical area one day, it has to be performed under good manufacturing and good laboratory practice procedure in the absence of xenogenic compounds such as animal serum (GMP and GLP; Eschenhagen et al. 2007). Besides this, various substances can be tested in the VE-Cadherin EHT model with respect to cardiotoxicity and influence on angiogenesis.

EC labeled EHTs could also successfully serve as grafts. A further goal of the future will be the connection of EHT vessel structures to the host myocardium. *In vivo*, a patch has to survive in a nonperfused environment (the surface of the heart). Sufficiently large patches for the human heart are likely to only survive if the patch contains a functioning vasculature that can be surgically connected to the host circulation. Fibrin-bound growth factors such as TG-VEGF, TG-PDGF and TG-IGF can help to improve vascularization of grafts *in vivo*. Fibrin-bound VEGF has been shown to be protected from clearance *in vivo*, induces vessel formation and improves morphogenesis (Ehrbar et al. 2008) and is therefore a promising candidate for further EHT-based implantation studies.

5 Summary

Cardiac tissue engineering may provide improved test beds for preclinical drug development and surrogate heart muscle for tissue replacement therapy. This thesis addressed three important questions: (1) Is the established engineered heart tissue (EHT) format suitable for '*in vitro* disease modeling', i.e. does it detect a phenotype of genetically determined cardiac diseases? (2) Do EHTs contain blood vessels and do they participate in vascularization after implantation? (3) Can this process be improved by angiogenic growth factors?

To answer these questions the fibrin-based rat EHT technology had to be adapted for neonatal mouse cardiac cells. To generate spontaneously beating murine EHTs some modifications were necessary, namely an increase in cell concentration, reduction in mastermix volume, the presence of Matrigel in the mastermix, insulin as a medium supplement, the use of a cell cycle inhibiting drug (AraC) between day 5-7 and the exclusive use of neonatal pups with an age of 0-1 day postnatal. Murine EHTs showed features of intact cardiac muscle in morphological, histological and pharmacological analyzes. To answer the first question the cardiac disease hypertrophic cardiomyopathy (HCM) was in the focus of interest. Hypertrophic cardiomyopathy (HCM) is frequently caused by mutations in *MYBPC3* encoding cardiac myosin-binding protein C (cMyBP-C). *Mybpc3*-targeted knock-out (KO) or knock-in (KI) mice recapitulate typical aspects of HCM. The objective of this study was to evaluate whether functional alterations observed in *Mybpc3*-targeted KO or KI mice can be reproduced in engineered heart tissue (EHT) and yield novel mechanistic information on the function of cMyBP-C. EHTs were generated from hearts of neonatal KO, KI or respective wild-type control (WT) mice and developed without apparent differences. Contractile function was monitored under spontaneous beating and electrical stimulation (5-6 Hz). KO and KI EHTs developed higher peak force than WT under physiological Ca^{2+} concentration, but times of contraction and relaxation were shorter. KO and KI exhibited 5-fold lower sensitivity to the negative inotropic effect of the Ca^{2+}-channel blocker verapamil and, at 0.6 mM Ca^{2+}, nearly no (KO, +2%) or a reduced (KI, +33%) positive inotropic response to the Ca^{2+} sensitizer EMD 57033 compared to WT (+110%). Additionally, the positive inotropic and lusitropic effect of isoprenaline was blunted in KO. In conclusion, hypercontractility at physiological Ca^{2+} concentrations and shortened times of contraction and relaxation in *Mybpc3*-targeted murine EHT suggest that the role of cMyBP-C is to suppress weak and stabilize strong actin-myosin interactions. Reduced sensitivity to verapamil and EMD points towards important differences in drug responses of *MYBPC3*-related HCM. EHTs are a suitable test bed to study functional consequences of gene

mutations. The present results shall be useful for future studies with induced-pluripotent stem cell (iPS)-mediated disease modeling of human HCM.

To answer the second and the third question, two transgenic mouse lines (BMX-/VE-Cadherin-Cre-ER^{T2}-Rosa26-LacZ) were established in which endothelial cells (ECs) were specifically labeled in a tamoxifen-inducible, cell-specific manner. The BMX-model labels only a subfraction of ECs with an arterial phenotype, the VE-Cadherin model all ECs. EHTs generated from BMX neonatal mouse hearts showed labeled ECs aligned along the force lines scattered within the matrix. VE-Cadherin EHTs showed an extensive primitive, but distinct vascular network under standard EHT culture conditions. Under serum-free conditions, EC density in VE-Cadherin EHTs was 1,000-fold lower. Angiogenesis-modifying soluble or matrix-bound growth factors such as VEGF, PDGF or IGF did not increase EC density under standard or serum-free conditions *in vitro*. Transfection of VE-Cadherin EHTs with microRNA-24 had an angiogenesis-inhibiting effect. Murine EHTs served as grafts for implantation studies. Labeled cells from VE-Cadherin EHT grafts could be detected after 2 weeks *in vivo*, forming multicellular layers. Future studies are planned to investigate whether angiogenesis-inducing growth factors immobilized in the EHT matrix will improve vessel connection to the host myocardium.

5 Zusammenfassung

Kardiales ‚*Tissue Engineering*' könnte im Rahmen der präklinischen Arzneistoffentwicklung ein verbessertes Testsystem darstellen und als Herzmuskeläquivalent zum Gewebeersatz dienen. Das Ziel dieser Doktorarbeit war es, drei wichtige Fragestellungen zu beantworten: (1) Eignet sich das *Engineered Heart Tissue* (EHT)-Format zur Krankheitsmodellierung *in vitro*? Ist es beispielsweise möglich, einen Phänotyp einer genetisch bedingten Herzerkrankung festzustellen? (2) Enthalten EHTs Blutgefäße und beteiligen sich diese nach Implantation an einer Gefäßneubildung? (3) Kann eine Gefäßbildung durch proangiogenetische Wachstumsfaktoren verbessert werden?

Um diese Fragen beantworten zu können, musste die bereits etablierte Fibrin-basierte Ratten-EHT-Technologie für neonatale Mausherzmuskelzellen angepasst werden. Folgende Faktoren erwiesen sich als kritisch: Erhöhung der Zellkonzentration, Reduzierung des Mastermixvolumens, Anwesenheit von Matrigel im Mastermix, Insulin als Bestandteil des Mediums, Einsatz eines Zellzyklusinhibitors (AraC) zwischen Tag 5-7 und der ausschließliche Gebrauch von neonatalen Mäusen im Alter von Tag 0-1 nach der Geburt. Murine EHTs zeigten Eigenschaften intakter Herzmuskulatur hinsichtlich Morphologie, Histologie und Pharmakologie. Um erstere Fragestellungen zu beantworten, wurde die hypertrophische Kardiomyopathie näher beleuchtet, welche oft durch Mutationen im *MYBPC3*-Gen, das kardiales Myosin-bindende Protein-C (cMyBP-C) kodiert, ausgelöst werden kann. Zwei repräsentative Mauslinien wurden als Modell für die hypertrophische Kardiomyopathie herangezogen. Eine davon bildet kein cMyBP-C (KO), bei der anderen ist eine häufige menschliche cMyBP-C Mutation in das Mausgenom insertiert worden (KI). Das Ziel dieser Studie war es, zu untersuchen, ob funktionelle Veränderungen, welche in KO- und KI-Mäusen beobachtet werden konnten, im EHT-Modell reproduziert werden können und ob neue mechanistische Informationen zur Funktion des cMyBP-C gefunden werden können. Für die EHT-Generierung wurden neonatale KO- und KI-Mäuse sowie entsprechende Wildtyp (WT)-Kontrollmäuse verwendet, welche sich ohne sichtliche Unterschiede entwickelten. Kontraktile Funktionsanalysen wurden unter spontanen Bedingungen oder unter elektrischer Stimulation (5-6 Hz) durchgeführt. KO- und KI-EHTs entwickelten unter physiologischen Ca^{2+}-Konzentrationen höhere Kontraktionskräfte als WT-Kontrollen, aber die Kontraktions- und Relaxationszeiten waren verkürzt. KO und KI zeichneten sich durch eine 5-fach reduzierte Empfindlichkeit gegenüber der negativ-inotropen Wirkung des Ca^{2+}-Kanal-Blockers Verapamil aus, und zeigten, bei einer Ca^{2+}-Konzentration von 0.6 mM, fast keine (KO, +2%) oder eine reduzierte (KI, +33%) positiv-inotrope Reaktion auf den Ca^{2+}-Sensitizer EMD 57033 im Vergleich zu WT (+110%).

Zusätzlich zeigten KO eine verminderte positiv-inotrope und -lusitrope Reaktion unter Isoprenalinstimulation. Zusammenfassend kann gesagt werden, dass Hyperkontraktilität unter physiologischen Ca^{2+}-Konzentrationen und verkürzte Kontraktions- und Relaxationszeiten in murinen KO- und KI-EHTs darauf schließen lassen, dass die physiologische Aufgabe von cMyBP-C ist, schwache Actin-Myosin Interaktionen zu unterdrücken und starke Actin-Myosin Interaktionen zu stabilisieren. Verminderte Empfindlichkeiten auf die Substanzen Verapamil und EMD deuten auf wichtige Unterschiede in der Wirkungsintensität von Arzneistoffen bei der *MYBPC3*-basierten HCM hin. Diese Untersuchungen haben gezeigt, dass das EHT-Modell ein geeignetes Testsystem darstellt, um funktionelle Auswirkungen von Genmutationen zu untersuchen. Die vorliegenden Ergebnisse könnten für weitere Untersuchungen mit induziert-pluripotenten Stammzellen (iPS) zur Krankheitsmodellierung von menschlicher HCM bedeutsam sein.

Um die zweite und die dritte Frage zu beantworten, wurden zwei transgene Mauslinien (BMX-/VE-Cadherin-Cre-ER^{T2}-Rosa26-LacZ) etabliert, in denen Endothelzellen Tamoxifen-abhängig markiert werden können. Das BMX-Modell markiert nur eine Untergruppe mit „arteriellen“ Eigenschaften, das VE-Cadherin-Modell alle Endothelzellen. EHTs, welche aus neonatalen BMX-Mauseherzen generiert wurden, zeigten markierte Endothelzellen, welche sich entlang der Kraftlinien angeordnet hatten und in der Matrix verteilt waren. VE-Cadherin-EHTs zeigten ein dichtes primitives, aber gerichtetes Netzwerk unter Standardkulturbedingungen für EHTs. Unter Serum-freien Kulturbedingungen war die Endothelzelldichte in VE-Cadherin-EHTs 1.000-fach geringer. Angiogenese-modifizierende, lösliche oder matrixgebundene Wachstumsfaktoren wie VEGF, PDGF oder IGF führten nicht zu einer erhöhten Endothelzelldichte, weder in An- noch Abwesenheit von Serum. Transfektion mit microRNA-24 hatte einen Angiogenese-hemmenden Effekt. Murine EHTs dienten als Implantate für Gewebeersatzstudien. Markierte Endothelzellen aus VE-Cadherin-EHTs konnten nach 2 Wochen *in vivo* detektiert werden und bildeten multizelluläre Schichten aus. In zukünftigen Studien soll untersucht werden, ob Angiogenese-induzierende Wachstumsfaktoren, welche in der EHT-Matrix gebunden sind, die Gefäßanbindung des EHTs an das native Myokard verbessern werden.

6 Literature

Ahmed, T.A., Griffith, M. & Hincke, M., 2007. Characterization and inhibition of fibrin hydrogel-degrading enzymes during development of tissue engineering scaffolds. *Tissue Eng Part* 13(7): 1469-1477.

Aikawa, R., Nawano, M., Gu, Y., Katagiri, H., Asano, T., Zhu, W., Nagai, R. & Komuro, I., 2000. Insulin Prevents Cardiomyocytes From Oxidative Stress-Induced Apoptosis Through Activation of PI3 Kinase/Akt. *Circulation*, 102(23): 2873-2879.

Alva, J.A., Zovein, A.C., Monvoisin, A., Murphy, T., Salazar, A., Harvey, N.L., Carmeliet, P. & Iruela-Arispe, M.L., 2006. VE-Cadherin-Cre-recombinase transgenic mouse: a tool for lineage analysis and gene deletion in endothelial cells. *Dev Dyn*, 235(3): 759-767.

Ashrafian, H., McKenna, W.J. & Watkins, H., 2011. Disease pathways and novel therapeutic targets in hypertrophic cardiomyopathy. *Circ Res*, 109(1): 86-96.

Badylak, S.F., Weiss, D.J., Caplan, A. & Macchiarini, P., 2012. Engineered whole organs and complex tissues. *Lancet*, 379(9819): 943-952.

Banai, S., Jaklitsch, M.T., Shou, M., Lazarous, D.F., Scheinowitz, M., Biro, S., Epstein, S.E. & Unger, E.F., 1994. Angiogenic-induced enhancement of collateral blood flow to ischemic myocardium by vascular endothelial growth factor in dogs. *Circulation*, 89(5): 2183-2189.

Barry, J.M., 2007. Hypertrophic cardiomyopathy. In: Libby, P., Bonow, R.O., Zipes, D.P. & Mann, D.L. (Ed.), Braunwald's Heart Disease: A Textbook of Cardiovascular Medicine (8th edition). *Elsevier Inc,* 65: 1763-1774.

Baudenbacher, F., Schober, T., Pinto, J.R., Sidorov, V.Y., Hilliard, F., Solaro, R.J., Potter, J.D. & Knollmann, B.C., 2008. Myofilament Ca2+ sensitization causes susceptibility to cardiac arrhythmia in mice. *J Clin Invest*, 118(12): 3893-3903.

Bers, D.M., 2000. Calcium Fluxes Involved in Control of Cardiac Myocyte Contraction. *Circ Res*, 87(4): 275-281.

Bers, D.M., 2002. Cardiac excitation-contraction coupling. *Nature*, 415(6868): 198-205.

Blondel, B., Roijen, I. & Cheneval, J.P., 1971. Heart cells in culture: a simple method for increasing the proportion of myoblasts. *Experientia*, 27(3): 356-8.

Bluhm, W.F., Kranias, E.G., Dillmann, W.H. & Meyer, M., 2000. Phospholamban: a major determinant of the cardiac force-frequency relationship. *Am J Physiol Heart Circ Physiol*, 278(1): H249-55.

Bonow, R.O., Dilsizian, V., Rosing, D.R., Maron, B.J., Bacharach, S.L. & Green, M.V., 1985. Verapamil-induced improvement in left ventricular diastolic filling and increased exercise tolerance in patients with hypertrophic cardiomyopathy: short- and long-term effects. *Circulation*, 72(4): 853-64.

Brooks, G., Poolman, R.A., McGill, C.J. & Li, J.M., 1997. Expression and activities of cyclins and cyclin-dependent kinases in developing rat ventricular myocytes. *J Mol Cell Cardiol*, 29(8): 2261-71.

Brown, K.J., Maynes, S.F., Bezos, A., Maguire, D.J., Ford, M.D. & Parish, C.R., 1996. A novel in vitro assay for human angiogenesis. *Lab Invest,* 75(4): 539-555.

Butler, J., Ezekowitz, J.A., Collins, S.P., Givertz, M.M., Teerlink, J.R., Walsh, M.N., Albert, N.M., Westlake Canary, C.A., Carson, P.E., Colvin-Adams, M., Fang, J.C., Hernandez, A.F., Hershberger, R.E., Katz, S.D., Rogers, J.G., Spertus, J.A., Stevenson, W.G., Sweitzer, N.K., Tang, W.H., Stough, W.G. & Starling, R.C., 2012. Update on aldosterone antagonists use in heart failure with reduced left ventricular ejection fraction heart failure society of america guidelines committee. *J Card Fail*, 18(4): 265-281.

Caldas, H.C., Hayashi, A.P. & Abbud-Filho, M., 2011. Repairing the chronic damaged kidney: the role of regenerative medicine. *Transplant P*, 43(10): 3573-3576.

Cambronero, F., Marín, F., Roldán, V., Hernández-Romero, D., Valdes, M. & Lip, G.Y.H., 2009. Biomarkers of pathophysiology in hypertrophic cardiomyopathy: implications for clinical management and prognosis. *Eur Heart J,* 30(2): 139-151.

Carrier, L., 2007. Cardiac myosin-binding protein C in the heart. *Arch Mal Coeur Vaiss*, 100(3): 238-243.

Carrier, L., Knoll, R., Vignier, N., Keller, D.I., Bausero, P., Prudhon, B., Isnard, R., Ambroisine, M.L., Fiszman, M., Ross Jr., J., Schwartz, K. & Chien, K.R., 2004. Asymmetric septal hypertrophy in heterozygous cMyBP-C null mice. *Cardiovasc Res*, 63(2): 293-304.

Carrier, L., Schlossarek, S., Willis, M.S. & Eschenhagen, T., 2010. The ubiquitin-proteasome system and nonsense-mediated mRNA decay in hypertrophic cardiomyopathy. *Cardiovasc Res*, 85(2): 330-338.

Carrier, R.L., Papadaki, M., Rupnick, M., Schoen, F.J., Bursac, N., Langer, R., Freed, L.E. & Vunjak-Novakovic, G., 1999. Cardiac tissue engineering: cell seeding, cultivation parameters, and tissue construct characterization. *Biotechnol Bioeng*, 64(5): 580-589.

Carroll, V.A. & Ashcroft, M., 2005. Targeting the molecular basis for tumour hypoxia. *Expert Rev Mol Med*, 7(6): 1-16.

Cazorla, O., Szilagyi, S., Vignier, N., Salazar, G., Krämer, E., Vassort, G., Carrier, L. & Lacampagne, A., 2006. Length and protein kinase A modulations of myocytes in cardiac myosin binding protein C-deficient mice. *Cardiovasc Res*, 69(2): 370-380.

Chiariello, M. & Perrone-Filardi, P., 1999. Pathophysiology of heart failure. *Miner Electrol Metab*, 25(1-2): 6-10.

Cleveland, D.W., 1983. Peptide mapping in one dimension by limited proteolysis of sodium dodecyl sulfate-solubilized proteins. *Method Enzymol*, 96(3): 222-229.

Coto, E., Palacín, M., Martín, M., Castro, M.G., Reguero, J.R., García, C., Berrazueta, J.R., Morís, C., Morales, B., Ortega, F., Corao, A.I., Díaz, M., Tavira, B. & Alvarez, V., 2010. Functional polymorphisms in genes of the Angiotensin and Serotonin systems and risk of hypertrophic cardiomyopathy: AT1R as a potential modifier. *J Transl Med*, 8: 64.

Cowie, M.R., Mosterdft, A., Wood, D.A., Deckers, J.W., Sutton, G.C. & Grobbeef, D.E., 1997. Review Article The epidemiology of heart failure. *Eur Heart J*, 18: 208-225.

Decker, R.S., Decker, M.L., Kulikovskaya, I., Nakamura, S., Lee, D.C., Harris, K., Klocke, F.J. & Winegrad, S., 2005. Myosin-binding protein C phosphorylation, myofibril structure, and contractile function during low-flow ischemia. *Circulation*, 111(7): 906-12.

Desai, A. & Fang, J.C., 2008. Heart failure with preserved ejection fraction: hypertension, diabetes, obesity/sleep apnea, and hypertrophic and infiltrative cardiomyopathy. *Heart Fail Clin*, 4(1): 87-97.

Dickstein, K., Cohen-Solal, A., Filippatos, G., McMurray, J.V., Ponikowski, P., Poole-Wilson, P.A., Strömberg, A., Veldhuisen, D.J. van, Atar, D., Hoes, A.W., Keren, A., Mebazaa, A., Nieminen, M., Priori, S. & Swedberg, K., 2008. ESC Guidelines for the diagnosis and treatment of acute and chronic heart failure 2008: the Task Force for the Diagnosis and Treatment of Acute and Chronic Heart Failure 2008 of the European Society of Cardiology. Developed in collaboration with the Heart. *Eur Heart J*, 29(19): 2388-2442.

van Dijk, S.J., Paalberends, E.R., Najafi, A., Michels, M., Sadayappan, S., Carrier, L., Boontje, N.M., Kuster, D.W., Slegtenhorst, M. van, Dooijes, D., dos Remedios, C., ten Cate, F.J., Stienen, G.J. & van der Velden, J., 2012. Contractile dysfunction irrespective of the mutant protein in human hypertrophic cardiomyopathy with normal systolic function. *Circ Heart Fail*, 5(1): 36-46.

Dorn, G.W., Robbins, J. & Sugden, P.H., 2003. Phenotyping hypertrophy: eschew obfuscation. *Circ Res*, 92(11): 1171-1175.

Ehrbar, M., Djonov, V.G., Schnell, C., Tschanz, S.A., Martiny-Baron, G., Schenk, U., Wood, J., Burri, P.H., Hubbell, J.A. & Zisch, A.H., 2004. Cell-demanded liberation of VEGF121 from fibrin implants induces local and controlled blood vessel growth. *Circ Res*, 94(8): 1124-1132.

Ehrbar, M., Zeisberger, S.M., Raeber, G.P., Hubbell, J.A., Schnell, C. & Zisch, A.H., 2008. The role of actively released fibrin-conjugated VEGF for VEGF receptor 2 gene activation and the enhancement of angiogenesis. *Biomaterials*, 29(11): 1720-1729.

Ekman, N., Lymboussaki, A., Västrik, I., Sarvas, K., Kaipainen, A. & Alitalo, K., 1997. Bmx tyrosine kinase is specifically expressed in the endocardium and the endothelium of large arteries. *Circulation*, 96(6): 1729-32.

El-Armouche, A., Boknik, P., Eschenhagen, T., Carrier, L., Knaut, M., Ravens, U. & Dobrev, D., 2006. Molecular determinants of altered Ca2+ handling in human chronic atrial fibrillation. *Circulation*, 114(7): 670-680.

El-Armouche, A., Pohlmann, L., Schlossarek, S., Starbatty, J., Yeh, Y.H., Nattel, S., Dobrev, D., Eschenhagen, T. & Carrier, L., 2007. Decreased phosphorylation levels of cardiac myosin-binding protein-C in human and experimental heart failure. *J Mol Cell Cardiol*, 43(2): 223-229.

Elliott, P., Andersson, B., Arbustini, E., Bilinska, Z., Cecchi, F., Charron, P., Dubourg, O., Kühl, U., Maisch, B., McKenna, W.J., Monserrat, L., Pankuweit, S., Rapezzi, C., Seferovic, P., Tavazzi, L. & Keren, A., 2008. Classification of the cardiomyopathies: a position statement from the European Society Of Cardiology Working Group on Myocardial and Pericardial Diseases. *Eur Heart J*, 29(2): 270-276.

Endoh, M., 2008. Cardiac Ca2+ signaling and Ca2+ sensitizers. *Circ J*, 72(12): 1915-1925.

Endoh, M., 2006. Signal Transduction and Ca2+ Signaling in Intact Myocardium. *J Pharmacol Sci*, 100(5): 525-537.

Eschenhagen, T., Reichenspurner H., Zimmermann, W.H., 2007. Tissue-engineered cardiovascular products. In: Lanza, R., Langer R. & Vacanti J. (Ed.), Principles of Tissue Engineering (3rd edition). *Elsevier Inc,* 82: 1237-1248.

Eschenhagen, T., 2008. Beta-adrenergic signaling in heart failure-adapt or die. *Nat Med*, 14(5): 485-487.

Eschenhagen, T., 2010. Is ryanodine receptor phosphorylation key to the fight or flight response and heart failure? *Journal Clin Invest*, 120(12): 4197-4203.

Eschenhagen, T., 2011. The beat goes on: human heart muscle from pluripotent stem cells. *Circ Res*, 109(1): 2-4.

Eschenhagen, T., Fink, C., Remmers, U., Scholz, H., Wattchow, J., Weil, J., Zimmermann, W., Dohmen, H.H., Schafer, H., Bishopric, N., Wakatsuki, T. & Elson, E.L., 1997. Three-dimensional reconstitution of embryonic cardiomyocytes in a collagen matrix: a new heart muscle model system. *FASEB J*, 11(8): 683-694.

Eschenhagen, T. & Zimmermann, W.H., 2005. Engineering myocardial tissue. *Circ Res*, 97(12): 1220-1231.

Feldman, D.S., Carnes, C.A., Abraham, W.T. & Bristow, M.R., 2005. Mechanisms of disease: beta-adrenergic receptors--alterations in signal transduction and pharmacogenomics in heart failure. *Nat Clin Pract Cardiovasc Med*, 2(9): 475-483.

Ferrans, V.J. & Rodríguez, E.R., 1983. Specificity of light and electron microscopic features of hypertrophic obstructive and nonobstructive cardiomyopathy. Qualitative, quantitative and etiologic aspects. *Eur Heart J*, 4 Suppl F: 9-22.

Fiedler, J., Jazbutyte, V., Kirchmaier, B.C., Gupta, S.K., Lorenzen, J., Hartmann, D., Galuppo, P., Kneitz, S., Pena, J.T., Sohn-Lee, C., Loyer, X., Soutschek, J., Brand, T., Tuschl, T., Heineke, J., Martin, U., Schulte-Merker, S., Ertl, G., Engelhardt, S., Bauersachs, J. & Thum, T., 2011. MicroRNA-24 regulates vascularity after myocardial infarction. *Circulation*, 124(6): 720-730.

Fink, C., Ergun, S., Kralisch, D., Remmers, U., Weil, J. & Eschenhagen, T., 2000. Chronic stretch of engineered heart tissue induces hypertrophy and functional improvement. *FASEB J*, 14(5): 669-679.

Flavigny, J., Souchet, M., Sébillon, P., Berrebi-Bertrand, I., Hainque, B., Mallet, A., Bril, A., Schwartz, K. & Carrier, L., 1999. COOH-terminal truncated cardiac myosin-binding protein C mutants resulting from familial hypertrophic cardiomyopathy mutations exhibit altered expression and/or incorporation in fetal rat cardiomyocytes. *J Mol Biol*, 294(2): 443-456.

Frank, D., Kuhn, C., Brors, B., Hanselmann, C., Lüdde, M., Katus, H.A. & Frey, N., 2008. Gene expression pattern in biomechanically stretched cardiomyocytes: evidence for a stretch-specific gene program. *Hypertension*, 51(2): 309-318.

Fraysse, B., Weinberger, F., Bardswell, S.C., Cuello, F., Vignier, N., Geertz, B., Starbatty, J., Krämer, E., Coirault, C., Eschenhagen, T., Kentish, J.C., Avkiran, M. & Carrier, L., 2012. Increased myofilament Ca(2+) sensitivity and diastolic dysfunction as early consequences of Mybpc3 mutation in heterozygous knock-in mice. *J Mol Cell Cardiol,* 52(6): 1299-307.

Frerich, B., Lindemann, N., Kurtz-Hoffmann, J. & Oertel, K., 2001. In vitro model of a vascular stroma for the engineering of vascularized tissues. *Int J Oral Maxillofac Surg*, 30(5): 414-20.

Friedrich, F.W., Bausero, P., Sun, Y., Treszl, A., Kramer, E., Juhr, D., Richard, P., Wegscheider, K., Schwartz, K., Brito, D., Arbustini, E., Waldenstrom, A., Isnard, R., Komajda, M., Eschenhagen, T., Carrier, L., 2009. A new polymorphism in human calmodulin III gene promoter is a potential modifier gene for familial hypertrophic cardiomyopathy. *Eur Heart J*, 30(13): 1648-1655.

Friedrich, F.W. & Carrier, L., 2012. Genetics of hypertrophic and dilated cardiomyopathy. *Curr Pharm Biotechnol*.

Fujio, Y., Nguyen, T., Wencker, D., Kitsis, R.N. & Walsh, K., 2000. Akt Promotes Survival of Cardiomyocytes In Vitro and Protects Against Ischemia-Reperfusion Injury in Mouse Heart. *Circulation*, 101(6): 660-667.

Geisterfer-Lowrance, A.A., Kass, S., Tanigawa, G., Vosberg, H.P., McKenna, W.J., Seidman, C.E. & Seidman, J.G., 1990. A molecular basis for familial hypertrophic cardiomyopathy: a beta cardiac myosin heavy chain gene missense mutation. *Cell*, 62(5): 999-1006.

Gersh, B.J., Maron, B.J., Bonow, R.O., Dearani, J.A., Fifer, M.A., Link, M.S., Naidu, S.S., Nishimura, R.A., Ommen, S.R., Rakowski, H., Seidman, C.E., Towbin, J.A., Udelson, J.E. & Yancy, C.W., 2011. 2011 ACCF/AHA guideline for the diagnosis and treatment of hypertrophic cardiomyopathy: executive summary: a report of the American College of Cardiology Foundation/American Heart Association Task Force on Practice Guidelines. *Circulation*, 124(24): 2761-96.

Gosain, A., Matthies, A.M., Dovi, J.V., Barbul, A., Gamelli, R.L. & DiPietro, L.A., 2006. Exogenous pro-angiogenic stimuli cannot prevent physiologic vessel regression. *J Surg Res*, 135(2): 218-25.

Griffioen, A.W. & Molema, G., 2000. Angiogenesis: potentials for pharmacologic intervention in the treatment of cancer, cardiovascular diseases, and chronic inflammation. *Pharmacol Rev*, 52(2): 237-68.

Grynkiewicz, G., Poenie, M. & Tsien, R.Y., 1985. A new generation of Ca2+ indicators with greatly improved fluorescence properties. *J Biol Chem*, 260(6): 3440-50.

Hanrath, P., Mathey, D.G., Kremer, P., Sonntag, F. & Bleifeld, W., 1980. Effect of verapamil on left ventricular isovolumic relaxation time and regional left ventricular filling in hypertrophic cardiomyopathy. *Am J Cardiol*, 45(6): 1258-64.

Hansen, A., Eder, A., Bönstrup, M., Flato, M., Mewe, M., Schaaf, S., Aksehirlioglu, B., Schwoerer, A.P., Schwörer, A., Uebeler, J. & Eschenhagen, T., 2010. Development of a drug screening platform based on engineered heart tissue. *Circ Res*, 107(1): 35-44.

Harris, S.P., 2002. Hypertrophic Cardiomyopathy in Cardiac Myosin Binding Protein-C Knockout Mice. *Circ Res*, 90(5): 594-601.

Hasenfuss, G., Mulieri, L.A., Blanchard, E.M., Holubarsch, C., Leavitt, B.J., Ittleman, F. & Alpert, N.R., 1991. Energetics of isometric force development in control and volume- overload human myocardium. Comparison with animal species. *Circ Res*, 68(3): 836-846.

Hasenfuss, G. & Pieske, B., 2002. Calcium cycling in congestive heart failure. *J Mol Cell Cardiol*, 34(8): 951-69.

Ho, K.K., Pinsky, J.L., Kannel, W.B. & Levy, D., 1993. The epidemiology of heart failure: the Framingham Study. *J Am Cell Cardiol*, 22(4 Suppl A): 6A-13A.

Hobai, I.A. & O'Rourke, B., 2001. Decreased sarcoplasmic reticulum calcium content is responsible for defective excitation-contraction coupling in canine heart failure. *Circulation*, 103(11): 1577-84.

Hofmann, P.A., Greaser, M.L. & Moss, R.L., 1991. C-protein limits shortening velocity of rabbit skeletal muscle fibres at low levels of Ca2+ activation. *J Physiol*, 439: 701-15.

Houser, S.R., Margulies, K.B., Murphy, A.M., Spinale, F.G., Francis, G.S., Prabhu, S.D., Rockman, H.A., Kass, D.A., Molkentin, J.D., Sussman, M.A. & Koch, W., 2012. Animal Models of Heart Failure: A Scientific Statement From the American Heart Association. *Circ Res*, 111(1): 131-150.

Hubbell, J.A., 2003. Materials as morphogenetic guides in tissue engineering. *Curr Opin Biotechnol*, 14(5): 551-8.

Huke, S. & Knollmann, B.C., 2010. Increased myofilament Ca2+-sensitivity and arrhythmia susceptibility. *J Mol Cell Cardiol,* 48(5): 824-33.

Indra, A.K., Warot, X., Brocard, J., Bornert, J.M., Xiao, J.H., Chambon, P. & Metzger, D., 1999. Temporally-controlled site-specific mutagenesis in the basal layer of the epidermis: comparison of the recombinase activity of the tamoxifen-inducible Cre-ER(T) and Cre-ER(T2) recombinases. *Nucleic Acids Res*, 27(22): 4324-7.

Isenberg, B.C., Williams, C. & Tranquillo, R.T., 2006. Small-diameter artificial arteries engineered in vitro. *Circ Res*, 98(1): 25-35.

Ishikawa, K., Tilemann, L., Fish, K. & Hajjar, R.J., 2011. Gene delivery methods in cardiac gene therapy. *J Gene Med*, 13(10): 566-72.

Itzhaki, I., Maizels, L., Huber, I., Zwi-Dantsis, L., Caspi, O., Winterstern, A., Feldman, O., Gepstein, A., Arbel, G., Hammerman, H., Boulos, M. & Gepstein, L., 2011. Modelling the long QT syndrome with induced pluripotent stem cells. *Nature*, 471(7337): 225-9.

Jackson, G., Gibbs, C.R., Davies, M.K. & Lip, G.Y., 2000. ABC of heart failure. Pathophysiology. *BMJ,* 320(7228): 167-70.

Jaisser, F., 2000. Inducible gene expression and gene modification in transgenic mice. *J Am Sac Nephrol*, 11 Suppl 1: S95-S100.

Jakob, W., Jentzsch, K.D., Mauersberger, B. & Heder, G., 1978. The chick embryo choriallantoic membrane as a bioassay for angiogenesis factors: reactions induced by carrier materials. *Exp Pathol*, 15(5): 241-9.

Janmey, P., Winer, J.P. & Weisel, J.W., 2009. Fibrin gels and their clinical and bioengineering applications. *J R Soc Interface*, 6(30): 1-10.

Janssen, P.M., Stull, L.B. & Marbán, E., 2002. Myofilament properties comprise the rate-limiting step for cardiac relaxation at body temperature in the rat. *Am J Physiol*, 282(2): H499-507.

Katz, A.M. & Katz, P.B., 1989. Homogeneity out of heterogeneity. *Circulation*, 79(3): 712-717.

Kelly, D.P. & Strauss, A.W., 1994. Inherited cardiomyopathies. *N Engl J Med*, 330(13): 913-9.

Kisanuki, Y.Y., Hammer, R.E., Miyazaki, J., Williams, S.C., Richardson, J.A. & Yanagisawa, M., 2001. Tie2-Cre transgenic mice: a new model for endothelial cell-lineage analysis in vivo. *Dev Biol*, 230(2): 230-42.

Kock, L., Donkelaar, C.C. van & Ito, K., 2012. Tissue engineering of functional articular cartilage: the current status. *Cell Tissue Res*, 347(3): 613-27.

Konno, T., Chang, S., Seidman, J.G. & Seidman, C.E., 2010. Genetics of hypertrophic cardiomyopathy. *Curr Opin Cardiol*, 25(3): 205-9.

Korte, F.S., McDonald, K.S., Harris, S.P. & Moss, R.L., 2003. Loaded shortening, power output, and rate of force redevelopment are increased with knockout of cardiac myosin binding protein-C. *Circ Res*, 93(8): 752-8.

Krenning, G., Zeisberg, E.M. & Kalluri, R., 2010. The origin of fibroblasts and mechanism of cardiac fibrosis. *J Cell Physiol*, 225(3): 631-7.

Kunst, G., Kress, K.R., Gruen, M., Uttenweiler, D., Gautel, M. & Fink, R.H., 2000. Myosin Binding Protein C, a Phosphorylation-Dependent Force Regulator in Muscle That Controls the Attachment of Myosin Heads by Its Interaction With Myosin S2. *Circ Res*, 86(1): 51-58.

Laks, M.M. & Morady, F., 1976. Norepinephrine--the myocardial hypertrophy hormone? *Am Heart J*, 91(5): 674-5.

Lampugnani, M.G., Corada, M., Caveda, L., Breviario, F., Ayalon, O., Geiger, B. & Dejana, E., 1995. The molecular organization of endothelial cell to cell junctions: differential association of plakoglobin, beta-catenin, and alpha-catenin with vascular endothelial cadherin (VE-cadherin). *J Cell Biol*, 129(1): 203-17.

de Lange, W.J., Hegge, L.F., Grimes, A.C., Tong, C.W., Brost, T.M., Moss, R.L. & Ralphe, J.C., 2011. Neonatal mouse-derived engineered cardiac tissue: a novel model system for studying genetic heart disease. *Circ Res*, 109(1): 8-19.

Lau, F., Ahfeldt, T., Osafune, K., Akustsu, H. & Cowan, C.A., 2009. Induced pluripotent stem (iPS) cells: an up-to-the-minute review. *F1000 Biol Rep*, 1:84.

Laugwitz, K.L., Moretti, A., Lam, J., Gruber, P., Chen, Y., Woodard, S., Lin, L., Cai, C., Lu, M.M., Reth, M., Platoshyn, O., Yuan, J., Evans, S. & Chien, K.R., 2005. Postnatal isl1+ cardioblasts enter fully differentiated cardiomyocyte lineages. *Nature*, 433(7026): 647-53.

Lecarpentier, Y., Vignier, N., Oliviero, P., Guellich, A., Carrier, L. & Coirault, C., 2008. Cardiac Myosin-binding protein C modulates the tuning of the molecular motor in the heart. *Biophys J*, 95(2): 720-8.

Leor, J., Aboulafia-Etzion, S., Dar, A., Shapiro, L., Barbash, I.M., Battler, A., Granot, Y. & Cohen, S., 2000. Bioengineered cardiac grafts: A new approach to repair the infarcted myocardium? *Circulation*, 102(19 Suppl 3): III56-61.

Li, R.K., Jia, Z.Q., Weisel, R.D., Mickle, D.A., Choi, A. & Yau, T.M., 1999. Survival and function of bioengineered cardiac grafts. *Circulation*, 100(19 Suppl): II63-9.

Lindner, G., Horland, R., Wagner, I., Ataç, B. & Lauster, R., 2011. De novo formation and ultra-structural characterization of a fiber-producing human hair follicle equivalent in vitro. *J Biotechnol*, 152(3): 108-12.

Long, C.S., Henrich, C.J. & Simpson, P.C., 1991. A growth factor for cardiac myocytes is produced by cardiac nonmyocytes. *Cell Regul*, 2(12): 1081-95.

Lopez, A.D., Mathers, C.D., Ezzati, M., Jamison, D.T. & Murray, C.J., 2006. Global and regional burden of disease and risk factors, 2001: systematic analysis of population health data. *Lancet*, 367(9524): 1747-57.

Lv, G., Shi, H., Fan, L., Feng, Z. & Wang, G., 2011. [Intensive insulin treatment protected the cardiac myocytes against apoptosis in severely scalded rats]. *Zhongguo Wei Zhong Bing Ji Jiu Yi Xue*, 23(12): 714-7.

Ma, T.K., Kam, K.K., Yan, B.P. & Lam, Y., 2010. Renin-angiotensin-aldosterone system blockade for cardiovascular diseases: current status. *Br J Pharmacol*, 160(6): 1273-92.

Mann, D.L., 2007. Pathophysiology of Heart Failure. In: Libby, P., Bonow, R.O., Zipes, D.P. & Mann, D.L. (Ed.), Braunwald's Heart Disease: A Textbook of Cardiovascular Medicine (8th edition). *Elsevier Inc,* 22: 541-560.

Maass, A., Langer, S.J., Oberdorf-Maass, S., Bauer, S., Neyses, L. & Leinwand, L.A., 2003. Rational promoter selection for gene transfer into cardiac cells. *J Mol Cell Cardiol*, 35(7): 823-31.

Maier, L.S., Bers, D.M. & Pieske, B., 2000. Differences in Ca(2+)-handling and sarcoplasmic reticulum Ca(2+)-content in isolated rat and rabbit myocardium. *J Mol Cell Cardiol*, 32(12): 2249-58.

Marian, A.J., 2010. Hypertrophic cardiomyopathy: from genetics to treatment. *Eur J Clin Invest*, 40(4): 360-9.

Marian, A.J. & Roberts, R., 2001. The molecular genetic basis for hypertrophic cardiomyopathy. *J Mol Cell Cardiol*, 33(4): 655-70.

Marolt, D., Campos, I.M., Bhumiratana, S., Koren, A., Petridis, P., Zhang, G., Spitalnik, P.F., Grayson, W.L. & Vunjak-Novakovic, G., 2012. Engineering bone tissue from human embryonic stem cells. *Proc Natl Acad Sci U S A,* 109(22): 8705-9.

Maron, B.J., Gardin, J.M., Flack, J.M., Gidding, S.S., Kurosaki, T.T. & Bild, D.E., 1995. Prevalence of hypertrophic cardiomyopathy in a general population of young adults. Echocardiographic analysis of 4111 subjects in the CARDIA Study. Coronary Artery Risk Development in (Young) Adults. *Circulation*, 92(4): 785-9.

Martino, M.M. & Hubbell, J.A., 2010. The 12th-14th type III repeats of fibronectin function as a highly promiscuous growth factor-binding domain. *FASEB J*, 24(12): 4711-21.

Martino, M.M., Tortelli, F., Mochizuki, M., Traub, S., Ben-David, D., Kuhn, G.A., Müller, R., Livne, E., Eming, S.A. & Hubbell, J.A., 2011. Engineering the growth factor microenvironment with fibronectin domains to promote wound and bone tissue healing. *Sci Transl Med*, 3(100): 100ra89.

Mattioni, T., Louvion, J.F. & Picard, D., 1994. Regulation of protein activities by fusion to steroid binding domains. *Methods Cell Biol*, 43 Pt A: 335-52.

Metzger, D. & Chambon, P., 2001. Site- and time-specific gene targeting in the mouse. *Methods*, 24(1): 71-80.

Monvoisin, A., Alva, J.A., Hofmann, J.J., Zovein, A.C., Lane, T.F. & Iruela-Arispe, M.L., 2006. VE-cadherin-CreERT2 transgenic mouse: a model for inducible recombination in the endothelium. *Dev Dyn,* 235(12): 3413-22.

Moretti, A., Bellin, M., Welling, A., Jung, C.B., Lam, J.T., Bott-Flügel, L., Dorn, T., Goedel, A., Höhnke, C., Hofmann, F., Seyfarth, M., Sinnecker, D., Schömig, A. & Laugwitz, K.L., 2010. Patient-specific induced pluripotent stem-cell models for long-QT syndrome. *N Engl J Med*, 363(15): 1397-409.

Müller, O.J., Leuchs, B., Pleger, S.T., Grimm, D., Franz, W.M., Katus, H.A. & Kleinschmidt, J.A., 2006. Improved cardiac gene transfer by transcriptional and transductional targeting of adeno-associated viral vectors. *Cardiovasc Res*, 70(1): 70-8.

Nabel, E.G., 2007. Principles of Cardiovascular Molecular Biology and Genetics. In: Libby, P., Bonow, R.O., Zipes, D.P. & Mann, D.L. (Ed.), Braunwald's Heart Disease: A Textbook of Cardiovascular Medicine (8th edition). *Elsevier Inc,* 7: 78-83.

Neumann, J., Eschenhagen, T., Grupp, I.L., Haverich, A., Herzig, J.W., Hirt, S., Kalmár, P., Schmitz, W., Scholz, H., Stein, B., Wenzlaff, H. & Zimmermann, N., 1996. Positive inotropic effects of the calcium sensitizer CGP 48506 in failing human myocardium. *J Pharmacol Exp Ther*, 277(3): 1579-85.

Olivotto, I., Maron, B.J., Appelbaum, E., Harrigan, C.J., Salton, C., Gibson, C.M., Udelson, J.E., O'Donnell, C., Lesser, J.R., Manning, W.J. & Maron, M.S., 2010. Spectrum and clinical significance of systolic function and myocardial fibrosis assessed by cardiovascular magnetic resonance in hypertrophic cardiomyopathy. *Am J Cardiol*, 106(2): 261-7.

Ollinger, K. & Brunmark, A., 1994. Effect of different oxygen pressures and N,N'-diphenyl-p-phenylenediamine on Adriamycin toxicity to cultured neonatal rat heart myocytes. *Biochem Pharmacol*, 48(9): 1707-15.

Opie, L.H., 2007. Mechanisms of Cardiac Contraction and Relaxation. In: Libby, P., Bonow, R.O., Zipes, D.P. & Mann, D.L. (Ed.), Braunwald's Heart Disease: A Textbook of Cardiovascular Medicine (8th edition). *Elsevier Inc,* 21: 509-539.

Packer, M., 1996. Beta-blockade in the management of chronic heart failure. Another step in the conceptual evolution of a neurohormonal model of the disease. *Eur Heart J*, 17 Suppl B: 21-3.

Palmer, B.M., Georgakopoulos, D., Janssen, P.M., Wang, Y., Alpert, N.R., Belardi, D.F., Harris, S.P., Moss, R.L., Burgon, P.G., Seidman, C.E., Seidman, J.G., Maughan, D.W. & Kass, D.A., 2004. Role of cardiac myosin binding protein C in sustaining left ventricular systolic stiffening. *Circ Res*, 94(9): 1249-55.

Pandya, N.M., Dhalla, N.S. & Santani, D.D., 2006. Angiogenesis--a new target for future therapy. *Vascul Pharmacol*, 44(5): 265-74.

Paşca, S.P., Portmann, T., Voineagu, I., Yazawa, M., Shcheglovitov, A., Paşca, A.M., Cord, B., Palmer, T.D., Chikahisa, S., Nishino, S., Bernstein, J.A., Hallmayer, J., Geschwind, D.H. & Dolmetsch, R.E., 2011. Using iPSC-derived neurons to uncover cellular phenotypes associated with Timothy syndrome. *Nat Med,* 17(12): 1657-62.

Pieske, B., Kretschmann, B., Meyer, M., Holubarsch, C., Weirich, J., Posival, H., Minami, K., Just, H. & Hasenfuss, G., 1995. Alterations in intracellular calcium handling associated with the inverse force-frequency relation in human dilated cardiomyopathy. *Circulation*, 92(5): 1169-78.

Pohlmann, L., Kroger, I., Vignier, N., Schlossarek, S., Kramer, E., Coirault, C., Sultan, K.R., El-Armouche, A., Winegrad, S., Eschenhagen, T. & Carrier, L., 2007. Cardiac myosin-binding protein C is required for complete relaxation in intact myocytes. *Circ Res*, 101(9): 928-938.

Pugh, C.W. & Ratcliffe, P.J., 2003. Regulation of angiogenesis by hypoxia: role of the HIF system. *Nat Med*, 9(6): 677-84.

Pyeritz, R.E., 2007. General Principles of Genetic Factors in Cardiovascular Disease. In: Libby, P., Bonow, R.O., Zipes, D.P. & Mann, D.L. (Ed.), Braunwald's Heart Disease: A Textbook of Cardiovascular Medicine (8th edition). *Elsevier Inc,* 8: 85-100.

Qian, L., Huang, Y., Spencer, C.I., Foley, A., Vedantham, V., Liu, L., Conway, S.J., Fu, J. & Srivastava, D., 2012. In vivo reprogramming of murine cardiac fibroblasts into induced cardiomyocytes. *Nature*, 485(7400): 593-598.

Redel, A., Baumgartner, W., Golenhofen, K., Drenckhahn, D. & Golenhofen, N., 2002. Mechanical activity and force-frequency relationship of isolated mouse papillary muscle: effects of extracellular calcium concentration, temperature and contraction type. *Pflugers Arch*, 445(2): 297-304.

Rosenkranz, S., Flesch, M., Amann, K., Haeuseler, C., Kilter, H., Seeland, U., Schlüter, K.D. & Böhm, M., 2002. Alterations of beta-adrenergic signaling and cardiac hypertrophy in transgenic mice overexpressing TGF-beta(1). *Am J Physiol Heart Circ Physiol*, 283(3): H1253-62.

Sadayappan, S., Gulick, J., Osinska, H., Martin, L.A., Hahn, H.S., Dorn, G.W., Klevitsky, R., Seidman, C.E., Seidman, J.G. & Robbins, J., 2005. Cardiac myosin-binding protein-C phosphorylation and cardiac function. *Circ Res*, 97(11): 1156-1163.

Sanbe, A., James, J., Tuzcu, V., Nas, S., Martin, L., Gulick, J., Osinska, H., Sakthivel, S., Klevitsky, R., Ginsburg, K.S., Bers, D.M., Zinman, B., Lakatta, E.G. & Robbins, J., 2005. Transgenic rabbit model for human troponin I-based hypertrophic cardiomyopathy. *Circulation*, 111(18): 2330-8.

Santos, S., Lança, V., Oliveira, H., Branco, P., Silveira, L., Marques, V., Brito, D., Madeira, H., Bicho, M. & Fernandes, A.R., 2011. Genetic diagnosis of hypertrophic cardiomyopathy using mass spectrometry DNA arrays and high resolution melting. *Rev Port Cardiol*, 30(1): 7-18.

Schaaf, S., Shibamiya, A., Mewe, M., Eder, A., Stöhr, A., Hirt, M.N., Rau, T., Zimmermann, W.H., Conradi, L., Eschenhagen, T. & Hansen, A., 2011. Human engineered heart tissue as a versatile tool in basic research and preclinical toxicology. *PloS One*, 6(10): e26397.

Schlossarek, S., Englmann, D.R., Sultan, K.R., Sauer, M., Eschenhagen, T. & Carrier, L., 2012. Defective proteolytic systems in Mybpc3-targeted mice with cardiac hypertrophy. *Basic Res Cardiol*, 107(1): 1-13.

Schlossarek, S., Mearini, G. & Carrier, L., 2011. Cardiac myosin-binding protein C in hypertrophic cardiomyopathy: mechanisms and therapeutic opportunities. *J Mol Cell Cardiol*, 50(4): 613-20.

Schober, T., Huke, S., Venkataraman, R., Gryshchenko, O., Kryshtal, D., Hwang, H.S., Baudenbacher, F.J., & Knollmann B.C., 2012. Myofilament Ca sensitization increases cytosolic Ca binding affinity, alters intracellular Ca homeostasis, and causes pause-dependent Ca-triggered arrhythmia. *Circ Res*, 111(2): 170-9.

Sekine, H., Shimizu, T., Hobo, K., Sekiya, S., Yang, J., Yamato, M., Kurosawa, H., Kobayashi, E. & Okano, T., 2008. Endothelial cell coculture within tissue-engineered cardiomyocyte sheets enhances neovascularization and improves cardiac function of ischemic hearts. *Circulation*, 118(14 Suppl): S145-52.

Senger, D.R., Galli, S.J., Dvorak, A.M., Perruzzi, C.A., Harvey, V.S. & Dvorak, H.F., 1983. Tumor cells secrete a vascular permeability factor that promotes accumulation of ascites fluid. *Science*, 219(4587): 983-5.

Shannon, T.R., Ginsburg, K.S. & Bers, D.M., 2000. Reverse mode of the sarcoplasmic reticulum calcium pump and load-dependent cytosolic calcium decline in voltage-clamped cardiac ventricular myocytes. *Biophys J*, 78(1): 322-33.

Shimizu, T., 2002. Fabrication of Pulsatile Cardiac Tissue Grafts Using a Novel 3-Dimensional Cell Sheet Manipulation Technique and Temperature-Responsive Cell Culture Surfaces. *Circ Res*, 90(3): 40e-48.

Shinoka, T., Matsumura, K., Hibino, N., Naito, Y., Murata, A., Kosaka, Y. & Kurosawa, H., 2003. [Clinical practice of transplantation of regenerated blood vessels using bone marrow cells]. *Nihon Naika Gakkai Zasshi*, 92(9): 1776-80.

Simpson, P., McGrath, A. & Savion, S., 1982. Myocyte hypertrophy in neonatal rat heart cultures and its regulation by serum and by catecholamines. *Circ Res*, 51(6): 787-801.

Staton, C.A., Stribbling, S.M., Tazzyman, S., Hughes, R., Brown, N.J. & Lewis, C.E., 2004. Current methods for assaying angiogenesis in vitro and in vivo. *Int J Exp Pathol,* 85(5): 233-248.

Stelzer, J.E., Dunning, S.B. & Moss, R.L., 2006. Ablation of cardiac myosin-binding protein-C accelerates stretch activation in murine skinned myocardium. *Circ Res*, 98(9): 1212-8.

Stevenson, L.W., 2003. Clinical use of inotropic therapy for heart failure: looking backward or forward? Part II: chronic inotropic therapy. *Circulation*, 108(4): 492-7.

Sun, N., Yazawa, M., Liu, J., Han, L., Sanchez-Freire, V., Abilez, O.J., Navarrete, E.G., Hu, S., Wang, L., Lee, A., Pavlovic, A., Lin, S., Chen, R., Hajjar, R.J., Snyder, M.P., Dolmetsch, R.E., Butte, M.J., Ashley, E.A., Longaker, M.T., Robbins, R.C & Wu, J.C., 2012. Patient-specific induced pluripotent stem cells as a model for familial dilated cardiomyopathy. *Sci Transl Med*, 4(130): 130ra47.

Sun, W., Julie Li, Y., Huang, H., Shyy, J.Y. & Chien, S., 2010. microRNA: a master regulator of cellular processes for bioengineering systems. *Annu Rev Biomed Eng*, 12: 1-27.

Sébillon, P., Bonne, G., Flavigny, J., Venin, S., Rouche, A., Fiszman, M., Vikstrom, K., Leinwand, L., Carrier, L. & Schwartz, K., 2001. COOH-terminal truncated human cardiac MyBP-C alters myosin filament organization. *C R Acad Sci III*, 324(3): 251-60.

Takahashi, K., Tanabe, K., Ohnuki, M., Narita, M., Ichisaka, T., Tomoda, K. & Yamanaka, S., 2007. Induction of pluripotent stem cells from adult human fibroblasts by defined factors. *Cell*, 131(5): 861-72.

Tamura, K., Yoshida, S., Iwai, T. & Watanabe, I., 1992. Effects of isoprenaline and ouabain on cytosolic calcium and cell motion in single rat cardiomyocytes. *Cardiovasc Res*, 26(2): 179-85.

Taniguchi, Y., Choi, P.J., Li, G.W., Chen, H., Babu, M., Hearn, J., Emili, A. & Xie, X.S., 2010. Quantifying E. coli proteome and transcriptome with single-molecule sensitivity in single cells. *Science*, 329(5991): 533-8.

Tarnavski, O., McMullen, J.R., Schinke, M., Nie, Q., Kong, S. & Izumo, S., 2004. Mouse cardiac surgery: comprehensive techniques for the generation of mouse models of human diseases and their application for genomic studies. *Physiol Genomics*, 16(3): 349-60.

Taylor, M.R., Carniel, E. & Mestroni, L., 2004. Familial hypertrophic cardiomyopathy: clinical features, molecular genetics and molecular genetic testing. *Expert Rev Mol Diagn*, 4(1): 99-113.

Tendera, M., Schneeweiss, A., Bartoszewski, A., Polonski, L., Wodniecki, J. & Salamon, A., 1993. The acute response of left ventricular filling dynamics to intravenous verapamil predicts the changes in exercise tolerance after oral verapamil therapy in patients with hypertrophic cardiomyopathy. *Eur Heart J,* 14(3): 410-5.

Tombe, P. de, 2003. Cardiac myofilaments: mechanics and regulation. *J Biomech*, 36(5): 721-30.

Tombe, P.P. de, Mateja, R.D., Tachampa, K., Ait Mou, Y., Farman, G.P. & Irving, T.C., 2010. Myofilament length dependent activation. *J Mol Cell Cardiol*, 48(5): 851-8.

Tong, C.W., Stelzer, J.E., Greaser, M.L., Powers, P.A. & Moss, R.L., 2008. Acceleration of crossbridge kinetics by protein kinase A phosphorylation of cardiac myosin binding protein C modulates cardiac function. *Circ Res*, 103(9): 974-82.

Tsutsui, H., Kinugawa, S., Ide, T., Hayashidani, S., Suematsu, N., Satoh, S., Nakamura, R., Egashira, K. & Takeshita, A., 2001. Positive inotropic effects of calcium sensitizers on normal and failing cardiac myocytes. *J Cardiovasc Pharmacol*, 37(1): 16-24.

Urech, L., Bittermann, A.G., Hubbell, J.A. & Hall, H., 2005. Mechanical properties, proteolytic degradability and biological modifications affect angiogenic process extension into native and modified fibrin matrices in vitro. *Biomaterials*, 26(12): 1369-79.

Vandenburgh, H., Shansky, J., Benesch-Lee, F., Barbata, V., Reid, J., Thorrez, L., Valentini, R. & Crawford, G., 2008. Drug-screening platform based on the contractility of tissue-engineered muscle. *Muscle Nerve*, 37(4): 438-47.

Vignier, N., Schlossarek, S., Fraysse, B., Mearini, G., Krämer, E., Pointu, H., Mougenot, N., Guiard, J., Reimer, R., Hohenberg, H., Schwartz, K., Vernet, M., Eschenhagen, T. & Carrier, L., 2009. Nonsense-mediated mRNA decay and ubiquitin-proteasome system regulate cardiac myosin-binding protein C mutant levels in cardiomyopathic mice. *Circ Res*, 105(3): 239-48.

Waagstein, F., Hjalmarson, A., Varnauskas, E. & Wallentin, I., 1975. Effect of chronic beta-adrenergic receptor blockade in congestive cardiomyopathy. *Br Heart J*, 37(10): 1022-36.

Watkins, H., Ashrafian, H. & Redwood, C., 2011. Inherited cardiomyopathies. *N Engl J Med*, 364(17): 1643-56.

Webster, K.A., Discher, D.J. & Bishopric, N.H., 1993. Induction and nuclear accumulation of fos and jun proto-oncogenes in hypoxic cardiac myocytes. *J Biol Chem*, 268(22): 16852-8.

Winegrad, S., 1999. Cardiac myosin binding protein C. *Circ Res*, 84(10): 1117-26.

Yang, Q., Hewett, T.E., Klevitsky, R., Sanbe, A., Wang, X. & Robbins, J., 2001. PKA-dependent phosphorylation of cardiac myosin binding protein C in transgenic mice. *Cardiovasc Res*, 51(1): 80-8.

Yang, Q., Sanbe, A., Osinska, H., Hewett, T.E., Klevitsky, R. & Robbins, J., 1998. A mouse model of myosin binding protein C human familial hypertrophic cardiomyopathy. *J Clin Invest*, 102(7): 1292-300.

Yang, Q., Sanbe, A., Osinska, H., Hewett, T.E., Klevitsky, R. & Robbins, J., 1999. In vivo modeling of myosin binding protein C familial hypertrophic cardiomyopathy. *Circ Res*, 85(9): 841-7.

Zeisberg, E.M., Tarnavski, O., Zeisberg, M., Dorfman, A.L., McMullen, J.R., Gustafsson, E., Chandraker, A., Yuan, X., Pu, W.T., Roberts, A.B., Neilson, E.G., Sayegh, M.H., Izumo, S. & Kalluri, R., 2007. Endothelial-to-mesenchymal transition contributes to cardiac fibrosis. *Nat Med*, 13(8): 952-61.

Zhang, J., Wilson, G.F., Soerens, A.G., Koonce, C.H., Yu, J., Palecek, S.P., Thomson, J.A. & Kamp, T.J., 2009. Functional cardiomyocytes derived from human induced pluripotent stem cells. *Circ Res*, 104(4): e30-41.

Zimmermann, W.H., Didié, M., Wasmeier, G.H., Nixdorff, U., Hess, A., Melnychenko, I., Boy, O., Neuhuber, W.L., Weyand, M. & Eschenhagen, T., 2002. Cardiac grafting of engineered heart tissue in syngenic rats. *Circulation*, 106(12 Suppl 1): I151-7.

Zimmermann, W.H., Melnychenko, I. & Eschenhagen, T., 2004. Engineered heart tissue for regeneration of diseased hearts. *Biomaterials*, 25(9): 1639-1647.

Zimmermann, W.H., Fink, C., Kralisch, D., Remmers, U., Weil, J. & Eschenhagen, T., 2000. Three-dimensional engineered heart tissue from neonatal rat cardiac myocytes. *Biotechnol Bioeng*, 68(1): 106-114.

Zimmermann, W.H., Melnychenko, I., Wasmeier, G., Didie, M., Naito, H., Nixdorff, U., Hess, A., Budinsky, L., Brune, K., Michaelis, B., Dhein, S., Schwoerer, A., Ehmke, H. & Eschenhagen, T., 2006. Engineered heart tissue grafts improve systolic and diastolic function in infarcted rat hearts. *Nat Med*, 12(4): 452-458.

Zimmermann, W.H., Schneiderbanger, K., Schubert, P., Didie, M., Munzel, F., Heubach, J.F., Kostin, S., Neuhuber, W.L. & Eschenhagen, T., 2002. Tissue engineering of a differentiated cardiac muscle construct. *Circ Res*, 90(2): 223-230.

7 Appendix

7.1 List of abbreviations

α-MHC	α-Myosin heavy chain
ACEI	Angiotensin-converting-enzyme inhibitor
Acta1	Mouse α-skeletal actin gene
A	Ampere
ADP	Adenosine diphosphate
AM	Acetoxymethyl ester
ANP	Atrial natriuretic peptide
β_1-AR	β_1-Adrenoceptor
AraC	Arabinofuranosyl cytidine
ARB	Angiotensin receptor blockers
APS	Ammonium persulfphate
ATP	Adenosine triphosphate
AU	Arbitrary unit
AV	Adenovirus
β-MHC	β-Myosin heavy chain
BMX	Bone marrow tyrosine kinase
BNP	Brain natriuretic peptide
bp	Base pair(s)
bpm	Beats per minute
BSA	Bovine serum albumin
BW	Body weight
°C	Degree Celsius
cAMP	3’,5’-Cyclic adenosine monophosphate

CBFHH	Calcium and bicarbonate Hank's buffered HEPES
CEE	Chick embryo extract
CICR	Ca^{2+}-induced Ca^{2+} release
cDNA	Complementary deoxyribonucleic acid
cMyBP-C	Cardiac myosin binding protein C
C_t	Threshold Cycle
cTn-C	Cardiac troponin C
cTn-I	Cardiac troponin I
cTn-T	Cardiac troponin T
Cy3	Cyanine-3
D	Day
Da	Dalton
DCM	Dilated cardiomyopathy
DM	Diameter
DMEM	Dulbecco's Modified Eagle's Medium
DMSO	Dimethyl sulfoxide
DNA	Deoxyribonucleic acid
dNTP	Deoxynucleoside triphosphate
EC	Endothelial cell
EC_{50}	Effective concentration causing 50% of maximal response
ECL	Enhanced chemiluminescence
ECM	Extracellular cell matrix
EDTA	Ethylene diamine tetraacetic acid
e.g.	*exempli gratia* (for example)
EGFP	Enhanced green fluorescent protein
EHT	Engineered Heart Tissue

EMD	EMD 57033
ER	Estrogen receptor
ESC	Embryonic stem cell
et al.	*et alii* (and others)
F340/380	Fluorescence ratio with 340 and 380 nm excitation wavelength
FCS	Foetal calf serum
FGF	Fibroblast growth factor
for	Forward, 5'-3' primer
FS	Fractional shortening
g	Gram
GAPDH	Glyceraldehyde 3-phosphate dehydrogenase
GFP	Green fluorescent protein
h	Hour
HBSS	Hank's Balacned Salt Solution
HCM	Hypertrophic cardiomyopathy
H&E	Hematoxylin/Eosin
HEPES	4-(2-Hydroxyethyl)-1-piperazineethanesulfonic acid
HF	Heart failure
HIF	Hypoxia-inducible factor
HRE	HIF-response elements
HRP	Horseradish peroxidase conjugated
HS	Horse serum
HW	Heart weight
Hz	Hertz (1/s)
i.e.	*id est* (that is)
IC_{50}	Effective concentration causing 50% of maximal inhibition

Ig	Immunoglobulin
IGF	Insulin growth factor
i.p.	intraperitoneal
IPS	Induced pluripotent stem cell
i.v.	intravenous
ISO	Isoprenaline
ITS+1	Insulin, transferrin, selenium, α-linoleic acid
kb	Kilobase
kDa	Kilodalton
KI	homozygous *Mybpc3*-targeted knock-in
KO	homozygous *Mybpc3*-targeted knock-out
l	Liter
LTCC	L-type Ca^{2+}-channel
LV	Left ventricular
dLVID	Diastolic left ventricular internal diameter
LVW/BW	Left ventricular weight / body weight ratio
m	Milli- (1×10^{-3})
M	Molar
mA	Milliampere
ml	Milliliter
mM	Millimolar
nM	Nanomolar
µM	Micromolar
min	Minute
MOI	Multiplicity of infection
MRA	Aldosterone antagonists

mRNA	Messenger ribonucleid acid
Mut	Mutant
MW	Molecular weight (marker)
MyBP-C	Myosin-binding protein-C
MYBPC3	Human cMyBP-C gene
Mybpc3	Mouse cMyBP-C gene
Myh7	Mouse β-myosin heavy chain gene
n	Number of biological replicates
N	Newton (unit of force: 1 kg*m*s^{-2})
NCX	Na^{+}/Ca^{2+} exchanger
NMD	Nonsense-mediated mRNA decay
Nppa	Mouse atrial natriuretic peptide gene
No.	Number
OHT	*o*-Hydroxytamoxifen
PAGE	Polyacrylamide gel electrophoresis
PBS	Phosphate buffered saline
PCR	Polymerase chain reaction
PDE	Phosphodiesterase
PDGF	Platelet derived growth factor
PKA	cAMP-dependent protein kinase
PLB	Phospholamban
RAAS	Renin-angiotensin-aldosterone system
RNA	Ribonucleic acid
RyR	Ryanodine receptor
RT	Resting tension
RT-PCR	Reverse transcripatase-PCR

s	Second
SA	Sinoatrial node
s.c.	Subcutaneous
SDS	Sodium-dodecylsulfate
SEM	Standard error of the mean
SERCA	Sarco-endoplasmatic reticulum ATPase
SR	Sarco-endoplasmatic reticulum
TBS	Tris buffered saline
TBS-T	Tris buffered saline with tween-20
TEMED	N,N,N’, N’-Tetramethylethylenediamine
TG	Transglutaminase
Tris	Tris-(hydroxymethyl)-aminoethane
T1	Contraction time
T2	Relaxation time
T3	Triiodothyronine
TTP	Time to 100% maximal twitch force
TTP 50	Time to 50% maximal twitch force
TTR 50	Time to 50% relaxation
TTR 90	Time to 90% relaxation
U	Unit
UPS	Ubiquitin-Proteasome system
UV	Ultra-violet
V	Volt
VE-Cadherin	Vascular endothelial cadherin
VEGF	Vascular endothelial growth factor
WT	Wild-type

SI prefixes

k	Kilo (10^3)
m	Milli (10^{-3})
µ	Micro (10^{-6})
n	Nano (10^{-9})

7.2 List of chemicals

Chemical	CAS No.	H- and P- phrases	Symbol	Order No.	Company
Acetic acid	64-19-7	H: 226-314 P: 280-301-330-331-305-351-338	1, 4		Merck
Acrylamide/bis solution (29:1)	79-06-1 (Acrylamide) 110-26-9 (N-N'-Methylene-bis-acrylamide)	H: 302-312-315-317-319-340-350-361f-372 P: 201-264-280-281-305-351-338	5, 7	161-0158	Bio-Rad
Ammonium persulfate (APS)	7727-54-0	H: 272-302-315-319-335-334-317 P: 280-305+351+338-302+352-304+341-342+311	3, 7, 8	1610700	Bio-Rad
Agarose (UltraPure™)				15510-019	Invitrogen
AmpliTaq Gold® polymerase				N8080244	Applied Biosystems
Aprotinin				A1153	Sigma
L-Ascorbic acid	50-81-7				Merck
Aqua ad iniectabilia					Baxter GmbH
Betadine®					Mundipharma
(-)-Blebbistatin	856925-71-8	H: 302-312-315-317-319-332-335 P: 261-280-305+351+338	7	B0560	Sigma
Bradford reagent		H: 314 P: 260-280 301+330+331-303+361+353-304+340-305+351+338	7, 8		Bio Rad

5-bromo-4-chloro-3-indolyl-β-D-galactopyranoside (X-Gal)	7240-90-6			B4252	Sigma
Bovine serum albumin (BSA)				15561-020	Invitrogen
Bromophenol blue	115-39-9				Merck
Buprenorphine hydrochloride	53152-21-9	H: 302-361 P: 281	7, 8	_B9275	Sigma
Calcium chloride dihydrate ($CaCl_2$ x 2 H_2O)	07774-34-7	H: 319 P: 305+351+338	7		Sigma
Cremophor® EL	61791-12-6			C5135	Sigma
Cytosine β-D-arabinofuranoside	147-94-4	H: 317-361 P: 280	7, 8	C1768	Sigma
DMEM				F0415	Gibco
Dimethyl sulfoxide (DMSO)	67-68-5			317275	Merck
1,4-Dithiothreitol (DTT)	3483-12-3	H: 302-315-319 P: 302+352-305+351+338	7	D0632	Sigma
ECL plus Western blotting detection system					Amersham Biosciences
EMD 57033 ((+)-5-(1-(3,4-Dimethoxybenzoyl)-1,2,3,4-tetrahydrochinolin-6-yl)-6-methyl-3,6-dihydro-2H-1,3,4-thiadiazin-2-on)	150151-10-3				Merck
Eosin solution	21514-87-4	H: 225-302-371 P: 210-233-240-260-403+235	2, 7, 8		Merck
Ethanol (96%)	64-17-5	H: 225 P: 210	2		Geyer
Ethidium bromide	1239-45-8	H: 341-330-302 P: 281-302+352-305+351+338-304+340-309-310	6, 8		Fluka
Eukitt	25608-33-7	H: 226-312-315-332 P: 280	2, 7		O. Kindler
Factor XIII (Fibrogammin®)					CSL Behring
Formaldehyde	50-00-0	H: 228-302-332-351-335-315-319-317 P: 281-302+352-305+351+338-405-501	4, 5, 7		Merck
Fura-2 AM	108964-32-5			F-1201	Invitrogen/Molecular Probes™

Gene Ruler™ 100 bp, 1 kb, 1 kb plus DNA ladder		H: 315-319-335-360 P: 201-261-305+351+338-308+313	7, 8		Fermentas
Fibrinogen (bovine)				F8630	Sigma
Fibrinogen (human)					Enzyme Research Laboratories
D-(+)-Glucose, anhydrous	50-99-7				Sigma
Glutaraldehyde	111-30-8	H: 331-301-314-334-317-400			Agar Scientific
Glycerol	56-81-5				Merck
Glycine	56-40-6				Roth
4-(2-hydroxyethyl)-1-piperazineethanesulfonic acid (HEPES)	7365-45-9				Roth
Hemalum/hematoxylin solution (Mayer)	517-28-2	H: 302-315-319-335 P: 261-305+351+338	7		Roth
Heparin sulphate sodium salt	9005-49-6				Sigma
Histofix®		H: 302+332-317-351 P: 281-302+352-308+313-501	7, 8		Roth
Hydrochloric acid, 37% solution	7647-01-0	H: 314-335 P: 260-301+330+331-303+361+353-305+351+338-405-501	5, 7		Merck
4-Hydroxy-tamoxifen	68392-35-8	H: 302-312-332-361 P: 280	7, 8	H6278	Sigma
IGF-1					Sigma
Insulin				I9278	Sigma
Isoprenaline hydrochloride	51-30-9	H: 315-319-335 P: 261-305+351+338	7		Sigma
Isopropyl alcohol	67-63-0	H: 225-319-336 P: 210-233-305+351+338	2, 7		Merck
Isotonic 0.9% sodium chloride solution					Baxter
ITS+1 (Insulin, transferring, selenium, linoleic acid)				I2521	Sigma
LipofectAMINE™ 2000					Invitrogen
Loading dye, 6x		H: 315-319-335-360 P: 201-261-305+351+338-	7, 8		Fermentas

		308+313			
Magnesium chloride hexahydrate ($MgCl_2$ x 6 H_2O)	7791-18-6				Merck
Magnesium sulphate heptahydrate ($MgSO_4$ x 7 H_2O)	10034-99-8				Merck
Matrigel				354234	BD Bioscience
Milk powder					Roth
Mowiol 4-88	9002-89-5				Hoechst
Novaminsulfon-ratiopharm® Tropfen					Ratiopharm
PDGF-BB					Sigma
Ponceau S	6226-79-5	H: 315-319-335 P: 261-305+351+338	7		Sigma
Potassium chloride (KCl)	7447-40-7				Merck
Potassium hydrogen carbonate ($KHCO_3$)	298-14-6				Merck
Potassium dihydrogen phosphate (KH_2PO_4)	7778-77-0				Merck
Potassium ferricyanide crystalline ($K_3[Fe(CN)_6]$)	13746-66-2				Merck
Potassium ferricyanide trihydrate ($K_4[Fe(CN)_6]$ x $3H_2O$)	14459-95-1				Merck
Precision Plus Protein Standard™		H: 228-311-302-335-315-319 P: 210-280-304+340-305+351+338-309+310	2, 6		Bio-Rad
Rompun® (1.6 mg xylazine/ 12 mg ketamine)	Xylazine: 7361-61-7 Ketamine: 6740-88-1	Xylazine: H: 301 P: 301+310 Ketamine: H: 302-315-319-335 P: 261-305+351+338	Xylazine: 6 Ketamine: 7		Bayer
Sodium azide	26628-22-8	H: 300-400-410 P: 273-309-310	6, 9		Sigma
Sodium chloride (NaCl)					J.T. Baker
Sodium dodecyl sulphate (SDS)	151-21-3	H: 228-311-302-335-315-319 P: 210-280-	2, 6		Roth

		304+340-305+351+338-309+310			
Sodium fluoride (NaF)	7681-49-4	H: 301-319-315 P: 305+351+338-302+352-309-310	6		Merck
Sodium dihydrogen phosphate monohydrate (NaH_2PO_4 x H_2O)	10049-21-5				Merck
Sodium hydrogen carbonate ($NaHCO_3$)	144-55-8				Merck
Sodium hydroxide (NaOH)	1310-73-2	H: 314 P: 280-301+330+331-309-310-305+351+338	5		Merck
SuperSignal® West Dura					Thermo Scientific
Tamoxifen	10540-29-1	H: 350-360-362 P: 201-263-308+313	8	T5648	Sigma
TaqMan® Universal PCR Master Mix					Applied Biosystems
N,N,N‘,N‘-Tetramethylethylenediamine (TEMED)	110-18-9	H: 225-332-302-314 P: 210-233-280-301+330+331-305+351+338-309+310	2, 5, 7		Bio-Rad
TG-IGF, TG-PDGF, TG-VEGF					Laboratory J. Hubbell; Mikael Martino, École Polytechnique Fédérale de Lausanne
Thrombin				T7513	Sigma
Trishydroxymethylaminomethane (Tris) base	77-86-1	H. 315-319-335 P: 261-305+351+338	7		Sigma
Tris hydrochloride (Tris-HCl)	1185-53-1				Promega
Triton X-100	9002-93-1	H: 302-318 P: 280-305+351+338	5, 7		Sigma
TRIzol®		H: 330-301-311-314-341-373-412 P: 301-330+331+310-304+340-305+351+338-303+361+353-309+311-403+233-280-284-271-	5, 6	15596026	Invitrogen

		260-264-273			
Trypsin				D0152-15	BD
Polyoxyethylene (20) sorbitan monolaurate (Tween® 20)	9005-64-5				Sigma
VEGF-A_{165}					R&B Systems
Verapamil hydrochloride	152-11-4	H301-311-331 P: 261-280-301+310-311	6	V4629	Sigma

7.3 H- & P-Phrases

H-Phrases **P-Phrases**

Code	Text	Code	Text
H200	Unstable explosive	P101	If medical advice is needed, have product container or label at hand
H201	Explosive; mass explosion hazard	P102	Keep out of reach of children
H202	Explosive; severe projection hazard	P103	Read label before use
H203	Explosive; fire, blast or projection hazard	P201	Obtain special instructions before use
H204	Fire or projection hazard	P202	Do not handle until all safety precautions have been read and understood
H205	May mass explode in fire	P210	Keep away from heat/sparks/open flames/hot surfaces – No smoking
H220	Extremely flammable gas	P211	Do not spray on an open flame or other igntion source
H221	Flammable gas	P220	Keep/Store away from clothing/…/combustible materials
H222	Extremely flammable material	P221	Take any precaustion to avoid mixinn with combustibles
H223	Flammable material	P222	Do not allow contact with air
H224	Extremely flammable liquid and vapour	P223	Keep away from any possible contact with water, because of violent reaction and possible flash fire
H225	Highly flammable liquid and vapour	P230	Keep wetted with …
H226	Flammable liquid and vapour	P231	Handle under inert gas
H227	Combustible liquid	P232	Protect from moisture
H228	Flammable solid	P233	Keep container tightly closed
H240	Heating may cause an explosion	P234	Keep only in original container
H241	Heating may cause a fire or explosion	P235	Keep cool
H242	Heating may cause a fire	P240	Ground/bond container and receiving equipment
H250	Catches fire spontaneously if	P241	Use explosion-proof electrical/ventilating/light/…/equipment

	exposed to air		
H251	Self-heating; may catch fire	P242	Use only non-sparking tools
H252	Self-heating in large quantities; may catch fire	P243	Take precautionary measures against static discharge
H260	In contact with water releases flammable gases which may ignite spontaneously	P244	Keep reduction valves free from grease and oil
H261	In contact with water releases flammable gas	P250	Do not subject to grinding/shock/…/friction
H270	May cause or intensify fire; oxidizer	P251	Pressurized container – Do not pierce or burn, even after use
H271	May cause fire or explosion; strong oxidizer	P260	Do not breathe dust/fume/gas/mist/vapours/spray
H272	May intensify fire; oxidizer	P261	Avoid breathing dust/fume/gas/mist/vapours/spray
H280	Contains gas under pressure; may explode if heated	P262	Do not get in eyes, on skin, or on clothing
H281	Contains refrigerated gas; may cause cryogenic burns or injury	P263	Avoid contact during pregnancy/while nursing
H290	May be corrosive to metals	P264	Wash … thoroughly after handling
H301	Toxic if swallowed	P270	Do not eat, drink or smoke when using this product
H302	Harmful if swallowed	P271	Use only outdoors or in a well-ventilated area
H303	May be harmful if swallowed	P272	Contaminated work clothing should not be allowed out of the workplace
H304	May be fatal if swallowed and enters airways	P273	Avoid release to the environment
H305	May be harmful if swallowed and enters airways	P280	Wear protective gloves/protective clothing/eye protection/face protection
H310	Fatal in contact with skin	P281	Use personal protective equipment as required
H311	Toxic in contact with skin	P282	Wear cold insulating gloves/face shield/eye protection
H312	Harmful in contact with skin	P283	Wear fire/flame resistant/retardant clothing
H313	May be harmful in contact with skin	P284	Wear respiratory protection
H314	Causes severe skin burns and eye damage	P285	In case of inadequate ventilation wear respiratory protection
H315	Causes skin irritation	P231+232	Handle under inert gas. Protect from moisture
H316	Causes mild skin irritation	P235+410	Keep cool. Protect from sunlight
H317	May cause an allergic skin reaction	P301	IF SWALLOWED:
H318	Causes serious eye damage	P302	IF ON SKIN:
H319	Causes serious eye irritation	P303	IF ON SKIN (or hair):
H320	Causes eye irritation	P304	IF INHALED:
H330	Fatal if inhaled	P305	IF IN EYES:

H331	Toxic if inhaled	P306	IF ON CLOTHING:
H332	Harmful if inhaled	P307	IF exposed:
H333	May be harmful if inhaled	P308	IF exposed or concerned:
H334	May cause allergy or asthma symptoms or breathing difficulties if inhaled	P309	IF exposed or you feel unwell:
H335	May cause respiratory irritation	P310	Immediately call a POISON CENTER or doctor/physician
H336	May cause drowsiness or dizziness	P311	Call a POISON CENTER or doctor/physician
H340	May cause genetic defects	P312	Call a POISON CENTER or doctor/physician if you feel unwell
H341	Suspected of causing genetic defects	P313	Get medical advice/attention
H350	May cause cancer	P314	Get Medical advice/attention if you feel unwell
H351	Suspected of causing cancer	P315	Get immediate medical advice/attention
H360	May damage fertility or the unborn child	P320	Specific treatment is urgent (see … on this label)
H361	Suspected of damaging fertility or the unborn child	P321	Specific treatment (see … on this label)
H362	May cause harm to breast-fed children	P322	Specific measures (see … on this label)
H370	Causes damage to organs	P330	Rinse mouth
H371	May cause damage to organs	P331	Do NOT induce vomiting
H372	Causes damage to organs through prolonged or repeated exposure	P332	If skin irritation occurs:
H373	May cause damage to organs through prolonged or repeated exposure	P333	If skin irritation or a rash occurs:
H400	Very toxic to aquatic life	P334	Immerse in cool water/wrap in wet bandages
H401	Toxic to aquatic life	P335	Brush off loose particles from skin
H402	Harmful to aquatic life	P336	Thaw frosted parts with lukewarm water. Do not rub affected areas
H410	Very toxic to aquatic life with long lasting effects	P337	If eye irritation persists:
H411	Toxic to aquatic life with long lasting effects	P338	Remove contact lenses if present and easy to do. continue rinsing
H412	Harmful to aquatic life with long lasting effects	P340	Remove victim to fresh air and keep at rest in a position comfortable for breathing
H413	May cause long lasting harmful effects to aquatic life	P341	If breathing is difficult, remove victim to fresh air and keep at rest in a position comfortable for breathing
EUH001	Explosive when dry	P342	If experiencing respiratory symptoms:
EUH006	Explosive with or without	P350	Gently wash with soap and water

	contact with air		
EUH014	Reacts violently with water	P351	Rinse continuously with water for several minutes
EUH018	In use may form flammable/explosive vapour-air mixture	P352	Wash with soap and water
EUH019	May form explosive peroxides	P353	Rinse skin with water/shower
EUH044	Risk of explosion if heated under confinement	P360	Rinse immediately contaminated clothing and skin with plenty of water before removing clothes
EUH029	Contact with water liberates toxic gas	P361	Remove/Take off immediately all contaminated clothing
EUH031	Contact with acids liberates toxic gas	P362	Take off contaminated clothing and wash before reuse
EUH032	Contact with acids liberates very toxic gas	P363	Wash contaminated clothing before reuse
EUH066	Repeated exposure may cause skin dryness or cracking	P370	In case of fire:
EUH070	Toxic by eye contact	P371	In case of major fire and large quantities:
EUH071	Corrosive to the respiratory tract	P372	Explosion risk in case of fire
EUH059	Hazardous to the ozone layer	P373	DO NOT fight fire when fire reaches explosives
EUH201	Contains lead. Should not be used on surfaces liable to be chewed or sucked by children.	P374	Fight fire with normal precautions from a reasonable distance
EUH201A	Warning! Contains lead.	P375	Fight fire remotely due to the risk of explosion
EUH202	Cyanoacrylate. Danger. Bonds skin and eyes in seconds. Keep out of the reach of children.	P376	Stop leak if safe to do so
EUH203	Contains chromium(VI). May produce an allergic reaction.	P377	Leaking gas fire – do not extinguish unless leak can be stopped safely
EUH204	Contains isocyanates. May produce an allergic reaction.	P378	Use … for extinction
EUH205	Contains epoxy constituents. May produce an allergic reaction.	P380	Evacuate area
EUH206	Warning! Do not use together with other products. May release dangerous gases (chlorine).	P381	Eliminate all ignition sources if safe to do so
EUH207	Warning! Contains cadmium. Dangerous fumes are formed	P390	Absorb spillage to prevent material damage

	during use. See information supplied by the manufacturer. Comply with the safety instructions.		
EUH208	Contains . May produce an allergic reaction.	P391	Collect spillagee
EUH209	Can become highly flammable in use.	P301+310	IF SWALLOWED: Immediately call a POISON CENTER or doctor/physician
EUH209A	Can become flammable in use.	P301+312	IF SWALLOWED: Call a POISON CENTER or doctor/physician if you feel unwell
EUH210	Safety data sheet available on request.	P301+330+331	IF SWALLOWED: Rinse mouth. Do NOT induce vomiting
EUH401	To avoid risks to human health and the environment, comply with the instructions for use.	P302+334	IF ON SKIN: Immerse in cool water/wrap in wet bandages
P371+380+375	In case of major fire and large quantities: Evacuate area. Fight fire remotely due to the risk of explosion	P302+350	IF ON SKIN: Gently wash with soap and water
P401	Store …	P302+352	IF ON SKIN: Wash with soap and water
P402	Store in a dry place	P303+361+353	IF ON SKIN (or hair): Remove/Take off immediately all contaminated clothing. Rinse skin with water/shower
P403	Store in a well ventilated place	P304+312	IF INHALED: Call a POISON CENTER or doctor/physician if you feel unwell
P404	Store in a closed container	P304+340	IF INHALED: Remove victim to fresh air and keep at rest in a position comfortable for breathing
P405	Store locked up	P304+341	IF INHALED: If breathing is difficult, remove victim to fresh air and keep at rest in a position comfortable for breathing
P406	Store in a corrosive resistant/… container with a resistant inner liner	P305+351+338	IF IN EYES: Rinse continuously with water for several minutes. Remove contact lenses if present and easy to do – continue rinsing
P407	Maintain air gap between stacks/pallets	P306+360	IF ON CLOTHING: Rinse immediately contaminated clothing and skin with plenty of water before removing clothes
P410	Protect from sunlight	P307+311	IF exposed: Call a POISON CENTER or doctor/physician
P411	Store at temperatures not exceeding … °C/… °F	P308+313	IF exposed or concerned: Get medical advice/attention
P412	Do not expose to temperatures exceeding 50 °C/122 °F	P309+311	IF exposed or you feel unwell: Call a POISON CENTER or doctor/physician
P420	Store away from other materials	P332+313	IF skin irritation occurs: Get medical advice/attention
P422	Store contents under …	P333+313	IF skin irritation or a rash occurs: Get medical advice/attention
P402+404	Store in a dry place. Store in a closed container	P335+334	Brush off loose particles from skin. Immerse in cool water/wrap in wet bandages
P403+233	Store in a well ventilated place. Keep container tightly closed	P337+313	Get medical advice/attention
P403+235	Store in a well ventilated place. Keep cool	P342+311	Call a POISON CENTER or doctor/physician
P410+403	Protect from sunlight. Store in a well ventilated place	P370+376	In case of fire: Stop leak if safe to do so

P410+412	Protect from sunlight. Do not expose to temperatures exceeding 50 °C/122 °F	P370+378	In case of fire: Use … for extinction
P411+235	Store at temperatures not exceeding … °C/… °F. Keep cool	P370+380	In case of fire: Evacuate area
P501	Dispose of contents/container to …	P370+380+375	In case of fire: Evacuate area. Fight fire remotely due to the risk of explosion

7.4 Consumable material

Materials	Company
Blotting paper (Watman 3 MM)	Schleicher & Schuell
Biosphere® pipette tips	Sarstedt
Cell strainer	Becton Dickinson
Cover glasses 24 x 60 mm	Marienfeld
Cuvettes (10 x 4 x 45 mm)	Sarstedt
Culture plates (24 well)	Nunc
Disposable syringes	Braun
Falcon tubes (15 and 50 ml)	Sarstedt
Glassware	Schott Duran
IWAKI® cell culture plate (24 well, glass bottom)	Dunn
Latex gloves	Paul Hartmann
Microscope slides	Paul Marienfeld
Micro tubes (1.5, 2.0 ml)	Sarstedt
Nitrile gloves	Ansell
Nitrocellulose membrane (Protran® BA 85)	Schleicher & Schuell
Nylon membrane (Hybond N+)	Amersham Biosciences
PCR tubes	Sarstedt
Petri dishes, 10 mm	Sarstedt
Serological pipettes (2, 5, 10 and 25 ml)	Sarstedt
Serological pipettes (10 ml, wide tip)	Becton Dickinson
Sterican® disposable cannulas	Braun
Sterile filter (0.22 µm)	Sarstedt

7.5 Laboratory equipment

Materials	Company
Accu jet® pipette controller	Brand
Agarose *GEL Electrophoresis System* GT	Bio-Rad
Analytical balance (GENIUS)	Sartorius AG
Arc lamp power supply	Caim Research
Benchtop centrifuge	Sarstedt AG & Co.
Blotting system (Mini Trans-Blot® cell)	Bio-Rad
Centrifuge (5810 R)	Eppendorf AG
Centrifuge (J-6B)	Beckman Instruments
Chemie Genius^2 Bio imaging system with Gene Tools software	Syngene
Electrophoresis system (Sub-Cell GT)	Bio-Rad
Electrophoresis system (Mini Protean® electrophoresis cell)	Bio-Rad
Fluorescence System Interface	IonOptix Corporation
Force transducers	G. Jäckel
Generation I (Set-up for video optical recording)	Own production
Generation II (Set-up for simultaneous force and Ca^{2+} transient measurements)	Own production
HyperSwitch high intensitiy arc lamp	IonOptix Corporation
Ice machine	Scotsman
Incubators (B 5050 E and Hera cell 240)	Heraeus Instruments
Incubator shaker (C25 classic)	New Brunswick Scientific
Magnetic stirrer (IKAMAG® RCT)	Janke & Kunkel GmbH
Microcentrifuge (5415 R)	Eppendorf AG
Microscope (Axiovert 25)	Carl Zeiss
Microscope (Axiovert 200M)	Carl Zeiss
Microscope (Axiovert 200M) with a 63x-oil objective and with a LSM 5 image system	Carl Zeiss
Microwave	Sharp
Multiplate reader	Tecan
MyoCam	IonOptix Corporation
MyoPacer field stimulator	IonOptix Corporation
Nano Drop spectrometer	ThermoFisher scientific

Neubauer chamber	Glaswarenfabrik Karl Hecht KG
PCR cycler (GeneAmp® PCR system 9700)	Applied Biosystems
PCR sprint thermal cycler	Thermo Hybaid
Perfusion system	Own production
Peristaltic pump	Pharmacia
pH-meter	Knick GmbH
Pipettes (10, 100, 1000 µl)	Eppendorf AG
Portable balance (Scout™ Pro)	Ohaus
Tissue Lyser	Quiagen
Spectrophotometer (Smart Spec™ 3000)	Bio-Rad
Sterile work bench (Lamin Air HB 2448)	Heraeus Instruments
Surgical instruments	Karl Hammacher GmbH
Taqman ABI Prism 7900HT SDS 2.4 software	Applied Biosystems
Thermomixer comfort	Eppendorf AG
Ultra-pure water system Milli-Q plus	Millipore
Videopower	IonOptix
Vortexer (Reax 200)	Heidolph
Water bath	GFL

7.6 Antibody list

Table 7.1. Antibodies used for Western blotting.

Primary antibody	Dilution	Company	Secondary antibody	Dilution
α-sarcomeric actinin (monoclonal)	1:1000	Sigma	anti-mouse HRP	1:20 000
ANP (monoclonal)	1:1000	Santa Cruz	anti-mouse HRP	1:10 000
β-MHC (monoclonal)	1:4000	Sigma	anti-mouse HRP	1:20 000
cMyBP-C (C0-C1; polyclonal)	1:15 000	Gift of S. Saddayappan	anti-rabbit HRP	1:6000
p44/42 MAPK (Erk1/2; polyclonal)	1:1000	Cell Signaling	anti-rabbit HRP	1:10 000

Table 7.2. Antibodies used for immunofluorescence or immunohistochemistry.

Primary antibody	Dilution	Company	Secondary antibody	Dilution
α-sarcomeric actinin (monoclonal)	1:800	Sigma	anti-mouse IgG, Alexa Fluor-488	1:800
β-galactosidase	1:400	Abcam	anti-rabbit IgG, Alexa Fluor-546	1:800
Connexin-43 (monoclonal)	1:250	BD Transduction Laboratories		
DRUQ5	1:1000	Biostatus Limited		
cMyBP-C (C0-C2; polyclonal)	1:200	Gift of S. Winegrad	anti-rabbit IgG, Alexa Fluor-546	1:800
Phalloidin Alexa Fluor-488	1:60	Molecular Probes		

7.7 Primer list and other tables

Table 7.3. Primers used for genotyping.

Mouse line	Primer name	Primer sequence (5'-3')
Rosa26R	R1295	GCGAAGAGTTTGTCCTCAACC
	R523	GGAGCGGGAGAAATGGATATG
	R26F2	AAAGTCGCTCTGAGTTGTTAT
BMX (PAC)-CreER^{T2}	BMX-s7	AAATACCTTCAGTTTTCATCT
	PAC-Cre-as1	TTGCGAACCTCATCACTCGTT
VE-Cadherin (PAC)-CreER^{T2}	CRE1	GCCTGCATTACCGGTCGATGCAACGA
	CRE2	GTGGCAGATGGCGCGGCAACACCATT

Table 7.4. Primers used for quantitative PCR.

Gene symbol	Full name	Nm number	Primer forward	Primer reverse	PCR product size
Acta1	α-skeletal Actin	NM_009606.2	CCCCTGAGGAGCACC CGACT	CGTTGTGGGTGACAC CGTCCC	169
Adrbk1	Adrenergic receptor kinase, beta 1	NM_130863.1	CACCTGCATCCGCAGC GTCA	TCCACCAAGGGCTTG GCCTCT	144
Atp2a2	ATPase, Ca^{2+} transporting, cardiac	NM_009722.2	TACTGACCCTGTCCCT GACC	CACCACCACTCCCAT AGCTT	103

	muscle, slow twitch 2				
Cacna1c	Calcium channel, voltage dependent, L type, alpha 1C	NM_009781.2	GTCCTCACCGTGTGGC CTGC	AGGGCTGTCCTGAC GAGGGC	109
Mybpc3	myosin-binding protein C, cardiac	NM_008653.2	GATGCGAGCCCTGATG AC	GACTTGAGACACTTT CTTCC	178
Myh6	Myosin, heavy chain 6, cardiac muscle, alpha	NM_010856.3	ATGGGGACTTCCGGCA GAGG	GCCTGGGCCTGGAT TCTGGT	232
Myh7	Myosin, heavy chain 7, cardiac muscle, beta	NM_080728.2	GAAGATGCGGCGGGA CCTGG	GAACGCTGCGTCTCC TCGGC	291
Nppa	Natriuretic peptide type A	NM_008725.2	CCTAAGCCCTTGTGGT GTGT	CAGAGTGGGAGAGG CAAGAC	153
Nppb	Natriuretic peptide type B	NM_008726.3	CCAGTCTCCAGAGCAA TTCAA	AGCTGTCTCTGGGCC ATTTC	
Gnas	Guanine nucleotide binding protein, alpha stimulating	NM_201618.1	CAAGGCTCTGTGGGA GGAT	CGAAGCAGGTCCTG GTCACT	147
Rn18s	18S ribosomal RNA	NC_000072.6	GCGGGGCCCGAAGCG TTTAC	AATACGAATGCCCCC GGCCG	
Slc8a1	Sodium/calcium exchanger	NM_011406.2	TGAAGCAGGCCCAGC CATTC	GGTGGGGACCAACA GCTGGA	200
Tnnc1	Troponin C, cardiac/slow skeletal	NM_009393.2	CCTGTCCTGTGAGCTG TCGCC	CTCCGCGCCCAGGA CAAAGA	120
Tnni3	Troponin I, cardiac 3	NM_009406.3	TGGAGTTGGATGGGCT GGGCT	ACTCTTCGGAGGGTG GGCCG	193
Tnnt2	Troponin T2, cardiac	NM_011619.1	AGGACACCAAACCCAA GCCCA	TCTCCACGCGCTTCC TGTGG	111

Table 7.5. Pre-miRNA references and sequences.

Pre-miRNAs	Reference	Mature miRNA Sequence
Pre-miR-24	PM10737 (Applied Biosystems)	UGGCUCAGUUCAGCAGGAACAG
Scrambled pre-miRNA	AM17111 (Applied Biosystems)	

7.8 Supplemental figures

7.8.1 Effect of soluble growth factors on endothelial cell density in BMX EHTs in the presence of AraC

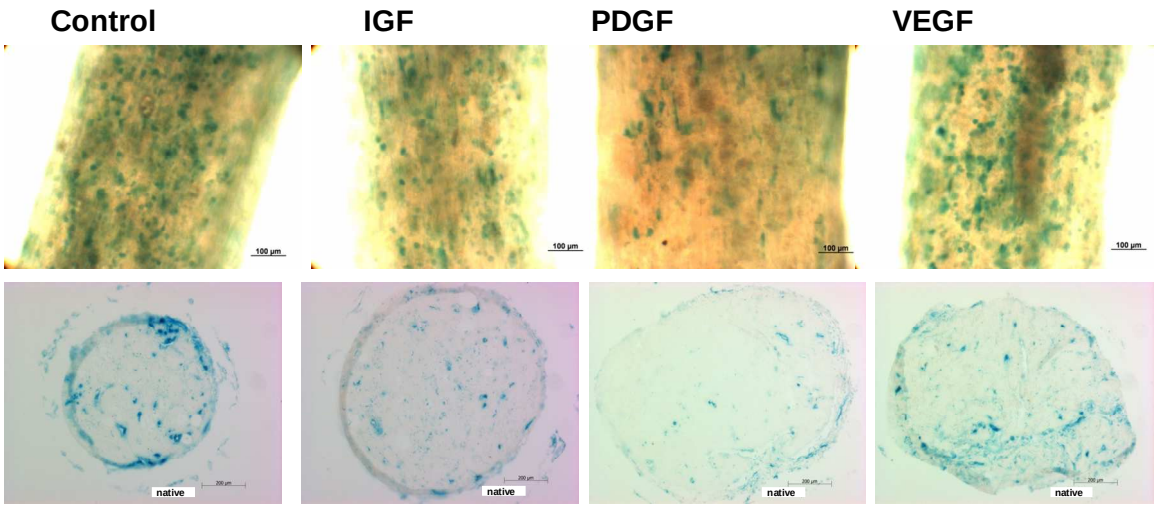

BMX EHTs after 30 days of culture.

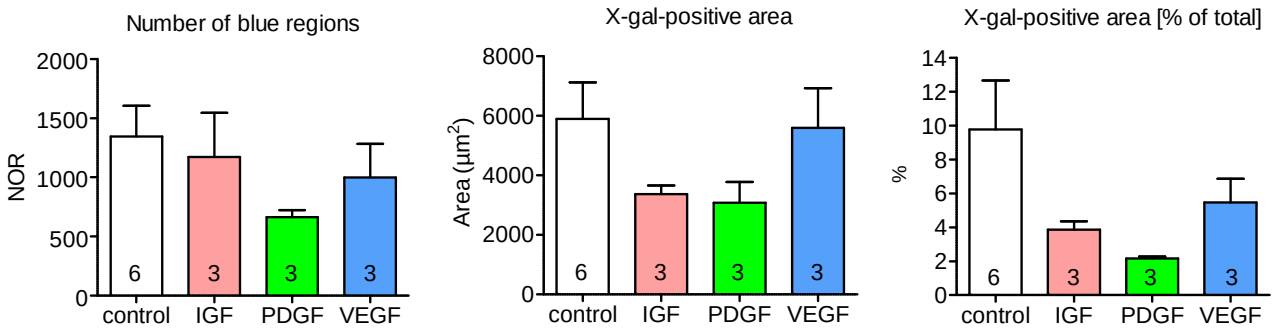

7.9 Structural formula

Tamoxifen

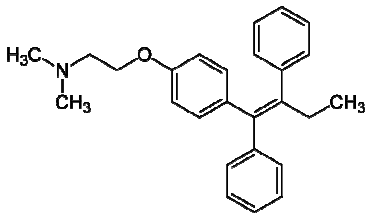

o-Hydroxytamoxifen

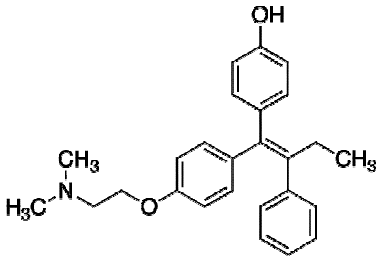

Isoprenaline

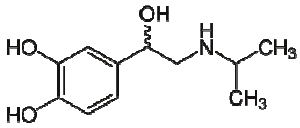

Verapamil

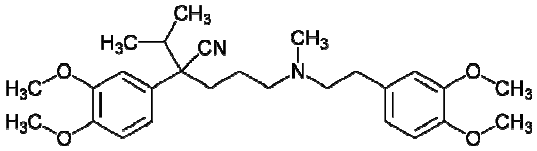

EMD 57033

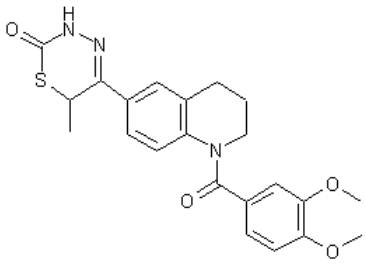

Levosimendan

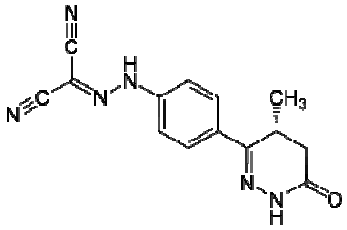

Blebbistatin

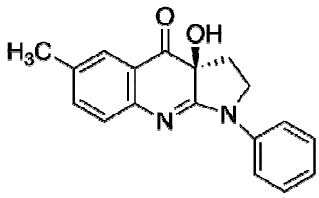

7.10 Curriculum vitae

Personal data

Name:	Andrea Stöhr
Date of birth:	07.06.1983
Place of birth:	Schwäbisch Hall

Education

1989 – 1993:	Grammar school Schwäbisch Hall-Hessental
1993 – 1999:	Schenkensee middle school Schwäbisch Hall
1999 – 2002:	Commercial high school Schwäbisch Hall
07/2002:	Abitur
2002 – 2003:	Study of business informatics at the University of cooperative education in Villingen-Schwenningen in cooperation with Bausparkasse Schwäbisch Hall AG
2003 – 2007:	Study of pharmacy at the Bavarian Julius-Maximilians-University Würzburg
09/2005:	1st part of the Pharmaceutical Examination
10/2007:	2nd part of the Pharmaceutical Examination
11/2007 – 04/2008:	Internship: Glockenapotheke in Würzburg
05/2008 – 10/2008:	Internship: Beiersdorf AG in Hamburg
12/2008	3rd part of the Pharmaceutical Examination and Licensed pharmacist (Approbation)
Since 01/2009	Ph.D. student at the Institute of Experimental Pharmacology and Toxicology (Director: Prof. Dr. med. Thomas Eschenhagen), University Center Hamburg-Eppendorf

Work experience

07/2003:	Internship: Institute of Pharmacology and Toxicology, University Würzburg
03/2004 – 04/2004:	Pharmacist at the Mohrenapotheke Schwäbisch Hall
08/2004 – 09/2004:	Pharmacist at the Ratsapotheke Bad Friedrichshall

7.11 Publications and congress participations

Original publications

Schaaf S, Shibamiya A, Mewe M, Eder A, **Stöhr A**, Hirt MN, Zimmermann WH, Conradi L, Eschenhagen T, Hansen A. Human engineered heart tissue for predictive toxicology. *PLoS One* 2011; 6, e26397

Hirt MN, Sörensen NA, Bartholdt LM, Schaaf S, Eder A, Vollert I, **Stöhr A**, Schulze T, Witten A, Stoll M, Hansen A, Eschenhagen T. Increased afterload induces pathological cardiac hypertrophy in a new in vitro model. *In revision*

Stöhr A, Friedrich FW, Flenner F, Geertz B, Eder A, Schaaf S, Hirt MN, Uebeler J, Schlossarek S, Carrier L, Eschenhagen T. Contractile abnormalities and reduced effect of verapamil and the Ca^{2+} sensitizer EMD 57033 in engineered heart tissue from *Mybpc3*-targeted knock-in and knock-out mice. *In revision*

Congress posters and presentations

Hirt MN, Conradi L, Hansen A, Eder A, **Stöhr A**, Nemchenko A, Gillette TG, Hill JA, Eschenhagen T. Acute increases in afterload in engineered heart tissue induces hypertrophy and autophagy. *8th Dutch-German Joint Meeting of the Molecular Cardiology Groups*, Rotterdam, Februrary 2010

Stöhr A, Eder A, Hansen A, Hirt MN, Schlossarek S, Carrier L, Eschenhagen T. Krankheitsmodellierung mit 3-dimensionalen Herzgeweben am Beispiel von kardialen Myosinbindungsprotein C Knockout Maus-Kardiomyozyten. *76. Jahrestagung der Deutschen Gesellschaft für Kardiologie.* Mannheim, Germany, April 2010

Hirt MN, Conradi L, Hansen A, Eder A, **Stöhr A**, Reinsch A, Flato M, Nemchenko A, Gillette TG, Hill JA, Eschenhagen T. A novel in vitro model of cardiac hypertrophy based on engineered heart tissue shows increased load-induced autophagy. *76. Jahrestagung der Deutschen Gesellschaft für Kardiologie.* Mannheim, Germany, April 2010

Stöhr A, Eder A, Hansen A, Hirt MN, Schaaf S, Schlossarek S, Carrier L, Eschenhagen T. Modelling cardiac diseases with engineered heart tissue. *Annual Meeting on Translational Basic Science of the Heart Failure Association of the European Society of Cardiology.* Berlin, Germany, April 2010

Schaaf S, Shibamiya A, Mewe M, Eder A, **Stöhr A**, Eschenhagen T, Hansen A. Human embryonic stem cell derived cardiomyocytes for engineered heart tissue. *Winter Meeting on Translational Basic Science of the Heart Failure Association of the European Society of Cardiology*, Les Diablerets, Switzerland, January 2011

Stöhr A, Eder A, Hansen A, Schlossarek S, Carrier L, Eschenhagen T. Engineered heart tissue as a three dimensional platform for modeling cardiac diseases. *Winter Meeting on Translational Basic Science of the Heart Failure Association of the European Society of Cardiology*, Les Diablerets, Switzerland, January 2011

Stöhr A, Eder A, Hansen A, Uebeler J, Hansen A, Schlossarek S, Hirt MN, Schaaf S, Carrier L, Eschenhagen T. Engineered heart tissue as a three dimensional platform for modeling cardiac diseases. *ISHR XXX European Section Meeting (in association with the ESC Heart Failure Association),* Haifa, Israel, June 2011

Stöhr A, Eder A, Uebeler J, Hansen A, Schaaf S, Schlossarek S, Carrier L, Eschenhagen T. Lack of Ca^{2+} Sensitization Induced by EMD 53998 in Engineered Heart Tissue Derived From *Mybpc3*-Knock-In and *Mybpc3*-Knock-Out Mice. *Scientific Sessions 2011 of the American Heart Association,* Orlando, United States, November 2011

Schaaf S, Shibamiya A, Mewe M, Eder A, **Stöhr A**, Hirt MN, Rau T, Zimmermann WH, Conradi L, Eschenhagen T, Hansen A. Detection of proarrhythmic effects with human engineered heart tissue. *9th annual meeting of the International Society for Stem Cell Research (ISSCR),* Canada, Toronto, 2011

Schaaf S, Shibamiya A, Mewe M, Eder A, **Stöhr A**, Hirt MN, Rau T, Zimmermann WH, Conradi L, Eschenhagen T, Hansen A. Fibrin-based engineered heart tissue for *in vitro* and *in vivo* applications. *Cardiac Stem Cell and Tissue Engineering Conference 2011*, Italy, San Servolo, 2011

8 Acknowledgement

It is a pleasure for me to thank those who made this thesis possible.

Foremost, I am heartily thankful to my supervisor Prof. Dr. Thomas Eschenhagen for giving me the opportunity to perform my Ph.D. thesis in his Institute of Experimental Pharmacology and Toxicology. Prof. Eschenhagen's supervision included not only broad knowledge, new impulses and ideas, practical support in performing experiments, but also fruitful and impulsive discussions that gave me room for self-reflection. I really learned a lot in all these years and I have always been proud to work at his side, although I could not always show it. I want to express my most profound thanks to him for giving me the opportunity to travel to many congresses and for showing me the world of science.

I thank Prof. Dr. Jürgen Duchstein for accepting the supervision of my Ph.D. thesis in the Department of Chemistry of the University of Hamburg. I am thankful for entertaining days of pharmacy with interesting talks and delicious buffets.

Many thanks go to Dr. Arne Hansen for providing me scientific guidance, which not only included practical help but also planning and explaining experiments. He always stayed calm and helped me to achieve a solid way of working without too much temper.

Further, I would like to thank Prof. Dr. Lucie Carrier for showing me her field of research. I enjoyed the friendly and scientific conversations with her and I am thankful for her help with the IonOptix analyses and for proofreading the paper.

Warm thanks got to Dr. Alexandra Eder for all her help, especially for teaching me all techniques in the first months. Her established work, her support and her knowledge helped me a lot throughout all these years. Further, I enjoyed her humor and funny conversations.

I would like to express my deep gratitude to Dr. Saskia Schlossarek for all her help, in particular, her reliable commitment to organize mouse matings and for proofreading parts of my thesis. Besides work, I enjoyed i.e. our sporting activities a lot.

I am infinitely grateful for having met Dr. Hannieh Sotoud. In all these years I have taken her to my heart and I don't want to miss her as a friend in my life for the future. I really enjoyed working closely together with her and all common activities beyond the lab.

Further, I want to thank Dr. Justus Stenzig for proofreading parts of my thesis and for the nice time in the ‘sandwich position’ in the office.

I offer my regards to all my colleagues for providing me a warm and nice working atmosphere, making me feel like home. In particular, I would like to thank Christina Baldauf, Doreen Stimpel, Kaja Breckwoldt, Dr. Marc Hirt, Dr. Sebastian Schaaf, Dr. Florian Weinberger, Dr. Felix Friedrich, Dr. Giulia Mearini, Dr. Christina Gedicke, Dr. Christiane Neuber, Sonia Singh, David Letuffe-Brenière, Ingra Vollert, Jasper Boeddinghaus, June Uebeler, Lisa Krämer, Angelika Piasecki, Silke Reischmann, Jutta Starbatty, Thomas Schulze, Birgit Geertz, Grit Höppner, Frank Neumann, Gerlinde Raasch and all the others.

Thank you to my former colleagues and friends Ute N., Sarah, Susi, Ute S. and Meike. I really enjoyed studying with those girls and I am looking forward to drink ‘Cubanicum verde’ in November again.

Thank you to my best friend Pamela in southern Germany. Without her continuous support and deep conversations I would not be that far today. I would also like to thank my friends Nicole, Lisa, Miri, Melanie, Sandra, Manuela, Saskia, Daniela and all the others from Schwäbisch Hall and my other friends Christian, Piret, Nathalie, Andrea, Björn and Stephan.

Another big thank you goes to my former teacher Helmtrud Fiegler who was like a second mother to me. She has always believed in me and I enjoyed all school lessons, class trips as well as fruitful and critical discussions with her.

Finally and especially, I would like to thank my family for their constant support throughout all these years. My warm thanks go to my mother Dorothea and my father Detlef, who were always there for me in good times as in bad. God bless my beloved grandparents. I further thank my aunty Susanne, my little sister Diane, my uncle Michael, and the woman with the big heart, namely Marion. We always stayed in touch and so I never felt lost in this big city in the north.

“The Lord is my strength and my shield; my heart trusts in him, and I am helped. My heart leaps for joy and I will give thanks to him…” – Psalm 28:7-9